Molecular modeling and design of selective histone deacetylase 11 (HDAC11) inhibitors

DISSERTATION

zur Erlangung des akademischen Grades

Doctor rerum naturalium (Dr. rer. nat.)

der Naturwissenschaftlichen Fakultät I Biowissenschaften

der Martin-Luther-Universität Halle-Wittenberg

vorgelegt von

Herrn M.Sc. Fady Noshy Ishak Baselious

This page left intentionally blank.

Gutachter:

Prof. Dr. Wolfgang Sippl, Halle, Germany.

Prof. Dr. Mike Schutkowski, Halle, Germany.

Prof. Dr. Cyril Barinka, Vestec, Czech Republic.

Verteidigungsdatum: 08-01-2025

This page left intentionally blank.

Abstract

Histone deacetylase 11 (HDAC11) is an enzyme that catalyzes the removal of acyl groups from acylated lysine residues. It is the most recently discovered isoform and the sole member of class IV of HDACs family. Multiple studies provided evidence for the involvement of HDAC11 in various biological processes and pathological conditions, thus establishing HDAC11 as an interesting target for potential therapeutic intervention. So far, no crystal structure for HDAC11 has been reported. HDAC11 is less homologous to other HDAC family members as the catalytic domain of HDAC11 shares only low sequence identity with these isoforms. This fact makes the conventional template-based homology modeling more challenging and less reliable to obtain models with high accuracy. AlphaFold2 (AF2) is an AI deep learning approach that was reported to predict the 3D structures of proteins with atomic accuracy. One limitation of using the models from this approach in SBDD is that it predicts the folding of the proteins in absence of small molecules such as cofactors and ligands. This leads to the prediction of collapsed binding sites, for which post-modeling refinement is necessary.

In this work, the HDAC11-AF2 model was optimized by adding the catalytic zinc ion followed by minimization in presence of transplanted ligands that were previously reported as HDAC11 inhibitors. The optimized model was then successfully employed to study the binding mode of selective HDAC11 inhibitors described in literature by molecular docking. Docking of the 16-carbon long alkyl hydrazide SIS17 was performed to explore the foot pocket and to identify the tunnel that can accommodate such long alkyl substituents.

The resulted model from the optimization process was further utilized to execute a comparative multistep structure-based virtual screening workflow to identify new selective HDAC11 inhibitors. In this workflow, multiple computational techniques, such as structure-based pharmacophore screening, molecular docking, pose filtering, and prioritization, were implemented. The workflow was successful in identifying potential hit that was subsequently evaluated by in vitro enzymatic assays. The hit compound exhibited an IC_{50} of 3.5 µM for HDAC11 and was able to selectively inhibit HDAC11 over other HDAC isoforms at 10 µM concentration.

Moreover, the optimized model was used for the structure-based design of selective HDAC11 inhibitors bearing a novel scaffold. For this purpose, the predicted docking pose of FT895 was utilized. The most promising compound showed an IC_{50} of 365 nM and could inhibit HDAC11

selectively. It also demonstrated promising activity on neuroblastoma cell line with an EC_{50} of 3.6 μM.

The model was also used to study the binding mode of alkyl hydrazide inhibitors from the in-house dataset. Furthermore, a ligand-based virtual screening workflow implementing a classification categorical model, developed using the in-house alkyl hydrazide inhibitors dataset, was devised and executed to identify new alkyl hydrazide HDAC11 inhibitors that lie within the in-house chemistry toolbox. The workflow successfully identified several potential hits. The binding mode of the hits of interest was studied using the optimized AF2 model. The predicted binding modes of the reported inhibitors, the identified virtual screening hits and the designed compounds were further evaluated by molecular dynamics simulation which could confirm the initial prediction.

Keywords: HDAC11, AlphaFold, model optimization, docking, molecular dynamics simulation, virtual screening, classification model, selective inhibitor, alkyl hydrazide, anti-neuroblastoma.

Kurzfassung

Die Histondeacetylase 11 (HDAC11) ist ein Enzym, das die Entfernung von Acylgruppen aus acylierten Lysinresten katalysiert. Es ist die zuletzt entdeckte Isoform und das einzige Mitglied der Klasse IV der HDAC-Familie. Mehrere Studien lieferten Beweise für die Beteiligung von HDAC11 an verschiedenen biologischen Prozessen und pathologischen Zuständen, was HDAC11 zu einem interessanten Ziel für potenzielle therapeutische Eingriffe macht. Bisher wurde noch keine Kristallstruktur für HDAC11 veröffentlicht. HDAC11 ist weniger homolog zu anderen Mitgliedern der HDAC-Familie, da die katalytische Domäne von HDAC11 nur eine geringe Sequenzidentität mit diesen Isoformen aufweist. Diese Tatsache macht die konventionelle, auf Vorlagen basierende Homologiemodellierung zu einer größeren Herausforderung und weniger zuverlässig, um Modelle mit hoher Genauigkeit zu erhalten. AlphaFold2 (AF2) ist ein KI-Ansatz für tiefes Lernen, der die 3D-Strukturen von Proteinen mit atomarer Genauigkeit vorhersagen kann. Eine Einschränkung bei der Verwendung der Modelle dieses Ansatzes in SBDD besteht darin, dass er die Faltung der Proteine ohne kleine Moleküle wie Kofaktoren und Liganden vorhersagt. Dies führt zur Vorhersage von kollabierten Bindungsstellen, für die eine Verfeinerung der Modellierung erforderlich ist.

In dieser Arbeit wurde das HDAC11-AF2-Modell durch Hinzufügen des katalytischen Zink-Ions optimiert, gefolgt von einer Minimierung in Gegenwart von eingefügten Liganden, die zuvor als HDAC11-Inhibitoren beschrieben wurden. Das optimierte Modell wurde dann erfolgreich eingesetzt, um den Bindungsmodus von selektiven HDAC11-Inhibitoren, die in der Literatur beschrieben sind, durch molekulares Docking zu untersuchen. Das Docking des 16-Kohlenstoff-Langalkylhydrazids SIS17 wurde durchgeführt, um die Fußtasche in HDAC11 zu erkunden und den Tunnel zu identifizieren, der solche langen Alkylsubstituenten aufnehmen kann.

Das aus dem Optimierungsprozess hervorgegangene Modell wurde dann zur Durchführung eines vergleichenden, mehrstufigen, strukturbasierten virtuellen Screenings verwendet, um neue selektive HDAC11-Inhibitoren zu identifizieren. In diesem Arbeitsablauf wurden mehrere computergestützte Techniken, wie strukturbasiertes Pharmakophor-Screening, molekulares Docking, Pose-Filterung und Priorisierung, eingesetzt. Die gewählte Prozedur war erfolgreich bei der Identifizierung eines potenziellen Inhibitors, der anschließend durch in vitro enzymatische Assays getestet wurde. Der gefundenen Hit wies einen IC_{50} von 3,5 µM für

HDAC11 auf und war in der Lage, HDAC11 gegenüber anderen HDAC-Isoformen bei einer Konzentration von 10 µM selektiv zu hemmen.

Darüber hinaus wurde das optimierte Modell für das strukturbasierte Design von selektiven HDAC11-Inhibitoren mit einem neuartigen Gerüst verwendet. Zu diesem Zweck wurde die vorhergesagte Docking-Position von FT895 verwendet. Die vielversprechendste Verbindung zeigte einen IC_{50} von 365 nM und konnte HDAC11 selektiv hemmen. Sie zeigte auch eine vielversprechende Aktivität bei Neuroblastom-Zelllinien mit einem EC_{50} von 3,6 µM.

Das Modell wurde auch verwendet, um den Bindungsmodus von Alkylhydrazid-Inhibitoren aus dem internen Datensatz zu untersuchen. Darüber hinaus wurde ein ligandenbasierter virtueller Screening-Workflow unter Verwendung eines kategorialen Klassifizierungsmodells entwickelt und ausgeführt, um neue Alkylhydrazid-HDAC11-Inhibitoren zu identifizieren, die in der hauseigenen chemischen Toolbox enthalten sind. Der Arbeitsablauf identifizierte erfolgreich mehrere potenzielle Treffer. Der Bindungsmodus der Treffer von Interesse wurde mit dem optimierten AF2-Modell untersucht. Die vorhergesagten Bindungsmodi der gemeldeten Inhibitoren, der identifizierten virtuellen Screening-Treffer und der entworfenen Verbindungen wurden durch Molekulardynamiksimulationen weiter evaluiert, die die anfängliche Vorhersage bestätigen konnten.

Schlagwörter: HDAC11, AlphaFold, Modelloptimierung, Docking, virtuelles Screening Molekulardynamiksimulationen, , Klassifikationsmodell, selektiver Inhibitor, Alkylhydrazid, Anti-Neuroblastom.

Acknowledgment

I would like to express my deep gratitude to **Professor Dr. Wolfgang Sippl** for giving me the chance to work for my PhD within his group and under his supervision. I am very thankful for his patience, guidance and kind support to overcome the challenges and get most of my work published.

I would also like to extend my gratitude to **Dr. Dina Robaa** and **PD Dr. habil. Matthias Schmidt**, as well as all my colleagues in the modeling and chemistry labs, specially **Christopher Vorreiter**, **Talha Zahid Yesiloglu**, **Dr. Ehab Ghazy**, **Dr. Mohamed Abdelsalam**, **Abdallah Alfayomy**, and **Assoc. Prof. Dr. Hany Ibrahim**. Their assistance and support have been invaluable and always available whenever needed.

Special thanks to my sister **Nancy Baselious** for her efforts, help and support.

Dedication

I dedicate this dissertation to the memory of my mother, **Amal Girgis Hanna Attia**.

Table of contents

List of figures

List of tables

List of abbreviations

ADP	Adenosine diphosphate
ADSCs	Adipose-derived stem cells
AF	AlphaFold
APC	Antigen-presenting cells
ATP	Adenosine triphosphate
BAT	Brown adipose tissue
CADD	Computer-aided drug design
CASP	Critical assessment of protein structure prediction
cccDNA	Covalently closed circular DNA
CDK20	Cyclin-dependent kinase 20
CoREST	Co-repressor of REST
CpG	Cytosine phosphate guanine
CSCs	Cancer stem cells
DNMT	DNA methyltransferases
Egr-1	Early growth response 1
ENV-71	Enterovirus 71
GPCR	G-protein coupled receptor
HAT	Histone acetyltransferase
HDAC	Histone deacetylase
HEY1	Hairy/enhancer-of-split related with YRPW motif 1
HFMD	Hand, foot and mouth disease
HKMT	Histone lysine methyltransferase
HM	Homology modeling
IFN	Interferon
IFNαR	Interferon alpha receptor
IL-10	Interleukin 10
LSD	Lysine-specific demethylase
MBT	Malignant brain tumor
MD	Molecular dynamics
MEF2	Myocyte enhancer factor 2
MiDAC	Mitotic deacetylase complex
mRNA	Messenger RNA

mSin3A	Mammalian switch-independent 3A
NAD	Nicotinamide adenine dinucleotide
NCoR	Nuclear receptor co-repressor
NSCLC	Non-small cell lung cancer
NuRD	Nucleosome remodeling and deacetylase complex
PAE	Predicted aligned error
pLDDT	Predicted local distance difference test
POLA1	DNA Polymerase alpha 1
PTM	Post-translational modification
QSAR	Quantitative structure-activity relationship
REOS	Rapid elimination of swill
RF	RoseTTAFold
RFAA	RoseTTAFold All-Atom
RFNA	RoseTTAFoldNA
RMSD	Root mean square deviation
RMSF	Root mean square fluctuation
Runx2	Runt-related transcription factor 2
SBDD	Structure-based drug design
SHMT2	Serine hydroxymethyltransferase 2
Sin3A	Switch-independent 3A
Sir2	Silent information regulator 2
SIRT	Sirtuin
SMRT	Silencing mediator for retinoid and thyroid receptors
SOX2	Sex-determining region Y-box 2
SRF	Serum response factor
TNFα	Tumor necrosis factor alpha
TSA	Trichostatin A
VS	Virtual screening
WAT	White adipose tissue
ZBG	Zinc binding group

1. Introduction

This page left intentionally blank.

1.1. Epigenetics

Epigenetics is the field of study of regulatory mechanisms which result in heritable and reversible gene expression alterations that do not involve DNA sequence modification [1]. Epigenetic mechanisms can alter the accessibility to genetic material, thus regulating the gene expression by promoting or repressing its transcription [2, 3]. Among the identified mechanisms to date are DNA methylation and chromatin post-translational modification (PTM) [1, 4]. Epigenetic modifications are vital for maintaining biological functions. However, aberrations in epigenetic regulatory mechanisms can lead to abnormal activation or repression of genes, resulting in pathophysiological conditions, especially cancers [5].

One of the earliest identified and most stable epigenetic alterations is DNA methylation [6]. In humans, it predominantly involves adding a methyl group on the fifth position of cytosine to produce 5-methylcytosine, mainly in the cytosine phosphate guanine dinucleotide (CpG) motifs that are often clustered to form the CpG islands [7, 8]. DNA methylation is controlled by a highly conserved protein family known as DNA methyltransferases (DNMTs) [9]. DNMT1 is a maintenance methyltransferase which is required to maintain the methyl mark through the methylation of hemi-methylated DNA. On the other hand, DNMT3a and DNMT3b are de novo methyltransferases that can produce new methylation pattern to unmodified DNA. DNMT3L is catalytically inactive but required for the activation of the de novo DNMT3a [7, 10]. DNA methylation represses gene expression by impairing the binding of transcriptional activators or recruiting proteins that inhibit the binding of transcription factors to DNA [9].

Since chromatin PTM is more relevant for this work, it will be discussed in more details in the following section.

1.2. Chromatin post-translational modification

The DNA in eukaryotic cells is stored folded inside the nucleus in a packed form within a nucleoprotein complex known as chromatin. Chromatin is a polymeric complex that comprises histone and non-histone proteins as well as genetic materials. Nucleosomes (**Figure 1**) are the basic building units of chromatin and are further composed of about 146 base pairs wrapped around octamers consisting of one pair of each of the core histone proteins H2A, H2B, H3 and H4. Nucleosomes are connected by linker H1 histone protein and linker DNA [2, 11]. Histone proteins consist of globular structure along with intrinsically disordered regions known as histone tails. Histone tails contain lysine and arginine and are highly positively charged [11,

12]. In general, histone tails interact with DNA, thus maintaining the compactness of the genetic material and limiting its accessibility to the transcription factors leading to transcription suppression [13].

Histone tails are protruding out from the core and represent the usual sites for PTM. Among these, the most common are acetylation and methylation of lysine residues [12, 14]. PTM reduces the net positive charge of histone proteins, thus weakening the electrostatic interactions with the negatively charged DNA. This leads to a less compact and accessible genetic material and consequently promotes transcription [15]. Growing evidence demonstrated that PTM of the chromatin is involved in regulating several cell functions, such as DNA replication and repair, chromatin packaging, gene expression, and chromosome dynamics [16].

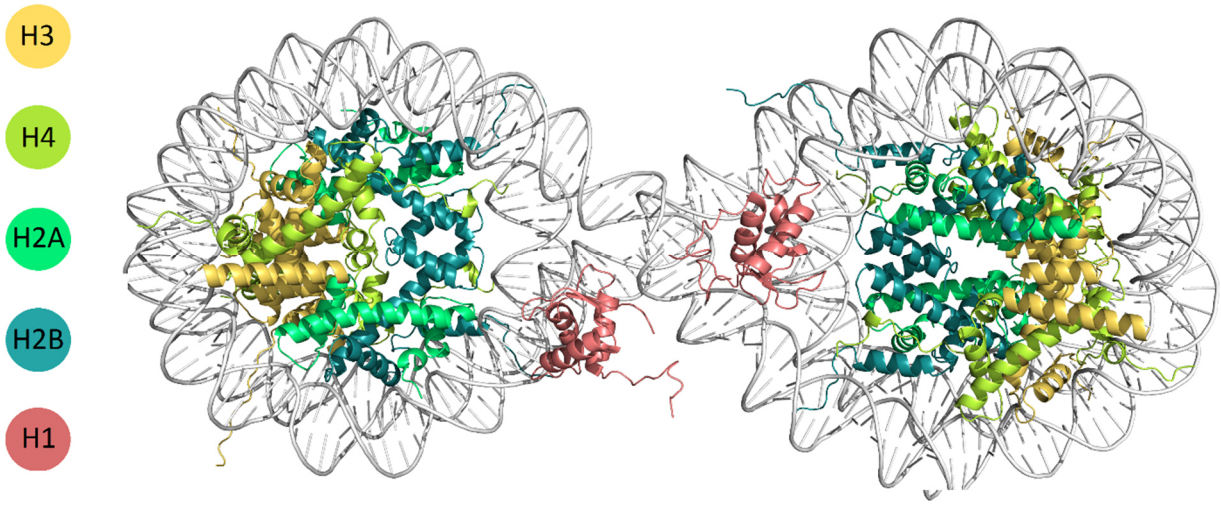

Figure 1. Nucleosome structure (PDB ID: 8YTI) showing the DNA as white cartoon wrapped around four core histone proteins: H3, H4, H2A and H2B along with the linker histone protein H1.

Enzymes involved in chromatin PTM can be classified into three classes, referred to as writers, reads and erasers [17]. Writers are capable of modifying the histone protein by adding marks. One example is the histone lysine methyltransferases (HKMTs) that can add up to three methyl groups on a single lysine residue [18]. Another example is the histone acetyltransferases family (HATs), which catalyzes the transfer of acetyl group from acetyl-CoA cofactor to the lysine residue side chain [19]. Readers are able to recognize specific epigenetic marks. Several protein domains have been identified as readers for histone epigenetic marks. Examples include bromodomains for the acetylated histone protein, as well as MBT, Tudor and chromo-domains for the methylated histones [20, 21].

Erasers are enzymes that are catalyzing the removal of epigenetic marks. The lysine-specific demethylase LSD1 is an example of eraser enzymes. It acts to eliminate the methyl mark from the modified lysine residues of the histone protein [22, 23]. Another example is the histone deacetylases family (HDACs), which catalyzes histone deacetylation by removing the ε-amino acetyl group from lysine residues [24].

1.3. Histone deacetylases (HDACs)

Mammalian histone deacetylase enzymes are grouped into two main groups (**Figure 2**) based on their catalytic domain and the associated cofactor [17]. The classical HDACs group comprises 11 zinc-dependent proteins and is further divided, based on sequence similarity to yeast deacetylases, into class I (HDAC1-3 and 8), class IIa (HDAC4, 5, 7, 9), class IIb (HDAC6 and 10) and class IV (HDAC11) [25]. The non-classical HDACs group constitutes class III, which includes seven proteins known as sirtuins (SIRT1-7). Sirtuins depend on nicotinamide adenine dinucleotide (NAD) as a cofactor for their deacetylase activity [26].

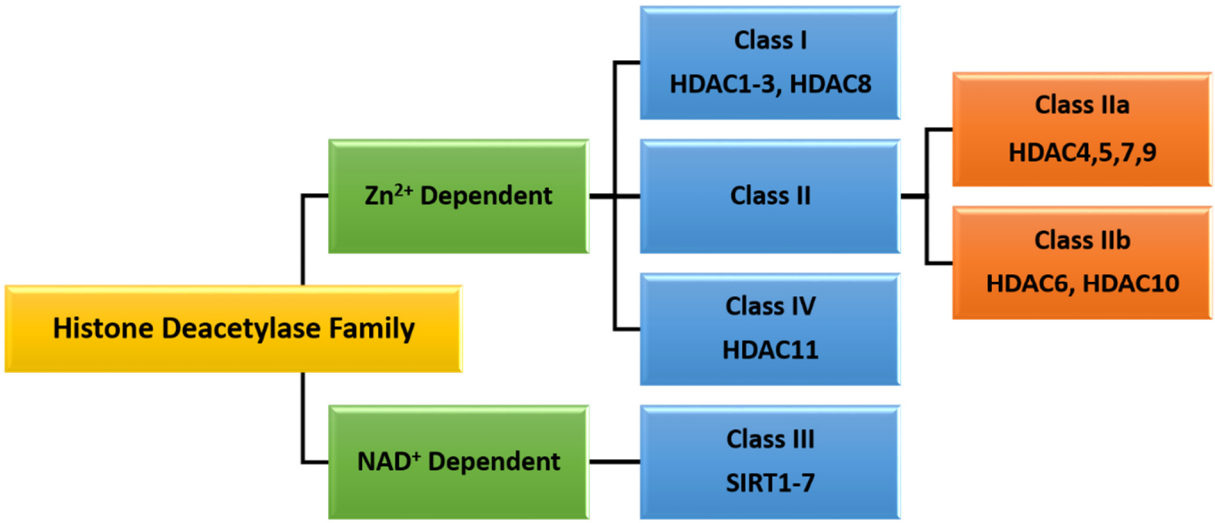

Figure 2. Classification of histone deacetylase family.

Class I HDACs are highly homologous to the yeast HDAC Rpd3. They are mainly localized in the nucleus and show ubiquitous expression [27]. HDAC1 and HDAC2 form the catalytic core in repressive complexes with the transcriptional regulatory protein Sin3A, nucleosome remodeling and deacetylase complex (NuRD) and co-repressor of REST (CoREST) [28]. They also represent an integral component of the mitotic deacetylase complex (MiDAC) [29].

HDAC3 can form complexes with the silencing mediator for retinoid and thyroid receptors (SMRT) and nuclear receptor co-repressor (NCoR) and is catalytically inactive when not recruited to these co-repressors [30]. In contrast, HDAC8 represents a unique member of class I HDACs as it can function catalytically without forming complexes [31]. Additionally, it possesses a defatty-acylase activity that has been demonstrated to be higher than its deacetylase activity, thus hypothesized to be of physiological function [32].

Class II HDACs demonstrate high homology with yeast HDA1 [33]. Besides their catalytic domain, class IIa HDACs possess a long N-terminal region [33]. Within this region, different transcriptional partners, such as myocyte enhancer factor 2 (MEF2) [34], serum response factor (SRF) [35] and Runx2 [36, 37], can bind. This N-terminal region contains serine residues that serve as sites for phosphorylation, thus leading to the binding of 14-3-3 proteins, which in turn influence the shuttling of these enzymes between the nucleus and the cytoplasm [27, 38]. While members of this class demonstrate very low deacetylase catalytic activity, due to the replacement of the conserved catalytic tyrosine residue in the catalytic core region by histidine [39], they can form a large complex with SMRT/N-CoR-HDAC3 complex [40].

Class IIb comprises HDAC6 and HDAC10, both of which are localized in the cytoplasm. HDAC6 possesses tandem deacetylase domains [41] as well as a C-terminal zinc finger ubiquitin binding domain [42], while HDAC10 contains a single deacetylase catalytic domain besides a C-terminal leucine-rich repeat domain [43]. HDAC6 can also catalyze the deacetylation of other substrates than histone proteins [44], such as cortactin [45], α-tubulin [46], IFNαR [47] and chaperones [48]. On the other hand, HDAC10 demonstrated a robust polyamine deacetylase activity [49].

Class III HDACs demonstrate homology to the yeast silent information regulator 2 (Sir2). The seven members of this class (SIRT1-7) show different subcellular localization and function [50]. SIRT1 is localized mainly in the nucleus but can shuttle to the cytoplasm, whereas SIRT2 is primarily present in the cytoplasm. SIRT3-5 are localized in the mitochondria, while SIRT6 and SIRT7 are found in the nucleus [17, 51]. Sirtuins have a variety of histone and non-histone protein substrates and possess a wide range of enzymatic activities [50].

Class IV contains HDAC11, which is homologous to yeast Hos3. HDAC11 is the latest identified member of the HDACs family and one of the least studied isoforms [52].

1.4. HDAC11

HDAC11 is the sole member of the zinc-dependent class IV HDACs with a predominant nuclear localization [52]. It contains 347 amino acid residues, making it the smallest member of HDACs family identified to date with molecular mass of 39 kDa. The catalytic domain of HDAC11 constitutes approximately 80% of the protein sequence, while the short N- and C-termini do not indicate for possible protein binding sites [52, 53]. Unlike class I and class II HDACs family members, HDAC11 does not form large functional complexes with mSin3A, N-CoR, or SMART. However, the co-immunoprecipitation of HDAC6 with HDAC11 suggests that HDAC11 can interact with other HDAC isoforms in vivo [52, 54].

Analysis of the aligned HDAC11 sequence with other HDAC isoforms confirmed the presence of the nine conserved sequence motifs, similar to other eukaryotic HDACs [31, 52, 55], which are probably important for the deacetylase activity. Additionally, the catalytic core region of HDAC11 contains the conserved amino acid residues resembling class I and class II HDACs [52]. The 3D structure of HDAC11 is not elucidated so far. HDAC11 shares high similarity with class I and class II HDAC members when comparing the catalytic core region [52, 56]. However, its overall protein sequence demonstrates slight homology to other HDAC isoforms [52]. The expression level of HDAC11 is primarily high in the skeletal muscle, brain, kidney, heart, and testis tissues [52]. Moreover, HDAC11 is expressed in pancreatic beta cells and regulated by cytokines [57].

Initially, It was found that the in vitro deacetylase activity of FLAG-tagged HDAC11, when expressed in 293 cells, is much lower than other HDAC isoforms [52]. The authors suggested that the lower expression level of the FLAG-tagged HDAC11, compared to the other tested FLAG-tagged isoforms, along with the utilization of a non-endogenous synthetic peptide derived from H4 histone protein as a substrate, might be the reason for the lower observed activity. However, more recent studies confirmed that HDAC11 possesses favorable and robust defatty-acylase activity, which is > 10,000 fold more efficient than its deacetylase activity. This finding suggests the defatty-acylation as a predominant enzymatic activity in vivo [58-61].

1.5. Biological relevance of HDAC11

Several studies have demonstrated that HDAC11 is implicated in various biological functions as well as pathophysiological processes. HDAC11 is involved in immune system modulation [62] and has been found to act as a repressor for IL-10 transcription in the antigen-presenting

cells (APC) [63]. Moreover, HDAC11 interacts with HDAC6 to form a complex through the C-terminus of HDAC6 and N-terminus of HDAC11 in the nucleus and cytoplasm of APC to regulate IL-10 transcription through playing divergent repression/activation roles [54].

HDAC11 plays a role in regulating type I IFN signaling, which is responsible for the activation of many genes that are crucial for immune response. This regulatory role is mediated through defatty-acylation of SHMT2. HDAC11 knockout in mice led to increased IFN signaling, which presents HDAC11 as an interesting target to develop therapeutics for diseases in which increased IFN signaling is beneficial, such as viral infections and multiple sclerosis [60]. In contrast, HDAC11 showed to exhibit antiviral activity against influenza A virus by playing a role in the host innate immune response [64]. Additionally, it restricts the replication of the hepatitis B virus through inhibiting the covalently closed circular DNA (cccDNA) transcription [65].

The link between HDAC11 and obesity development has been investigated by multiple studies [66-68]. HDAC11 expression levels showed to be higher in the white adipose tissue (WAT) of different obese mice models compared to the wild-type mice. Knockout of HDAC11 protected high-fat diet mice model from hyperlipidemia and gaining weight. It also could improve glucose tolerance, alleviate insulin resistance and reduce hepatic steatosis [69]. Moreover, it augmented the metabolic activity by elevating the calorie expenditure and oxygen consumption [70]. Additionally, the depletion of HDAC11 stimulated the differentiation of the adipose-derived stem cells (ADSCs) into brown adipocyte-like cells [69]. It was also found to enhance the function of the metabolically active brown adipose tissue (BAT) as well as the transformation of WAT into beige fat [71]. Collectively, these findings suggest HDAC11 as a feasible target for the treatment of obesity-related and metabolic diseases [72].

Furthermore, a number of studies discussed the involvement of HDAC11 in cancer development and progression [73, 74]. It has been reported that HDAC11 messenger RNA (mRNA) levels are extremely high in many cancer cells [52]. HDAC11 was found to be overexpressed in both squamous cell lung cancer and lung adenocarcinoma. The overexpression of HDAC11 in lung cancer is correlated with poor prognosis and low survival rate [75]. Another study demonstrated that the high expression level of HDAC11 in liver cancer cells is inversely correlated with the expression of tumor suppressor p53. HDAC11 forms a complex with the transcription factor Egr1 and induces its deacetylation. This process leads to the suppression of p53 gene transcription and the inhibition of cell apoptosis [76]. A similar

effect of HDAC11 overexpression was observed in pituitary tumor cells through complex formation with HEY1 transcription factor [77]. Moreover, the inhibition of HDAC11 demonstrated beneficial effects in carcinoma. For example, HDAC11 inhibition induced apoptosis and suppressed the proliferation of myeloproliferative neoplasms [78], while its depletion caused neuroblastoma cell death via caspase-mediated apoptosis [79].

Although not fully elucidated, the biological function of HDAC11 and its role in multiple pathological conditions discussed above highlight the potential of HDAC11 as an interesting target in therapeutics development for the treatment of various ailments.

1.6. HDAC11 inhibitors

1.6.1. General pharmacophore of HDAC inhibitors

The general pharmacophore of HDACs inhibitors comprises three main substructures: a zinc binding group (ZBG) and a capping group that are connected by a linker (**Figure 3**). The ZBG coordinates the zinc cofactor in the depth of the binding site through either a monodentate or a bidentate chelation mode. The capping group can act to make further interactions with any of the four solvent-exposed surface loops of the binding site rim. Among the known ZBGs, hydroxamic acid is the most well-characterized and common functionality [80-82]. Other defined ZBGs include 2-aminobenzamide [83, 84], alkyl hydrazide [85-88], thiols [89], alkyl ketones [90], aryl ketones [91], trifluoromethyl ketones [92], epoxy ketones [93], trifluoromethyloxadiazoles [94] and amino acid/ketone derivatives [95]. Some ZBGs can influence selectivity according to their sub-structural attachments that target an internal cavity perpendicular to the catalytic binding site known as foot pocket [80]. For example, 2-aminobenzamides are selective class I HDAC inhibitors over other classes [84], while alkyl hydrazide inhibitors can show selectivity for class I over class II, which lacks the foot pocket that can accommodate the N`-alkyl attachment to the hydrazide moiety [85]. Isoform selective HDAC inhibition can be also targeted by adjusting the structure and position of the linker and the capping group to target sub-pockets within the binding site [80]. One example is the characteristic lower pocket in class IIa HDACs. This sub-pocket is formed near the zinc ion as a result of the flipped-out conformation of the histidine residue in loop 7, which is a replacement of the conserved catalytic tyrosine residue in other classic HDACs [96, 97]. Another example of HDACs binding site sub-pockets is the proposed side pocket characteristic for HDAC8, which is lined by the catalytic tyrosine residue and residues from loop 1 and loop 6 [80, 98].

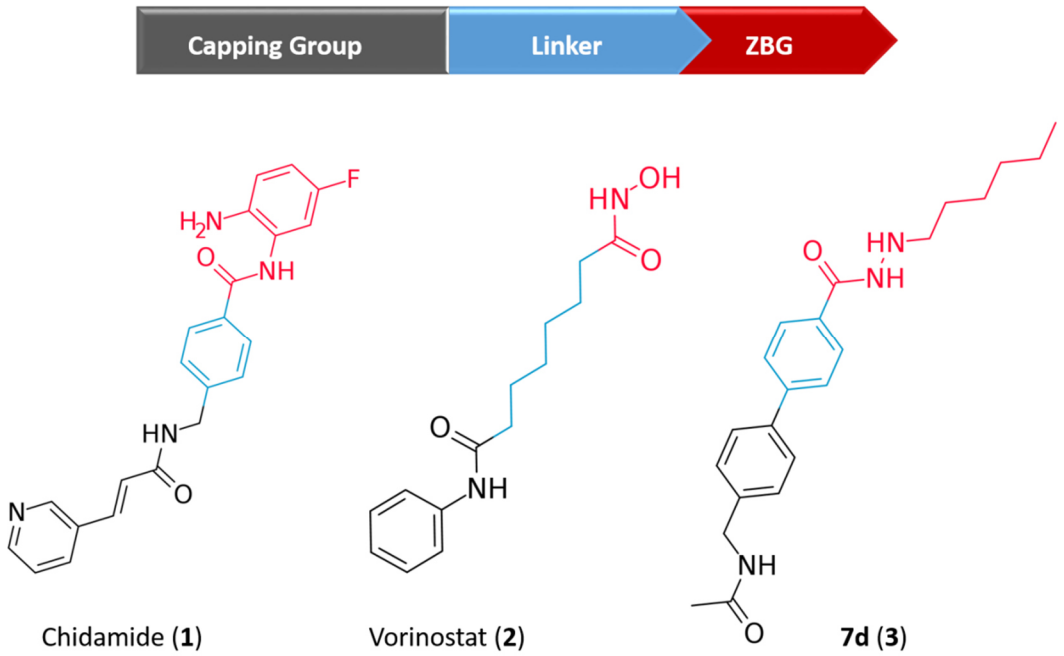

Figure 3. General pharmacophore of zinc-dependent histone deacetylase inhibitors and examples of inhibitors with different zinc binding groups including the aminobenzamide derivative chidamide, the hydroxamic acid derivative vorinostat and the alkyl hydrazide derivative compound **7d** [85].

1.6.2. Reported HDAC11 inhibitors

Several nonselective HDAC ligands of various scaffolds, such as hydroxamic acids, 2-aminobenzamides and cyclic peptide inhibitors, which were described in literature (**Figure 4**), were also reported to inhibit HDAC11. These compounds demonstrated inhibitory activity in the range of sub-nanomolar to sub-micromolar IC_{50}. The hydroxamic acid derivative quisinostat (**4**) [99] and the natural product romidepsin (**5**), which is a cyclic peptide derivative bearing a thiol ZBG [100], showed a sub-nanomolar IC_{50} for HDAC11. While other hydroxamic acid compounds such as dacinostat (**6**) [101], fimepinostat (**7**) [102] and trichostatin A (**8**) [103-106] were reported to inhibit HDAC11 at a low nanomolar IC_{50}. For the 2-aminobenzamide analogue mocetinostat (**9**) [99, 107] and the cyclic peptide with epoxy ketone ZBG trapoxin A (**10**) [59], a weaker sub-micromolar IC_{50} was observed.

While the inhibitors mentioned above demonstrate promising inhibition for HDAC11, re-evaluation of their IC_{50} using a substrate that is structurally closer to the HDAC11 physiological substrates showed great variation. Taking into consideration the confirmed robust defatty-acylase activity of HDAC11 and the less preference of HDAC11 for acetylated substrates, Kutil et al. [61] re-assayed these inhibitors using a long alkyl chain acylated peptide (peptide 1) as a substrate. The peptide substrate is derived from the tumor necrosis factor (TNFα), in which the

in vivo myristoylation site corresponding to the side chain of Lys20 is acylated with fluorescent N-anthraniloylated 11-aminoundecanoic acid, while an L-3-nitrotyrosine quencher replaces the adjacent naturally occurring threonine residue. Interestingly, in this study, only trapoxin A and fimepinostat could retain considerable HDAC11 inhibitory activity, with an IC_{50} lying approximately within the same range that was previously reported in other literature. In contrast, all other inhibitors which were re-evaluated in this study showed much less activity towards HDAC11, with IC_{50} lying in the micromolar range.

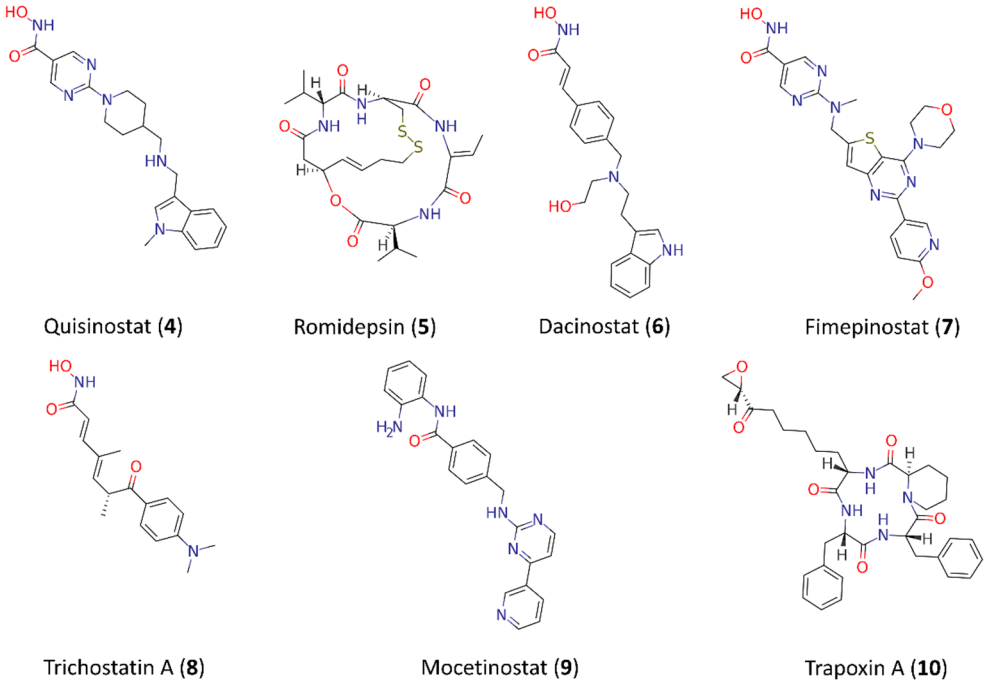

Figure 4. 2D structures of previously reported non-selective HDAC11 inhibitors.

Few selective HDAC11 inhibitors have been reported in literature (**Figure 5**). FT895 (**11**) is an isoindoline derivative with hydroxamic acid ZBG and is one of the first HDAC11 selective inhibitors discovered by Forma Therapeutics. FT895 also showed variation in its inhibitory activity when changing the substrates utilized in the in vitro assay. When using triflouroacetyl lysine peptide as a substrate, IC_{50} in a nanomolar range was observed (3 nM) [108]. However, using the more physiologically relevant myristoyl lysine substrate resulted in IC_{50} in a sub-micromolar range (740 nM) [109]. As HDAC11 inhibitor, FT895 was found to be effective in the inhibition of enterovirus 71 (ENV-71) replication and was suggested as potential candidate for the treatment of the hand, foot and mouth disease (HFMD) caused by such viral infection [110]. FT895 could also exert beneficial effects in combating tumors. For example, it showed significant inhibition of the self-renewal ability of cancer stem cells (CSCs) from non-small

cell lung cancer (NSCLC) and reduced Sox2 transcription factor expression, which is essential for CSCs survival [75]. PB94 (**12**) is a selective HDAC11 hydroxamic acid inhibitor bearing a methoxy substitution in the ortho position to the hydroxamic acid functionality. Inhibition of HDAC11 using PB94 demonstrated beneficial effect in a neuropathic pain mouse model. Thus it is suggested as potential drug candidate for neurological disorders. [111]

Taking advantage of the ability of HDAC11 to accommodate longer alkyl chain, reflected by its confirmed defatty-acylase activity, researchers designed and developed ligands bearing long alkyl chains as selective HDAC11 inhibitors. SIS17 (**13**) is an alkyl hydrazide derivative bearing 16-carbon long alkyl chain that showed inhibitory activity for HDAC11 in a sub-micromolar range (IC_{50} = 830 nM) [109]. Another example is TD034 (**14**), which is an analogue of trapoxin A with IC_{50} in a low nanomolar range (5.1 nM) [112].

MIR002 is a hydroxamic acid dual inhibitor bearing a bulky adamantine group. It could inhibit HDAC11 and DNA polymerase alpha 1 (POLA1) simultaneously and showed selective inhibition of HDAC11 over other isoforms. MIR002 (**15**) demonstrated promising wide spectrum antitumor activity. However, it is worth noting that it exhibited only weak inhibition for HDAC11 (IC_{50} = 6.09 μM) [113].

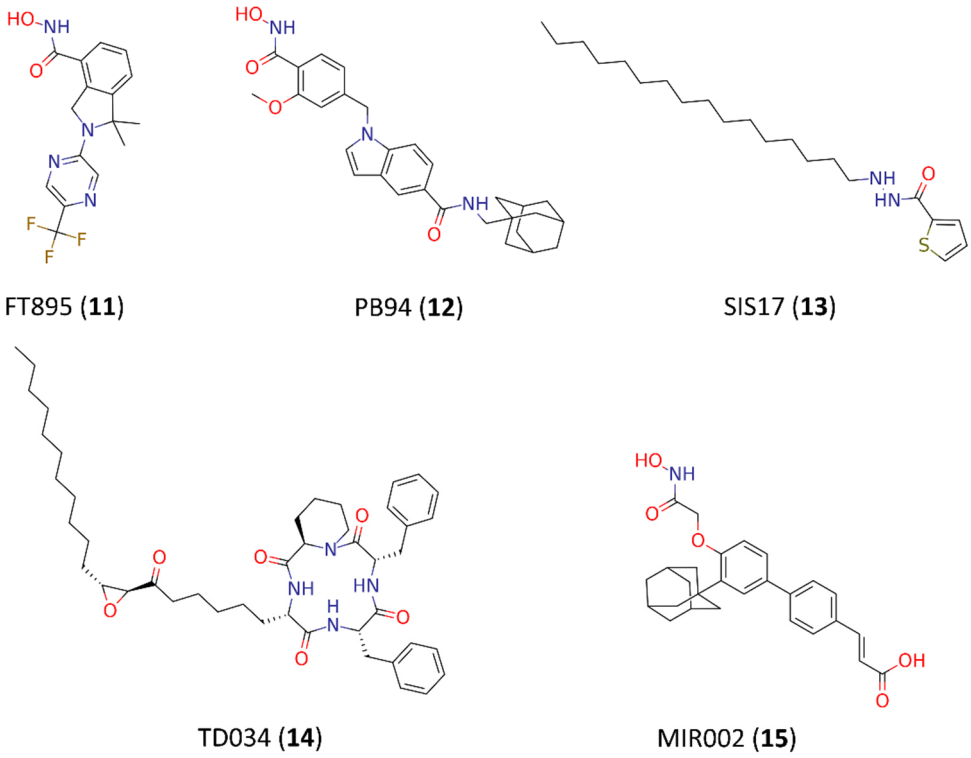

Figure 5. 2D structures of previously reported selective HDAC11 inhibitors.

1.7. Computer-aided drug design

Computer-aided drug design (CADD) combines and utilizes various computational techniques of molecular modeling to design or discover novel molecules possessing biological activity as therapeutics against diseases [114]. CADD significantly reduces the cost and time required for novel drug hits identification [115]. There is a steady growth in commercial drugs discovered through CADD. One or more computational methods played a significant role in the discovery and development process of around 70 commercially available drugs. However, it is worth noting that the initial lead, rather than the final commercial product, was discovered through CADD [116].

CADD techniques include molecular docking, virtual screening (VS), pharmacophore modeling, quantitative structure-activity relationship (QSAR) studies and molecular dynamics (MD) simulation [117]. In general, CADD methods can be classified into two categories. Structure-based methods are used whenever the 3D structure of the target protein is known [118]. Otherwise, ligand-based methods are of benefit. In structure-based drug design (SBDD), important information regarding the binding site of the macromolecule, in addition to the binding mode of ligands to the target protein and their key interactions, can be extracted from the 3D structure. This information is then utilized to guide the design of new molecules possessing the necessary features for activity [118].

In absence of the experimental 3D structure of the target, SBDD becomes challenging. To solve this challenge, homology modeling (HM) can be used. HM is a computational method for the prediction of the 3D structure of protein based on its amino acid sequence and utilizing a protein template with known 3D structure to guide the folding. Template identification and selection is a critical step in HM and can significantly affect the accuracy of the folding [119]. The accuracy of the folding prediction is dependent on the extent of identity or similarity between the query sequence and the selected template sequence. Therefore, a high accuracy of the homology model is expected when the query and template sequences share adequate similarity. In general, more than 80% of C-α atoms are expected to lie within 3.5 Å of their actual positions if the sequence identity ranges between 30% and 50%. Using a template structure with sequence identity of less than 30% will likely lead to significant errors and consequently will affect the quality of the predicted model [120]. Recently, AI-driven methods, such as AlphaFold, were developed to predict the protein 3D structure and could demonstrate high accuracy even when there is no available homologous structures [121].

1.8. AlphaFold

AlphaFold2 (AF2) is a computational approach utilizing neural network machine learning model to predict the 3D structures of proteins from their amino acid sequences. It demonstrated superior performance compared to other methods in the 14th Critical Assessment of Protein Structure Prediction (CASP14) and showed to predict protein structures with near experimental atomic accuracy even in absence of similar template structures. The improvement in the accuracy of protein structure prediction introduced by AF2 comes from incorporating biological and physical knowledge, including evolutionary, geometric and physical constraints of protein structures, as training procedures within novel neural network architectures [121]. The 3D structures of the whole human proteome were predicted by AF2 and were made available for public [122, 123].

In general, AF2 models provide enhanced accuracy compared to the conventional template-based homology models. However, one limitation to utilizing these models in drug design and discovery is that they are predicted in absence of biologically relevant small molecules such as cofactors, ligands, as well as water molecules [123, 124]. Several studies have assessed the usability of AF2-predicted structures in drug design and discovery studies by evaluating the performance of the output models as targets for docking of small ligands relative to their experimental structures. While most of the reported studies focused on a certain protein class, such as G-protein coupled receptor (GPCR) [125-128], another study [129] used an expanded dataset of 2474 human protein structures obtained from PDBbind database [130]. Despite the high accuracy of AF2 predictions, the results from these studies were not in favor of AF2 models, as they demonstrated worse performance compared to their corresponding crystal structures. Consequently, these results suggested that AF2 models are not suitable for direct use in real-world docking-based virtual screening campaigns [126, 131, 132].

The disappointing performance of AF2 models in docking studies may be attributed to inaccuracies in the binding site predictions. These inaccuracies can arise from minor variations in the side chain conformation or even more pronounced variations at the backbone level as well as regions with low confidence that interfere with the binding site. This indicates that post-modeling refinement or optimization, such as addressing the flexibility of binding site residues and handling the low-confidence regions, is necessary to obtain more suitable models for docking [125-127, 129, 131-133].

Ren et al. [134] demonstrated a successful case in which AF2 model was used in combination with AI-driven molecular generation methods to develop a potent inhibitor for cyclin-dependent kinase 20 (CDK20). However, it is worth noting that the direct utilization of the AF2 model was not possible, as the low-confidence predicted C-terminal exhibited a conformation that was interfering with the solvent-exposed region of the protein. Moreover, residue Arg305 was blocking the ATP binding pocket. A post-modeling refinement, involving the removal of the C-terminal, was mandatory to make the model usable for the design of inhibitors that can bind to the ATP pocket. It is also important to highlight here that these novel inhibitors were discovered using a pocket-based molecular generation method, wherein the modified model was employed as input structure, rather than conventional docking approaches.

In an attempt to overcome the limitation of using AF2 models in SBDD, AlphaFill [135] aimed to tackle the challenge of AlphaFold predicting protein structures in the apo form and without cofactors by introducing an automated enrichment approach for the output models. AlphaFill is an algorithm that utilizes structure and sequence similarity in query for homologous protein templates to transplant ions and small molecules, such as ligands and cofactors, into AF2 models from experimentally determined protein structures.

RoseTTAFold (RF) [136] is a deep learning approach for the prediction of 3D structure of proteins with accuracy approaching that of AF2. Taking into consideration the problem of biomolecular complexes that contain proteins associated with metals, small molecules and nucleic acids, RF was first extended to RoseTTAFoldNA (RFNA) [137]. In RFNA, the amino acid alphabet, consisting of 20 natural amino acids, was expanded to 28 by adding four DNA bases and four RNA bases. Through this modification, RFNA enabled the accurate modeling of proteins and nucleic acids in complex biomolecular systems. Recently, a new extension of RF named RoseTTAFold All-Atom (RFAA) [138] was introduced. The RFAA scope goes beyond proteins and nucleic acids to incorporate metal ions, small molecules such as ligands and cofactors, as well as protein covalent modifications. This was achieved by integrating an atomic graph representation of small molecules and a sequence-based description of proteins and nucleic acids. Very recently, Google DeepMind and Isomorphic Labs have reported their next generation AlphaFold3 (AF3) which is also capable of predicting protein structures in complex with ions, small molecules and nucleic acids. AF3 demonstrated higher accuracy in predicting protein-ligand complexes compared to conventional docking protocols. However, it is worth noting that the full version of AF3 (esp. including small molecule ligands) is not yet publicly available [139].

This page left intentionally blank.

2. Objectives

This page left intentionally blank.

The implication of HDAC11 in various biological functions, including immune system modulation, and its involvement in multiple pathophysiological processes, such as cancer and metabolic diseases, has identified it as a promising target for therapeutic intervention. However, to date, only a limited number of HDAC11 inhibitors have been developed.

The main aim of this work is the molecular modeling, design and development of novel selective HDAC11 inhibitors. One challenge for this objective is the lack of structural information of HDAC11 as no x-ray crystal structures for HDAC11 have been reported so far. While HDAC11 shares similarity within the catalytic core region with other isoforms from the HDAC family, the overall sequence comparison indicates that HDAC11 is less homologous to other family members. This complicates the process of conventional template-based HM and results in decreased reliability for predicting a high-quality model.

The utilization of AF2 was proposed as a solution for modeling HDAC11, thanks to its atomic accuracy and public availability. However, the lack of coordinates for the catalytic zinc cofactor and ligands during the protein folding prediction leads to a collapsed binding site and hinders the direct use of the "as is" model. For this reason, adjustments to HDAC11-AF2 model, including adding the zinc ion and optimizing the binding site, are necessary.

Following the model optimization and in order to get more insight into the binding mode of HDAC11 inhibitors, docking of the few reported hydroxamic acid selective inhibitors in the modified model will be performed. As a preferential defatty-acylase activity of HDAC11 was identified, docking of the previously reported alkyl hydrazide selective inhibitor SIS17, which bears a 16-carbon long alkyl chain, will also be performed in an attempt to explore the foot pocket and identify the tunnel that can accommodate such long alkyl chain. MD simulation will be utilized to assess the predicted binding mode of the docked ligands and investigate the stability of the optimized model.

The optimized model will be further utilized to study the binding mode of the synthesized inhibitors from our in-house database. It will also be used to identify new HDAC11 inhibitors along with targeting selectivity over other HDAC isoforms by employing various computational techniques. For this purpose, multistep structure-based and ligand-based virtual screening workflows will be applied. Moreover, the docking poses of the reported selective ligands will be analyzed as a first step for the structure-based design and development of novel selective inhibitors with the aim of maximizing potency and maintaining selectivity.

This page left intentionally blank.

3. Results

The results of the work in this dissertation are published in the following scientific articles. Additionally more unpublished results are discussed in **chapter 4**.

This page left intentionally blank.

3.1. Utilization of AlphaFold models for drug discovery: Feasibility and challenges. Histone deacetylase 11 as a case study

Fady Baselious, Dina Robaa and Wolfgang Sippl

Comput. Biol. Med. ***2023****, 167, 107700*

https://doi.org/10.1016/j.compbiomed.2023.107700

Abstract

Histone deacetylase 11 (HDAC11), an enzyme that cleaves acyl groups from acylated lysine residues, is the sole member of class IV of HDAC family with no reported crystal structure so far. The catalytic domain of HDAC11 shares low sequence identity with other HDAC isoforms which complicates the conventional template-based homology modeling. AlphaFold is a neural network machine learning approach for predicting the 3D structures of proteins with atomic accuracy even in absence of similar structures. However, the structures predicted by AlphaFold are missing small molecules as ligands and cofactors. In our study, we first optimized the HDAC11 AlphaFold model by adding the catalytic zinc ion followed by assessment of the usability of the model by docking of the selective inhibitor FT895. Minimization of the optimized model in presence of transplanted inhibitors, which have been described as HDAC11 inhibitors, was performed. Four complexes were generated and proved to be stable using three replicas of 50 ns MD simulations and were successfully utilized for docking of the selective inhibitors FT895, MIR002 and SIS17. For SIS17, the most reasonable pose was selected based on structural comparison between HDAC6, HDAC8 and the HDAC11 optimized AlphaFold model. The manually optimized HDAC11 model is thus able to explain the binding behavior of known HDAC11 inhibitors and can be used for further structure-based optimization.

Computers in Biology and Medicine 167 (2023) 107700

Contents lists available at ScienceDirect

Computers in Biology and Medicine

journal homepage: www.elsevier.com/locate/compbiomed

Utilization of AlphaFold models for drug discovery: Feasibility and challenges. Histone deacetylase 11 as a case study

Fady Baselious, Dina Robaa, Wolfgang Sippl *

Department of Medicinal Chemistry, Institute of Pharmacy, Martin-Luther-University of Halle-Wittenberg, Halle (Saale), Germany

ARTICLE INFO

Keywords:
AlphaFold model
HDAC11
AlphaFill
Model optimization
Drug design and discovery
Docking
Molecular dynamics simulation

ABSTRACT

Histone deacetylase 11 (HDAC11), an enzyme that cleaves acyl groups from acylated lysine residues, is the sole member of class IV of HDAC family with no reported crystal structure so far. The catalytic domain of HDAC11 shares low sequence identity with other HDAC isoforms which complicates the conventional template-based homology modeling. AlphaFold is a neural network machine learning approach for predicting the 3D structures of proteins with atomic accuracy even in absence of similar structures. However, the structures predicted by AlphaFold are missing small molecules as ligands and cofactors. In our study, we first optimized the HDAC11 AlphaFold model by adding the catalytic zinc ion followed by assessment of the usability of the model by docking of the selective inhibitor FT895. Minimization of the optimized model in presence of transplanted inhibitors, which have been described as HDAC11 inhibitors, was performed. Four complexes were generated and proved to be stable using three replicas of 50 ns MD simulations and were successfully utilized for docking of the selective inhibitors FT895, MIR002 and SIS17. For SIS17, The most reasonable pose was selected based on structural comparison between HDAC6, HDAC8 and the HDAC11 optimized AlphaFold model. The manually optimized HDAC11 model is thus able to explain the binding behavior of known HDAC11 inhibitors and can be used for further structure-based optimization.

1. Introduction

HDAC11 is the smallest member of the histone deacetylase family and it is the sole member of class IV and one of the least studied HDAC isoforms [1]. It is mainly expressed in the skeletal muscle, heart, kidney, and brain tissues [2] with potential preferential expression in the gall bladder [3]. Additionally, HDAC11 can be secreted by pancreatic beta cells [4] and interacts with other members of histone deacetylase family to regulate the expression of a number of cytokines [5].

Evidence has demonstrated that HDAC11 is involved in various physiological and pathological processes. HDAC11 is involved in modulating the immune system [6–8] and is a potential target for the treatment of some diseases including multiple sclerosis and viral infection [9]. Moreover, studies showed that HDAC11 knock-out can protect mice from high-fat diet-induced obesity and metabolic syndrome suggesting HDAC11 as an interesting target for the treatment of obesity-related diseases [10,11].

HDAC11 was found to be involved in the modulation of cancer growth and is overexpressed in many cancers, including hepatocellular [12–15], prostate [16], pituitary [17] and myeloma [18,19]. Additionally, inhibition of HDAC11 showed beneficial effects in neuroblastoma cells [20] indicating that HDAC11 can be considered as a target for the treatment of cancer.

Robust and preferential defatty-acylase activity for HDAC11 was identified. The defatty-acylase activity is > 10,000 times more efficient than its deacetylase activity, concluding that it may represent the major enzymatic activity in vivo [9,21–23].

Several HDAC11 inhibitors were described in the literature, however demonstrating variation in IC_{50} values when varying the substrate (acetyl/trifluoroacetyl vs. myristoyl peptides from different proteins) used in the enzymatic assay. For example, Kutil et al. re-evaluated the inhibitory activity of reported HDAC11 inhibitors utilizing a myristoylated peptide (peptide 1), which is structurally closer to the myristoylated in vivo substrates [23]. This substrate was derived from the known myristoylation site TNFα-Lys20 in which the naturally occurring threonine residue is replaced by the quencher L-3-nitrotyrosine and the lysine side chain corresponding to Lys20 of TNFα is acylated with fluorescent N-anthraniloylated 11-aminoundecanoic acid.

* Corresponding author.
E-mail address: wolfgang.sippl@pharmazie.uni-halle.de (W. Sippl).

https://doi.org/10.1016/j.compbiomed.2023.107700
Received 31 August 2023; Received in revised form 3 November 2023; Accepted 7 November 2023
Available online 10 November 2023

In this study Trapoxin A showed an IC_{50} in the nanomolar range (IC_{50} = 10 nM) vs. an IC_{50} of 170 nM using a myristoylated peptide substrate [22]. Fimepinostat, another reported HDAC11 inhibitor could retain an IC_{50} in the nanomolar range when assayed using peptide 1 (IC_{50} = 23 nM) and a trifluoroacetylated substrate (IC_{50} = 5.4 nM) [24]. Meanwhile, Quisinostat activity dropped from the nanomolar range to single digit micromolar IC_{50} when using myristoylated peptide 1 (IC_{50} = 3270 nM) [23] as a substrate rather than an acetylated peptide (IC_{50} = 0.37 nM) [25]. For the pan-HDAC inhibitor TSA, higher drop in activity was observed when using myristoylated peptide 1 (IC_{50} = 22000 nM) instead of the acetylated flurogenic pentapeptide (IC_{50} = 17.3 nM) substrate [26], which show agreement with obtained IC_{50} using myristoylated substrate (IC_{50} = 32000 nM) [22]. Several inhibitors that were reported in literature were also re-tested for their inhibitory activity of HDAC11 using the substrates considered in the current study and showed different activities [23].

While Trapoxin A, Quisinostat and TSA are non-selective inhibitors of HDAC11, there are few selective inhibitors that were described in literature. FT895 showed same variation as discussed above as it exhibited activity in a low nanomolar range (IC_{50} = 3 nM) [27] when assayed using a triflouroacetyl lysine peptide, while when assayed using the physiological myristoyl lysine substrate, activity of sub-micromolar range was observed (IC_{50} = 740 nM) [28]. The alkyl hydrazide inhibitor SIS17 [28] inhibited HDAC11 at a sub-micromolar range (IC_{50} = 830 nM). Recently Trapoxin A analogues bearing long alkyl chains were developed as potent and selective HDAC11 inhibitors with the most active compound TD034 showing activity in low nanomolar range using myristoylated H3K9 peptide as substrate (IC_{50} = 5.1 nM) [29]. MIR002 [30] showed inhibition of HDAC11 in micromolar range (IC50 = 6090 nM) using triflouroacetyl lysine substrate indicating for weak inhibition. Therefore, for modeling studies it is recommended to use and compare only inhibitors and in vitro values that have been tested in the same assay/laboratory.

Computer aided drug design (CADD) combines various molecular modeling techniques that are used to design and discover new molecules bearing bio-molecular activities [31,32]. The combination of molecular docking, molecular dynamics simulations and de novo design approaches have significantly contributed to the conventional drug discovery processes by reducing time and resources required for hit identification and lead optimization phases [33]. Sabe and coauthors in their review [32] listed around 70 approved drugs for which the development process included one or several computational methods including molecular docking, structure-based design, structure-based virtual screening, ligand-based pharmacophore screening, homology modeling, quantitative structure activity relationship studies and molecular dynamics simulations. In most of these discoveries, the initial hit or lead was identified using CADD [32]. One limitation to the structure based drug design is the shortage of structural data for the target protein, a challenge that can be solved with the aid of homology modeling technique [34].

So far no crystal structure of HDAC11 has been reported. The catalytic core region of HDAC11 shares sequence similarity to class I and class II HDAC members, however, comparison over the full length of the protein shows that HDAC11 is only slightly homologues to other HDAC family members [1,2]. Calculating the sequence identity for HDAC11 with the primary sequences of the catalytic domains available in the PDB databank for other human HDAC isoforms, shows low sequence identity percent ranging between 16 % and 22 %. This lowers the probability to get a reliable homology model via template based folding and suggests that applying a different approach for the prediction of the 3D structure of HDAC11 as AlphaFold is of advantage.

AlphaFold is a neural network machine learning approach for predicting the 3D structures of proteins and it was shown to predict protein structures with atomic accuracy even in absence of known similar structures [35].

The database of the 3D structures of the whole human proteome was constructed by AlphaFold and it includes HDAC11 model. While the AlphaFold predictions in general provide improved accuracy when compared to template based homology modeling [36], the models from AlphaFold should be carefully considered when used for docking or drug design studies because the folding is predicted in absence of ligands and cofactors as zinc ion in the case of HDAC11.

Trying to solve this problem, AlphaFill [37] introduced an algorithm for enrichment of the models in the AlphaFold database by transplanting such small molecules and ions utilizing structure and sequence similarity with experimentally determined protein structures.

In order to assess the usability of the AlphaFold HDAC11 model for the aim of drug discovery, the available AlphaFill results for HDAC11 were analyzed. Since the findings from this analysis were not satisfactory, we considered the optimization of the AlphaFold model of HDAC11 by adding the zinc ion and minimization of model-ligand complexes obtained by merging three selected, previously described potent HDAC11 inhibitors for which X-ray structures with the related HDAC8 are available, namely, Trapoxin A (PDB 5VI6) [38], Quisinostat (PDB 6HSK and 6HSH) [39] and TSA (PDB 5D1B) [40] (Fig. 1). While the selected ligands show variation in the inhibitory activity for HDAC11 as discussed above, scaffold diversity of the selection was meant to expand the chances of obtaining an optimized complex that can further be used for drug discovery. The obtained HDAC11-ligand complexes were further utilized for docking of HDAC11 selective inhibitors, FT895 and MIR002. The obtained HDAC11-ligand complexes as well as the poses obtained from the docking study were subjected to classical molecular dynamics simulation to access the stability of the optimized model as well as the obtained ligand poses. As the defatty-acylase activity preference of HDAC11 is confirmed, the presence of the so called foot pocket that theoretically accommodates the longer alkyl chain was explored. For this purpose stepwise docking and minimization of the reported selective HDAC11 ligand SIS17 which bears a 16 carbon alkyl chain as well as docking in loop 1 remodeled AlphaFold model were performed.

2. Materials and methods

Schrodinger Suite 2019 was used for all modeling work except zinc ion docking into the homology model. Maestro [41] was utilized for visualization.

The AlphaFold HDAC11 model was obtained from the AlphaFold website (https://alphafold.ebi.ac.uk/entry/Q96DB2/).

2.1. Protein preparation

All protein structures were preprocessed using Protein Preparation Wizard [42,43] by adding hydrogens and assigning bond orders. Zero order bonds to metals were created and water beyond 5 Å from the ligands was deleted. Ionization states of the ligands were generated using Epik [44–46] at pH 7.0 ± 2.0. For crystal structures with hydroxamic acid inhibitors (PDB 6HSK, 6HSH and 5D1B), the hydroxamate form was selected for further hydrogen bond optimization and minimization. Hydrogen bond optimization was assigned automatically with sampling water orientation and using PROPKA at pH 7.0. Restrained minimization was performed with RMSD cutoff of 0.3 Å for heavy atoms using the OPLS3e force field [47–50].

2.2. Ligand preparation

Ligands including the original ligands were prepared utilizing LigPrep [51] panel with OPLS3e force fields. Hydroxamic acid ligands were prepared in the deprotonated form, while other ligands were prepared in the neutral from. No further ionization states, tautomers or isomers were generated.

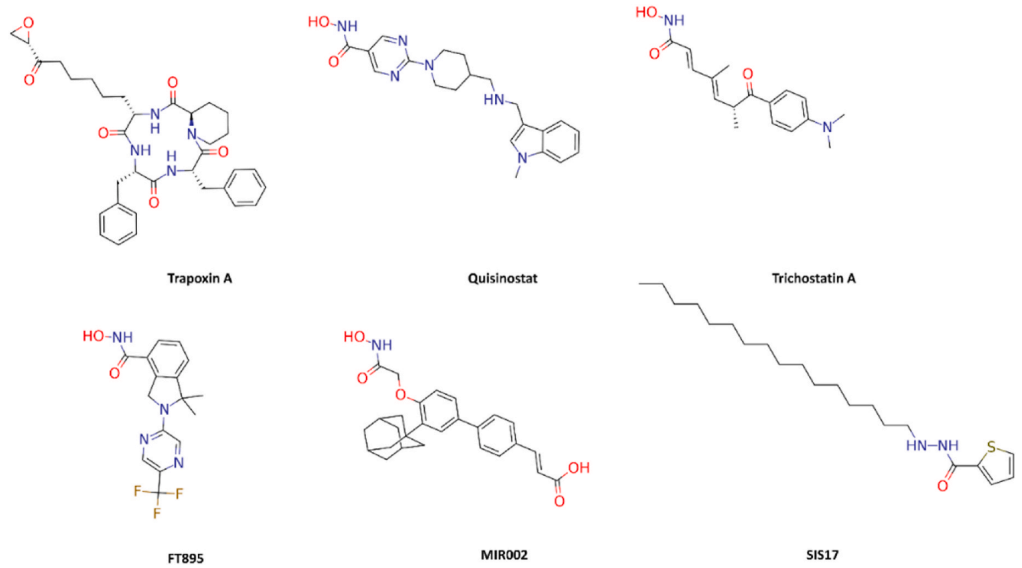

Fig. 1. Structures of HDAC inhibitors included in this study.

2.3. Model optimization

2.3.1. Zinc ion docking

The zinc ion was docked using the Metal Ion-Binding Site Prediction and Docking Server (MIB) (http://bioinfo.cmu.edu.tw/MIB/) and the top scored model was selected for further optimization.

2.3.2. Coordination distance optimization

The obtained model was then prepared using the protein preparation settings mentioned above. Protonation states of titratable residues in the catalytic pocket were assigned. To adjust the coordination distance, refinement of loop 4 was performed. Loop 4 (residues: 180–185) was refined using Prime Refine Loops panel [52–54], with extended loop sampling and generating 10 structures. The structure with the lowest potential energy was then selected for further utilization. Preparation and restrained minimization were performed for the selected refined model using the settings stated above.

2.4. Site mapping

Site mapping of the AlphaFold HDAC11 with the zinc ion was performed using SiteMap [55–57] panel and by identifying top ranked potential receptor binding sites. The site mapping was performed for two models with different Phe152 rotamers with reporting up to five sites and requiring at least 15 site points per reported site. The top ranked site map for each model was used to generate grid for docking.

2.5. Binding site optimization

2.5.1. Placing ligands

The prepared and minimized crystal structures were aligned to the refined AlphaFold model using Protein Structure Alignment panel and selecting all residues as reference residues. The ligand from the crystal structure was then placed into the AlphaFold model by merging.

2.5.2. Unrestrained minimization

All model-ligand complexes were solvated in SPC water model using an orthorhombic box and 10 Å distance between the solute structures and the simulation box boundary. The box volume was then minimized. The system was neutralized by adding chloride ions that were placed 4 Å away from the ligand.

The complexes were then minimized using Minimization panel from Desmond [58,59], each for 100 ps without restraints.

2.6. Remodeling loop 1

Loop 1 (residues 21–40) of the TSA-HDAC11 AlphaFold model was remodeled using HDAC6 (PDB 5EDU) as template and by utilizing the Build Homology Model Panel in the Multiple sequence viewer. A knowledge based model was generated utilizing the composite/chimera option in presence of TSA as ligand. The generated homology model was then preprocessed and restrained minimization was further applied using the same settings as mentioned above to resolve overlapping atoms.

2.7. Grid generation

Receptor grids were generated using the Receptor Grid Generation panel. In case of the apoform receptor, the site map was used to generate the grids. While for the optimized complexes, the centroid of the complexed ligand was used. For the apoform and each of the optimized complexes, two grids were generated utilizing the original and the flipped-out Phe152 rotamers (lowest energy rotamer). For docking of the hydroxamic acid ligands, FT895 and MIR002, grids were generated with the protonated His142 in HIP state, while for SIS17, grids with the HID state were generated. For SIS17, dock ligands with length $\geq$ 20 Å option was selected.

For the docking of SIS17 in the TSA-HDAC11- AlphaFold model with remodeled loop 1 the inner box (ligand diameter midpoint box) length were set to be 15 Å for each side.

2.8. Docking

2.8.1. Docking of hydroxamic acid inhibitors

All hydroxamic acid inhibitors were docked in the hydroxamate form. Initially, FT895 was docked in the two grids obtained from the site mapping of the apoform and as these results were not satisfactory the docking was further tried with the 8 grids generated from the optimized

complexes. For all trials, docking was performed using Glide [60–63] with standard precision mode and flexible ligand sampling utilizing OPLS3e force field.

For MIR002, docking was performed in the grid obtained from TSA-HDAC11 AlphaFold model complex with flipped-out Phe152 as it showed the best performance regarding the docking of FT895. Different settings were applied for each ligand regarding the output. For FT895 and MIR002, top-ranked docking poses were subjected to post-docking minimization.

2.8.2. Docking of alkyl hydrazide inhibitors

Initial docking of SIS17 was performed in the 8 grids using standard precision mode and flexible ligand sampling utilizing OPLS3e force field and specifying 5 poses to be subjected to post-docking minimization and reporting a single top scored pose.

For the stepwise docking and minimization process, docking of SIS17 was performed using two grids, obtained from TSA-HDAC11 AlphaFold complex, one grid with the original Phe152 rotamer and the other with the flipped-out rotamer. A series of 16 SIS17 derivatives were generated virtually, starting with a single carbon as alkyl chain substitution to the hydrazide moiety and increasing one carbon atom at a time till reaching the original ligand SIS17 with 16 carbon alkyl chain.

For each grid the series was docked with standard precision mode and flexible ligand sampling utilizing OPLS3e force field and specifying 100 poses to be subjected to post-docking minimization and reporting a single top scored pose. For each grid the pose of the ligand with the maximum alkyl chain length (1 carbon alkyl chain ligand for the grid with original Phe152 rotamer and 5 carbon alkyl chain ligand for the flipped lowest energy Phe152 rotamer) that could show a bidentate chelation mode (distance to zinc ion less than 2.6 Å) was selected as core containing molecule to be utilized as reference pose for restricted docking of ligands with longer alkyl chains using maximum common substructure and same output settings as mentioned above.

The ligands poses with maximum alkyl chain length that could fit with a bidentate chelation mode using the core restricted method in complex with the HDAC11 AlphaFold model (13 carbon alkyl chain ligand for the grid with original Phe152 rotamer and 11 carbon alkyl chain ligand for the flipped-out Phe152 rotamer) were then subjected to minimization using Desmond Minimization panel and same settings as reported above.

The obtained poses from the Desmond minimization step were further used for core restricted docking of the ligands that could not fit in the first core restricted docking step. While this was successful to place the SIS17 for the grid with the original Phe152 rotamer, further alignment of SIS17 to the longest alkyl chain virtual derivative that could fit (14 alkyl chain ligand) was performed for the grid with flipped-out Phe152 rotamer using Flexible Ligand Alignment panel. The obtained poses were then subjected again to Desmond minimization.

SIS17 was also docked in the TSA-HDAC11- AlphaFold model with remodeled loop 1 using standard precision mode and flexible ligand sampling utilizing OPLS3e force field and specifying 100 poses to be subjected to post-docking minimization and reporting a single top scored pose.

2.9. Molecular dynamics simulation

The optimized apoform before further optimization of the binding site as well as the four optimized complexes and the selected docking poses were subjected to molecular dynamics simulation using Desmond. Each pose was simulated for 50 ns and the simulation was repeated three times for each pose applying different random seeds. The poses of the selective ligands FT895 and MIR002 as well as the vertical pose of SIS17 were further subjected to 500 ns molecular dynamics simulations. For SIS17 poses, zero order bonds to the metal were created using Protein Preparation Panel before submitting to system preparation. The system was solvated in SPC water model using an orthorhombic box and 10 Å distance between the solute structures and the simulation box boundary. The box volume was then minimized. The system was neutralized by adding chloride ions that were placed 4 Å away from the ligand.

The prepared system was relaxed using the default Desmond relaxation protocol for NPT ensemble followed by a production run utilizing the NPT ensemble at the temperature of 300 K using a Nose–Hoover chain thermostat and pressure of 1.01325 bar using Martyna-Tobias-Klein barostat. The progress of the simulation was recorded every 100 ps.

For analysis, the Simulation Event Analysis panel was used for RMSD and distance calculations. The RMSD of the protein was calculated using the backbone atoms while the ligand and zinc ion RMSD was calculated by fitting to the protein backbone. The Simulation Interaction Diagram panel was used for analyzing the RMSF and the interaction persistence (also known as occupancy) of the ligands. RMSD and RMSF of the protein were calculated excluding the termini (residues: 1–14 and 321–347).

3. Results and discussion

3.1. AlphaFill results analysis

As a first step, the quality of the automated approach of AlphaFill in transplanting missing ligands and cofactors was assessed. To this end, the AlphaFill results for HDAC11 AlphaFold model containing compounds transplanted from structures with percent identity up to 25 % were analyzed. While for the catalytic zinc ion, the transplant clash score (TCS) is low as would be expected for a single atom ion but the local RMSd score for two transplants is high showing 2.48 and 6.43 indicating for medium to low confidence for these transplants. Visual inspection of the zinc ion that is transplanted into the binding pocket shows that it is not ideally placed into the binding pocket and subsequently the expected metal ion-coordination by the neighboring residues (Asp181, Asp261 and His183) is partially missing. Distances of 1.42 Å, 3.45 Å and 2.95 Å between the zinc ion and Asp181-OD1, Asp261-OD1 and His183-ND1, respectively, were observed.

Additionally, AlphaFill transplanted four ligands, namely the nonselective inhibitors SAHA, Quisinostat, MS-344 and Trichostatin A (TSA), into the AlphaFold model. All transplants showed medium to low confidence with either local RMSd or the TCS values except for TSA which was transplanted from the HDAC6 crystal structure (PDB ID: 5EDU) [64] and MS-344 which was obtained from the HDAC8 crystal structure (PDB ID 1T67) [65]. While it can be easily understandable why such ligands with alkyl linkers are showing low TCS, the visual inspection (Fig. 2) of the transplanted ligands in the model shows that both are suffering from severe clashes with neighboring residues (His142, Leu268 and Tyr304 for MS-344 and His142, Glu94, Leu268 and Tyr304 for TSA). Furthermore, the zinc ion coordination by the hydroxamic acid moiety of both ligands is not optimal as would be expected due to the misplacement of the zinc ion.

3.2. Alphafold model optimization

3.2.1. Zinc ion docking and coordination optimization

Since the automated approach using AlphaFill results for HDAC11 were not satisfactory, we adapted another approach for the optimization of the original AlphaFold model. As a first step, the catalytic zinc ion was docked into the AlphaFold model using the MIB server. The top scored model showed that the zinc ion was properly placed at the depth of the lysine-binding pocket and the expected metal coordination pattern by neighboring residues could be observed. The distances between the zinc ion and the coordinating residues were 2.04 Å, 1.55 Å and 2.00 Å for Asp181-OD1, His183-ND1 and Asp261-OD1, respectively (Fig. 3). While the distance between the zinc ion and both Asp181 and Asp261 is within the range observed in crystal structures of other histone deacetylase isoforms from class I and II, the distance to His183 of 1.55 Å is lower

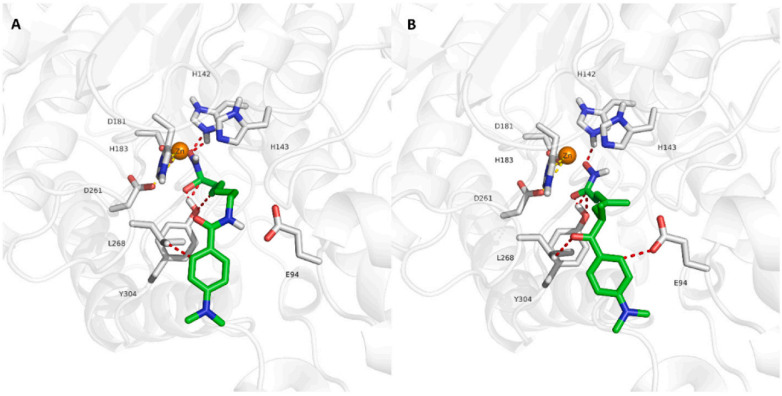

Fig. 2. AlphaFill transplants showing non-optimal zinc ion coordination and clashes between the ligands and the protein. The protein backbone is represented as white cartoon, the zinc ion as orange sphere, the binding site residues as grey sticks and the ligands as green sticks. Coordination bonds are represented as yellow dashed lines and clashes as red dashed lines. **A** and **B** are MS-344 and TSA respectively.

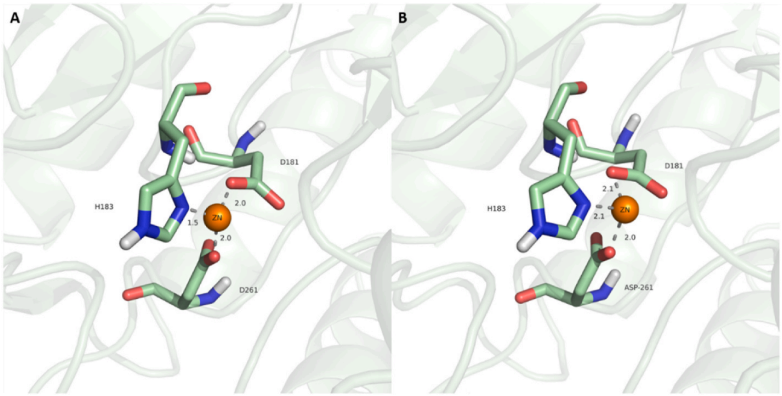

Fig. 3. Zinc ion coordination optimization. **A**, the top scored model from zinc ion docking using MIB server showing shorter distance to His183 than that observed in crystal structures from other HDAC family members. **B**, the optimized model showing coordination distances in agreement with the experimentally observed distances.

than the expected value. By refinement of loop 4 (residues: 180–185) (**Methods** section 3.2), a model with reasonably coordinated zinc ion (2.05 Å, 2.07 Å and 2.03 Å for Asp181, His183 and Asp261, respectively) was obtained.

Three runs of molecular dynamics simulation each of 50 ns were performed in order to assess the stability of the protein and the docked zinc ion which was confirmed as the RMSD for both the protein and zinc ion is stabilizing below 2 Å (Fig. S1).

RMSF plot of the three runs shows the fluctuations of the surface-exposed loops with RMSF for loop 1 and 2 reaching up to 2 Å whereas for loops 5 and 6, RMSF between 2 Å and 2.5 Å was observed. While such values can be expected for long loops that are solvent-exposed, other regions of the protein show RMSF-values almost below 1 Å confirming the protein stability (Fig. S2).

Docking of the selective HDAC11 inhibitor FT895 into the optimized AlphaFold model containing the zinc ion, however, failed and no poses could be generated, a result that goes in agreement with previous studies evaluating the usability of AlphaFold models for docking. In one study, docking of the original ligands was used to compare the performance of 2474 AlphaFold predictions and their corresponding crystal structures. Re-docking in crystal structures showed success rate of 41 % compared to 17 % for AlphaFold predictions taking 2 Å as threshold for RMSD considering the top ranked poses [66]. In another study four docking software were used to assess the accuracy and usefulness of AlphaFold models for docking and drug discovery utilizing a set of 22 targets form diverse protein families. While results demonstrated a worse performance for AlphaFold models when compared to crystal structures, the authors suggested this could be due to large variation in the binding site backbone leading to its distortion or small variations at the backbone or even the side chain levels within the binding site [67]. In agreement with this, it was demonstrated that manipulation of the binding site in terms of inducing flexibility or manual modification of the low confidence regions could enhance the docking results [66].

Analyzing the results of the MD simulation revealed that the side chain of Phe152 shows high fluctuation and can adopt two conformations (Fig. S3); a flipped-in and flipped-out conformation. It's worth noting that the flipping of this conserved Phe residue in the lysine binding pocket was also observed in HDAC8 crystal structures (6ODC, 6ODB and 6ODA). Hence, in subsequent docking studies we considered both rotameric forms of Phe152. Docking of FT895 in the generated grid with the Phe152 rotamer flipped-out of the pocket, resulted in a pose that could not reach the zinc ion in the depth of the binding site and none of the expected interactions were observed (Fig. 4). It hence appeared that the binding site in the AlphaFold model needs further optimization

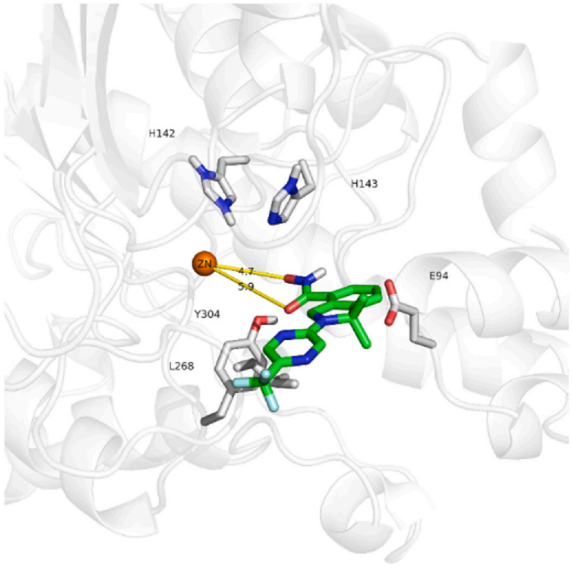

Fig. 4. Docked pose of FT895 in the model with the optimized coordination of the zinc ion and flipped-out Phe152 without further binding site optimization. The inhibitor is not able to coordinate to the zinc ion. The protein backbone is represented as white cartoon, the interacting binding site residues as grey sticks, zinc ion as orange sphere and the ligands as green sticks.

in presence of active ligands prior docking studies.

3.2.2. *Binding site optimization*

Since docking of the selective HDAC11 inhibitor FT895 in the optimized AlphaFold model was not successful, further optimization of the binding site was considered mandatory. To this end, we transplanted (**Methods section 5.1**) three nonselective inhibitors, namely Trapoxin A, Quisinostat and TSA from HDAC8 crystal structures co-crystallized with the respective inhibitor into the model. Subsequently, the protein structure was optimized by minimization of the model in the presence of these different ligands using Desmond minimization.

It's worth noting, that the initial protein-ligand complexes obtained by transplanting Trapoxin A, TSA and Quisinostat into the zinc containing AlphaFold model suffered from severe clashes with the side chains of some residues lining the binding site, especially Glu94, Phe152, His183, Leu268, and Tyr304. These complexes also suffered from non-optimal chelation of the zinc ion that the hydroxamate moiety of the ligands showed a monodentate chelation of the zinc ion only through the oxygen of the hydroxyl group while for all ligands only a single hydrogen bond was observed to either His142 or His143.

Minimization of these protein-ligand complexes in Desmond (**Methods section 5.2**) resulted in the removal of the clashes with neighboring residues and optimization of the interactions of the Zn-binding moiety (Figs. 5 and 6). The expected bidentate chelation mode to the catalytic zinc ion was observed for the four HDAC11 AlphaFold protein-ligand complexes with distances between the zinc ion and the chelator ligand atoms ranging between 2.03 Å and 2.16 Å. The hydrogen bonding pattern for the complexed ligands resembles what is commonly observed in HDAC crystal structures. The hydroxamate moiety is showing the three main interactions namely a salt bridge to His142 and hydrogen bond interactions to His143 and Tyr304. For Trapoxin A, the gemdiol zinc binding group forms two hydrogen bond interactions with the side chains of His142 or His143 and Tyr304.

Additional salt bridge and hydrogen bond interactions between each of the protonated-NH group in the linker of Quisinostat from the first pose (transplanted from 6HSH) and the three amide-NH groups in the macrocycle capping group of Trapoxin A, respectively, and the Glu94 side chain were observed. These interactions are missing for TSA, while in the second pose of Quisinostat (transplanted from 6HSK), the methyl indole capping group is aligned towards loop 5 leading to a higher distance allowing only for ionic interactions, compared to the first pose in which the capping group is directed towards loop 2. Pi-Pi interactions are observed in the second pose of Quisinostat between the indole and pyrimidine rings and Tyr209 and Phe152 respectively.

3.3. *Docking*

3.3.1. *Docking of hydroxamic acid inhibitors*

3.3.1.1. FT895. In order to examine the usability of the optimized models, docking of the selective ligand FT895 was performed in all eight grids. For the docking, 2 grids for each complex obtained from the previous step were generated with different Phe152 rotamers.

Docking of FT895 was considered successful in three grids as the ligand was placed in the binding site and showing the expected interactions. The best pose in terms of bidentate chelation, hydrogen bond interactions and docking score (Table 1), was obtained by docking in TSA-HDAC11 grid with the flipped-out Phe152 rotamer (Fig. 7A). The

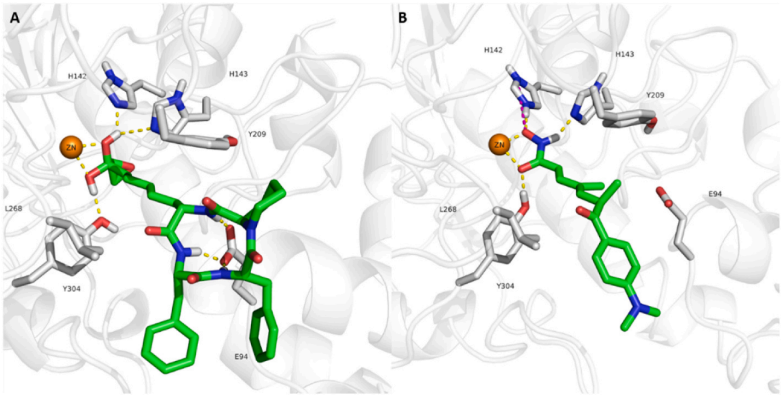

Fig. 5. Desmond minimized poses of ligands used to optimize the HDAC11 AlphaFold model. **A**, Trapoxin A, **B**, TSA. The protein backbone is represented as white cartoon, the interacting binding site residues as grey sticks, zinc ion as orange sphere and the ligands as green sticks. Hydrogen bonds and coordination bonds are represented as yellow dashed lines and the ionic interactions as magenta dashed lines.

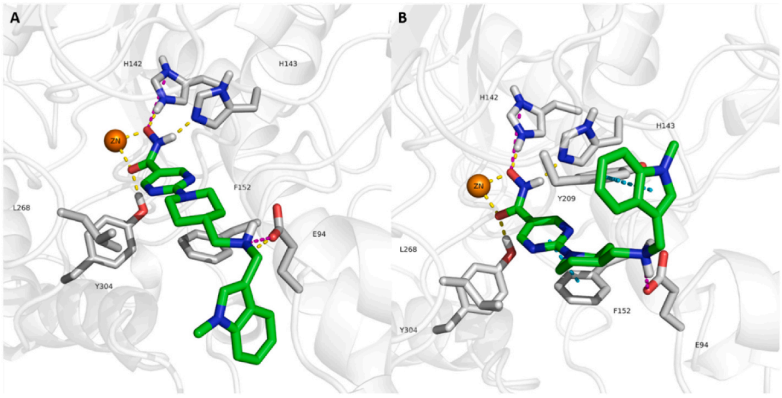

Fig. 6. Desmond minimized poses of ligands used to optimize the HDAC11 AlphaFold model. **A** and **B**, are the first and the second poses of Quisinostat, respectively. The protein backbone is represented as white cartoon, the interacting binding site residues as grey sticks, zinc ion as orange sphere and the ligands as green sticks. Hydrogen bonds and coordination bonds are represented as yellow dashed lines, the ionic interactions as magenta dashed lines and the pi-pi interactions as cyan dashed lines.

Table 1
Docking results of FT895 into the 8 grids generated using the optimized complexes.

				Distance to Zn		HB/salt bridge		
Grid	docking score	glide gscore	glide emodel	C═O	NO^-	His142	His143	Tyr304
Q1	−5.389	−5.389	−48.833	4.14	2.08		+	+
Q1-flipped	−4.906	−4.906	−55.088	3.83	2.15			
Q2	−5.325	−5.325	−55.041	4.08	2.11		+	+
Q2-flipped	−6.967	−6.967	−63.957	2.54	2.16	+	+	+
Trapoxin	−4.171	−4.171	−44.526	Wrong orientation-Hydroxamic acid facing the solvent				
Trapoxin-flipped	−5.161	−5.161	−52.861	4.17	2.06			+
TSA	−6.989	−6.989	−70.085	2.97	2.03	+	+	+
TSA-flipped	−7.979	−7.979	−80.866	2.47	2.16	+	+	+

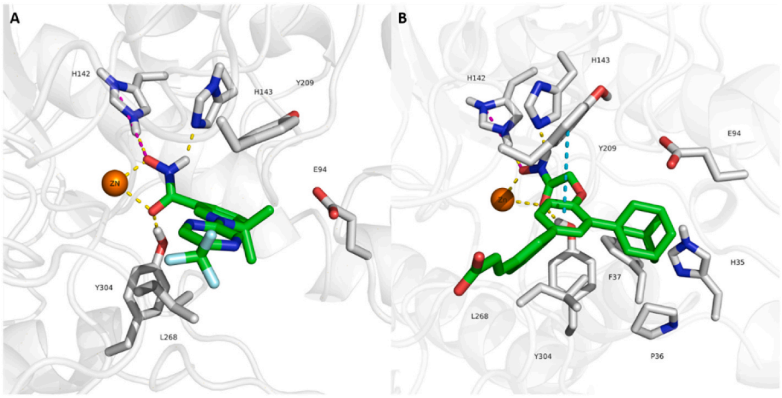

Fig. 7. Docked poses of ligands in the HDAC11 AlphaFold model after binding site optimization. **A** and **B** are FT895 and MIR002, respectively. The protein backbone is represented as white cartoon, the interacting binding site residues as grey sticks, zinc ion as orange sphere and the ligands as green sticks. Hydrogen bonds and coordination bonds are represented as yellow dashed lines, the ionic interactions as magenta dashed lines and the pi-pi interactions as cyan dashed lines.

ligand is showing bidentate chelation of the zinc ion with distances of 2.47 Å and 2.16 Å to the carbonyl and hydroxyl oxygens, respectively. The common salt bridge as well as the two hydrogen bond interactions between the zinc binding group of FT895 and His142, His143 and Tyr304, respectively, were also observed. The linear structure of the ligand is sandwiched between the side chains of Leu268 and Tyr209 with which it forms hydrophobic interactions.

3.3.1.2. MIR002. The HDAC11 selective inhibitor MIR002 was also successfully docked in the optimized AlphaFold model using the TSA-HDAC11 grid with the flipped-out Phe152 rotamer. The obtained pose shows monodendate chelation of the zinc ion with distances of 2.84 Å and 2.07 Å between the zinc ion and the carbonyl and hydroxyl oxygens, respectively. The zinc binding group of the ligand could fulfill the salt bridge and the two hydrogen bond interactions to His142, His143 and Tyr304, respectively (Fig. 7B). In the obtained pose the linear biphenyl

system is accommodated between the side chains of Tyr209 and Leu268 of loop 5 and loop 6, respectively, while the bulky adamantine moiety is directed towards loop 1 and forming hydrophobic interactions with Pro36. Other hydrophobic interactions can also be observed between the biphenyl ring system and Tyr304 and Leu268. Pi-Pi interactions between one of the phenyl rings and Tyr209 can be observed.

3.3.2. *Docking of alkyl hydrazide inhibitors*

In order to explore the so called foot pocket, docking of the selective ligand SIS17 was performed in all eight generated grids, however the docking was not successful since no reasonable pose could be obtained. In all poses the long 16 carbon alkyl chain was placed out of the pocket and exposed to the solvent (Fig. S4 and **S5)**. For this reason, two different approaches for further optimization of the model were considered, namely, remodeling loop1 and using a stepwise docking and minimization process.

3.3.2.1. Loop 1 remodeling. For the evaluation of the predicted models, AlphaFold uses two methods. The first is per residue confidence score, called predicted local distance difference test (pLDDT), which applies a scale from 0 to 100, and the second score is the predicted aligned error which is useful in assessment of the domain accuracy with expected position error scale in angstrom.

For the HDAC11 model, some residues in loop 1 show low model confidence score (70 > pLDDT >50) while the whole loop shows expected position error between 25 Å and 30 Å approximately (Fig. 8). While the structural heterogeneity due to loop flexibility can be considered as significant factor, shortage in sequence coverage can also account for such lowered scores [68].

Taking into consideration the AlphaFold scoring, the remodeling of loop 1 of the AlphaFold HDAC11 model was considered. Using HDAC6 as template, a knowledge based hybrid model was generated as described in the Methods section. The model was built in presence of TSA that was previously transplanted into HDAC11 (Fig. 9A).

Docking of SIS17 directly into the grid generated from this model resulted in a pose that is fulfilling the three hydrogen bond interactions with Tyr304, His142 and His143. The bidentate chelation mode was also observed with distances of 2.27 Å and 2.57 Å between the zinc and each of the carbonyl oxygen and the nitrogen of the hydrazide group respectively (Fig. 9B). Interestingly remodeling of loop 1 allowed enough room for the long alkyl chain of SIS17 to be accommodated between loop 1 and loop 7.

3.3.2.2. Docking and refinement by minimization. For the second approach, the final poses of the alkyl hydrazide inhibitor SIS17 obtained by docking and minimization (**Methods section 8.2**) of the virtually generated ligand series with varying the alkyl chain length, showed different orientation of the alkyl chain in the two different grids (Fig. 10). The determinant of the direction of the alkyl chain is the rotamer of Phe152. Superposing both poses shows that the stem of the alkyl chain (first five carbons) is accommodated in the same space that is lined with residues Phe37, Gly140, Phe141, His142, His143, Gly151, Phe152, Cys153, Ser301, Gly302 and Tyr304. The branching of the alkyl chain then starts at carbon 6. The original flipped-in Phe152 allows enough space for the alkyl chain to be directed horizontally and accommodated between loop 1 and loop 2. In the second grid, in which the Phe152 is flipped-out of the binding pocket, this direction is blocked and the alkyl chain of SIS17 is directed more deeply into the binding pocket along loop 3 and loop 7.

For both final poses the chelation mode is bidentate through the carbonyl oxygen and the nitrogen of the hydrazide zinc binding group with distances ranging between 2.29 Å and 2.4 Å respectively. The three hydrogen bonds to Tyr304, His142 and His143 are observed in both poses.

While the optimization of the binding site was mandatory for docking in our study. It is worth to note that in recent work by Ren et al. [69], modification to the original CDK20 AlphaFold model was necessary to be useable for the aim of drug discovery, for example the removal of the C terminus that was blocking the solvent exposed region of the protein and occupying the ATP binding pocket through Arg305. However, the reliable identity percentage between CDK20 and related structures from the cyclin dependent kinase family reaching up to around 40 % [70] with multiple crystal structures available in the protein data bank suggests that the template based homology model might has been a more convenient methodology, which is not the case for HDAC11 (Table S1).

3.4. *Molecular dynamics simulations*

One limitation of the docking approach is ignoring the protein flexibility by treating the protein as rigid body, which limits the ability to guarantee the stability of the observed interactions of a ligand docked pose and rightly predict the binding mode. On the other hand, molecular dynamics (MD) simulation techniques can account for the flexibility of the protein along with solvent effects thus allowing for deeper insight and investigation of the behavior of the ligand and its stability in a dynamic environment. Such information, provides chances for structure based design of better performing ligands. Common objective measures for the analysis of the MD simulation results are root mean square deviation (RMSD), root mean square fluctuation (RMSF) and interactions persistence/occupancy. These measures are used to evaluate protein-

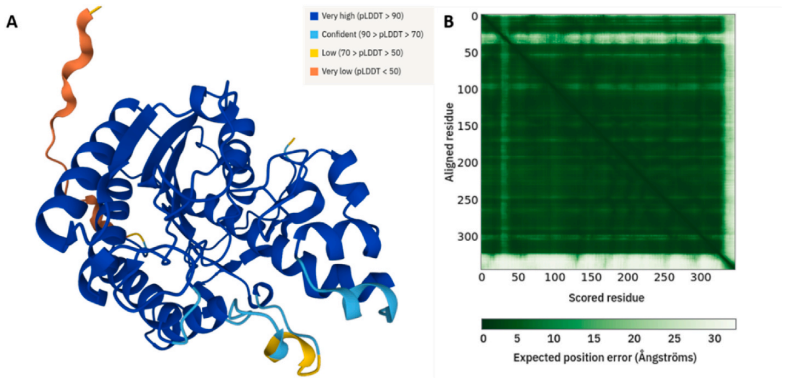

Fig. 8. HDAC11 AlphaFold model scoring. **A**, model cartoon colored according to the per residue confidence score, showing residues of lower scores in loop 1 (70>pLDDT>50). **B**, expected position error score showing distance of approximately 25 Å to 30 Å for loop 1. Pictures acquired from AlphaFold website (https://alphafold.ebi.ac.uk/entry/Q96DB2).

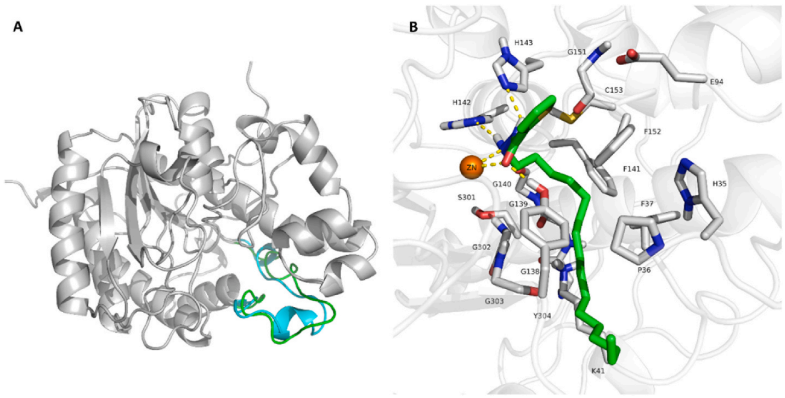

Fig. 9. Remodeling loop 1. **A**, cartoon representation of the superposition of the original and the modified model, loop 1 colored cyan and green respectively. **B**, docked pose of SIS17 in the modified loop 1 HDAC11 model. The protein backbone is represented as white cartoon, the interacting binding site residues as grey sticks, zinc ion as orange sphere and the ligands as green sticks. Hydrogen bonds and coordination bonds are represented as yellow dashed lines.

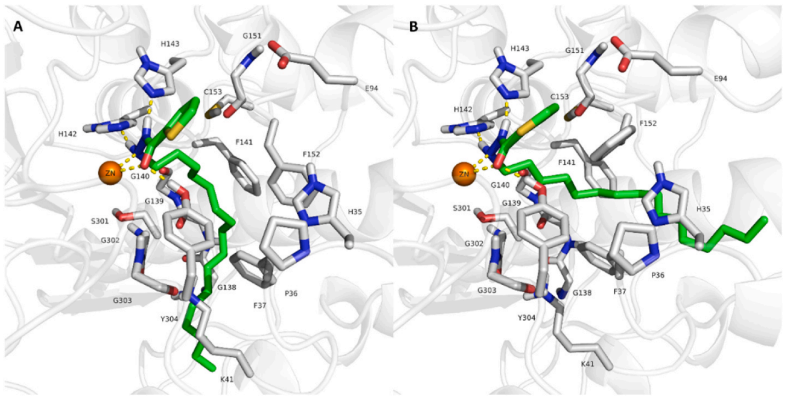

Fig. 10. Docked poses of SIS17. **A** and **B,** are poses with the vertical and horizontal orientation of the alkyl chain, respectively. The protein backbone is represented as white cartoon, the interacting binding site residues as grey sticks, zinc ion as orange sphere and the ligands as green sticks. Hydrogen bonds and coordination bonds are represented as yellow dashed lines.

ligand complex stability and the reliability of the predicted docking poses [34,71]. The initially obtained ligand HDAC11 model complexes which were obtained by transplanting the respective ligand coordinates from HDAC8 crystal structures as well as the selected docked poses were subjected to molecular dynamics simulation to examine the stability of the model after performing the optimization as well as the stability of the obtained ligand poses.

For all the molecular dynamics simulations the RMSD plots shows that the protein is stabilizing between 1 Å and 2 Å, while the zinc ion is stabilizing at around or below 1 Å (Fig. S6, **S7**, **S20**, **S21**, **S31** and **S36**).

3.4.1. Minimized complexes

The bidentate chelation mode was monitored through the stability of the distances between the zinc ion and chelator atoms in the zinc binding group during the molecular dynamics simulations and could be confirmed for the four protein-ligand complexes (Figs. S9 and S10).

Ligand RMSD shows that Trapoxin A and TSA are both stabilizing at about 3 Å (Fig. 11A and B) but with few extreme fluctuations for TSA especially in the first and third run. The RMSD of the first pose of Quisinostat is high reaching up to 6 Å (Fig. 11C) and less repeatable between the three runs with fluctuations over simulation time, while the second pose is showing different behavior in which the ligand is stabilizing at around 2 Å and repeatability could be observed for the three runs (Fig. 11D).

Trapoxin A hydrogen bonding to His142 or His143 showed moderate to high stability with occupancy ranging between 44 % and 75 % for the three runs (Table S2, Figs. S14 and S15). The occupancy percent of the hydrogen bond to Tyr304 is repeatable for two runs with almost 100 % for the second and third runs, while for the first run the occupancy is as low as 46 %. Hydrogen bonds between the three NH groups of the macrocycle of Trapoxin A and the side chain oxygens of Glu94 are highly stable and showing persistence above 83 % almost for all the three bonds in the three runs.

The salt bridge and the hydrogen bond to His142 and His143, respectively, for both poses of Quisinostat are stable with persistence ranging between 76 and 100 % (Tables S3 and S4, Fig. S11, **S12** and **S13**). For the first pose the hydrogen bond to Tyr304 is showing week stability or almost completely lost, while in the second pose, the first and third runs demonstrate good stability of hydrogen bond to Tyr304 with occupancy of 80 and 70 % respectively, but almost completely lost for the second run. For the first pose of Quisinostat the overall persistence of the salt bridge to Glu94 is average with occupancy between 50 % and 75 % considering both side chain and backbone interactions. In the second pose and during the simulation, a salt bridge which was not observed in

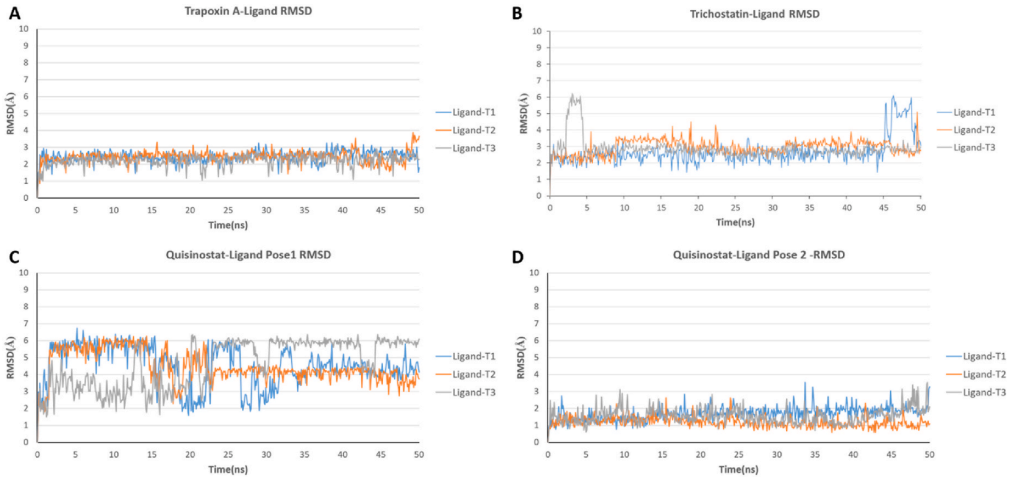

Fig. 11. RMSD plots of ligand heavy atoms for 3 repeated MD runs each for 50 ns. **A**, minimized pose of Trapoxin A. **B**, minimized pose of TSA. **C**, first minimized pose of Quisinostat. **D**, second minimized pose of Quisinostat.

the initial merged and minimized pose between the NH group of the linker and Glu94 was established and showing high stability between 80 % and 91 % for the three runs.

For TSA, the salt bridge to His142 is highly persistent with almost 100 % for all three runs while for the hydrogen bond to His143, week to average persistence between 27 % and 55 % is observed (Table S5, Figs. S14 and S16). The persistence percent of hydrogen bond to Tyr304 is varied strongly between the three runs between high and average

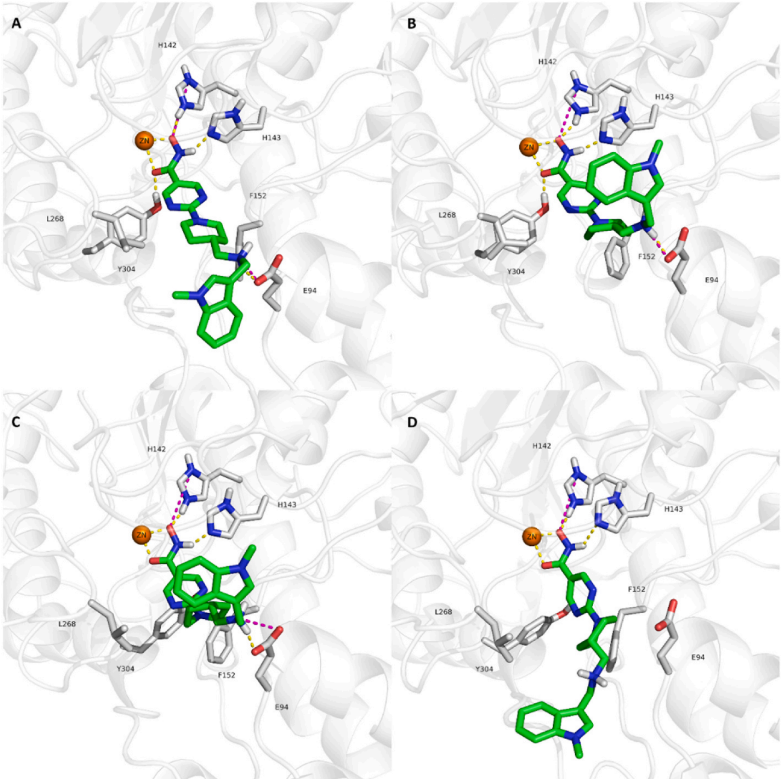

Fig. 12. Selected snapshots from the first MD run of the first pose of Quisinostat showing the fluctuation of the methyl indole capping group. **A**, frame 1. **B**, frame 125. **C**, frame 250. **D**, frame 500. The protein backbone is represented as white cartoon, the interacting binding site residues as grey sticks, zinc ion as orange sphere and the ligands as green sticks. Hydrogen bonds and coordination bonds are represented as yellow dashed lines and the ionic interactions as magenta dashed lines.

persistence or even almost lost completely.

Analyzing the RMSF plots for Trapoxin A shows that the most fluctuating part of the ligand is a terminal phenyl ring that is exposed to the solvent (Figs. S8A and S18). For Quisinostat pose 1, the methyl indole capping group is the most fluctuating substructure of the ligand while in pose 2 the fluctuation of the ligand is below 2 Å (Fig. 12, **S8C**, **S8D** and **S17**). While this fluctuation disturbs the salt bridge to Glu94 that was initially observed in the first pose leading to the demonstrated lower stability, the slight movement of the capping group allows for the formation of the same salt bridge in the second pose during the simulation. The high fluctuation of this part of the ligand reaching up to 6 Å, is responsible mostly for the high RMSD observed in the first pose. The capping group of TSA also show higher RMSF value (Figs. S8B and S19) indicating that it is responsible for the few fluctuations in the RMSD observed in runs one and three.

Analysis of the results of the hydrogen bond persistence of the zinc binding group presented above, shows that the hydrogen bond interaction to Tyr304 is less stable or almost completely lost in some MD runs especially for TSA and both poses of quisinostat. It is worth noting that this conserved tyrosine residue can adopt different conformations in HDACs crystal structures (HDAC8 PDB: 3SFF and 3SFH, HDAC2 PDB: 7KBH) [72,73] which reflects its flexibility. We observed this flexibily alsoin previously reported MD simulations of available HDAC X-ray structures [74].

3.4.2. *Docked hydroxamic acid inhibitors*

3.4.2.1. FT895. Examining the results obtained from the short time scale molecular dynamics simulations (50 ns) demonstrates that the RMSD of the docked pose of FT895 is stabilizing at 2 Å (Fig. 13A). Furthermore, the interaction persistence results reveal that the salt bridge stability to His142 is very high with persistence of almost 100 % for all the runs (Table S6, Fig. S26 and **S29).** The Hydrogen bond to His143 shows moderate to good persistence between 59 % and 88 %, and the stability of the hydrogen bond to Tyr304 was not confirmed.

Extra hydrogen bond between one nitrogen atom in the pyrazine ring in the capping group of FT895 and His183 that was not observed in the initial docked pose was established during the simulation and showed persistence between 63 % and 78 % in the three runs.

The RMSF plot for the ligand shows that all FT895 atoms are fluctuating at around 1 Å (Fig. S22A) thus indicating for the high stability observed in the RMSD. The bidentate chelation was confirmed by monitoring the stability of the distances between the zinc ion and the chelator atoms of the hydroxamate moiety except for few sharp fluctuations for the distance between the zinc ion and the carbonyl oxygen. (Figs. S23A and S24A).

The RMSD resulted from the longer molecular dynamics simulation (500 ns) shows that FT895 is stabilizing at around 2 Å for about 250 ns after which a slight shift in the pose causing the RMSD to reach 4 Å was observed (Fig. 13B and **S27B**). Analyzing the RMSF of the ligand atoms revealed that only the trifluoromethylpyrazine shows slight fluctuations, however the RMSF values still remain below 2.2 Å (Fig. 14 and **S22A**), indicating that no major shifts occurred during the MD-simulation. Additionally, the observed ligand-protein interactions remained stable throughout the simulation; the bidentate chelation mode of the zinc ion was maintained (Fig. S25A), and the salt bridge and hydrogen bond interactions to His142, His143 and His183 remained stable with persistence of 99 %, 80 % and 58 %, respectively (Figs. S27A and S29).

Overall, the predicted binding mode of FT895 in HDAC11 showed good stability during the long MD simulation and the key interactions were preserved, despite the slight shift in the position of the capping group.

3.4.2.2. MIR002. For MIR002, the RMSD plot shows that the ligand is stabilizing at about 3 Å (Fig. 15A) and the salt bridge stability to His142 was confirmed showing almost 100 % persistence for all three runs (Table S7, Fig. S26 and **S30).** More fluctuation of the persistence percent between the three runs for the hydrogen bond to His143 and Tyr304 was observed ranging between 34 % to 71 % and 50 %–81 %, respectively.

For MIR002 the most fluctuating part is the cinnamic acid capping group that is exposed to the solvent reaching up to 3 Å (Fig. S22B). The starting distance between the carbonyl oxygen and the zinc ion observed in the docked pose of 2.84 Å was adjusted during the simulation to below the threshold of 2.6 Å. The stability of the bidentate chelation mode can be confirmed as the distances between the zinc ion and the chelator atoms of the zinc binding group are stable, however, few sharp fluctuations can also be observed for the carbonyl oxygen (Figs. S23B and S24B**)**.

Long molecular dynamics simulation on the predicted binding mode of MIR002 showed similar behavior as compared to the shorter runs with the RMSD of the ligand stabilizing at around 3 Å (Fig. 15B). The highest fluctuations were observed for the cinnamic acid moiety of the capping group with RMSF reaching 3 Å (Fig. 16, **S22B** and **S28B**).

Analysis of the protein ligand interactions shows that the salt bridge and hydrogen bond interactions to His142 and His143, respectively, are maintained with persistence of 99 % and 62 %, respectively. (Figs. S28A and S30). Additionally, the bidentate chelation of the zinc is majorly preserved as confirmed by monitoring the distance between the zinc ion and the chelator atoms of the hydroxamate moiety (Fig. S25B).

3.4.3. *Docked alkyl hydrazide inhibitors*

3.4.3.1. Loop1-remodeled pose. Inspecting the results from the molecular dynamics simulation for the docked pose of SIS17 in the loop 1 remodeled HDAC11, shows that SIS17 is stabilizing between 2 Å and 3 Å all over the simulation and for the three replica except for the third simulation as a raise of the RMSD reaching 5 Å can be observed by the end of the simulation (Fig. 17). Repeating this third run starting from the same seed but for longer duration of 100 ns could confirm the observation that there is a shift in the initially obtained pose leading the RMSD to fluctuate to such higher values of 5 Å to 7 Å starting from around 50 ns till the end of the simulation.

The hydrogen bonds stability to His142 and His143 was confirmed

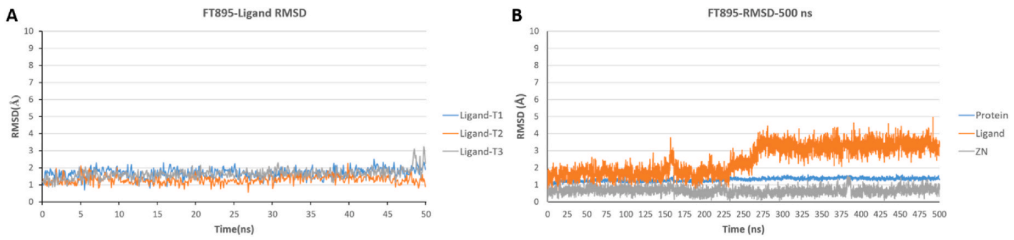

Fig. 13. FT895 RMSD. **A,** RMSD plots of ligand heavy atoms for 3 repeated MD simulation each for 50 ns. **B**, RMSD plot of protein backbone heavy atoms, zinc ion and ligand heavy atoms for 500 ns MD simulation.

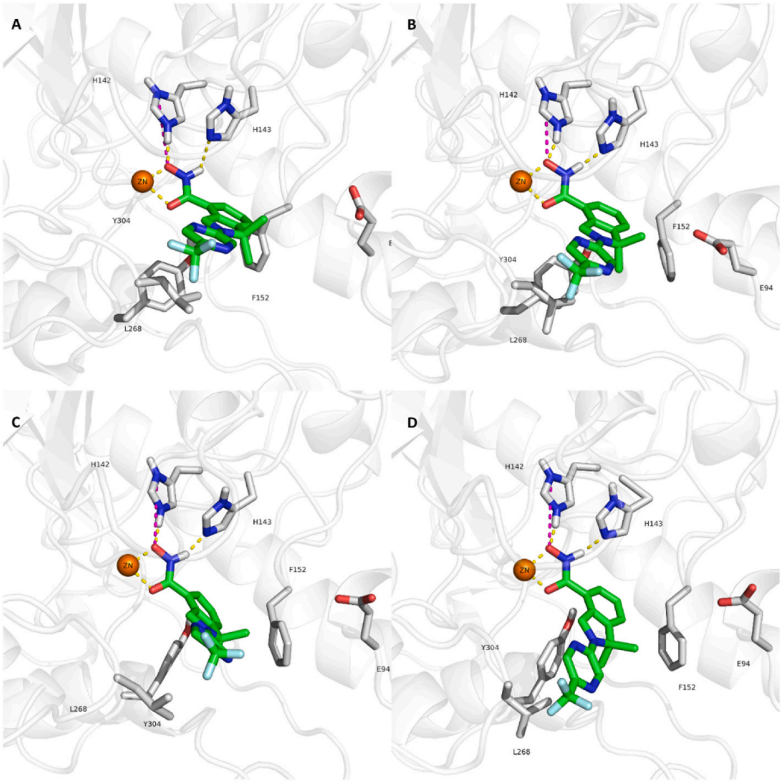

Fig. 14. Selected snapshots from the long MD run (500 ns) of FT895 showing the fluctuation of the trifluoromethylpyrazine capping group and the slight shift in the pose. **A**, frame 1. **B**, frame 1250. **C**, frame 2500. **D**, frame 5000. The protein backbone is represented as white cartoon, the interacting binding site residues as grey sticks, zinc ion as orange sphere and the ligands as green sticks. Hydrogen bonds and coordination bonds are represented as yellow dashed lines and the ionic interactions as magenta dashed lines.

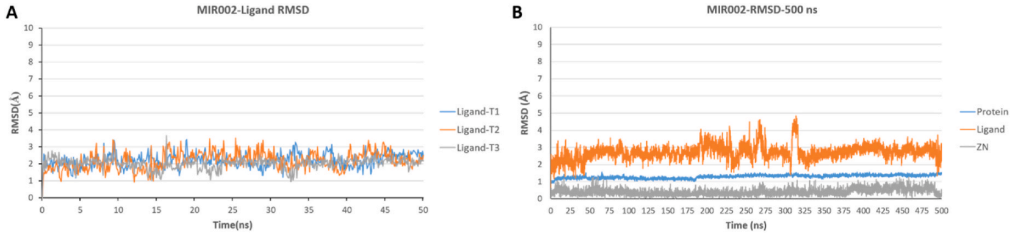

Fig. 15. MIR002 RMSD. **A,** RMSD plots of ligand heavy atoms for 3 repeated MD simulation each for 50 ns. **B**, RMSD plot of protein backbone heavy atoms, zinc ion and ligand heavy atoms for 500 ns MD simulation.

with persistence ranging between 73 % and 100 % (Table S10, Fig. S33, S34 and S35) indicating that this shift in the pose observed is not affecting interactions of the zinc binding group. The RMSF of the repeated longer run indicates that the most fluctuating part of the ligand is the distal part of the long alkyl chain (Fig. S32). By inspecting the trajectory frames, a shift of the alkyl chain from its initial docked pose that is accommodated between loop 1 and loop 7 to a different direction ending up resting between loop 1 and loop 2 was observed.

3.4.3.2. Stepwise docking and minimization poses. The RMSD and the RMSF plots of SIS17 in both the horizontal and the vertical poses indicate stable poses that reflects the probability of the long alkyl chain being conveniently accommodated within either direction (Fig. 18 and S37). The ligand in both poses is stabilizing below 3 Å. The ligand RMSF in the vertical pose is less than 2 Å for all ligand atoms, while the terminal part of the alkyl chain is showing slightly higher fluctuation for the horizontal pose.

The hydrogen bond stability is comparable between both poses. The hydrogen bond persistence to His142 and His143 is above 90 % for all runs, while for Tyr304 the hydrogen bond is almost completely lost (Tables S8 and S9, Figs. S38–S40 and **S42**).

Superposing the structures of HDAC11 AlphaFold model, HDAC6 and HDAC8 shows that the folding of loop 3 is more homologues to HDAC8 than to HDAC6 which can be expected due to higher similarity of this region to HDAC8 than to HDAC6 (Fig. 19). In HDAC8 and the AlphaFold model of HDAC11 three similar residues of Gly139, Gly140

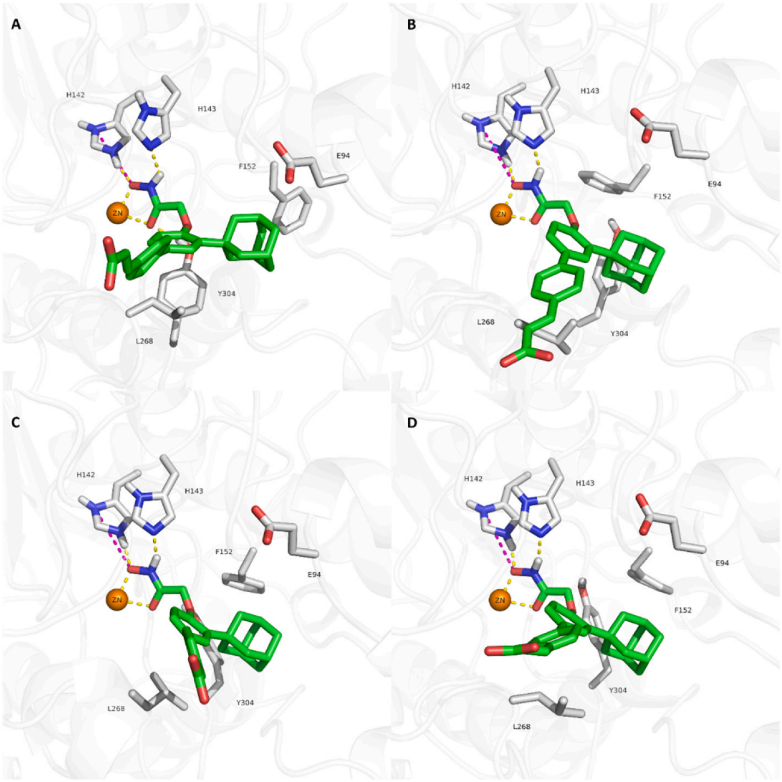

Fig. 16. Selected snapshots from the long MD run (500 ns) of MIR002 showing the fluctuation of the cinnamic acid capping group. **A**, frame 1. **B**, frame 1250. **C**, frame 2500. **D**, frame 5000. The protein backbone is represented as white cartoon, the interacting binding site residues as grey sticks, zinc ion as orange sphere and the ligands as green sticks. Hydrogen bonds and coordination bonds are represented as yellow dashed lines and the ionic interactions as magenta dashed lines.

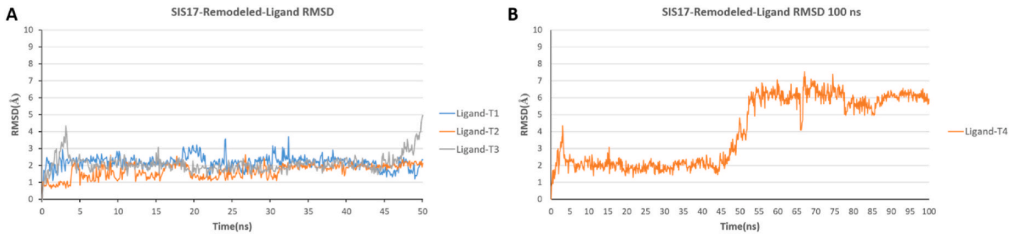

Fig. 17. RMSD plots of ligand heavy atoms for SIS17 in the loop 1 remodeled HDAC11. **A**, 3 repeated MD runs each for 50 ns. **B**, repeated third run for 100 ns.

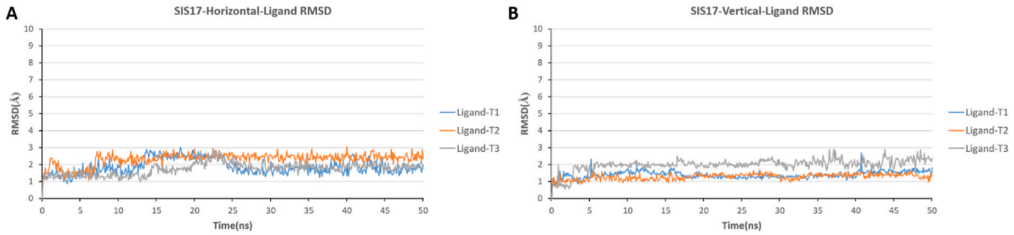

Fig. 18. RMSD plots of ligand heavy atoms for 3 repeated MD runs each for 50 ns. **A** and **B,** the horizontal and vertical poses of SIS17, respectively.

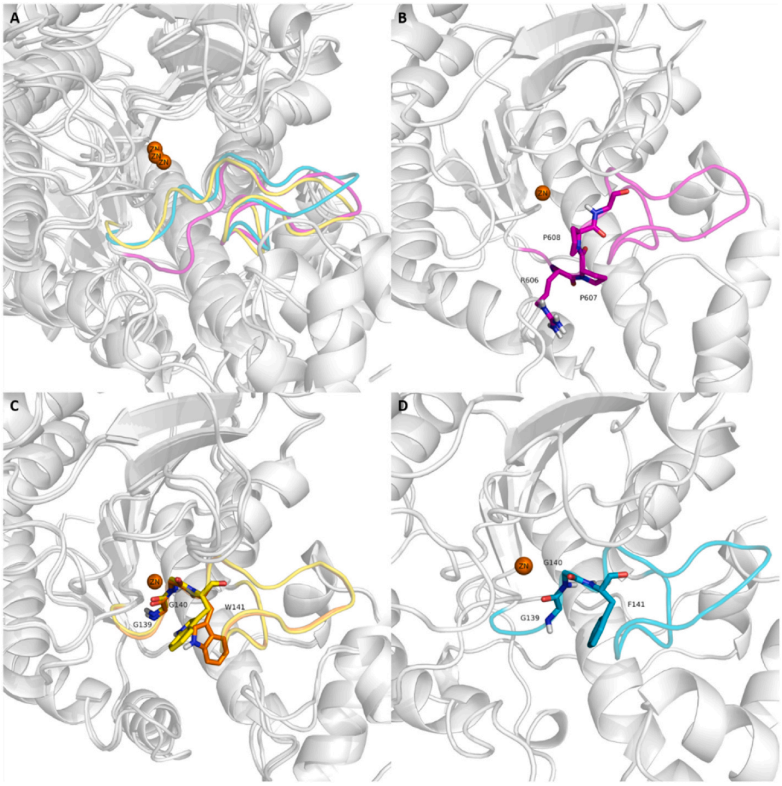

Fig. 19. Loop 3 comparison between HDAC6, HDAC8 and HDAC 11 AlphaFold model. Protein backbone is represented as white cartoon and zinc as orange sphere. **A**, Superposition of HDAC6 PDB 5EDU, HDAC8 PDB 5FCW and HDAC11 AlphaFold model. Loop 3 colored as magenta, yellow and cyan for HDAC6, HDAC8 and HDAC11 respectively. **B**, HDAC6 PDB 5EDU, loop 3 residues represented as magenta sticks. **C**, Superposition of 2 HDAC8 crystal structures showing the flexibility of the gate keeper Trp141. Loop 3 residues are colored yellow and orange for 5FCW and 6ODC, respectively. **D**, HDAC11 AlphaFold model, loop 3 residues represented as cyan sticks.

and Trp141 in HDAC8 and Phe141 in HDAC11 are shaping the entrance of what so called foot pocket and the flexible Trp141 and Phe141 side chains are acting as the gate keeper residues. These three residues are replaced by Arg606, Pro607 and Pro608 in HDAC6. The bulkier non-flexible side chains of Pro607 and Pro608 along with the bulky side chain of Arg606 that is directed towards loop 1 to form polar interactions with Glu502 [21] are causing this part of the loop to fold into the opposite direction thus blocking the space required for the formation of the foot pocket.

Since HDAC8 is also well known for the deacylase activity [75] this observed similarity can suggest the pose of SIS17 with its alkyl chain directed vertically into the binding pocket along loop 3 and loop 7 to be the most reasonable pose for SIS17.

As the vertical pose was considered the most reasonable pose regarding the orientation of the alkyl chain of SIS17, longer molecular dynamics simulation run of 500 ns was also performed. The RMSD of the

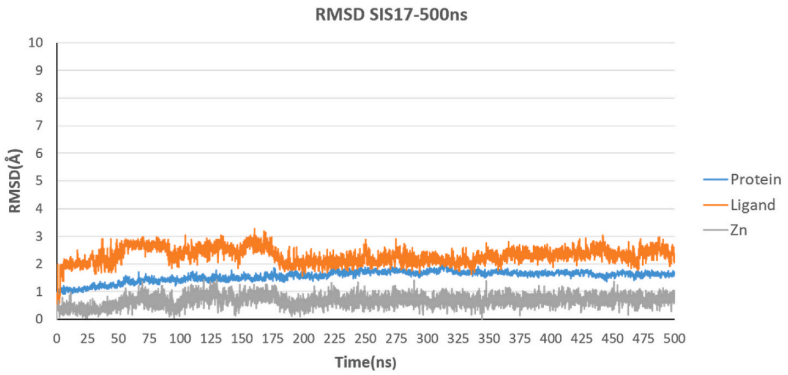

Fig. 20. SIS17 vertical pose RMSD plot of protein backbone heavy atoms, zinc ion and ligand heavy atoms for 500 ns MD simulation.

ligand is stabilizing between 2 Å and 3 Å (Fig. 20) and the hydrogen bond stability to His142 and His143 was confirmed with persistence of about 99 % and 92 %, respectively (Figs. S41A and S42).

The RMSF of the ligand showed that the long alkyl chain is fluctuating more than observed in the shorter runs however, still below 2 Å (Fig. 21, **S37A** and **S41B**).

4. Conclusion

In this study, the HDAC11 AlphaFold model was successfully optimized by adding and adjusting the coordination of the zinc ion. Furthermore the binding site was optimized by minimizations in presence of different inhibitors resulting in four protein ligand complexes. The stability of the protein and the binding mode in terms of the hydrogen bond pattern and metal chelation observed after the minimization was confirmed by molecular dynamics simulation for these four complexes which reflects the validity of the optimization process and usability of the obtained optimized complexes for the next step.

Utilization of the obtained complexes of the optimized model to generate grids for docking of selective inhibitors was successful and supported by molecular dynamics simulation that confirmed the stability of the obtained poses and their initial observed interactions.

Furthermore, the selective HDAC11 inhibitor SIS17 was used to explore the foot pocket using different approaches including a stepwise docking and minimization process as well as direct docking in loop 1 modified model. The two approaches resulted in docked poses of SIS17 with three different orientations, identifying three different tunnels as possible foot pocket that can accommodate such long alkyl chain, however the docking solution that is placing the alkyl chain deeper into the protein along loop 3 and loop 7 was considered the most reasonable.

Considering the results obtained from this study along with inspecting the transplants from AlphaFill indicate that the AlphaFill approach was not successful in obtaining optimal complexes in terms of zinc coordination and clash free inhibitor poses. This can be understandable knowing that AlphaFill is using a sequence and structure similarity approach for searching for homologous templates for alignment and small molecule transplantation and suggesting that AlphaFill would be more successful with protein sequence showing higher similarity and identity percent with crystal structures available in the protein data bank which is not observed for HDAC11.

As a conclusion, for the aim of drug design and inhibitor optimization, whenever there is reliable identity and similarity percent for the protein sequence of interest with available experimentally determined structures, the conventional template based homology modeling in presence of ligands and cofactors is recommended. The current study also showed that the models obtained from the AlphaFold approach can still be utilized but with caution. The main aim of our study was to develop a suitable 3D model of the studied target protein (HDAC11) using previously reported inhibitors and assessing its usability for drug design studies. Nevertheless, some limitations of the herein used in silico drug design methodologies have to be put into consideration. The nanoscale time scale of classical MD simulation limits the possibility to study several biological events including larger conformational changes observed for ligand binding and unbinding processes. Moreover, since classical MD simulations uses molecular mechanics force fields, only potential energies are considered whereas entropic contributions are

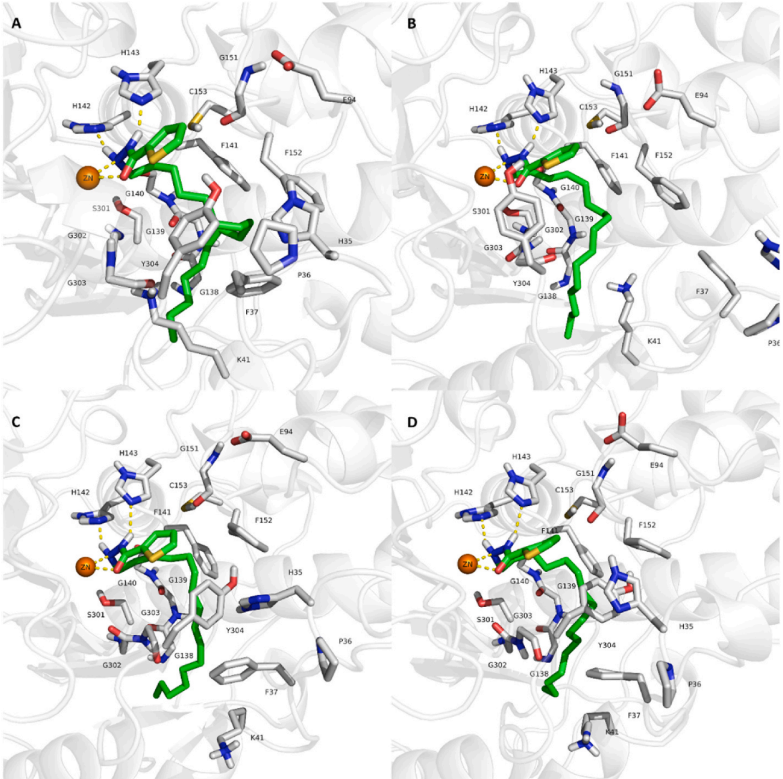

Fig. 21. Selected snapshots from the long MD run (500 ns) of SIS17 showing the fluctuation of the long alkyl chain. **A**, frame 1. **B**, frame 1250. **C**, frame 2500. **D**, frame 5000. The protein backbone is represented as white cartoon, the interacting binding site residues as grey sticks, zinc ion as orange sphere and the ligands as green sticks. Hydrogen bonds and coordination bonds are represented as yellow dashed lines.

neglected. Therefore, only the enthalpic part of the ligand binding is calculated usually. Another general limitation of the working with homology models is the lacking of water molecules that might affect the ligand and the stability of the interactions during the simulation. Verification through experimental 3D structure determination or design and evaluation of ligands based on the presented model is still required for further confirmation of the generated models.

Author contributions

FB and DR did the computational studies and wrote the manuscript. WS supervised the experiments and revised the manuscript.

Declaration of competing interest

The authors declare that they have no known competing financial interests or personal relationships that could have appeared to influence the work reported in this paper.

Appendix A. Supplementary data

Supplementary data to this article can be found online at https://doi.org/10.1016/j.compbiomed.2023.107700.

References

[1] S.S. Liu, F. Wu, Y.M. Jin, W.Q. Chang, T.M. Xu, HDAC11: a rising star in epigenetics, Biomed. Pharmacother. (2020) 131.
[2] L. Gao, M.A. Cueto, F. Asselbergs, P. Atadja, Cloning and functional characterization of HDAC11, a novel member of the human histone deacetylase family, J. Biol. Chem. 277 (28) (2002) 25748–25755.
[3] T.A. Boltz, S. Khuri, S. Wuchty, Promoter conservation in HDACs points to functional implications, BMC Genom. 20 (1) (2019).
[4] M. Lundh, D.P. Christensen, D.N. Rasmussen, P. Mascagni, C.A. Dinarello, N. Billestrup, L.G. Grunnet, T. Mandrup-Poulsen, Lysine deacetylases are produced in pancreatic beta cells and are differentially regulated by proinflammatory cytokines, Diabetologia 53 (12) (2010) 2569–2578.
[5] F. Cheng, M. Lienlaf, P. Perez-Villarroel, H.W. Wang, C. Lee, K. Woan, D. Woods, T. Knox, J. Bergman, J. Pinilla-Ibarz, A. Kozikowski, E. Seto, E.M. Sotomayor, A. Villagra, Divergent roles of histone deacetylase 6 (HDAC6) and histone deacetylase 11 (HDAC11) on the transcriptional regulation of IL10 in antigen presenting cells, Mol. Immunol. 60 (1) (2014) 44–53.
[6] C. Yanginlar, C. Logie, HDAC11 is a regulator of diverse immune functions, Biochim Biophys Acta - Gene Regul Mech. 1861 (1) (2018) 54–59.
[7] A. Villagra, F. Cheng, H.W. Wang, I. Suarez, M. Glozak, M. Maurin, D. Nguyen, K. L. Wright, P.W. Atadja, K. Bhalla, J. Pinilla-Ibarz, E. Seto, E.M. Sotomayor, The histone deacetylase HDAC11 regulates the expression of interleukin 10 and immune tolerance, Nat. Immunol. 10 (1) (2009) 92–100.
[8] H. Yang, J. Yang, H. Cheng, H. Cao, S. Tang, Q. Wang, J. Zhao, B. Li, Y. Ding, C. Ma, Probiotics ingestion prevents HDAC11-induced DEC205+ dendritic cell dysfunction in night shift nurses, Sci. Rep. 9 (1) (2019).
[9] J. Cao, L. Sun, P. Aramsangtienchai, N.A. Spiegelman, X. Zhang, W. Huang, E. Seto, H. Lin, HDAC11 regulates type I interferon signaling through defatty-acylation of SHMT2, Proc. Natl. Acad. Sci. U.S.A. 116 (12) (2019) 5487–5492.
[10] L. Sun, C. Marin de Evsikova, K. Bian, A. Achille, E. Telles, H. Pei, E. Seto, Programming and regulation of metabolic homeostasis by HDAC11, EBioMedicine 33 (2018) 157–168.
[11] R.A. Bagchi, B.S. Ferguson, M.S. Stratton, T. Hu, M.A. Cavasin, L. Sun, Y.H. Lin, D. Liu, P. Londono, K. Song, M.F. Pino, L.M. Sparks, S.R. Smith, P.E. Scherer, S. Collins, E. Seto, T.A. McKinsey, HDAC11 suppresses the thermogenic program of adipose tissue via BRD2, JCI insight 3 (15) (2018 Aug 9).
[12] W. Wang, B. Ding, W. Lou, S. Lin, Promoter hypomethylation and miR-145-5p downregulation- mediated HDAC11 overexpression promotes sorafenib resistance and metastasis of hepatocellular carcinoma cells, Front. Cell Dev. Biol. 8 (2020).
[13] Q. Fei, F. Song, X. Jiang, H. Hong, X. Xu, Z. Jin, X. Zhu, B. Dai, J. Yang, C. Sui, M. Xu, LncRNA ST8SIA6-AS1 promotes hepatocellular carcinoma cell proliferation and resistance to apoptosis by targeting miR-4656/HDAC11 axis, Cancer Cell Int. 20 (1) (2020).
[14] K. Freese, T. Seitz, P. Dietrich, S.M.L. Lee, W.E. Thasler, A. Bosserhoff, C. Hellerbrand, Histone deacetylase expressions in hepatocellular carcinoma and functional effects of histone deacetylase inhibitors on liver cancer cells in vitro, Cancers 11 (10) (2019).
[15] D. Gong, Z. Zeng, F. Yi, J. Wu, Inhibition of histone deacetylase 11 promotes human liver cancer cell apoptosis, Am. J. Transl. Res. 11 (2) (2019) 983–990.
[16] W. Huo, F. Qi, K. Wang, Long non-coding RNA BCYRN1 promotes prostate cancer progression via elevation of HDAC11, Oncol. Rep. 44 (3) (2020 Jul 7) 1233–1245.
[17] W. Wang, L. Fu, S. Li, Z. Xu, X. Li, Histone deacetylase 11 suppresses p53 expression in pituitary tumor cells, Cell Biol. Int. 41 (12) (2017) 1290–1295.
[18] L. Yue, V. Sharma, N.P. Horvat, A.A. Akuffo, M.S. Beatty, C. Murdun, C. Colin, J.M. R. Billington, W.E. Goodheart, E. Sahakian, L. Zhang, J.J. Powers, N.E. Amin, Q. T. Lambert-Showers, L.N. Darville, J. Pinilla-Ibarz, G.W. Reuther, K.L. Wright, C. Conti, J.Y. Lee, X. Zheng, P.Y. Ng, M.W. Martin, C.G. Marshall, J.M. Koomen, R. L. Levine, A. Verma, H.L. Grimes, E.M. Sotomayor, Z. Shao, P.K. Epling-Burnette, HDAC11 deficiency disrupts oncogene-induced hematopoiesis in myeloproliferative neoplasms, Blood 135 (3) (2020) 191–207.
[19] S. Mithraprabhu, A. Kalff, A. Chow, T. Khong, A. Spencer, Dysregulated Class I histone deacetylases are indicators of poor prognosis in multiple myeloma, Epigenetics 9 (11) (2014 Nov 2) 1511–1520.
[20] T.M. Thole, M. Lodrini, J. Fabian, J. Wuenschel, S. Pfeil, T. Hielscher, A. Kopp-Schneider, U. Heinicke, S. Fulda, O. Witt, A. Eggert, M. Fischer, H.E. Deubzer, Neuroblastoma cells depend on HDAC11 for mitotic cell cycle progression and survival, Cell Death Dis. 8 (3) (2017).
[21] Z. Kutil, Z. Novakova, M. Meleshin, J. Mikesova, M. Schutkowski, C. Barinka, Histone deacetylase 11 is a fatty-acid deacylase, ACS Chem. Biol. 13 (3) (2018 Mar 16) 685–693.
[22] C. Moreno-Yruela, I. Galleano, A.S. Madsen, C.A. Olsen, Histone deacetylase 11 is an ε-N-myristoyllysine hydrolase, Cell Chem. Biol. 25 (7) (2018 Jul), 849–56.e8.
[23] Z. Kutil, J. Mikešová, M. Zessin, M. Meleshin, Z. Nováková, G. Alquicer, A. Kozikowski, W. Sippl, C. Bařinka, M. Schutkowski, Continuous activity assay for HDAC11 enabling reevaluation of HDAC inhibitors, ACS Omega 4 (22) (2019) 19895–19904.
[24] Y. Chen, X. Wang, W. Xiang, L. He, M. Tang, F. Wang, T. Wang, Z. Yang, Y. Yi, H. Wang, T. Niu, L. Zheng, L. Lei, X. Li, H. Song, L. Chen, Development of purine-based hydroxamic acid derivatives: potent histone deacetylase inhibitors with marked in vitro and in vivo antitumor activities, J. Med. Chem. 59 (11) (2016 Jun 9) 5488–5504.
[25] J. Arts, P. King, A. Mariën, W. Floren, A. Beliën, L. Janssen, I. Pilatte, B. Roux, L. Decrane, R. Gilissen, I. Hickson, V. Vreys, E. Cox, K. Bol, W. Talloen, I. Goris, L. Andries, M. Du Jardin, M. Janicot, M. Page, K. Van Emelen, P. Angibaud, JNJ-26481585, a novel "second-generation" oral histone deacetylase inhibitor, shows broad-spectrum preclinical antitumoral activity, Clin. Cancer Res. 15 (22) (2009 Nov 15) 6841–6851.
[26] C.W. Yu, P.T. Chang, L.W. Hsin, J.W. Chern, Quinazolin-4-one derivatives as selective histone deacetylase-6 inhibitors for the treatment of Alzheimer's disease, J. Med. Chem. 56 (17) (2013 Sep 12) 6775–6791.
[27] M.W. Martin, J.Y. Lee, D.R. Lancia, P.Y. Ng, B. Han, J.R. Thomason, M.S. Lynes, C. G. Marshall, C. Conti, A. Collis, M.A. Morales, K. Doshi, A. Rudnitskaya, L. Yao, X. Zheng, Discovery of novel N-hydroxy-2-arylisoindoline-4-carboxamides as potent and selective inhibitors of HDAC11, Bioorg. Med. Chem. Lett 28 (12) (2018) 2143–2147.
[28] S.I. Son, J. Cao, C.L. Zhu, S.P. Miller, H. Lin, Activity-guided design of HDAC11-specific inhibitors, ACS Chem. Biol. 14 (7) (2019) 1393–1397.
[29] T.T. Ho, C. Peng, E. Seto, H. Lin, Trapoxin A analogue as a selective nanomolar inhibitor of HDAC11, ACS Chem. Biol. 18 (4) (2023) 803–809.
[30] S. Dallavalle, L. Musso, R. Cincinelli, N. Darwiche, S. Gervasoni, G. Vistoli, M. B. Guglielmi, I. La Porta, M. Pizzulo, E. Modica, F. Prosperi, G. Signorino, F. Colelli, F. Cardile, A. Fucci, E.L. D'Andrea, A. Riccio, C. Pisano, Antitumor activity of novel POLA1-HDAC11 dual inhibitors, Eur. J. Med. Chem. (2022) 228.
[31] F.D. Prieto-Martínez, E. López-López, K. Eurídice Juárez-Mercado, J.L. Medina-Franco, Computational drug design methods—current and future perspectives, in: Silico Drug Design: Repurposing Techniques and Methodologies, Elsevier, 2019, pp. 19–44.
[32] V.T. Sabe, T. Ntombela, L.A. Jhamba, G.E.M. Maguire, T. Govender, T. Naicker, H. G. Kruger, Current trends in computer aided drug design and a highlight of drugs discovered via computational techniques: a review, Eur. J. Med. Chem. 224 (2021 Nov), 113705.
[33] C. Athanasiou, Z. Cournia, From computers to bedside: computational Chemistry contributing to FDA approval, in: Biomolecular Simulations in Structure-Based Drug Discovery, 2018, pp. 163–203.
[34] T.I. Adelusi, A.Q.K. Oyedele, I.D. Boyenle, A.T. Ogunlana, R.O. Adeyemi, C. D. Ukachi, M.O. Idris, O.T. Olaoba, I.O. Adedotun, O.E. Kolawole, Y. Xiaoxing, M. Abdul-Hammed, Molecular modeling in drug discovery, Inform. Med. Unlocked 29 (2022), 100880.
[35] J. Jumper, R. Evans, A. Pritzel, T. Green, M. Figurnov, O. Ronneberger, K. Tunyasuvunakool, R. Bates, A. Žídek, A. Potapenko, A. Bridgland, C. Meyer, S.A. A. Kohl, A.J. Ballard, A. Cowie, B. Romera-Paredes, S. Nikolov, R. Jain, J. Adler, T. Back, S. Petersen, D. Reiman, E. Clancy, M. Zielinski, M. Steinegger, M. Pacholska, T. Berghammer, S. Bodenstein, D. Silver, O. Vinyals, A.W. Senior, K. Kavukcuoglu, P. Kohli, D. Hassabis, Highly accurate protein structure prediction with AlphaFold, Nature 596 (7873) (2021) 583–589.
[36] A. David, S. Islam, E. Tankhilevich, M.J.E. Sternberg, The AlphaFold database of protein structures: a biologist's guide, J. Mol. Biol. 434 (2) (2022).
[37] M.L. Hekkelman, I. de Vries, R.P. Joosten, A. Perrakis, AlphaFill: enriching AlphaFold models with ligands and cofactors, Nat. Methods 20 (2) (2023) 205–213.
[38] N.J. Porter, D.W. Christianson, Binding of the microbial cyclic tetrapeptide Trapoxin A to the class i histone deacetylase HDAC8, ACS Chem. Biol. 12 (9) (2017) 2281–2286.
[39] M. Marek, T.B. Shaik, T. Heimburg, A. Chakrabarti, J. Lancelot, E. Ramos-Morales, C. Da Veiga, D. Kalinin, J. Melesina, D. Robaa, K. Schmidtkunz, T. Suzuki, R. Holl, E. Ennifar, R.J. Pierce, M. Jung, W. Sippl, C. Romier, Characterization of histone deacetylase 8 (HDAC8) selective inhibition reveals specific active site structural and functional determinants, J. Med. Chem. 61 (22) (2018) 10000–10016.

[40] C. Decroos, N.H. Christianson, L.E. Gullett, C.M. Bowman, K.E. Christianson, M. A. Deardorff, D.W. Christianson, Biochemical and structural characterization of HDAC8 mutants associated with cornelia de Lange syndrome spectrum disorders, Biochemistry 54 (42) (2015) 6501–6513.
[41] Schrödinger Release 2019-1, Maestro, Schrödinger, LLC, New York, NY, 2019.
[42] G. Madhavi Sastry, M. Adzhigirey, T. Day, R. Annabhimoju, W. Sherman, Protein and ligand preparation: parameters, protocols, and influence on virtual screening enrichments, J. Comput. Aided Mol. Des. 27 (2013) 221–234.
[43] Schrödinger Release 2019-1: Protein Preparation Wizard, Epik, Schrödinger, LLC, New York, NY, 2019. Impact, Schrödinger, LLC, New York, NY, 2019; Prime, Schrödinger, LLC, New York, NY, 2019., in.
[44] J.R. Greenwood, D. Calkins, A.P. Sullivan, J.C. Shelley, Towards the comprehensive, rapid, and accurate prediction of the favorable tautomeric states of drug-like molecules in aqueous solution, J. Comput. Aided Mol. Des. 24 (2010) 591–604.
[45] J.C. Shelley, A. Cholleti, L. Frye, J.R. Greenwood, M.R. Timlin, M. Uchimaya, Epik: a software program for pKa prediction and protonation state generation for drug-like molecules, J. Comp.-Aided Mol. Design 21 (2007) 681–691.
[46] Schrödinger Release 2019-1, Epik, Schrödinger, LLC, New York, NY, 2019.
[47] E. Harder, W. Damm, J. Maple, C. Wu, M. Reboul, J.Y. Xiang, L. Wang, D. Lupyan, M.K. Dahlgren, J.L. Knight, J.W. Kaus, D.S. Cerutti, G. Krilov, W.L. Jorgensen, R. Abel, R.A. Friesner, OPLS3: a force field providing broad coverage of drug-like small molecules and proteins, J. Chem. Theor. Comput. (2015), https://doi.org/10.1021/acs.jctc.5b00864.
[48] D. Shivakumar, J. Williams, Y. Wu, W. Damm, J. Shelley, W. Sherman, Prediction of absolute solvation free energies using molecular dynamics free energy perturbation and the OPLS force field, J. Chem. Theor. Comput. 6 (2010) 1509–1519.
[49] W.L. Jorgensen, D.S. Maxwell, J. Tirado-Rives, Development and testing of the OPLS all-atom force field on conformational energetics and properties of organic liquids, J. Am. Chem. Soc. 118 (45) (1996) 11225–11236.
[50] W.L. Jorgensen, J. Tirado-Rives, The OPLS [optimized potentials for liquid simulations] potential functions for proteins, energy minimizations for crystals of cyclic peptides and crambin, J. Am. Chem. Soc. 110 (6) (1988) 1657–1666.
[51] Schrödinger Release 2019-1, LigPrep, Schrödinger, LLC, New York, NY, 2019.
[52] M.P. Jacobson, D.L. Pincus, C.S. Rapp, T.J.F. Day, B. Honig, D.E. Shaw, R. A. Friesner, A hierarchical approach to all-atom protein loop prediction, Proteins: Struct., Funct., Bioinf. 55 (2004) 351–367.
[53] M.P. Jacobson, R.A. Friesner, Z. Xiang, B. Honig, On the role of crystal packing forces in determining protein sidechain conformations, J. Mol. Biol. 320 (2002) 597–608.
[54] Schrödinger Release 2019-1: Prime, Schrödinger, LLC, New York, NY, 2019.
[55] T. Halgren, Identifying and characterizing binding sites and assessing druggability, J. Chem. Inf. Model. 49 (2009) 377–389.
[56] T. Halgren, New method for fast and accurate binding-site identification and analysis, Chem. Biol. Drug Des. 69 (2007) 146–148.
[57] Schrödinger Release 2019-1, SiteMap, Schrödinger, LLC, New York, NY, 2019.
[58] Kevin J. Bowers, Edmond Chow, Huafeng Xu, O. Ron, Michael P. Eastwood Dror, Brent A. Gregersen, John L. Klepeis, Istvan Kolossvary, Mark A. Moraes, Federico D. Sacerdoti, John K. Salmon, Yibing Shan, David E. Shaw, Scalable algorithms for molecular dynamics simulations on commodity clusters, in: Proceedings of the ACM/IEEE Conference on Supercomputing (SC06), Tampa, Florida, 2006, November, pp. 11–17.
[59] Schrödinger Release 2019-1; Desmond Molecular Dynamics System, D.E. Shaw Research, New York, NY, USA, 2019. Maestro-Desmond Interoperability Tools, Schrödinger: New York, NY, USA, 2019.
[60] R.A. Friesner, R.B. Murphy, M.P. Repasky, L.L. Frye, J.R. Greenwood, T.A. Halgren, P.C. Sanschagrin, D.T. Mainz, Extra precision glide: docking and scoring incorporating a model of hydrophobic enclosure for protein− ligand complexes, J. Med. Chem. 49 (2006) 6177–6196.
[61] R.A. Friesner, J.L. Banks, R.B. Murphy, T.A. Halgren, J.J. Klicic, D.T. Mainz, M. P. Repasky, E.H. Knoll, M. Shelley, J.K. Perry, Glide: a new approach for rapid, accurate docking and scoring. 1. Method and assessment of docking accuracy, J. Med. Chem. 47 (2004) 1739–1749.
[62] T.A. Halgren, R.B. Murphy, R.A. Friesner, H.S. Beard, L.L. Frye, W.T. Pollard, J. L. Banks, Glide: a new approach for rapid, accurate docking and scoring. 2. Enrichment factors in database screening, J. Med. Chem. 47 (2004) 1750–1759.
[63] Schrödinger Release 2019-1: Glide, Schrödinger, LLC, New York, NY, 2019.
[64] Y. Hai, D.W. Christianson, Histone deacetylase 6 structure and molecular basis of catalysis and inhibition, Nat. Chem. Biol. 12 (9) (2016) 741–747. #.
[65] A.J. Jennings, J.R. Somoza, C. Mol, J.J. Buggy, A. Arvai, B.A. Katz, R.J. Skene, E. Chi, C. Luong, J.D. Ho, Structural snapshots of human HDAC8 provide insights into the class I histone deacetylases, Structure 12 (7) (2004) 1325–1334.
[66] M. Holcomb, Y.T. Chang, D.S. Goodsell, S. Forli, Evaluation of AlphaFold2 structures as docking targets, Protein Sci. 32 (1) (2023).
[67] V. Scardino, J.I. Di Filippo, C.N. Cavasotto, How good are AlphaFold models for docking-based virtual screening? iScience 26 (1) (2023).
[68] T.J. Lane, Protein structure prediction has reached the single-structure frontier, Nat. Methods 20 (2) (2023) 170–173.
[69] F. Ren, X. Ding, M. Zheng, M. Korzinkin, X. Cai, W. Zhu, A. Mantsyzov, A. Aliper, V. Aladinskiy, Z. Cao, S. Kong, X. Long, B.H. Man Liu, Y. Liu, V. Naumov, A. Shneyderman, I.V. Ozerov, J. Wang, F.W. Pun, D.A. Polykovskiy, C. Sun, M. Levitt, A. Aspuru-Guzik, A. Zhavoronkov, AlphaFold accelerates artificial intelligence powered drug discovery: efficient discovery of a novel CDK20 small molecule inhibitor, Chem. Sci. 14 (6) (2023) 1443–1452.
[70] L. Lai, G.Y. Shin, H. Qiu, The role of cell cycle regulators in cell survival—dual functions of cyclin-dependent kinase 20 and p21cip1/waf1, Int. J. Mol. Sci. 21 (22) (2020) 1–14.
[71] F. He, X. Wang, Q. Wu, S. Liu, Y. Cao, X. Guo, S. Yin, N. Yin, B. Li, M. Fang, Identification of potential ATP-competitive cyclin-dependent kinase 1 inhibitors: de novo drug generation, molecular docking, and molecular dynamics simulation, Comput. Biol. Med. 155 (2023 Mar), 106645.
[72] L. Whitehead, M.R. Dobler, B. Radetich, Y. Zhu, P.W. Atadja, T. Claiborne, J. E. Grob, A. McRiner, M.R. Pancost, A. Patnaik, W. Shao, M. Shultz, R. Tichkule, R. A. Tommasi, B. Vash, P. Wang, T. Stams, Human HDAC isoform selectivity achieved via exploitation of the acetate release channel with structurally unique small molecule inhibitors, Bioorg. Med. Chem. 19 (15) (2011 Aug) 4626–4634.
[73] J. Liu, Y. Yu, J. Kelly, D. Sha, A.B. Alhassan, W. Yu, M.M. Maletic, J.L. Duffy, D. J. Klein, M.K. Holloway, S. Carroll, B.J. Howell, R.J.O. Barnard, S. Wolkenberg, J. A. Kozlowski, Discovery of highly selective and potent HDAC3 inhibitors based on a 2-substituted benzamide zinc binding group, ACS Med. Chem. Lett. 11 (12) (2020 Dec 10) 2476–2483.
[74] E.F. Bülbül, J. Melesina, H.S. Ibrahim, M. Abdelsalam, A. Vecchio, D. Robaa, M. Zessin, M. Schutkowski, W. Sippl, Docking, binding free energy calculations and in vitro characterization of pyrazine linked 2-aminobenzamides as novel class I histone deacetylase (HDAC) inhibitors, Molecules 27 (8) (2022 Apr 14) 2526.
[75] P. Aramsangtienchai, N.A. Spiegelman, B. He, S.P. Miller, L. Dai, Y. Zhao, H. Lin, HDAC8 catalyzes the hydrolysis of long chain fatty acyl lysine, ACS Chem. Biol. 11 (10) (2016) 2685–2692.

3.2. Comparative structure-based virtual screening utilizing optimized AlphaFold model identifies selective HDAC11 inhibitor

Fady Baselious, Sebastian Hilscher, Dina Robaa, Cyril Barinka, Mike Schutkowski and Wolfgang Sippl

Int. J. Mol. Sci. **2024**, *25*(2), 1358

https://doi.org/10.3390/ijms25021358

Abstract

HDAC11 is a class IV histone deacylase with no crystal structure reported so far. The catalytic domain of HDAC11 shares low sequence identity with other HDAC isoforms, which makes conventional homology modeling less reliable. AlphaFold is a machine learning approach that can predict the 3D structure of proteins with high accuracy even in absence of similar structures. However, the fact that AlphaFold models are predicted in the absence of small molecules and ions/cofactors complicates their utilization for drug design. Previously, we optimized an HDAC11 AlphaFold model by adding the catalytic zinc ion and minimization in the presence of reported HDAC11 inhibitors. In the current study, we implement a comparative structure-based virtual screening approach utilizing the previously optimized HDAC11 AlphaFold model to identify novel and selective HDAC11 inhibitors. The stepwise virtual screening approach was successful in identifying a hit that was subsequently tested using an in vitro enzymatic assay. The hit compound showed an IC_{50} value of 3.5 μM for HDAC11 and could selectively inhibit HDAC11 over other HDAC subtypes at 10 μM concentration. In addition, we carried out molecular dynamics simulations to further confirm the binding hypothesis obtained by the docking study. These results reinforce the previously presented AlphaFold optimization approach and confirm the applicability of AlphaFold models in the search for novel inhibitors for drug discovery.

International Journal of
Molecular Sciences

MDPI

Article

Comparative Structure-Based Virtual Screening Utilizing Optimized AlphaFold Model Identifies Selective HDAC11 Inhibitor

Fady Baselious [1], Sebastian Hilscher [1], Dina Robaa [1], Cyril Barinka [2], Mike Schutkowski [3] and Wolfgang Sippl [1,*]

[1] Department of Medicinal Chemistry, Institute of Pharmacy, Martin-Luther-University of Halle-Wittenberg, 06120 Halle (Saale), Germany; f_noshy@yahoo.com (F.B.); sebastian.hilscher@pharmazie.uni-halle.de (S.H.); dina.robaa@pharmazie.uni-halle.de (D.R.)
[2] Institute of Biotechnology of the Czech Academy of Sciences, BIOCEV, 252 50 Vestec, Czech Republic; cyril.barinka@ibt.cas.cz
[3] Charles Tanford Protein Center, Department of Enzymology, Institute of Biochemistry and Biotechnology, Martin-Luther-University of Halle-Wittenberg, 06120 Halle (Saale), Germany; mike.schutkowski@biochemtech.uni-halle.de
* Correspondence: wolfgang.sippl@pharmazie.uni-halle.de

Abstract: HDAC11 is a class IV histone deacylase with no crystal structure reported so far. The catalytic domain of HDAC11 shares low sequence identity with other HDAC isoforms, which makes conventional homology modeling less reliable. AlphaFold is a machine learning approach that can predict the 3D structure of proteins with high accuracy even in absence of similar structures. However, the fact that AlphaFold models are predicted in the absence of small molecules and ions/cofactors complicates their utilization for drug design. Previously, we optimized an HDAC11 AlphaFold model by adding the catalytic zinc ion and minimization in the presence of reported HDAC11 inhibitors. In the current study, we implement a comparative structure-based virtual screening approach utilizing the previously optimized HDAC11 AlphaFold model to identify novel and selective HDAC11 inhibitors. The stepwise virtual screening approach was successful in identifying a hit that was subsequently tested using an in vitro enzymatic assay. The hit compound showed an IC_{50} value of 3.5 µM for HDAC11 and could selectively inhibit HDAC11 over other HDAC subtypes at 10 µM concentration. In addition, we carried out molecular dynamics simulations to further confirm the binding hypothesis obtained by the docking study. These results reinforce the previously presented AlphaFold optimization approach and confirm the applicability of AlphaFold models in the search for novel inhibitors for drug discovery.

Keywords: AlphaFold; HDAC11; virtual screening; modelling; in vitro assay; pharmacophore; docking; molecular dynamics simulation

Citation: Baselious, F.; Hilscher, S.; Robaa, D.; Barinka, C.; Schutkowski, M.; Sippl, W. Comparative Structure-Based Virtual Screening Utilizing Optimized AlphaFold Model Identifies Selective HDAC11 Inhibitor. *Int. J. Mol. Sci.* **2024**, *25*, 1358. https://doi.org/10.3390/ijms25021358

Academic Editor: Antonio Rescifina

Received: 11 December 2023
Revised: 14 January 2024
Accepted: 20 January 2024
Published: 22 January 2024

1. Introduction

Histone deacetylases (HDACs) form a protein family responsible for catalyzing the elimination of acetyl groups from lysine residue of histone proteins as well as other substrates [1]. The histone deacetylase family is classified into four main classes, three of which are constituted by eleven zinc-dependent HDACs, namely, class I (HDAC1, 2, 3 and 8), class IIa (HDAC4, 5, 7 and 9), class IIb (HDAC6 and 10), and class IV (HDAC11) [2].

HDAC11, the sole member of class IV of the HDAC family, is the smallest member of the family and one of the least studied HDAC subtypes [3,4]. It is expressed in multiple organs, including the heart, kidney, brain tissues, skeletal muscles, and gall bladder [4,5]. Evidence has demonstrated that HDAC11 is involved in various physiological processes such as modulation of the immune system [6,7] and maintaining genomic integrity [8]. It was also evident that HDAC11 is connected to some pathological processes and represents a potential target for the treatment of several diseases, including multiple sclerosis, viral

infections, and obesity-related diseases [9–11]. HDAC11 was also found to be involved in the modulation of cancer growth and is overexpressed in different cancer forms [12–19]. For example, inhibition of HDAC11 showed beneficial effects in neuroblastoma cells [20], suggesting that HDAC11 represents a promising target for the treatment of some cancer forms.

HDAC11 has been found to have robust fatty acid deacylase activity. This activity is more than 10,000-fold more efficient than the deacetylase activity, suggesting that this activity may be the major activity of the enzyme in vivo [21–23].

To date, only a few selective HDAC11 inhibitors have been reported. Hydroxamic acid-based inhibitors include FT895 [24], the only weakly active MIR002 [25], and the recently developed inhibitor BP94 [26]. FT895 showed beneficial effects in reducing non-small cell lung cancer cells' viability [27], while BP94 was able to ameliorate neuropathic pain in mouse model [26]. Due to its preference to remove long-chain fatty acyl groups, it has been postulated that HDAC11 contains a hydrophobic pocket near its catalytic Zn^{2+} center. Therefore, inhibitors containing long alkyl chains have been described, such as SIS17 [28], which contains an alkyl hydrazide moiety and inhibits HDAC11 in vitro in the submicromolar range. Alkyl hydrazides have also recently been described for other HDACs, such as HDAC3 and HDAC8, as novel zinc binding groups. [29,30]. Similarly, the trapoxin A analog TD034 [31] possesses a long alkyl chain that might be the reason for the observed HDAC11 selectivity [31].

No crystal structure of HDAC11 has been reported, and its catalytic domain shows low sequence identity (<30%) when compared to the primary sequences of the catalytic domains available in the PDB databank for other human HDAC isoforms. This fact complicates the conventional template-based homology modeling [32].

AlphaFold is a machine learning approach for predicting the 3D structures of proteins with atomic accuracy even in absence of known similar structures [33]. A database containing the 3D structures of the whole human proteome was built by AlphaFold [34]. The models from AlphaFold should be carefully considered when used for structure-based drug design studies because the folding is predicted in absence of small molecules like water molecules, ligands, and cofactors.

In a recent study by Ren et al. [35], AI-driven molecular generation was combined with utilization of the AlphaFold model for the aim of drug discovery for cyclin-dependent kinase 20 (CDK20). In this study, modification of the AlphaFold model by removing the C-terminus which was blocking the solvent-exposed region of the protein and occupying the ATP binding pocket through Arg305 was performed in order to make the model usable. In another study, Zhu et al. [36] utilized a similar approach to successfully design new inhibitors for salt-inducible kinase 2 (SIK2).

The two studies discussed above used AlphaFold models for protein targets sharing reliable sequence identity with other proteins within the same family for which crystal structures are available and utilized AI-driven molecular generation techniques rather than docking. Several other studies addressed the usability of AlphaFold models for docking [37–41] and real-world virtual screening scenarios [39,42,43]. One of these studies assessed the usability of AlphaFold structures predicted while excluding structural templates with more than 30% identity, thus imitating a virtual screening process with a model based on low prior structural information. Results from these studies demonstrated a worse performance of the AlphaFold models compared to crystal structures, suggesting that using unmodified AlphaFold models is not an ideal scenario. This poorer performance could be due to incorrect binding site geometry, resulting from minor variation at the side-chain level or larger variation of the backbone, suggesting that post-modeling or optimization is required to obtain more realistic holo models [38–43].

In agreement with these results, it was demonstrated that optimization of the binding site by inducing flexibility or manually modifying of the low confidence regions could enhance the docking results [37,39,40,44]. In our recent work, we showed that binding site optimization of the HDAC11 AlphaFold model by adding the catalytic zinc ion and performing minimization in the presence of inserted ligands resulted in a model that

could be used for docking of the known selective HDAC11 inhibitors FT895, MIR002, and SIS17 [32].

In the current study, we present an application of an optimized AlphaFold model for virtual screening while addressing HDAC subtype selectivity [45]. We demonstrate herein that our previously optimized HDAC11 AlphaFold model was successfully utilized for picking a selective hit through a comparative virtual screening approach. In the developed multistep screening, various approaches, including structure-based pharmacophore screening as pre-filtering of large databases, ligand docking, pose filtering, and prioritization, were applied as described in Section 3. To experimentally confirm the virtual screening results, the most promising hit was synthesized and tested in vitro using different HDAC subtypes. In addition, we analyzed the predicted binding mode from docking by means of molecular dynamics (MDs) and MetaDynamics simulations.

2. Results and Discussion

2.1. Dataset Selection and Curation

Hydroxamates comprise a well-defined and characterized pharmacophore for HDAC inhibitors and are considered the most commonly used zinc binding group in HDAC inhibitors [46,47]. Some of the inhibitors bearing the hydroxamate scaffold, such as vorinostat (SAHA), belinostat (PXD-101), and panobinostat (LBH589), have been approved by the FDA in the past for the treatment of hematological malignancies [48]. Benzohydroxamates constitute an important class of HDAC inhibitors, and their development entails an active field within inhibitor design for several HDAC subtypes [47]. ZINC20 is a publicly available database that includes nearly two billion compounds, in 2D and 3D downloadable formats, through a website that allows for rapid analogue searching [49]. Initially, a focused database of 407,834 benzohydroxamates was acquired from the ZINC20 database. The library was further prepared by generating possible ionization states at physiological pH 7.0 ± 2.0. The preparation step resulted in a library that contained 510,529 ligands with various ionization states; this library was then subjected to filtration to select the ligands with a hydroxamate state only. The Lipinski rule of five is an important early measure for identifying bioavailable drug-like candidates. According to this rule, a compound must possess the following properties: molecular weight < 500 Da, logP < 5, H-bond donors < 5, and H-bond acceptors < 10. To further select drug-like molecules, the prepared library was filtered to remove any molecule that violated Lipinski's rule of five [50,51]. The initial curation resulted in a library of 18,113 ligands. The multistep virtual screening process was then performed as presented in the workflow (Figure 1).

2.2. Virtual Screening

The E-pharmacophore module implemented in Schrödinger's PHASE automatically generates a pharmacophore hypothesis that is based on the complementarity of the protein and ligand features from a protein–ligand complex. This involves using Glide XP scoring terms to determine which features contribute the most to the binding. The hypothesis obtained from using the previously optimized complex of TSA and the HDAC11 AlphaFold model exhibited four features (Figure 2), namely, a hydrogen bond acceptor feature assigned for the carbonyl-O, a hydrogen bond donor assigned to the NH, a negative feature for the deprotonated hydroxyl group of the hydroxamate zinc binding group, and an aromatic feature for the phenyl capping group. Excluded volumes that are based on the occupation of space by protein atoms were also added. Pharmacophore screening was performed to select the ligands that matched the four features, with the aim of filtering out very small ligands/fragments as well as compounds larger than what could be accommodated in the HDAC11 pocket. Thus, the pharmacophore formed by the excluded volumes was primarily used to reduce the very large number of compounds for the subsequent and more computationally demanding docking method.

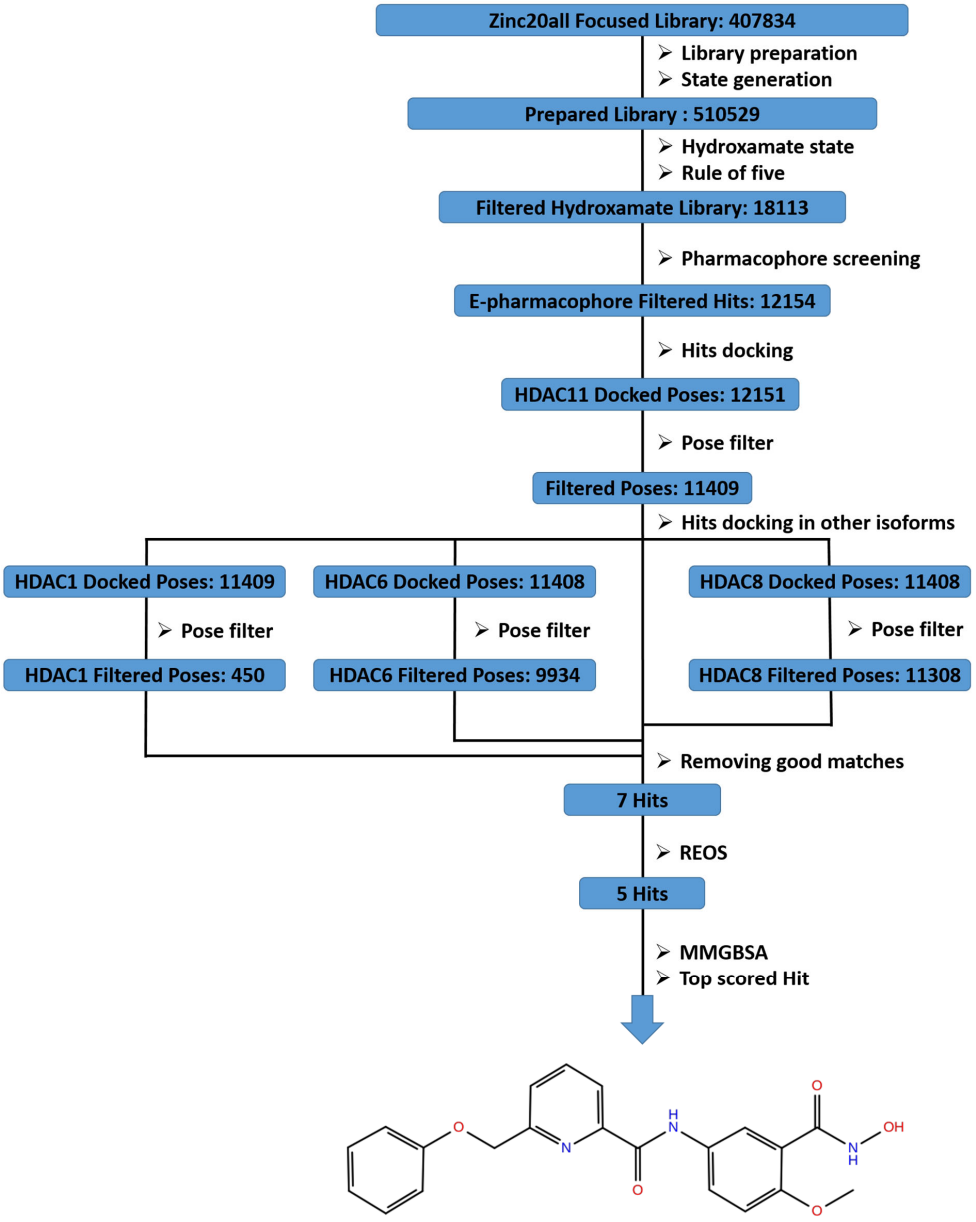

Figure 1. Workflow of the stepwise virtual screening.

The pharmacophore screening step was effective and could filter out 5959 compounds. Docking-based virtual screening of the remaining 12,154 structures was then performed using the grid generated from the HDAC11-TSA-optimized AlphaFold model. In our previous study, we successfully obtained four optimized complexes by minimization of the HDAC11 AlphaFold model with previously reported active ligands of HDAC11, for which X-ray crystal structures with HDAC8 are available in the protein databank (PDB). The selection of the TSA-HDAC11 complex for the virtual screening was based on the results obtained from the previous study, since it showed the best performance regarding the docking of the selective inhibitor FT895 (Figure 3) and was further utilized in docking of other selective inhibitors such as MIR002 and SIS17. Almost all of the hits from the

pharmacophore screening step were able to pass the docking-based screening. Furthermore, filtration of the obtained docking poses was performed to select the ligands that can show a bidentate chelation mode to the catalytic zinc ion. Pose filtration was performed utilizing the distances between the chelator carbonyl and hydroxyl oxygen atoms of the hydroxamate moiety to the zinc ion. Compounds showing distances more than a cut off of 2.6 Å between any of the chelator atoms and the zinc ion were removed.

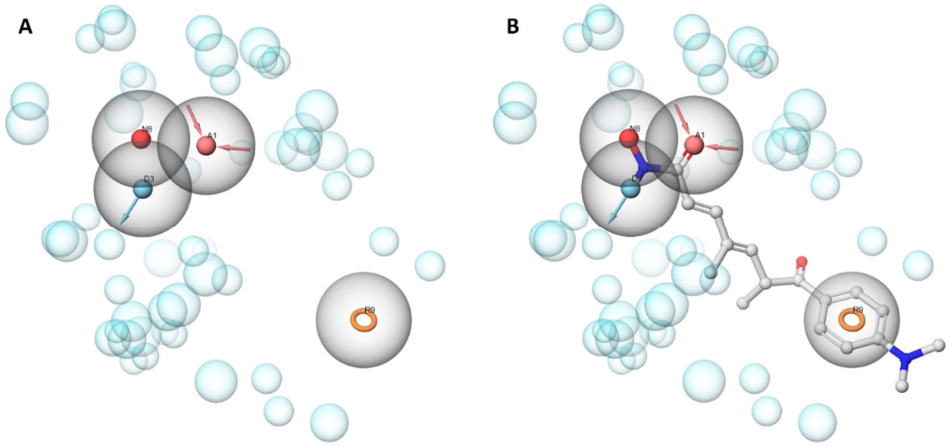

Figure 2. E-pharmacophore model. (**A**) Pharmacophore features: HB donor represented as cyan arrows, HB acceptor as orange arrows, negative features as red dots, and aromatic features as orange rings. Allowed volumes for pharmacophore features are shown as grey spheres. Excluded volumes are represented as cyan transparent spheres and feature matching tolerance as grey transparent spheres. (**B**) Superposition of the inhibitor TSA on the features of the generated hypothesis. Ligand is represented as stick model (grey = carbon, blue = nitrogen, red = oxygen).

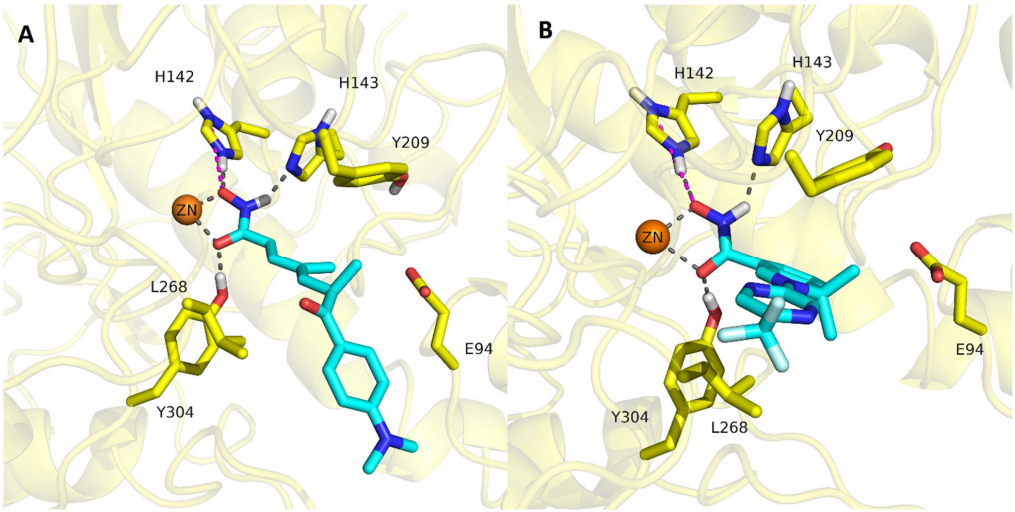

Figure 3. (**A**) Minimized pose of TSA in HDAC11-optimized AlphaFold model. (**B**) Docked pose of FT895 in the optimized HDAC11 AlphaFold model. The protein backbone is represented as yellow cartoon, the interacting binding site residues as yellow sticks, zinc ion as orange sphere, and the ligands as sticks (cyan = carbon, blue = nitrogen, red = oxygen, grey = polar hydrogens). Hydrogen bonds and coordination bonds are represented as grey dashed lines and ionic interactions as magenta dashed lines.

With the aim of searching for selective HDAC11 ligands, a comparative docking-based virtual screening approach was then applied. The hits obtained from the docking in HDAC11 which could pass the pose filtration step were then screened by docking into HDAC1, HDAC6, and HDAC8 crystal structures. The obtained hits from every screening were further subjected to pose filter screening. Ligands which could show correct docking pose with bidentate chelation of the catalytic zinc ion in any of HDAC1, HDAC6, and HDAC8 were removed from the HDAC11 hit list. For HDAC6, ligands which could chelate the zinc ion in a monodentate fashion were also removed. This step was very effective and could filter out most of the compounds, leaving only seven compounds (Table S1, Supplementary Materials) that could show a correct chelation mode in HDAC11 but not in any of the other isoforms.

Rapid elimination of swill (REOS) [52,53] filter was then applied to remove compounds containing reactive or toxic moieties which might also interfere with biological assays. Two compounds containing nitro groups were removed by using this filter. Interestingly, the final five hits (Table 1) all bear a methoxy, ethoxy, or chloro substituent on the ortho position of the hydroxamate moiety, which indicates that substitution at this position might represent a selectivity determinant for HDAC11 inhibition.

Table 1. Final hits and MM-GBSA dG binding values (black = carbon, blue = nitrogen, red = oxygen, chlor = green).

Title	Structure	MM-GBSA dG Bind
ZINC000028464438 (**9**)	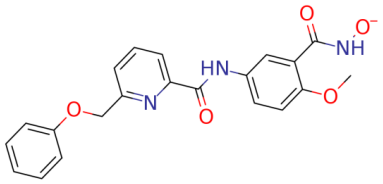	−49.76
ZINC000671998736	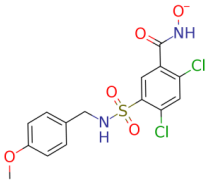	−39.75
ZINC000742823399	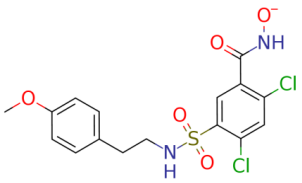	−48.68
ZINC000916666211	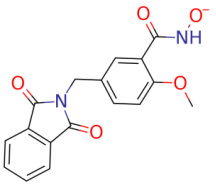	−48.21

Table 1. *Cont.*

Title	Structure	MM-GBSA dG Bind
ZINC000916666264	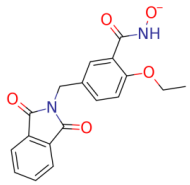	−41.45

In the last step of the virtual screening workflow, the five final hits were prioritized through MM-GBSA calculations. MM-GBSA calculations showed that the top-ranked molecule is ZINC000028464438 (**9**), which bears a methoxy group as ortho substitution to the hydroxamate moiety and an amide linker in the meta-position. It is worth noting that a selective HDAC11 inhibitor (PB94) was recently presented by Bai et al. [26]. Based on the structure–activity relationship, the authors reported that a methoxy group in the ortho position of their developed benzohydroxamate inhibitors is a key factor for HDAC11 selectivity, which is in agreement with our results from the virtual screening.

2.3. In Vitro Enzymatic Evaluation

Due to the unavailability of the top-ranked hit ZINC000028464438, we decided to resynthesize the compound (**9**) as reported [54]. We purified it, confirmed the structure by NMR and MS, and tested it at a concentration of 10 µM against HDAC11 as well as all other HDAC subtypes (HDAC1–10) to determine the selectivity. The synthesis and analytical characterization are described in detail in Section 3. Compound **9** showed inhibition of around 85% in the enzymatic activity for HDAC11, almost no inhibition for nearly all HDAC subtypes, and only around 20% inhibition of HDAC6 (Figure 4A). Interestingly, the findings from the in vitro screening confirm the results obtained from the theoretical study, as the hit compound was not able to adopt reasonable poses in any of HDAC1, HDAC6, and HDAC8. On the other hand, a perfect pose with a bidentate chelation mode that also demonstrates the expected interactions of a benzohydroxamate-based HDAC inhibitor was observed in HDAC11 and proved to be stable during MD simulations. These results further confirm that HDAC11 can accommodate such bulkier substitutions in the ortho position of the benzohydroxamate moiety of the inhibitor, providing a unique feature that can be used to target isoform selectivity when designing new inhibitors.

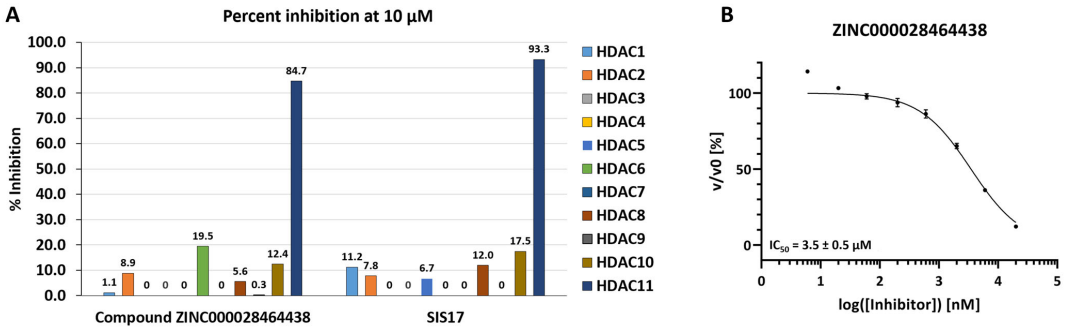

Figure 4. (**A**) Relative inhibition of enzymatic activity for all HDAC subtypes at 10 µM of **9** (ZINC000028464438) and SIS17. (**B**) Determination of IC_{50} value of **9** (ZINC000028464438) for HDAC11.

Furthermore, the IC_{50} for HDAC11 was determined to be about 3.5 µM (Figure 4B). While this virtual screening hit showed only moderate HDAC11 inhibitory activity, it still can be considered a promising hit compound due to the good selectivity. Further

chemical optimization is required that might include manipulation of the size and structure of the ortho substituent at the benzohydroxamate moiety, changing the position and structure of the amide linker, or changing the structure and decorations of the capping group. The obtained results can be assessed in the light of capabilities of virtual screening and the role it plays for hit identification and finding new scaffold leads by screening large compound libraries, a process that is commonly followed by lead optimization. We included the well-characterized HDAC11 inhibitor SIS17 as a reference compound in our enzyme inhibition assay, and it showed IC_{50} of 0.17 μM, which is in line with reported data [28] (Figures 4A and S6).

2.4. Analysis of the Docked Poses

Analyzing the docked poses of the confirmed hit revealed that the obtained pose of the hit compound in the optimized HDAC11 AlphaFold model (Figure 5) showed bidentate chelation, with distances of 2.41 Å and 2.17 Å between the zinc ion and the carbonyl and hydroxyl oxygen atoms of the hydroxamate moiety, respectively. A salt bridge to His142 as well as hydrogen bond interactions with His143 and Tyr304 were observed. The ligand also demonstrated π–π interactions between the phenyl ring of the benzohydroxamate and His183. The phenoxymethyl capping group adopts a bent conformation and is directed towards loop1. For HDAC1, the hit ligand showed a pose in which no metal chelation was observed, as the hydroxamate moiety could not reach the zinc ion in the depth of the binding pocket, barely reaching His178, with which the ligand forms a hydrogen bond through the hydroxyl oxygen of the hydroxamate moiety. Another hydrogen bond was observed between the NH of the amide linker and Asp99 side chain. In HDAC6, the docking resulted in a flipped orientation, with the hydroxamate moiety facing the solvent, which indicates that the ligand could not fit into the binding site. No interactions could be observed for the obtained pose in HDAC6. The hit ligand could not show the bidentate zinc chelation commonly observed for co-crystallized HDAC8 inhibitors.

In previous studies, we performed a structural comparison of the optimized HDAC11 AlphaFold model with HDAC6 and HDAC8 as candidates of class I and class II HDACs [32]. The comparison showed that the folding of loop 3 of HDAC11 is more similar to HDAC8, suggesting the formation of the so-called foot pocket in HDAC11, similarly to HDAC8. Thus, the HDAC11 model shows a large foot pocket that justifies the binding of ligands with long alkyl chains, such as the alkyl hydrazide derivative SIS17. The entrance of the foot pocket in HDAC11 is formed by the residues Gly139, Gly140, and Phe141, whereas in HDAC8, the Phe141 is replaced by the bulkier residue Trp141. In HDAC6, loop 3 residues are replaced by the bulkier Pro607 and Pro608 as well as the larger residue Arg606. In addition, the Arg606 side chain is directed towards loop 1, forming polar interactions with Glu50, thus causing loop 3 to fold in the opposite direction and blocking the formation of the foot pocket in HDAC6.

Since we found that the optimized HDAC11-AlphaFold model in complex with TSA and the lowest energy rotamer of Phe152 (flipped-out conformation) showed the best results in docking of selective ligands such as FT895 and SIS17, we used this model for virtual screening in the current study. To better understand the structural basis of the HDAC11 inhibition, we analyzed the shape of the binding pockets of the crystal structures and the HDAC11 AlphaFold model. The analysis revealed that the flipping of Phe152 in HDAC11 together with the less bulky residue Phe141 as foot pocket gatekeeper allows for a wider binding pocket that can accommodate the bulky methoxy substituent in the ortho position of the benzohydroxamate moiety of the hit **9**. Analysis of the crystal structures of HDAC1 (5ICN) and HDAC6 (5EDU) (Figure 6A,B) shows that, here, the different conformation of this conserved phenyl alanine brings it closer to the residues from loop 1 and loop 2 (such as Tyr24 and Lys31 in HDAC1 and Glu502 in HDAC6) and narrows the pocket in HDAC1 as well as HDAC6. As a result, this pocket cannot accommodate ortho-substituted benzohydroxamates (no zinc chelation is possible) like the hit compound **9**.

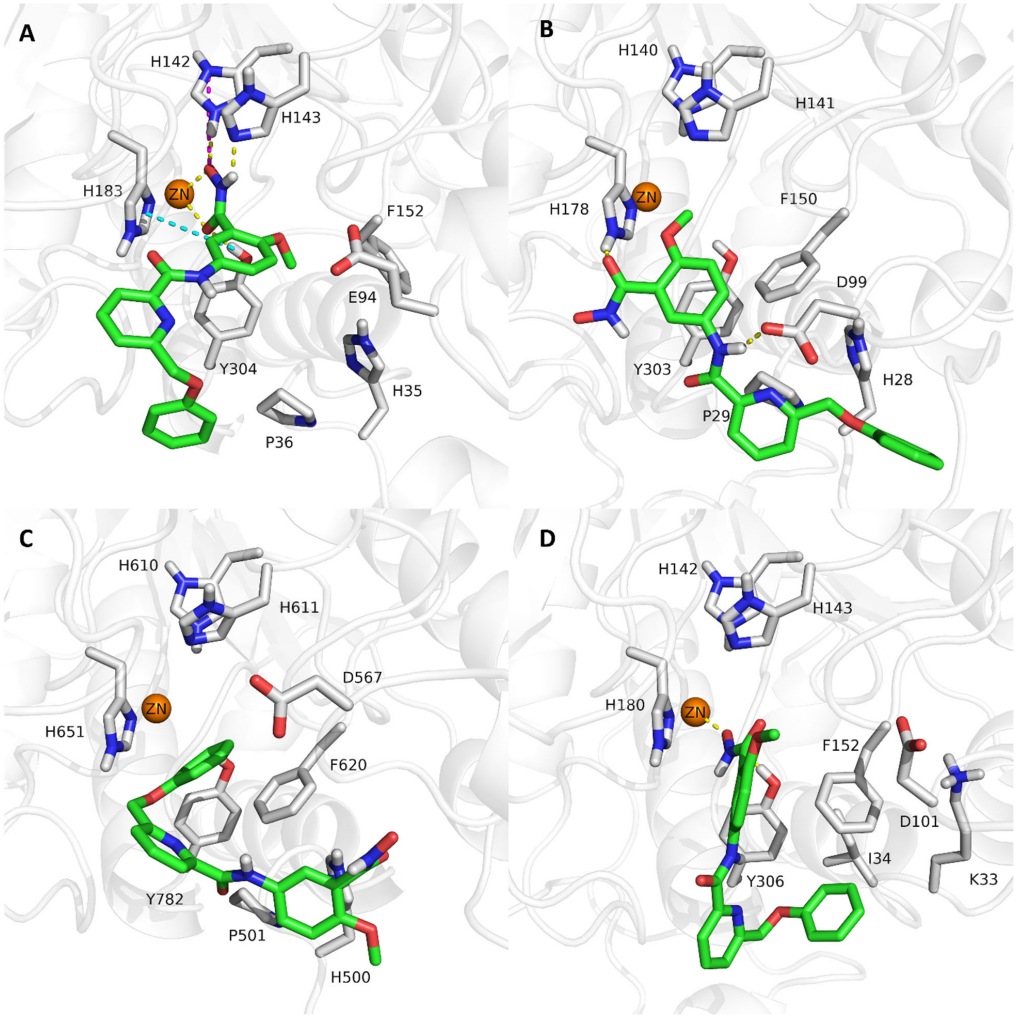

Figure 5. Docked poses of ZINC000028464438 (**9**). (**A**) HDAC11. (**B**) HDAC1. (**C**) HDAC6. (**D**) HDAC8. The protein backbone is shown as white cartoon, zinc ion as orange sphere, the binding site residues as grey sticks, and the ligands as sticks (green = carbon, blue = nitrogen, red = oxygen, grey = polar hydrogens). Coordination and hydrogen bonds are shown as yellow dashed lines, π–π interactions as cyan dashed lines, and the ionic interactions as magenta dashed lines.

The HDAC8 crystal structure 5FCW was used as an "anti-target" for virtual screening in this study, as, to our knowledge, it has the best resolution for a wild-type human HDAC8 crystal structure co-crystallized with a hydroxamic acid. A closer look and comparison of the docked poses of the hit compound in HDAC11 and HDAC8 show that the ligand in the HDAC11 pocket is oriented slightly differently (Figure 6C,D), allowing for a better fit to the ortho substitution. Another observation is that in the docking poses in HDAC8, a considerable portion of the ligand is exposed to the solvent due to the shorter loop 1 of HDAC8, whereas the ligand in HDAC11 is stabilized by the longer loop 1, as shown in the MD studies. In the case of HDAC8-selective inhibitors, a more L-shaped conformation was observed in docking studies and X-ray structures [45,55,56]. Consideration of these observations may explain the preferential binding of the hit compound in HDAC11.

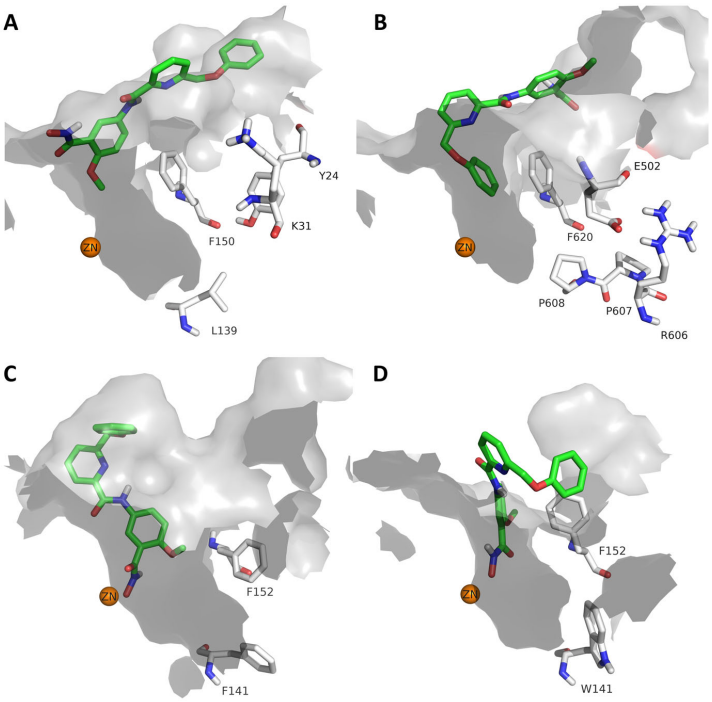

Figure 6. Docking poses of the hit compound **9** and demonstration of the binding site shape and size. (**A**) HDAC1 (PDB ID 5ICN), (**B**) HDAC6 (PDB ID 5EDU), (**C**) HDAC11 (AlphaFold model), (**D**) HDAC8 (PDB ID 5FCW). The ligand is represented as stick model (green = carbon, blue = nitrogen, red = oxygen, grey = polar hydrogens).

2.5. Molecular Dynamics Simulations

Docking methods are limited by not considering the flexibility of the protein but treating the receptor as rigid body. On the other hand, the MD simulation technique takes into account the flexibility of the complex, thus providing a deeper insight regarding the binding mode of the ligand and its behavior in a dynamic environment. Therefore, we decided to study the binding mode of the confirmed hit extensively, using short and long MD simulations. The docking pose of the hit compound in the optimized HDAC11 AlphaFold model was subjected to three short (50 ns) molecular dynamics simulations using different random seeds. Furthermore, a longer MD simulation (500 ns) was performed to assess the stability of the obtained pose over a longer time scale.

In all MD simulations, the protein and the zinc ion demonstrated high stability that could be observed through the calculated RMSD plots. The protein backbone stabilizes between 1 Å and 2 Å while the zinc ion stabilizes at almost 1 Å (Figure 7A,B).

The results of the three independent short MD simulations were comparable. The RMSD plot of the ligand demonstrated that there is a shift in the pose directly after the simulation started and that the ligand stabilizes between 3 Å and 4 Å till the end of the simulation (Figure 8A). Analyzing the RMSF of the ligand-heavy atoms showed that the phenoxymethyl capping group is the most fluctuating substructure of the ligand, with an RMSF reaching 2 Å (Figure 8B).

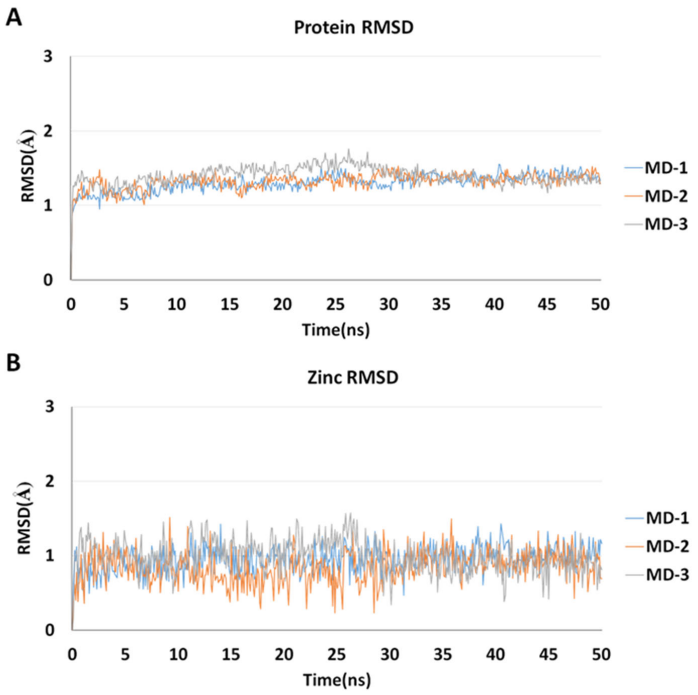

Figure 7. RMSD plots of ZINC000028464438 (**9**) for 3 repeated MD runs each for 50 ns. (**A**) RMSD plots of protein backbone-heavy atoms. (**B**) RMSD plots of zinc ion.

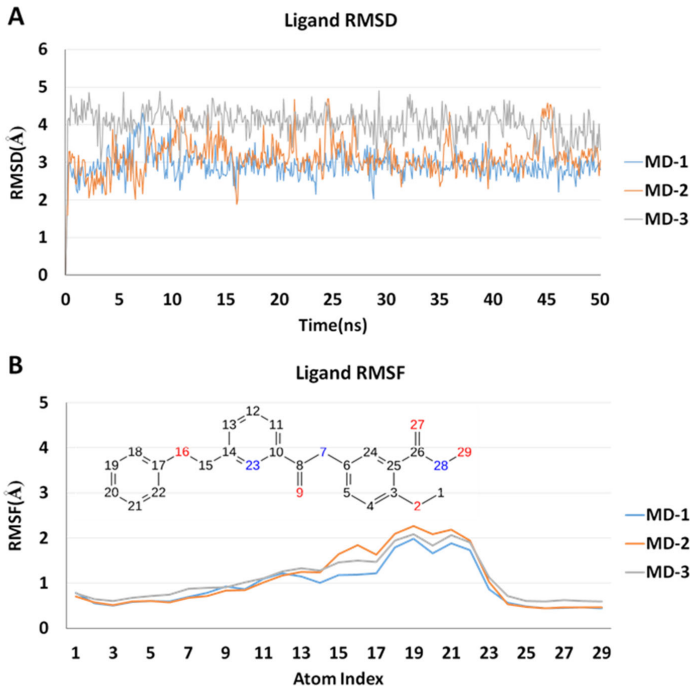

Figure 8. RMSD and RMSF plots of ZINC000028464438 (**9**) for 3 repeated MD runs each for 50 ns. (**A**) RMSD plots of ligand-heavy atoms. (**B**) RMSF plots of ligand-heavy atoms.

Inspecting the MD trajectories showed that there is a slight shift of the initial docking pose, allowing for the benzohydroxamate moiety to be accommodated deeper into the binding pocket, which also leads to a better accommodation of the capping group through the relaxation of the conformation (Figure 9).

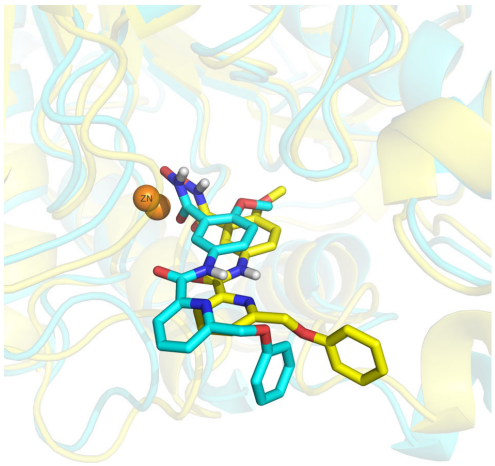

Figure 9. Superposition of the first and last frames of ZINC000028464438 (**9**), showing the shift in the pose during the simulation from the first MD run of 50 ns. The zinc ion is represented as orange sphere, the protein backbone as cartoon, and ligand as sticks (cyan and yellow = carbon, blue = nitrogen, red = oxygen, grey = polar hydrogens). The protein backbone and the ligand are colored in cyan and yellow for the first and last frames, respectively.

The stability of the bidentate chelation mode was confirmed for the three runs by monitoring the distances between the chelator atoms of the hydroxamate zinc binding group and the zinc ion (Figure 10A,B). The salt bridge to His142 showed very high stability, with persistence of almost 100% for the three runs. The hydrogen bond interaction to His143 showed moderate stability, with persistence ranging between 54% and 72%. It is worth noting that we observed similar weak to moderate stability of the hydrogen bond interaction with His143 during MD simulation with some of the ligands we utilized for the model optimization in our previous study, such as TSA and some of the selective docked ligands, e.g., FT895 and MIR002 [32].

The slight shift in the pose discussed above leads to almost complete loss of the hydrogen bond between Tyr304 and the carbonyl oxygen of the hydroxamate moiety but allowed for the formation of another hydrogen bond between the same residue and the oxygen of the methoxy substituent in the ortho position of the benzohydroxamate substructure that showed high stability, with persistence ranging between 72% and 87%. This shift in the pose also allowed for the formation of another hydrogen bond interaction that was not observed in the initial docked pose between His183 and the carbonyl oxygen of the amide linker; however, low stability of this interaction was observed with persistence between 26% and 37%. (Table S2, Supplementary Materials).

The longer molecular dynamics simulation was able to confirm the stability of the obtained pose of the hit in the HDAC11 AlphaFold model over a long time scale. Inspecting the RMSD plot of the ligand showed that it is stabilizes between 4 Å and 5 Å (Figure 11A), with the RMSF indicating that the substructure that fluctuates most is the phenoxymethyl group (Figure 11B).

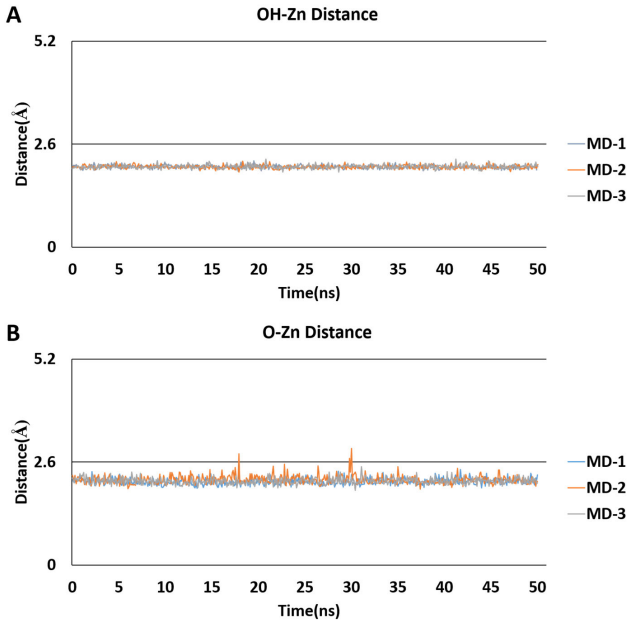

Figure 10. (**A**,**B**) Distances to the zinc ion for three repeated MD runs each for 50 ns for the hydroxyl and the carbonyl oxygen atoms of the hydroxamate zinc binding group, respectively.

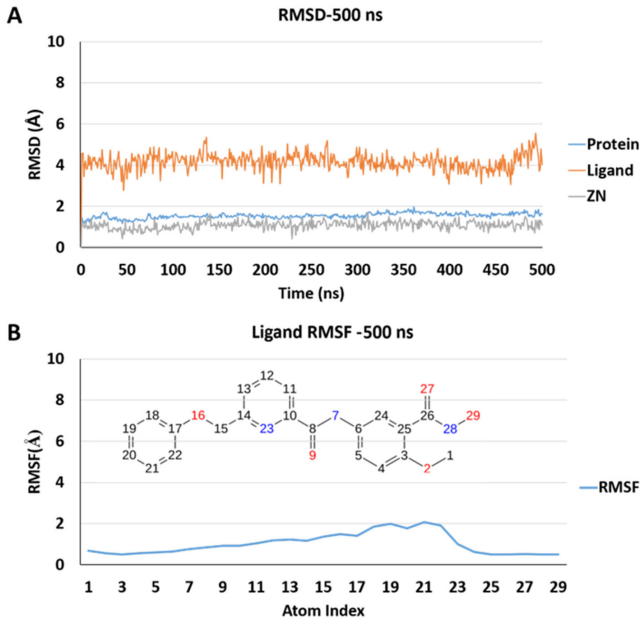

Figure 11. (**A**) RMSD plots of the protein backbone-heavy atoms, zinc ion, and ligand-heavy atoms for the long MD run (500 ns). (**B**) RMSF plots of the ligand- and ZINC000028464438 (**9**)-heavy atoms for the long MD run (500 ns).

Distances between the zinc ion and the chelator atoms of the hydroxamate zinc binding group were shown to be stable, thus confirming the bidentate chelation mode (Figure 12A,B).

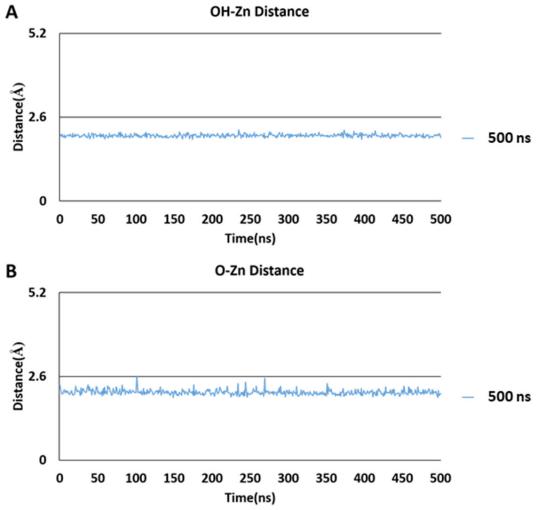

Figure 12. (**A**,**B**) Distances to the zinc ion for the hydroxyl and the carbonyl oxygen atoms of the hydroxamate zinc binding group, respectively, for the long MD run (500 ns).

MD simulation trajectory analysis demonstrated the same slight shift in the pose, with the benzohydroxamate moiety inserted deeper into the binding pocket, along with the relaxation of the phenoxymethyl capping group (Figure 13), as observed in the three independent and shorter MD runs.

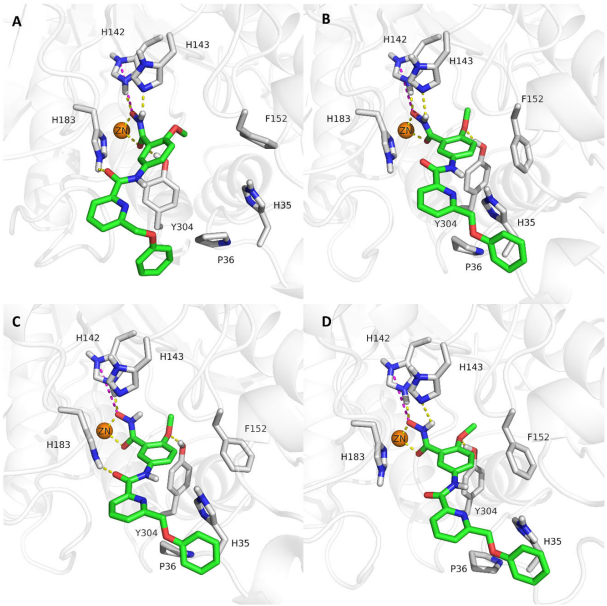

Figure 13. Selected snapshots from the long MD simulation (500 ns) of ZINC000028464438 (**9**)-HDAC11-docked pose showing the shift in the pose and fluctuation in the phenoxymethyl capping group. (**A**) Frame 1. (**B**) Frame 1250. (**C**) Frame 2500. (**D**) Frame 5000. The protein backbone is shown as white cartoon, zinc ion as orange sphere, the binding site residues as grey sticks, and the ligands as atom-colored sticks (green = carbon, blue = nitrogen, red = oxygen, grey = polar hydrogens). Coordination and hydrogen bonds are shown as yellow dashed lines and the ionic interactions as magenta dashed lines.

The salt bridge between the deprotonated hydroxyl oxygen of the zinc binding group and His142 showed very high stability, with persistence of about 100%, while, for His143, the hydrogen bond interaction with the carbonyl oxygen of the hydroxamate moiety demonstrated average stability, with persistence of 68%. The same observations could be made concerning the other hydrogen bond interactions during the simulation in the short runs. The hydrogen bond interaction between the oxygen of the methoxy group in the ortho position to the hydroxamate moiety and Tyr304 demonstrated persistence of 85%, while for His183, a weakly stable hydrogen bond with the carbonyl of the amide linker showing persistence of 42% could be observed. Overall, the predicted binding mode of the hit compound demonstrated good stability during the MD simulation. The key interactions of the zinc binding group were not affected by the slight shift of the ligand from the initial docked pose or the fluctuation in the capping group (Figures 14 and 15).

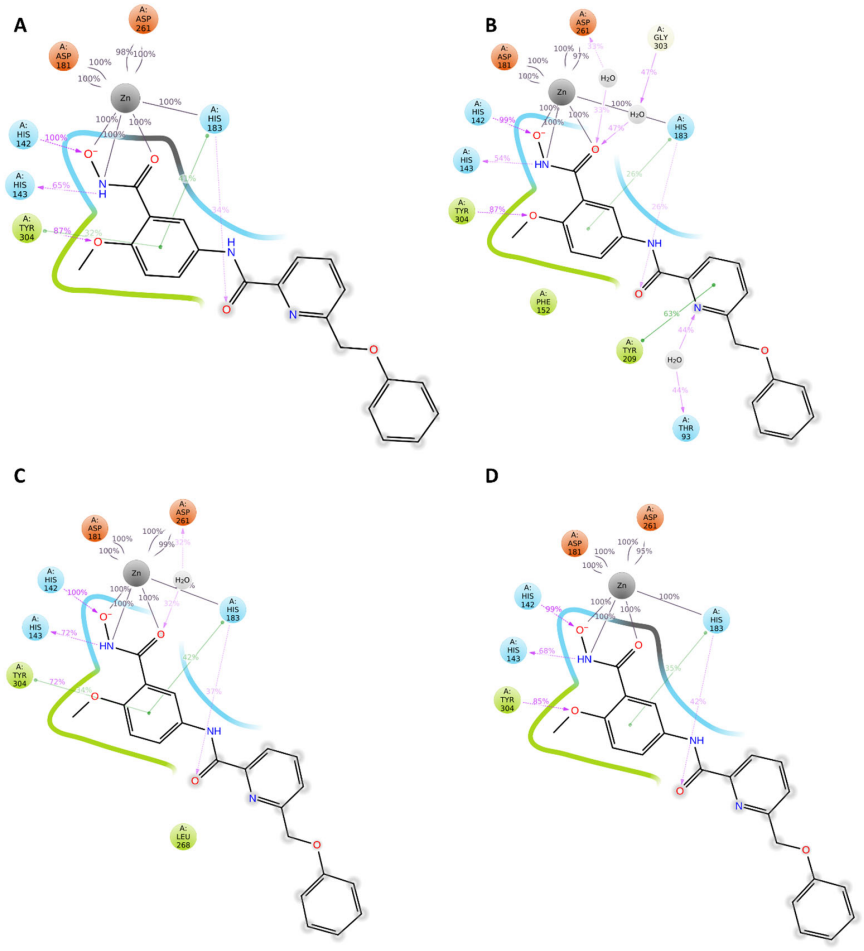

Figure 14. (**A**–**C**) Ligand interaction persistence diagram for the three independent short MD runs (**A**) MD1, (**B**) MD2, (**C**) MD3) (50 ns) and (**D**) the long MD run (500 ns), respectively, of HDAC11-ZINC000028464438 (**9**).

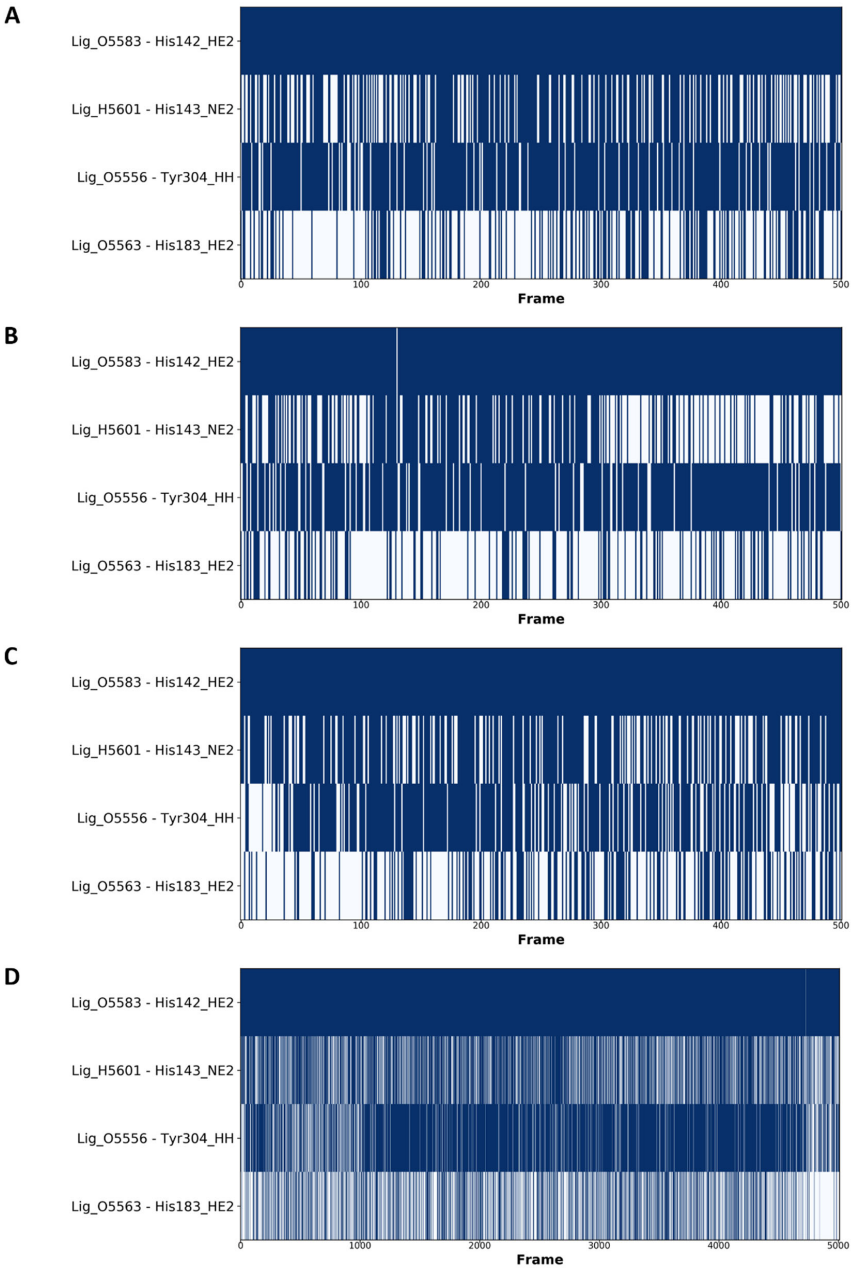

Figure 15. (**A**–**C**) Hydrogen bond occupancy diagrams for the three independent short MD runs (50 ns, (**A**) MD1, (**B**) MD2, (**C**) MD3) and (**D**) the long MD run (500 ns), respectively, of HDAC11-ZINC000028464438 (**9**).

Metadynamics is an enhanced sampling technique that is able to capture the structural dynamics more efficiently in limited time scale by using a history-dependent bias potential as a function of a collective variable [57]. This process helps the system escape energy minima and previously sampled regions, thus accelerating sampling of the entire complex free-energy landscape.

Binding pose metadynamics (BPMD) application [58] implemented in Schrödinger was originally developed to rank docking poses of a single ligand in a single protein binding site by running a series of metadynamics simulations. We utilized this methodology to further explore the stability of the predicted binding mode observed for the hit compound in the HDAC11 AlphaFold model.

For this purpose, and because we observed a slight shift in the original docked pose during the classical MD simulation, we applied BPMD for the obtained docked pose and the last frame (500 ns) of the classical MD simulation representing the equilibrated ligand pose.

The BPMD method employs the RMSD of the ligand from its initial pose as a collective variable. The stability of the protein ligand complex is evaluated in terms of the ligand's RMSD fluctuations and the persistence of important contacts between the ligand and the receptor over the course of the simulation. The PoseScore indicates the average RMSD of the ligand, the persistence score (PersScore) indicates the persistence of the interactions over the course of the simulation, and the composite score (CompScore) combines the PoseScore and PersScore [58,59].

The results from BPMD demonstrated a PoseScore of 3.226 and 1.747 for the original docked pose and the last MD frame, respectively (Figure 16). Generally, ligand poses with a PoseScore $\leq$ 2 Å were considered stable [58]. The resulting PoseScore indicates that the stabilized pose during the MD simulation is more stable when compared to the starting docked pose, thus reinforcing the results obtained from the classical MD simulation which showed a slight shift of the ligand during the run.

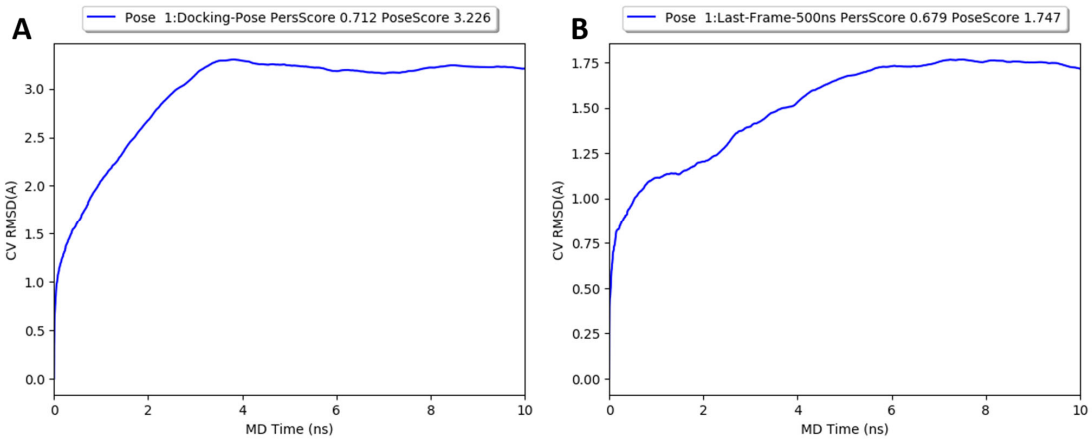

Figure 16. Plots of the average value of the collective variable (RMSD) over the metadynamics simulation. (**A**) The original docked pose and (**B**) the pose from last frame of the 500 ns MD simulation, respectively, of HDAC11-ZINC000028464438 (**9**).

The resulting persistence of the interactions is almost equivalent for both poses and showed a PersScore of 0.712 and 0.679 for the original docked pose and the last MD frame pose, respectively. The results match the defined threshold of $\geq$0.6 [58], indicating that the contact network was maintained during the course of the simulation. The CompScore for the original pose and the last frame pose of the hit ligand were found to be $-$0.335 and $-$1.647, respectively, with increasingly negative values indicating better stability.

Overall, the results from the metadynamics studies confirmed the stability of the predicted binding pose in terms of the ligand RMSD and persistence of the observed interactions and further supported the results from the classical MD simulations.

3. Materials and Methods

Schrödinger Suite 2019 was used for all of the modeling work. Maestro [60] was utilized for visualization (Release 2019-1, Schrödinger, LLC: New York, NY, USA).

All ligands were docked in the deprotonated hydroxamate form while the grids for docking were all generated with the His142 (HDAC11 numbering) in the protonated HIP form. According to our experience from our previous study [32], this methodology shows better performance with the docking software used, Glide (Release 2019-1, Schrödinger, LLC: New York, NY, USA), in terms of reproducing the bidentate chelation native poses of the co-crystallized ligands.

3.1. Protein Preparation

All protein structures were preprocessed using Protein Preparation Wizard (Release 2019-1, Schrödinger, LLC: New York, NY, USA) [61,62] by adding hydrogen atoms and assigning bond orders. Water molecules beyond 5 Å from the ligands were deleted and zero order bonds to metals were added. Filling in missing side chains and loops using Prime [63–65] was performed. Ionization states of the ligands were generated using Epik (Release 2019-1, Schrödinger, LLC: New York, NY, USA) [66–68] at pH 7.0 ± 2.0. The deprotonated hydroxamates form [32,69–72] was selected for further hydrogen bond optimization. Hydrogen bond optimization was assigned with sampling water orientation, using PROPKA (Release 2019-1, Schrödinger, LLC: New York, NY, USA) at pH 7.0.

3.2. Grid Generation

For all protein–ligand complexes, grids were generated using the Receptor Grid Generation panel, utilizing the centroid of the ligand as the center of the grid.

3.3. Ligand Preparation

Ligands were prepared in the predominant form at pH 7, utilizing the LigPrep [73] panel with OPLS3e force fields.

3.4. Database Acquiring and Curation

3.4.1. Acquiring Ligand Database

A focused library of benzohydroxamic acids (SMARTS=C1=CC=C(C(=O)NO)C=C1) comprising 407,834 ligands was downloaded from https://tldr.docking.org/ using the zinc20-all database (accessed on 1 August 2023) [49].

3.4.2. Ligand Preparation

The library was prepared using Ligprep and resulted in 510,529 structures using OPLS2005 (Release 2019-1, Schrödinger, LLC: New York, NY, USA) [74–77]; possible states were generated at pH 7.2 ± 2 using Epik. Specified chiralities from the original dataset were retained.

3.4.3. Property Calculation

The rule of five properties was calculated for all ligands in the database using QikProp (Release 2019-1, Schrödinger, LLC: New York, NY, USA) [78] properties from the Molecular Descriptor panel.

3.4.4. Database Filtering

The prepared library was filtered to select the hydroxamate form [32,69–72] of the ligands using a defined custom pattern of [O-]N([H])C(=O)c1ccccc1. The library was filtered using the calculated rule of five properties, thereby discarding all structures which showed one or more violations of the rule of five, using the Ligand Filtering panel. A total of 18,113 compounds successfully passed the aforementioned filters.

3.5. Virtual Screening

3.5.1. Structure-Based Pharmacophore Modeling

Pharmacophore Generation

The E-pharmacophore [79,80] hypothesis was generated using the Develop Pharmacophore Model panel form in Phase (Release 2019-1, Schrödinger, LLC: New York, NY, USA) [81–83] utilizing the optimized AlphaFold TSA-HDAC11 complex with the flipped-out Phe152 rotamer [32]. The auto E-pharmacophore method was used to specify the maximum number of features to be generated and assign the receptor-based excluded-volume shell.

Pharmacophore Screening

The prepared database was screened through Phase Ligand Screening panel using the previously generated E-pharmacophore and implementing the four obtained features and excluded volumes. Up to 50 conformers were generated during the search and specifying, leading us to report, at most, one hit per ligand. A total of 12,154 hits successfully passed the pharmacophore screening.

3.5.2. Docking into HDAC11 AlphaFold Model

The hits obtained from the pharmacophore screening were docked into the HDAC11 AlphaFold model using Glide (Release 2019-1, Schrödinger, LLC: New York, NY, USA) [84–87] with standard precision and flexible ligand sampling. A total of 15 poses were subjected to post-docking minimization and reporting of the top-scored pose. A total of 12,151 compounds could be successfully docked.

3.5.3. Pose Filtering

The obtained docking poses in the HDAC11 AlphaFold model were filtered using Pose Filter panel, utilizing the distance between the carbonyl and the hydroxyl oxygens of the hydroxamate moiety and the zinc ion while specifying maximum contact distance to be 2.6 Å. A total of 11,409 poses successfully passed the filter.

3.5.4. Docking and Pose Filtering in Other HDACs' Isoforms

The following crystal structures were used for the docking studies in other HDAC subtypes:

Isoform	PDB ID	Resolution	Organism	Bound Inhibitor
HDAC1	5ICN	3.30 Å	Homo sapiens	Hydroxamic acid inhibitor
HDAC6	5EDU	2.79 Å	Homo sapiens CD2	Hydroxamic acid inhibitor
HDAC8	5FCW	1.98 Å	Homo sapiens	Hydroxamic acid inhibitor

Validation by Redocking of the Native Ligand

To validate the docking protocol, redocking of the co-crystallized ligands of HDAC1, HDAC6, and HDAC8 was performed, and RMSD for the docked and the native poses was calculated. RMSD was found to be 2.018 Å, 1.192 Å, and 0.416 Å for HDAC1, HDAC6, and HDAC8, respectively.

Docking and Pose Filtering

The filtered poses from the HDAC11 docking results were further docked into HDAC1, HDAC6, and HDAC8. The obtained docking poses were further subjected to Pose Filter. Ligand docking and pose filtering were performed using the same settings as mentioned for HDAC11. In total, 450, 9934, and 11,308 hits were successfully docked to HDAC1, HDAC6, and HDAC8, respectively. Compounds that were able to show correct poses and

zinc chelation in HDAC1, HDAC6, and HDAC8 were removed from the final HDAC11 inhibitor hit list.

3.6. REOS Filtering and MM-GBSA Calculations

To remove compounds with reactive groups that may interfere with biological evaluation, rapid elimination of swill (REOS) filter was applied using structure filter in Canvas [88–90].

To prioritize the hits for further evaluation, ligand binding energies were calculated using the molecular mechanics with Generalized Born and surface area solvation (MM-GBSA). For this purpose, the Prime MM-GBSA panel was utilized, the variable-dielectric Generalized Born (VSGB) solvation model was specified, and sampling was carried out by minimizing all atoms using OPLS3e force field.

3.7. Molecular Dynamics Simulation

The predicted binding mode of the virtual screening hit of HDAC11 was further analyzed by means of molecular dynamics simulation using the program Desmond [91,92]. The HDAC11-inhibitor complex was simulated for 50 ns, and the simulation was repeated three times, applying different random seeds. Furthermore, a single longtime scale MD run was performed for 500 ns. The system was solvated in SPC water model using an orthorhombic box and a buffer distance of 10 Å distance between the solute structures and the simulation box boundary. The box volume was then minimized. The system was neutralized by adding chloride ions that were placed 4 Å away from the ligand.

Relaxation of the prepared system was performed using the default Desmond relaxation protocol for NPT ensemble followed by a production run utilizing the NPT ensemble at 300 K using a Nosé–Hoover chain thermostat and a pressure of 1.01325 bar using Martyna–Tobias–Klein barostat.

The Simulation Event Analysis panel was utilized for the calculation of RMSD and distance to the zinc ion. The RMSD of the protein was calculated using the backbone atoms, while the RMSD of the ligand and the zinc ion was calculated by fitting to the protein backbone. The Simulation Interaction Diagram panel was used for analyzing the RMSF and the interaction persistence of the ligands. RMSD of the protein was calculated excluding the termini (residues: 1–14 and 321–347).

Metadynamics (implemented in the Schrödinger software, (Release 2019-1, Schrödinger, LLC: New York, NY, USA) was used to assess the stability of the original docked pose compared to the stabilized pose resulting from the 500 ns MD run. For this purpose, Binding Pose Metadynamics panel was utilized, with the default settings of 10 trials per pose each of 10 ns. Binding pose metadynamics (BPMD) application [53] implemented in Schrödinger was originally developed to rank docking poses of a single ligand in a single protein binding site by running a series of metadynamics simulations. We utilized this methodology to further explore the stability of the predicted binding modes.

3.8. Chemistry

3.8.1. General

Materials and reagents were purchased from Sigma-Aldrich Co., Ltd. (St. Louis, MO, USA) and abcr GmbH (Karlsruhe, Germany). Solvents used during the synthesis and purification were analytically pure and dry. Thin-layer chromatography was carried out using aluminum sheets coated with silica gel 60 F254 (Merck, Darmstadt, Germany). For medium-pressure chromatography (MPLC), columns containing silica gel Biotage® (Biotage, Uppsala, Sweden) SNAP ultra-HP-sphere 25 μm were used.

The purity of the hit compound was determined using high-pressure liquid chromatography (HPLC) (Figure S3) and was measured by UV absorbance at 254 nm. The HPLC system consisted of two LC-10AD pumps, a SPD-M10A VP PDA detector, and a SIL-HT autosampler from the manufacturer Shimadzu (Kyoto, Japan). For the stationary phase, Merck LiChrospher 100 RP18, 125 mm × 4 mm, 5 μm column was used. The mobile phase was composed of methanol, H_2O, and 0.05% trifluroacetic acid.

Mass spectrometry (MS) analyses were carried out on a Finnigan MAT710C (Thermo Separation Products, Planegg/Martinsried, Germany) for the ESI MS spectra (Figure S4). High-resolution mass spectrometry (HRMS-ESI) analyses were performed with an LTQ (linear ion trap) Orbitrap XL hybrid mass spectrometer (Thermo FisherScientific, Planegg/Martinsried, Germany) (Figure S5). Varian Inova 400 (Varian, Darmstadt, Deutschland) was used to measure ^{1}HNMR and ^{13}CNMR spectra using deuterated dimethyl sulfoxide (DMSO-d6) as solvent. Chemical shifts were referenced to the residual solvent signals (Figures S1 and S2).

The hit compound was synthesized according to Scheme 1.

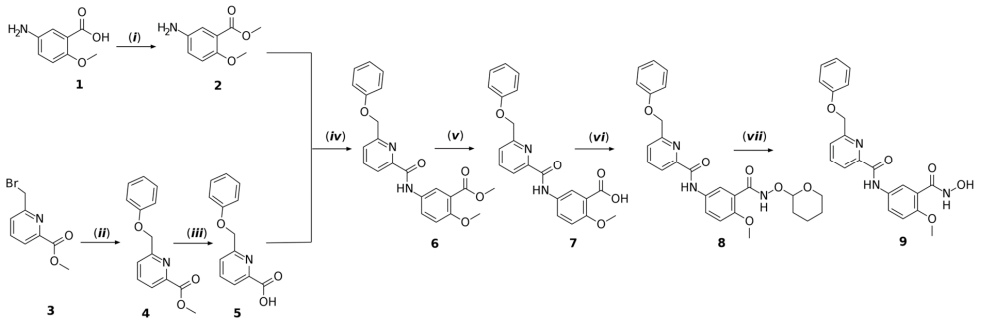

Scheme 1. Synthesis of target compound. Reagents and conditions: (*i*) $SOCl_2$/methanol/reflux/3 h; (*ii*) C_6H_6OH/Cs_2CO_3/DMF/RT/18 h; (*iii*) LiOH.H_2O/THF:H_2O (50:50)/RT/1 h; (*iv*) **5**/$C_2O_2Cl_2$/DCM/RT/2 h then **2**/DIPEA/RT/overnight; (*v*) LiOH.H_2O/THF:H_2O (50:50)/RT/4 h; (*vi*) O-(Tetrahydro-2H-pyran-2-yl)-hydroxylamin/HATU/DIPEA/DMF/RT/4 h; (*vii*) THF/aq. HCl/RT/overnight.

3.8.2. Synthesis Procedure

Methyl 5-amino-2-methoxybenzoate hydrochloride (**2**).

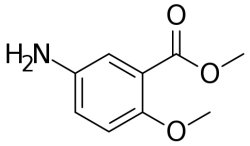

To a stirred solution of 5-amino-2-methoxybenzoic acid **1** (0.5 g, 3 mmol) in methanol, thionyl chloride, (0.33 mL, 4.5 mmol) was added dropwise. The mixture was heated under reflux for 3 h and then cooled and evaporated using rotary evaporator to afford the product as hydrochloride salt; ^{1}H NMR (400 MHz, DMSO-d_6) δ 10.29 (s, 3H), 7.64 (d, *J* = 2.8 Hz, 1H), 7.53 (dd, *J* = 8.9, 2.8 Hz, 1H), 7.24 (d, *J* = 9.0 Hz, 1H), 3.81 (s, 3H), 3.78 (s, 3H). MS *m*/*z*: $[M + H]^+$ 182; yield, 98.31%.

Methyl 6-(phenoxymethyl)pyridine-2-carboxylate (**4**).

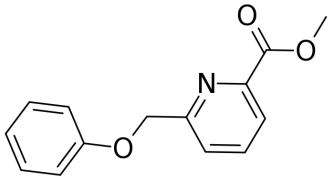

A mixture of methyl 6-(bromomethyl) picolinate **3** (1.38 g, 6 mmol), phenol (0.71 g, 7.5 mmol), and cesium carbonate (2.94 g, 9 mmol) in 20 mL DMF was stirred at room temperature for 18 h. The reaction mixture was then added dropwise to iced water and the formed precipitate was filtered and washed with water; ^{1}H NMR (400 MHz, DMSO-d_6) δ

8.06–7.95 (m, 2H), 7.77–7.70 (m, 1H), 7.33–7.23 (m, 2H), 7.06–6.97 (m, 2H), 6.97–6.88 (m, 1H), 5.22 (s, 2H), 3.87 (s, 3H). MS *m*/*z*: $[M + H]^+$ 244; yield, 82.92%.

6-(phenoxymethyl)pyridine-2-carboxylic acid (**5**).

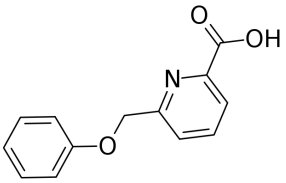

A mixture of **4** (1.21 g, 5 mmol) and lithium hydroxide monohydrate (1.05 g, 25 mmol) was stirred in a mixture of water and tetrahydrofuran (50:50) for one hour at room temperature. The reaction mixture then was added dropwise to iced water and neutralized by adding acetic acid. The mixture was then extracted with ethyl acetate and the organic layer was dried over anhydrous sodium sulfate and evaporated using rotary evaporator to afford the solid product; ^{1}H NMR (400 MHz, DMSO-d_6) δ 13.20 (s, 1H), 8.03–7.93 (m, 2H), 7.71 (dd, *J* = 7.1, 1.8 Hz, 1H), 7.33–7.24 (m, 2H), 7.07–6.98 (m, 2H), 6.97–6.90 (m, 1H), 5.21 (s, 2H). MS *m*/*z*: $[M + H]^+$ 230; yield, 92.09%.

Methyl 2-methoxy-5-[6-(phenoxymethyl)pyridine-2-amido]benzoate (**6**).

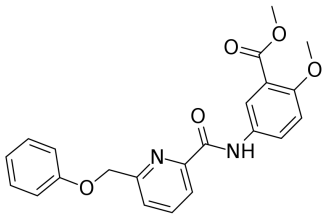

To a stirred solution of **5** (0.55 g, 2.4 mmol) in DCM, oxalyl chloride (0.26 mL, 3 mmol) was added dropwise, and the mixture was stirred for 3 h at room temperature. The mixture was then added dropwise to a solution of (0.52 g, 2.4 mmol) of **2** and N,N-diisopropylethylamine (DIPEA) (1.09 g, 8.4 mmol) in DCM, and the mixture was stirred overnight at room temperature. The reaction mixture was washed with saturated aqueous solutions of ammonium chloride and sodium carbonate followed by brine. The organic layer was then dried over anhydrous sodium sulfate and evaporated using rotary evaporator. The product was purified with medium-pressure liquid chromatography (MPLC) using mixture of n-heptane and ethyl acetate; ^{1}H NMR (400 MHz, DMSO-d_6) δ 10.51 (s, 1H), 8.19 (d, *J* = 2.7 Hz, 1H), 8.09–8.02 (m, 2H), 8.00 (dd, *J* = 9.0, 2.8 Hz, 1H), 7.73 (dd, *J* = 6.4, 2.4 Hz, 1H), 7.34–7.25 (m, 2H), 7.16 (d, *J* = 9.1 Hz, 1H), 7.09–7.00 (m, 2H), 6.98–6.91 (m, 1H), 5.32 (s, 2H), 3.80 (s, 3H), 3.79 (s, 3H). MS *m*/*z*: $[M + H]^+$ 393.1; yield, 74.35%.

2-methoxy-5-[6-(phenoxymethyl)pyridine-2-amido]benzoic acid (**7**).

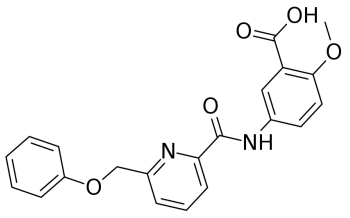

An amount (0.68 g, 1.7 mmol) of **6** was dissolved in a mixture of tetrahydrofuran and water (50:50), an amount (0.355 g, 8.5 mmol) of lithium hydroxide monohydrate was added, and the reaction mixture was stirred for 4 h at room temperature. The reaction mixture was added dropwise to iced water and neutralized by acetic acid. The solution was then

saturated with sodium chloride, and the solid precipitate was filtered and washed with water; ^{1}H NMR (400 MHz, DMSO-d_6) δ 12.70 (s, 1H), 10.48 (s, 1H), 8.15 (d, *J* = 2.7 Hz, 1H), 8.10–8.01 (m, 2H), 7.96 (dd, *J* = 9.0, 2.8 Hz, 1H), 7.73 (dd, *J* = 6.8, 2.1 Hz, 1H), 7.34–7.26 (m, 2H), 7.12 (d, *J* = 9.0 Hz, 1H), 7.08–7.00 (m, 2H), 6.98–6.90 (m, 1H), 5.32 (s, 2H), 3.79 (s, 3H). MS *m*/*z*: $[M + H]^+$ 379,1; yield, 94.56%

N-{4-methoxy-3-[(oxan-2-yloxy)carbamoyl]phenyl}-6-(phenoxymethyl)pyridine-2-carboxamide (**8**).

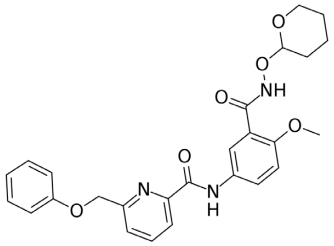

A mixture of **7** (0.57 g, 1.5 mmol) and hexafluorophosphate azabenzotriazole tetramethyl uronium (HATU) (0.68 g, 1.8 mmol) in DMF was stirred for 15 min, after which, O-(tetrahydro-2H-pyran-2-yl)-hydroxylamin (0.2 g, 1.7 mmol) and DIPEA (0.58 g, 4.5 mmol) were added and stirring was continued for 4 h. The reaction mixture was diluted with water and extracted with ethyl acetate. The organic layer was washed with saturated solutions of ammonium chloride and sodium carbonate followed by brine. The organic layer was dried over anhydrous sodium sulfate and evaporated using rotary evaporator. The product was purified using medium-pressure liquid chromatography (MPLC) using a mixture on n-heptane and ethyl acetate; ^{1}H NMR (400 MHz, DMSO-d_6) δ 11.02 (s, 1H), 10.49 (s, 1H), 8.13–8.00 (m, 3H), 7.96 (dd, *J* = 8.9, 2.8 Hz, 1H), 7.73 (dd, *J* = 6.5, 2.3 Hz, 1H), 7.35–7.25 (m, 2H), 7.12 (d, *J* = 9.0 Hz, 1H), 7.08–7.00 (m, 2H), 6.99–6.91 (m, 1H), 5.32 (s, 2H), 5.06–4.96 (m, 1H), 4.08–3.97 (m, 1H), 3.82 (s, 3H), 3.55–3.44 (m, 1H), 1.81–1.62 (m, 3H), 1.60–1.44 (m, 3H). MS *m*/*z*: $[M + H]^+$ 478.2; yield, 84.8%

N-[3-(hydroxycarbamoyl)-4-methoxyphenyl]-6-(phenoxymethyl)pyridine-2-carboxamide (**9**).

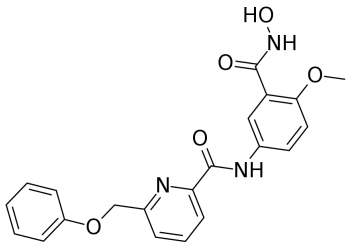

An amount (0.58 g, 1.2 mmol) of **8** was dissolved in 20 mL of tetrahydrofuran, 1 mL of 2N aqueous HCl was added, and the mixture was stirred overnight. The reaction mixture was then added dropwise to iced water, and the precipitate was filtered and washed with water; ^{1}H NMR (400 MHz, DMSO-d_6) δ 10.62 (s, 1H), 10.47 (s, 1H), 9.09 (s, 1H), 8.13–8.00 (m, 3H), 7.93 (dd, *J* = 9.0, 2.8 Hz, 1H), 7.73 (dd, *J* = 6.6, 2.2 Hz, 1H), 7.36–7.25 (m, 2H), 7.11 (d, *J* = 9.0 Hz, 1H), 7.08–7.00 (m, 2H), 6.99–6.90 (m, 1H), 5.32 (s, 2H), 3.82 (s, 3H). ^{13}C NMR (101 MHz, DMSO-d_6) δ 163.15, 162.49, 158.44, 156.55, 153.46, 149.75, 139.36, 131.68, 130.07, 124.98, 124.01, 122.77, 122.53, 121.65, 121.52, 115.20, 112.48, 70.13, 56.35. MS *m*/*z*: $[M + H]^+$ 394.3, HRMS *m*/*z*: $[M + H]^+$ 394.1394; calculated $C_{21}H_{20}O_5N_3$: 394.1403. HPLC: rt 13.123 min (purity 95.755%); yield 77.43%.

3.9. In Vitro Enzymatic Inhibition Evaluation

In the case of HDAC11, the full-length human was expressed and purified as described in previous work [22]. A fluorescence-based HDAC11 assay was used. The fluorescence measurements were performed using a PerkinElmer Envision 2104 multilabel plate reader (Waltham, MA, USA) at λex = 320 nm and λem = 430 nm. The reaction mixture consisted of HDAC11 and the fatty acid-acylated peptide substrate derived from TNFα in a reaction buffer—comprising 50 mM HEPES, 2 mg/mL BSA, and 70 µM TCEP—at pH 7.4, which was adjusted with NaOH (total volume 40 µL). The reactions were incubated in black 384-well plates for 30 min (scan every 30 s) at room temperature, and the increase in relative fluorescence reflecting the product formation was monitored. Positive (HDAC11, substrate, DMSO, and buffer) and negative controls (substrate, DMSO, and vuffer) were included in every measurement. They were set as 100 and 0%, respectively, and the measured values were normalized accordingly.

For HDAC1, 2, 3, 6, and HDAC6, the recombinant proteins were purchased from ENZO Life Sciences AG (Lausen, Switzerland), whereas HDAC4–7, 9, and 10 were produced as described in previous work [93]. All inhibitors were tested in an enzymatic in vitro assay (Table S3), as described previously, using 384-well plates (GreinerONe, catalogue no. 784900) [55,93]. After five minutes of incubation of inhibitors with the respective enzyme (HDAC1: 10 nM, HDAC2 and 3: 3 nM, HDAC4: 5 nM, HDAC5: 10 nM, HDAC6: 1 nM, HDAC7: 5 nM, HDAC8: 2 nM, HDAC 9: 20 nM, HDAC10: 5 nM), the reactions were started by the addition of the substrate.

For HDAC1, 2, 3, and 6, an acetylated peptide substrate derived from p53 (Ac-RHKK(Acetyl)-AMC) was used in a discontinuous fluorescence assay, as described previously [55]. All reactions were performed in assay buffer (20 mM HEPES, 140 mM NaCl, 10 mM $MgCl_2$, 1 mM TCEP, and 0.2 mg/mL BSA, pH 7.4 adjusted with NaOH) at 37 °C. After 1 h, the reaction was quenched by adding trypsin and SAHA. The fluorescence intensity was measured after 1 h of incubation using an Envision 2104 Multilabel Plate Reader (PerkinElmer, Waltham, MA, USA) with an excitation wavelength of 380 ± 8 nm and an emission wavelength of 430 ± 8 nm.

HDAC4–7, 8, 9, and 10 were measured in a continuous manner using the thioacetylated peptide substrate (Abz-SRGGK(thio-TFA)FFRR-NH2) which was described previously [93]. For HDAC 10, an internal quenched spermidine-like substrate was used. The fluorescence increase was followed for 1 h with two reads per min with an excitation wavelength of 320 ± 8 nm and an emission wavelength of 430 ± 8 nm. For all measurements, positive (enzyme, substrate, DMSO, and buffer) and negative (substrate, DMSO, and buffer) controls were included in every measurement and were set as 100 and 0%, respectively. The measured values were normalized accordingly.

4. Conclusions

In the current study, a structure-based pharmacophore model utilizing our previously optimized HDAC11 AlphaFold model was generated as the preliminary step for screening a large, focused library of benzohydroxamate compounds. The resulting hits were further docked in an HDAC11 model and followed by pose filtration to select compounds that could show bidentate chelation of the catalytic zinc ion. A comparative approach was then applied by docking the hits obtained from docking in HDAC11 using different selected HDAC isoform (HDAC1, HDAC6, and HDAC8) crystal structures and eliminating compounds that showed good poses in other HDAC isoforms. This approach proved effective in filtering the initially obtained hit compounds to find a selective ligand. The obtained hits that showed good poses in HDAC11 but not in the other isoforms were subjected to a final filtration step using the REOS filter, and the final hits were further prioritized by MM-GBSA calculations. It is interesting to see that all top-ranked hits have a substituent in ortho-position to the aromatic hydroxamate group. This ortho-substituent is sterically accepted in the HDAC11 binding pocket only. In all other HDAC structures studied in the current work, this substitution leads to the abolition of the correct chelation of the zinc

ion. The experimentally confirmed selectivity for HDAC11 underpins the usefulness of the optimized HDAC11 AlphaFold model for structure-based drug design.

Moreover, the binding mode of the confirmed hit in HDAC11 was further analyzed by several MD simulations. MD simulation studies proved the stability of the initially observed binding mode in terms of ligand RMSD, RMSF, bidentate chelation of the zinc ion, and interaction stability.

In conclusion, a multistep and comparative virtual screening approach was successfully implemented in an attempt to identify novel selective HDAC11 inhibitors utilizing a previously optimized HDAC11 AlphaFold model. This study experimentally verifies the HDAC11 AlphaFold model optimization approach we adopted in our previous study. Additionally, it confirms that AlphaFold models can be utilized for the aim of drug design and discovery subsequent to a prior optimization.

Supplementary Materials: The following supporting information can be downloaded at: https://www.mdpi.com/article/10.3390/ijms25021358/s1.

Author Contributions: F.B. carried out the computational studies, synthesized the compound, and wrote the manuscript. D.R. supervised the computational studies and wrote part of the manuscript. S.H. performed the HDAC in vitro testing of the hit compound. C.B. expressed the HDAC11 protein for in vitro testing. M.S. and W.S. supervised the experiments and revised the manuscript. All authors have read and agreed to the published version of the manuscript.

Funding: This study was supported by the Deutsche Forschungsgemeinschaft (DFG) grants 469954457 and 471614207. This work was supported in part by the CAS (RVO: 86652036) and the Grant Agency of the Czech Republic (24-12155S) (C.B.).

Institutional Review Board Statement: Not applicable.

Informed Consent Statement: Not applicable.

Data Availability Statement: Data are contained within the article and Supplementary Materials.

Conflicts of Interest: The authors declare no conflicts of interest.

References

1. Lombardi, P.M.; Cole, K.E.; Dowling, D.P.; Christianson, D.W. Structure, mechanism, and inhibition of histone deacetylases and related metalloenzymes. *Curr. Opin. Struct. Biol.* **2011**, *21*, 735–743. [CrossRef]
2. Marek, M.; Shaik, T.B.; Romier, C. Structural Biology of Epigenetic Targets: Exploiting Complexity. In *Epigenetic Drug Discovery*; Methods and Principles in Medicinal Chemistry; VCH-Wiley: Weinheim, Germany, 2019; pp. 11–44.
3. Liu, S.-S.; Wu, F.; Jin, Y.-M.; Chang, W.-Q.; Xu, T.-M. HDAC11: A rising star in epigenetics. *Biomed. Pharmacother.* **2020**, *131*, 110607. [CrossRef]
4. Gao, L.; Cueto, M.A.; Asselbergs, F.; Atadja, P. Cloning and functional characterization of HDAC11, a novel member of the human histone deacetylase family. *J. Biol. Chem.* **2002**, *277*, 25748–25755. [CrossRef]
5. Boltz, T.A.; Khuri, S.; Wuchty, S. Promoter conservation in HDACs points to functional implications. *BMC Genom.* **2019**, *20*, 613. [CrossRef]
6. Yanginlar, C.; Logie, C. HDAC11 is a regulator of diverse immune functions. *Biochim. Biophys. Acta (BBA)-Gene Regul. Mech.* **2018**, *1861*, 54–59. [CrossRef]
7. Villagra, A.; Cheng, F.; Wang, H.W.; Suarez, I.; Glozak, M.; Maurin, M.; Nguyen, D.; Wright, K.L.; Atadja, P.W.; Bhalla, K.; et al. The histone deacetylase HDAC11 regulates the expression of interleukin 10 and immune tolerance. *Nat. Immunol.* **2009**, *10*, 92–100. [CrossRef]
8. Glozak, M.A.; Seto, E. Acetylation/deacetylation modulates the stability of DNA replication licensing factor Cdt1. *J. Biol. Chem.* **2009**, *284*, 11446–11453. [CrossRef]
9. Cao, J.; Sun, L.; Aramsangtienchai, P.; Spiegelman, N.A.; Zhang, X.; Huang, W.; Seto, E.; Lin, H. HDAC11 regulates type I interferon signaling through defatty-acylation of SHMT2. *Proc. Natl. Acad. Sci. USA* **2019**, *116*, 5487–5492. [CrossRef]
10. Bagchi, R.A.; Ferguson, B.S.; Stratton, M.S.; Hu, T.; Cavasin, M.A.; Sun, L.; Lin, Y.H.; Liu, D.; Londono, P.; Song, K.; et al. HDAC11 suppresses the thermogenic program of adipose tissue via BRD2. *JCI Insight* **2018**, *3*, e120159. [CrossRef]
11. Sun, L.; Marin de Evsikova, C.; Bian, K.; Achille, A.; Telles, E.; Pei, H.; Seto, E. Programming and Regulation of Metabolic Homeostasis by HDAC11. *eBioMedicine* **2018**, *33*, 157–168. [CrossRef] [PubMed]
12. Fei, Q.; Song, F.; Jiang, X.; Hong, H.; Xu, X.; Jin, Z.; Zhu, X.; Dai, B.; Yang, J.; Sui, C.; et al. LncRNA ST8SIA6-AS1 promotes hepatocellular carcinoma cell proliferation and resistance to apoptosis by targeting miR-4656/HDAC11 axis. *Cancer Cell Int.* **2020**, *20*, 232. [CrossRef]

13. Freese, K.; Seitz, T.; Dietrich, P.; Lee, S.M.L.; Thasler, W.E.; Bosserhoff, A.; Hellerbrand, C. Histone Deacetylase Expressions in Hepatocellular Carcinoma and Functional Effects of Histone Deacetylase Inhibitors on Liver Cancer Cells In Vitro. *Cancers* **2019**, *11*, 1587. [CrossRef]
14. Gong, D.; Zeng, Z.; Yi, F.; Wu, J. Inhibition of histone deacetylase 11 promotes human liver cancer cell apoptosis. *Am. J. Transl. Res.* **2019**, *11*, 983–990.
15. Huo, W.; Qi, F.; Wang, K. Long non-coding RNA BCYRN1 promotes prostate cancer progression via elevation of HDAC11. *Oncol. Rep.* **2020**, *44*, 1233–1245. [CrossRef]
16. Wang, W.; Ding, B.; Lou, W.; Lin, S. Promoter Hypomethylation and miR-145-5p Downregulation-Mediated HDAC11 Overexpression Promotes Sorafenib Resistance and Metastasis of Hepatocellular Carcinoma Cells. *Front. Cell Dev. Biol.* **2020**, *8*, 724. [CrossRef]
17. Wang, W.; Fu, L.; Li, S.; Xu, Z.; Li, X. Histone deacetylase 11 suppresses p53 expression in pituitary tumor cells. *Cell Biol. Int.* **2017**, *41*, 1290–1295. [CrossRef] [PubMed]
18. Mithraprabhu, S.; Kalff, A.; Chow, A.; Khong, T.; Spencer, A. Dysregulated Class I histone deacetylases are indicators of poor prognosis in multiple myeloma. *Epigenetics* **2014**, *9*, 1511–1520. [CrossRef] [PubMed]
19. Yue, L.; Sharma, V.; Horvat, N.P.; Akuffo, A.A.; Beatty, M.S.; Murdun, C.; Colin, C.; Billington, J.M.R.; Goodheart, W.E.; Sahakian, E.; et al. HDAC11 deficiency disrupts oncogene-induced hematopoiesis in myeloproliferative neoplasms. *Blood* **2020**, *135*, 191–207. [CrossRef] [PubMed]
20. Thole, T.M.; Lodrini, M.; Fabian, J.; Wuenschel, J.; Pfeil, S.; Hielscher, T.; Kopp-Schneider, A.; Heinicke, U.; Fulda, S.; Witt, O.; et al. Neuroblastoma cells depend on HDAC11 for mitotic cell cycle progression and survival. *Cell Death Dis.* **2017**, *8*, e2635. [CrossRef]
21. Kutil, Z.; Mikešová, J.; Zessin, M.; Meleshin, M.; Nováková, Z.; Alquicer, G.; Kozikowski, A.; Sippl, W.; Bařinka, C.; Schutkowski, M. Continuous Activity Assay for HDAC11 Enabling Reevaluation of HDAC Inhibitors. *ACS Omega* **2019**, *4*, 19895–19904. [CrossRef]
22. Kutil, Z.; Novakova, Z.; Meleshin, M.; Mikesova, J.; Schutkowski, M.; Barinka, C. Histone Deacetylase 11 Is a Fatty-Acid Deacylase. *ACS Chem. Biol.* **2018**, *13*, 685–693. [CrossRef]
23. Moreno-Yruela, C.; Galleano, I.; Madsen, A.S.; Olsen, C.A. Histone Deacetylase 11 Is an ε-N-Myristoyllysine Hydrolase. *Cell Chem. Biol.* **2018**, *25*, 849–856.e8. [CrossRef]
24. Martin, M.W.; Lee, J.Y.; Lancia, D.R.; Ng, P.Y.; Han, B.; Thomason, J.R.; Lynes, M.S.; Marshall, C.G.; Conti, C.; Collis, A.; et al. Discovery of novel N-hydroxy-2-arylisoindoline-4-carboxamides as potent and selective inhibitors of HDAC11. *Bioorg. Med. Chem. Lett.* **2018**, *28*, 2143–2147. [CrossRef]
25. Dallavalle, S.; Musso, L.; Cincinelli, R.; Darwiche, N.; Gervasoni, S.; Vistoli, G.; Guglielmi, M.B.; La Porta, I.; Pizzulo, M.; Modica, E.; et al. Antitumor activity of novel POLA1-HDAC11 dual inhibitors. *Eur. J. Med. Chem.* **2022**, *228*, 113971. [CrossRef]
26. Bai, P.; Liu, Y.; Yang, L.; Ding, W.; Mondal, P.; Sang, N.; Liu, G.; Lu, X.; Ho, T.T.; Zhou, Y.; et al. Development and Pharmacochemical Characterization Discover a Novel Brain-Permeable HDAC11-Selective Inhibitor with Therapeutic Potential by Regulating Neuroinflammation in Mice. *J. Med. Chem.* **2023**, *66*, 16075–16090. [CrossRef]
27. Bora-Singhal, N.; Mohankumar, D.; Saha, B.; Colin, C.M.; Lee, J.Y.; Martin, M.W.; Zheng, X.; Coppola, D.; Chellappan, S. Novel HDAC11 inhibitors suppress lung adenocarcinoma stem cell self-renewal and overcome drug resistance by suppressing Sox2. *Sci. Rep.* **2020**, *10*, 4722. [CrossRef]
28. Son, S.I.; Cao, J.; Zhu, C.L.; Miller, S.P.; Lin, H. Activity-Guided Design of HDAC11-Specific Inhibitors. *ACS Chem. Biol.* **2019**, *14*, 1393–1397. [CrossRef]
29. Sun, P.; Wang, J.; Khan, K.S.; Yang, W.; Ng, B.W.; Ilment, N.; Zessin, M.; Bülbül, E.F.; Robaa, D.; Erdmann, F.; et al. Development of Alkylated Hydrazides as Highly Potent and Selective Class I Histone Deacetylase Inhibitors with T cell Modulatory Properties. *J. Med. Chem.* **2022**, *65*, 16313–16337. [CrossRef]
30. Pulya, S.; Himaja, A.; Paul, M.; Adhikari, N.; Banerjee, S.; Routholla, G.; Biswas, S.; Jha, T.; Ghosh, B. Selective HDAC3 Inhibitors with Potent In Vivo Antitumor Efficacy against Triple-Negative Breast Cancer. *J. Med. Chem.* **2023**, *66*, 12033–12058. [CrossRef] [PubMed]
31. Ho, T.T.; Peng, C.; Seto, E.; Lin, H. Trapoxin A Analogue as a Selective Nanomolar Inhibitor of HDAC11. *ACS Chem. Biol.* **2023**, *18*, 803–809. [CrossRef] [PubMed]
32. Baselious, F.; Robaa, D.; Sippl, W. Utilization of AlphaFold models for drug discovery: Feasibility and challenges. Histone deacetylase 11 as a case study. *Comput. Biol. Med.* **2023**, *167*, 107700. [CrossRef]
33. Jumper, J.; Evans, R.; Pritzel, A.; Green, T.; Figurnov, M.; Ronneberger, O.; Tunyasuvunakool, K.; Bates, R.; Žídek, A.; Potapenko, A.; et al. Highly accurate protein structure prediction with AlphaFold. *Nature* **2021**, *596*, 583–589. [CrossRef]
34. David, A.; Islam, S.; Tankhilevich, E.; Sternberg, M.J.E. The AlphaFold Database of Protein Structures: A Biologist's Guide. *J. Mol. Biol.* **2022**, *434*, 167336. [CrossRef]
35. Ren, F.; Ding, X.; Zheng, M.; Korzinkin, M.; Cai, X.; Zhu, W.; Mantsyzov, A.; Aliper, A.; Aladinskiy, V.; Cao, Z.; et al. AlphaFold accelerates artificial intelligence powered drug discovery: Efficient discovery of a novel CDK20 small molecule inhibitor. *Chem. Sci.* **2023**, *14*, 1443–1452. [CrossRef]
36. Zhu, W.; Liu, X.; Li, Q.; Gao, F.; Liu, T.; Chen, X.; Zhang, M.; Aliper, A.; Ren, F.; Ding, X.; et al. Discovery of novel and selective SIK2 inhibitors by the application of AlphaFold structures and generative models. *Bioorg. Med. Chem.* **2023**, *91*, 117414. [CrossRef]

37. Holcomb, M.; Chang, Y.T.; Goodsell, D.S.; Forli, S. Evaluation of AlphaFold2 structures as docking targets. *Protein Sci.* **2023**, *32*, e4530. [CrossRef]
38. He, X.-H.; You, C.-Z.; Jiang, H.-L.; Jiang, Y.; Xu, H.E.; Cheng, X. AlphaFold2 versus experimental structures: Evaluation on G protein-coupled receptors. *Acta Pharmacol. Sin.* **2023**, *44*, 1–7. [CrossRef]
39. Lee, S.; Kim, S.; Lee, G.R.; Kwon, S.; Woo, H.; Seok, C.; Park, H. Evaluating GPCR modeling and docking strategies in the era of deep learning-based protein structure prediction. *Comput. Struct. Biotechnol. J.* **2023**, *21*, 158–167. [CrossRef]
40. Heo, L.; Feig, M. Multi-state modeling of G-protein coupled receptors at experimental accuracy. *Proteins* **2022**, *90*, 1873–1885. [CrossRef] [PubMed]
41. Karelina, M.; Noh, J.J.; Dror, R.O. How accurately can one predict drug binding modes using AlphaFold models? *eLife* **2023**, *12*, RP89386. [CrossRef] [PubMed]
42. Díaz-Rovira, A.M.; Martín, H.; Beuming, T.; Díaz, L.; Guallar, V.; Ray, S.S. Are Deep Learning Structural Models Sufficiently Accurate for Virtual Screening? Application of Docking Algorithms to AlphaFold2 Predicted Structures. *J. Chem. Inf. Model.* **2023**, *63*, 1668–1674. [CrossRef]
43. Scardino, V.; Di Filippo, J.I.; Cavasotto, C.N. How good are AlphaFold models for docking-based virtual screening? *iScience* **2023**, *26*, 105920. [CrossRef]
44. Zhang, Y.; Vass, M.; Shi, D.; Abualrous, E.; Chambers, J.M.; Chopra, N.; Higgs, C.; Kasavajhala, K.; Li, H.; Nandekar, P.; et al. Benchmarking Refined and Unrefined AlphaFold2 Structures for Hit Discovery. *J. Chem. Inf. Model.* **2023**, *63*, 1656–1667. [CrossRef]
45. Melesina, J.; Simoben, C.V.; Praetorius, L.; Bülbül, E.F.; Robaa, D.; Sippl, W. Strategies To Design Selective Histone Deacetylase Inhibitors. *ChemMedChem* **2021**, *16*, 1336–1359. [CrossRef]
46. Zhang, L.; Zhang, J.; Jiang, Q.; Zhang, L.; Song, W. Zinc binding groups for histone deacetylase inhibitors. *J. Enzym. Inhib. Med. Chem.* **2018**, *33*, 714–721. [CrossRef]
47. De Vreese, R.; D'Hooghe, M. Synthesis and applications of benzohydroxamic acid-based histone deacetylase inhibitors. *Eur. J. Med. Chem.* **2017**, *135*, 174–195. [CrossRef]
48. Hu, Z.; Wei, F.; Su, Y.; Wang, Y.; Shen, Y.; Fang, Y.; Ding, J.; Chen, Y. Histone deacetylase inhibitors promote breast cancer metastasis by elevating NEDD9 expression. *Signal Transduct. Target. Ther.* **2023**, *8*, 11. [CrossRef]
49. Irwin, J.J.; Tang, K.G.; Young, J.; Dandarchuluun, C.; Wong, B.R.; Khurelbaatar, M.; Moroz, Y.S.; Mayfield, J.; Sayle, R.A. ZINC20—A Free Ultralarge-Scale Chemical Database for Ligand Discovery. *J. Chem. Inf. Model.* **2020**, *60*, 6065–6073. [CrossRef] [PubMed]
50. Lipinski, C.A.; Lombardo, F.; Dominy, B.W.; Feeney, P.J. Experimental and computational approaches to estimate solubility and permeability in drug discovery and development settings. *Adv. Drug Deliv. Rev.* **2001**, *46*, 3–26. [CrossRef] [PubMed]
51. Kumari, S.; Chakraborty, S.; Ahmad, M.; Kumar, V.; Tailor, P.B.; Biswal, B.K. Identification of probable inhibitors for the DNA polymerase of the Monkeypox virus through the virtual screening approach. *Int. J. Biol. Macromol.* **2023**, *229*, 515–528. [CrossRef] [PubMed]
52. Walters, W.P.; Stahl, M.T.; Murcko, M.A. Virtual screening—An overview. *Drug Discov. Today* **1998**, *3*, 160–178. [CrossRef]
53. Walters, W.P.; Namchuk, M. Designing screens: How to make your hits a hit. *Nat. Rev. Drug Discov.* **2003**, *2*, 259–266. [CrossRef]
54. Dan, A.; Shiyama, T.; Yamazaki, K.; Kusunose, N.; Fujita, K.; Sato, H.; Matsui, K.; Kitano, M. Discovery of hydroxamic acid analogs as dual inhibitors of phosphodiesterase-1 and -5. *Bioorg. Med. Chem. Lett.* **2005**, *15*, 4085–4090. [CrossRef]
55. Heimburg, T.; Kolbinger, F.R.; Zeyen, P.; Ghazy, E.; Herp, D.; Schmidtkunz, K.; Melesina, J.; Shaik, T.B.; Erdmann, F.; Schmidt, M.; et al. Structure-Based Design and Biological Characterization of Selective Histone Deacetylase 8 (HDAC8) Inhibitors with Anti-Neuroblastoma Activity. *J. Med. Chem.* **2017**, *60*, 10188–10204. [CrossRef]
56. Marek, M.; Ramos-Morales, E.; Picchi-Constante, G.F.A.; Bayer, T.; Norström, C.; Herp, D.; Sales-Junior, P.A.; Guerra-Slompo, E.P.; Hausmann, K.; Chakrabarti, A.; et al. Species-selective targeting of pathogens revealed by the atypical structure and active site of Trypanosoma cruzi histone deacetylase DAC2. *Cell Rep.* **2021**, *37*, 110129. [CrossRef]
57. Barducci, A.; Bonomi, M.; Parrinello, M. Metadynamics. *WIREs Comput. Mol. Sci.* **2011**, *1*, 826–843. [CrossRef]
58. Fusani, L.; Palmer, D.S.; Somers, D.O.; Wall, I.D. Exploring Ligand Stability in Protein Crystal Structures Using Binding Pose Metadynamics. *J. Chem. Inf. Model.* **2020**, *60*, 1528–1539. [CrossRef]
59. Clark, A.J.; Tiwary, P.; Borrelli, K.; Feng, S.; Miller, E.B.; Abel, R.; Friesner, R.A.; Berne, B.J. Prediction of Protein–Ligand Binding Poses via a Combination of Induced Fit Docking and Metadynamics Simulations. *J. Chem. Theory Comput.* **2016**, *12*, 2990–2998. [CrossRef]
60. *Maestro Schrödinger Release 2019-1*; Schrödinger, LLC: New York, NY, USA, 2019.
61. Sastry, G.M.; Adzhigirey, M.; Day, T.; Annabhimoju, R.; Sherman, W. Protein and ligand preparation: Parameters, protocols, and influence on virtual screening enrichments. *J. Comput. Aided Mol. Des.* **2013**, *27*, 221–234. [CrossRef]
62. *Protein Preparation Wizard Schrödinger Release 2019-1*; Schrödinger, LLC: New York, NY, USA, 2019.
63. Jacobson, M.P.; Pincus, D.L.; Rapp, C.S.; Day, T.J.; Honig, B.; Shaw, D.E.; Friesner, R.A. A hierarchical approach to all-atom protein loop prediction. *Proteins* **2004**, *55*, 351–367. [CrossRef]

64. Jacobson, M.P.; Friesner, R.A.; Xiang, Z.; Honig, B. On the role of the crystal environment in determining protein side-chain conformations. *J. Mol. Biol.* **2002**, *320*, 597–608. [CrossRef] [PubMed]
65. *Prime Schrödinger Release 2019-1*; Prime, Schrödinger, LLC: New York, NY, USA, 2019.
66. Greenwood, J.R.; Calkins, D.; Sullivan, A.P.; Shelley, J.C. Towards the comprehensive, rapid, and accurate prediction of the favorable tautomeric states of drug-like molecules in aqueous solution. *J. Comput. Aided Mol. Des.* **2010**, *24*, 591–604. [CrossRef] [PubMed]
67. Shelley, J.C.; Cholleti, A.; Frye, L.L.; Greenwood, J.R.; Timlin, M.R.; Uchimaya, M. Epik: A software program for pK(a) prediction and protonation state generation for drug-like molecules. *J. Comput. Aided Mol. Des.* **2007**, *21*, 681–691. [CrossRef] [PubMed]
68. *Epik Schrödinger Release 2019-1*; Schrödinger, LLC: New York, NY, USA, 2019.
69. Ghazy, E.; Heimburg, T.; Lancelot, J.; Zeyen, P.; Schmidtkunz, K.; Truhn, A.; Darwish, S.; Simoben, C.V.; Shaik, T.B.; Erdmann, F.; et al. Synthesis, structure-activity relationships, cocrystallization and cellular characterization of novel smHDAC8 inhibitors for the treatment of schistosomiasis. *Eur. J. Med. Chem.* **2021**, *225*, 113745. [CrossRef] [PubMed]
70. Ghazy, E.; Zeyen, P.; Herp, D.; Hügle, M.; Schmidtkunz, K.; Erdmann, F.; Robaa, D.; Schmidt, M.; Morales, E.R.; Romier, C.; et al. Design, synthesis, and biological evaluation of dual targeting inhibitors of histone deacetylase 6/8 and bromodomain BRPF1. *Eur. J. Med. Chem.* **2020**, *200*, 112338. [CrossRef]
71. Marek, M.; Shaik, T.B.; Heimburg, T.; Chakrabarti, A.; Lancelot, J.; Ramos-Morales, E.; Da Veiga, C.; Kalinin, D.; Melesina, J.; Robaa, D.; et al. Characterization of Histone Deacetylase 8 (HDAC8) Selective Inhibition Reveals Specific Active Site Structural and Functional Determinants. *J. Med. Chem.* **2018**, *61*, 10000–10016. [CrossRef]
72. Vögerl, K.; Ong, N.; Senger, J.; Herp, D.; Schmidtkunz, K.; Marek, M.; Müller, M.; Bartel, K.; Shaik, T.B.; Porter, N.J.; et al. Synthesis and Biological Investigation of Phenothiazine-Based Benzhydroxamic Acids as Selective Histone Deacetylase 6 Inhibitors. *J. Med. Chem.* **2019**, *62*, 1138–1166. [CrossRef]
73. *LigPrep Schrödinger Release 2019-1*; Schrödinger, LLC: New York, NY, USA, 2019.
74. Harder, E.; Damm, W.; Maple, J.; Wu, C.; Reboul, M.; Xiang, J.Y.; Wang, L.; Lupyan, D.; Dahlgren, M.K.; Knight, J.L.; et al. OPLS3: A Force Field Providing Broad Coverage of Drug-like Small Molecules and Proteins. *J. Chem. Theory Comput.* **2016**, *12*, 281–296. [CrossRef]
75. Shivakumar, D.; Williams, J.; Wu, Y.; Damm, W.; Shelley, J.; Sherman, W. Prediction of Absolute Solvation Free Energies using Molecular Dynamics Free Energy Perturbation and the OPLS Force Field. *J. Chem. Theory Comput.* **2010**, *6*, 1509–1519. [CrossRef]
76. Jorgensen, W.L.; Maxwell, D.S.; Tirado-Rives, J. Development and Testing of the OPLS All-Atom Force Field on Conformational Energetics and Properties of Organic Liquids. *J. Am. Chem. Soc.* **1996**, *118*, 11225–11236. [CrossRef]
77. Jorgensen, W.L.; Tirado-Rives, J. The OPLS [optimized potentials for liquid simulations] potential functions for proteins, energy minimizations for crystals of cyclic peptides and crambin. *J. Am. Chem. Soc.* **1988**, *110*, 1657–1666. [CrossRef] [PubMed]
78. *QikProp Schrödinger Release 2019-1*; Schrödinger, LLC: New York, NY, USA, 2019.
79. Salam, N.K.; Nuti, R.; Sherman, W. Novel method for generating structure-based pharmacophores using energetic analysis. *J. Chem. Inf. Model.* **2009**, *49*, 2356–2368. [CrossRef] [PubMed]
80. Loving, K.; Salam, N.K.; Sherman, W. Energetic analysis of fragment docking and application to structure-based pharmacophore hypothesis generation. *J. Comput. Aided Mol. Des.* **2009**, *23*, 541–554. [CrossRef]
81. Dixon, S.L.; Smondyrev, A.M.; Knoll, E.H.; Rao, S.N.; Shaw, D.E.; Friesner, R.A. PHASE: A new engine for pharmacophore perception, 3D QSAR model development, and 3D database screening: 1. Methodology and preliminary results. *J. Comput. Aided Mol. Des.* **2006**, *20*, 647–671. [CrossRef] [PubMed]
82. Dixon, S.L.; Smondyrev, A.M.; Rao, S.N. PHASE: A Novel Approach to Pharmacophore Modeling and 3D Database Searching. *Chem. Biol. Drug Des.* **2006**, *67*, 370–372. [CrossRef] [PubMed]
83. *Phase Schrödinger Release 2019-1*; Schrödinger, LLC: New York, NY, USA, 2019.
84. Friesner, R.A.; Murphy, R.B.; Repasky, M.P.; Frye, L.L.; Greenwood, J.R.; Halgren, T.A.; Sanschagrin, P.C.; Mainz, D.T. Extra precision glide: Docking and scoring incorporating a model of hydrophobic enclosure for protein-ligand complexes. *J. Med. Chem.* **2006**, *49*, 6177–6196. [CrossRef] [PubMed]
85. Friesner, R.A.; Banks, J.L.; Murphy, R.B.; Halgren, T.A.; Klicic, J.J.; Mainz, D.T.; Repasky, M.P.; Knoll, E.H.; Shelley, M.; Perry, J.K.; et al. Glide: A new approach for rapid, accurate docking and scoring. 1. Method and assessment of docking accuracy. *J. Med. Chem.* **2004**, *47*, 1739–1749. [CrossRef]
86. Halgren, T.A.; Murphy, R.B.; Friesner, R.A.; Beard, H.S.; Frye, L.L.; Pollard, W.T.; Banks, J.L. Glide: A New Approach for Rapid, Accurate Docking and Scoring. 2. Enrichment Factors in Database Screening. *J. Med. Chem.* **2004**, *47*, 1750–1759. [CrossRef]
87. *Glide Schrödinger Release 2019-1*; Schrödinger, LLC: New York, NY, USA, 2019.
88. Duan, J.; Dixon, S.L.; Lowrie, J.F.; Sherman, W. Analysis and comparison of 2D fingerprints: Insights into database screening performance using eight fingerprint methods. *J. Mol. Graph. Model.* **2010**, *29*, 157–170. [CrossRef]
89. Sastry, M.; Lowrie, J.F.; Dixon, S.L.; Sherman, W. Large-Scale Systematic Analysis of 2D Fingerprint Methods and Parameters to Improve Virtual Screening Enrichments. *J. Chem. Inf. Model.* **2010**, *50*, 771–784. [CrossRef]
90. *Canvas Schrödinger Release 2019-1*; Schrödinger, LLC: New York, NY, USA, 2019.
91. Bowers, K.J.; Chow, D.E.; Xu, H.; Dror, R.O.; Eastwood, M.P.; Gregersen, B.A.; Klepeis, J.L.; Kolossvary, I.; Moraes, M.A.; Sacerdoti, F.D.; et al. Scalable Algorithms for Molecular Dynamics Simulations on Commodity Clusters. In Proceedings of the SC'06: Proceedings of the 2006 ACM/IEEE Conference on Supercomputing, Tampa, FL, USA, 11–17 November 2006; p. 43.

92. *Desmond Schrödinger Release 2019-1*; Schrödinger LLC: New York, NY, USA, 2019.
93. Zessin, M.; Kutil, Z.; Meleshin, M.; Nováková, Z.; Ghazy, E.; Kalbas, D.; Marek, M.; Romier, C.; Sippl, W.; Bařinka, C.; et al. One-Atom Substitution Enables Direct and Continuous Monitoring of Histone Deacylase Activity. *Biochemistry* **2019**, *58*, 4777–4789. [CrossRef] [PubMed]

3.3. Utilization of an optimized AlphaFold protein model for structure-based design of a selective HDAC11 inhibitor with anti-neuroblastoma activity

Fady Baselious, Sebastian Hilscher, Sven Hagemann, Sunita Tripathee, Dina Robaa, Cyril Barinka, Stefan Hüttelmaier, Mike Schutkowski, Wolfgang Sippl

Arch. Pharm. ***2024****, e2400486.*

https://doi.org/10.1002/ardp.202400486

Abstract

AlphaFold is an artificial intelligence approach for predicting the three-dimensional (3D) structures of proteins with atomic accuracy. One challenge that limits the use of AlphaFold models for drug discovery is the correct prediction of folding in the absence of ligands and cofactors, which compromises their direct use. We have previously described the optimization and use of the histone deacetylase 11 (HDAC11) AlphaFold model for the docking of selective inhibitors such as FT895 and SIS17. Based on the predicted binding mode of FT895 in the optimized HDAC11 AlphaFold model, a new scaffold for HDAC11 inhibitors was designed, and the resulting compounds were tested in vitro against various HDAC isoforms. Compound **5a** proved to be the most active compound with an IC_{50} of 365 nM and was able to selectively inhibit HDAC11. Furthermore, docking of **5a** showed a binding mode comparable to FT895 but could not adopt any reasonable poses in other HDAC isoforms. We further supported the docking results with molecular dynamics simulations that confirmed the predicted binding mode. **5a** also showed promising activity with an EC_{50} of 3.6 µM on neuroblastoma cells.

Received: 14 June 2024 | Revised: 26 June 2024 | Accepted: 27 June 2024

DOI: 10.1002/ardp.202400486

SHORT COMMUNICATION

ARCH PHARM DPhG
Archiv der Pharmazie

Utilization of an optimized AlphaFold protein model for structure-based design of a selective HDAC11 inhibitor with anti-neuroblastoma activity

Fady Baselious[1] | Sebastian Hilscher[1] | Sven Hagemann[2] | Sunita Tripathee[2] | Dina Robaa[1] | Cyril Barinka[3] | Stefan Hüttelmaier[2] | Mike Schutkowski[4] | Wolfgang Sippl[1]

[1]Department of Medicinal Chemistry, Institute of Pharmacy, Martin-Luther-University of Halle-Wittenberg, Halle (Saale), Germany

[2]Institute of Molecular Medicine, Martin Luther University Halle-Wittenberg, Halle (Saale), Germany

[3]Institute of Biotechnology of the Czech Academy of Sciences, BIOCEV, Vestec, Czech Republic

[4]Charles Tanford Protein Center, Department of Enzymology, Institute of Biochemistry and Biotechnology, Martin-Luther-University of Halle-Wittenberg, Halle (Saale), Germany

Correspondence
Wolfgang Sippl, Department of Medicinal Chemistry, Institute of Pharmacy, Martin-Luther-University of Halle-Wittenberg, 06120 Halle (Saale), Germany.
Email: wolfgang.sippl@pharmazie.uni-halle.de

Funding information
Deutsche Forschungsgemeinschaft (DFG), Grant/Award Numbers: 469954457, 471614207; CAS, Grant/Award Number: 86652036; Grant Agency of the Czech Republic, Grant/Award Number: 24-12155 S

Abstract

AlphaFold is an artificial intelligence approach for predicting the three-dimensional (3D) structures of proteins with atomic accuracy. One challenge that limits the use of AlphaFold models for drug discovery is the correct prediction of folding in the absence of ligands and cofactors, which compromises their direct use. We have previously described the optimization and use of the histone deacetylase 11 (HDAC11) AlphaFold model for the docking of selective inhibitors such as FT895 and SIS17. Based on the predicted binding mode of FT895 in the optimized HDAC11 AlphaFold model, a new scaffold for HDAC11 inhibitors was designed, and the resulting compounds were tested in vitro against various HDAC isoforms. Compound **5a** proved to be the most active compound with an IC_{50} of 365 nM and was able to selectively inhibit HDAC11. Furthermore, docking of **5a** showed a binding mode comparable to FT895 but could not adopt any reasonable poses in other HDAC isoforms. We further supported the docking results with molecular dynamics simulations that confirmed the predicted binding mode. **5a** also showed promising activity with an EC_{50} of 3.6 µM on neuroblastoma cells.

KEYWORDS
AlphaFold, HDAC11, model optimization, molecular dynamics simulation, neuroblastoma

1 | INTRODUCTION

Histone deacetylases (HDACs) are enzymes that catalyze the removal of the acetyl group from the lysine residue of histone protein leading to condensed chromatin structures, a process that suppresses transcription.[1] The HDACs family is classified into four classes. Eleven zinc-dependent HDACs have been identified so far and constitute class I, class II, and class IV of the family with HDAC11 being the only member of class IV.[2] There is growing evidence that HDAC11 is implicated in various pathophysiological processes[3,4] including various carcinomas.[4–8] These findings establish HDAC11 as a potential target for anticancer therapeutics.

Few selective HDAC11 inhibitors have been reported in the literature. FT895 is a hydroxamic acid-based HDAC11 selective

inhibitor that was reported by Forma Therapeutics[9] and could significantly reduce non-small cell lung cancer cell viability.[10] Recently, Bai et al. reported the development of PB94, which also bears a hydroxamic acid moiety as a zinc-binding group and demonstrated a beneficial effect in a neuropathic pain mouse model.[11] Since the defatty-acylase activity of HDAC11 is confirmed,[12,13] the ability of HDAC11 to accommodate a longer alkyl chain was exploited for the design and development of selective inhibitors as the alkyl hydrazide derivative SIS17 which bears a 16 carbon long alkyl chain[14] and the natural product trapoxin A analog TD034.[15]

Currently, there is no crystal structure reported for HDAC11. The low sequence identity of the HDAC11 catalytic domain with other HDAC family members[16,17] affects the reliability of the conventional template-based homology modeling. AlphaFold models, which are produced by a neural network artificial intelligence (AI) approach, demonstrate highly accurate predictions of the three-dimensional (3D) protein structures even in the absence of known similar structures.[18,19] Two studies reported the successful utilization of AlphaFold models using AI molecular generation methods to design novel inhibitors for cyclin-dependent kinase 20 (CDK20) and salt-inducible kinase 2 (SIK2).[20,21]

However, AlphaFold models demonstrated worse performance in several studies when assessed for docking or virtual screening in comparison to their corresponding crystal structures[22–26] which suggests that further refinement is required for AlphaFold models before utilization for the aim of drug design and discovery.

We previously optimized the HDAC11 AlphaFold model[16] by docking the zinc ion into the protein model followed by minimization in the presence of HDAC11 inhibitors which were also found co-crystallized with HDAC8. Moreover, we showed that the optimized model could be successfully used for docking of HDAC11 selective inhibitors such as FT895 and SIS17 and was successfully utilized for virtual screening to identify new selective HDAC11 inhibitors.[27] In the current study, we further employed the predicted binding mode of HDAC11 inhibitors in the AlphaFold model for the rational structure-based design of selective inhibitors with novel scaffolds. The developed compounds were assessed by in vitro testing and the most active and selective compound was evaluated for its anti-neuroblastoma activity in cancer cells. Additionally, we conducted a comparative docking study as well as molecular dynamics simulations to investigate the binding mode and rationalize the detected activity and selectivity.

2 | RESULTS AND DISCUSSION

2.1 | Structure-based design

As shown in our previous study,[16] the predicted binding mode of the selective inhibitor FT895 in the refined HDAC11 AlphaFold model demonstrated the typical interactions for hydroxamic acids showing a bidentate chelation of the zinc ion through the two oxygen atoms of the hydroxamate moiety along with the salt bridge and two hydrogen bond interactions with His142, His143, and Tyr304, respectively. Additionally, the ligand was sandwiched between the side chains of Tyr209 and Leu268 of loop 5 and loop 6, respectively with which it formed hydrophobic interactions (Figure 1a).

To further examine the significance of the predicted binding mode of FT895 and the applicability of the optimized model, we aimed to develop probes bearing new scaffolds based on the observed docked pose of FT895. In the newly designed compounds, the linear shape of the ligand along with the ortho substitution pattern to the hydroxamic acid moiety

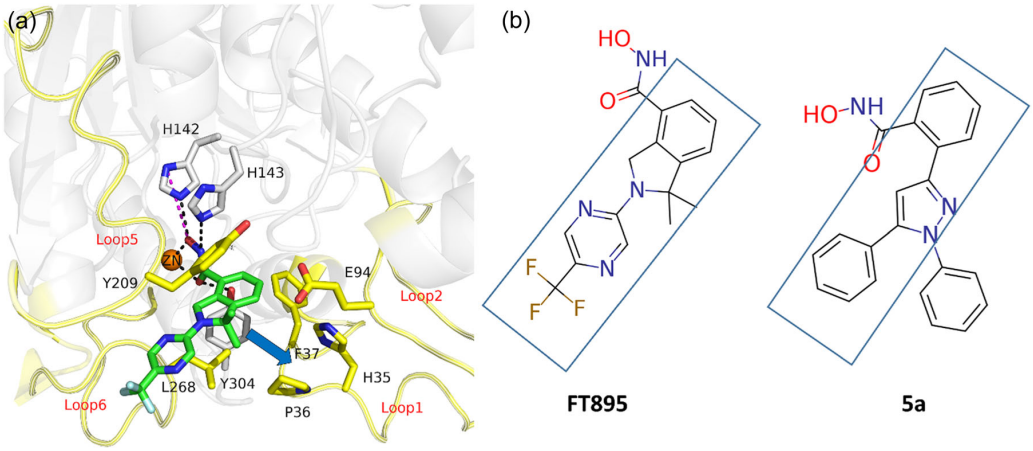

FIGURE 1 Representation of the structure-based design strategy applied in the current study. (a) Docking pose of the selective ligand FT895 in the optimized HDAC11 AlphaFold model. The protein backbone appears as a white cartoon, the zinc cofactor as an orange sphere, and FT895 as green sticks. Surface loops (loops 1, 2, 5, and 6) are highlighted in yellow. Hydrogen bonds and coordination bonds are represented as grey dashed lines and ionic interactions as magenta dashed lines. The blue arrow points towards loop1, highlighting the position for additional structure features. (b) Schematic diagram representing the design of compound **5a** based on the ligand FT895, highlighting the similarities in linear structure along with ortho substitution and additional structural features in **5a** directed toward loop 1.

was kept, since these were considered selectivity determinants for HDAC11. As the structure of FT895 is accommodated between the side chains of residues Tyr209 and Leu268 of loops 5 and 6 respectively, we thought of designing branched ligands (Figure 1b) by extending various groups that are directed toward loop 1, thus making interactions with loop 1 residues and blocking the binding site from both sides to maintain selectivity and increase activity. The new scaffold was designed to be synthetically accessible through Claisen–Schmidt condensation followed by cyclization using substituted hydrazines, a pathway that would allow for the chemical modification of the branching substructures and their substitutions easily.

2.2 | Molecular docking

Docking of compound **5a** was performed in the refined HDAC11 AlphaFold model as well as HDAC1, HDAC6, and HDAC8. For the optimized HDAC11 AlphaFold model the docking was performed in the complex minimized in the presence of trichostatin A (TSA) and using the grid with flipped-out Phe152 as it showed the best docking results in our previous study.[16] The obtained pose of **5a** in HDAC11, showed bidentate chelation of the zinc ion through the two oxygen atoms of the hydroxamate group with distances of 2.18 and 2.17 Å for the hydroxyl oxygen and the carbonyl oxygen, respectively. A salt bridge is formed between the deprotonated oxygen of the hydroxamate and His142. Furthermore, a hydrogen bond interaction is observed between the carbonyl oxygen of the hydroxamate moiety and Tyr304. Additionally, the inhibitor formed two π–π interactions through the pyrazole ring and one terminal phenyl ring with Tyr304 and Tyr209, respectively (Figure 2).

The comparison of the docking poses of **5a** and FT895 (Figure 3a) shows that the benzohydroxamate moiety of **5a** is inserted deeper in the binding pocket allowing for one terminal phenyl ring to be sandwiched between the side chains of Tyr209 and Leu268 with which it forms hydrophobic interactions, while the other phenyl ring attached to the pyrazole nitrogen is directed toward loop 1 and forming hydrophobic interactions with Pro36 thus fulfilling the aim of the design. Hydrophobic interactions with Phe37, Phe152, and Tyr304 were also observed. Docking of **5a** in HDAC1 and HDAC6 (Figure 3b,c) demonstrated that the ligand could not be placed into the binding site and failed to show effective chelation of the zinc ion. The obtained pose of **5a** in HDAC8 showed an orientation in which the ligand was not able to chelate the zinc ion in the correct bidentate fashion or show the interactions commonly observed for HDAC8 co-crystallized hydroxamic acid inhibitors (Figure 3d).

2.3 | Chemistry

Compounds were synthesized as described in Scheme 1. Starting from the commercially available 2-methylacetophenone **1** and by reaction with aromatic aldehydes in the presence of alcoholic NaOH, the corresponding chalcones **2a–b** were obtained. The chalcones were further cyclized using substituted hydrazines in the presence of thiamine hydrochloride as a catalyst.[28] The reaction afforded a mixture of pyrazole/pyrazoline products. The crude product from the cyclization reaction was used without further purification for the oxidation reaction by heating under reflux with potassium permanganate in a mixture of water and pyridine to afford the corresponding carboxylic acid pyrazole derivatives **3a–d**. The

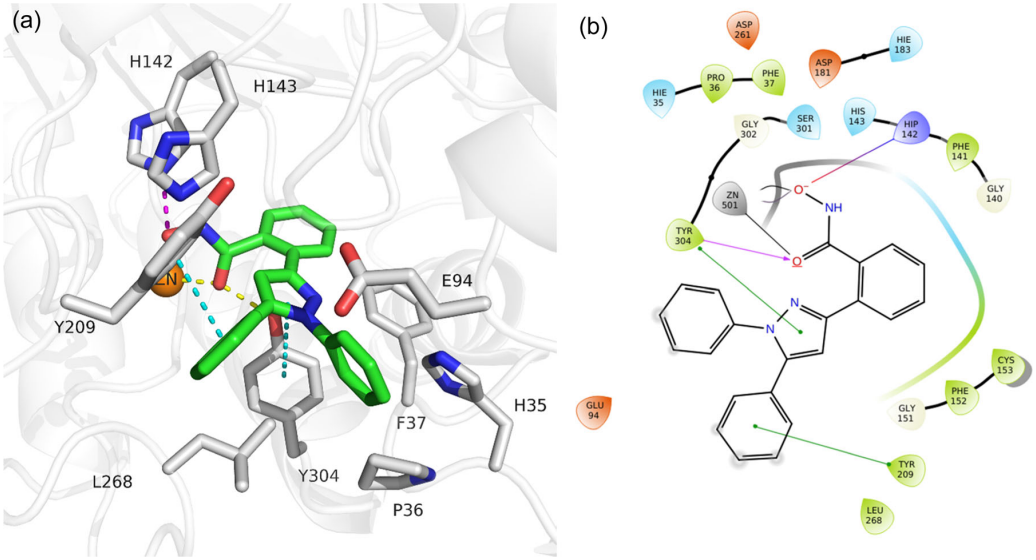

FIGURE 2 (a) Docked pose of **5a** in HDAC11. The protein backbone appears as a white cartoon, residues as grey sticks, zinc cofactor as orange sphere, and compound **5a** as green sticks. Hydrogen bonds and coordination bonds are represented as yellow dashed lines, salt bridges as magenta dashed lines, and π–π interactions as cyan dashed lines. (b) Two-dimensional (2D) representation of ligand interactions for **5a** in HDAC11.

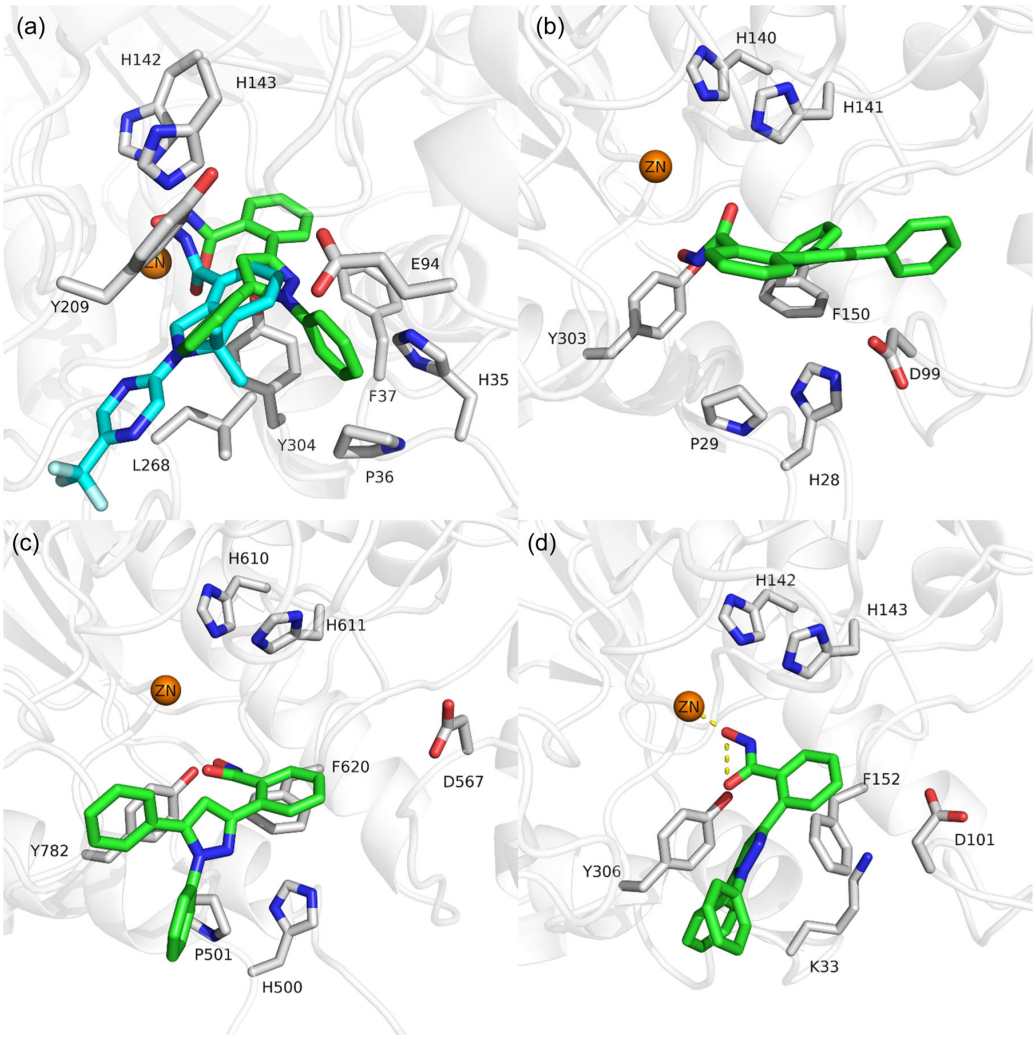

FIGURE 3 (a) Superposition of the docked poses of FT895 and **5a** in HDAC11 highlighting the difference in the orientation of the benzohydroxamate and the position of the terminal phenyl ring extension. Docked poses of **5a** in (b) HDAC1 (PDB 5ICN), (c) HDAC6 (PDB 5EDU), and (d) HDAC8 (PDB 5FCW). The protein backbone appears as a white cartoon, residues as grey sticks, zinc cofactor as an orange sphere, compound **5a** as green sticks, and FT895 as cyan sticks.

obtained acid was then coupled with *O*-(tetrahydro-2*H*-pyran-2-yl)-hydroxylamine (THP-hydroxylamine) in the presence of hexafluorophosphate azabenzotriazole tetramethyl uronium (HATU) and using N,N-diisopropylethylamine (DIPEA) as a base to afford the corresponding THP-protected derivatives **4a–d**, which were subsequently de-protected using aqueous HCl in THF to afford the final hydroxamic acid products **5a–d**.

2.4 | In vitro enzymatic evaluation and anti-neuroblastoma activity

The four synthesized compounds were first screened for their enzymatic inhibitory activity at 10 µM concentration against the main target, HDAC11. The screening was also performed for HDAC1, HDAC6, and HDAC8 as representative candidates from class I and class II HDACs. For HDAC1 and HDAC6 no inhibition could be observed for all compounds. For HDAC11, the compounds demonstrated inhibition percent ranging between 79% and 98%. For HDAC8 weak inhibition between 30% and 65% was observed (Figure 4a, Table 1). Profiling the IC_{50} values of the four compounds for HDAC11 showed that the most active compound is **5a** demonstrating an IC_{50} value of 365 ± 16 nM, while the IC_{50} values of the other three compounds are in the micromolar range between 3 and 4 µM (Figure 4b, Table 2). Interestingly the most active compound **5a** is also the most selective one showing only around 30% inhibition of HDAC8. Furthermore, we screened compound **5a** against all other

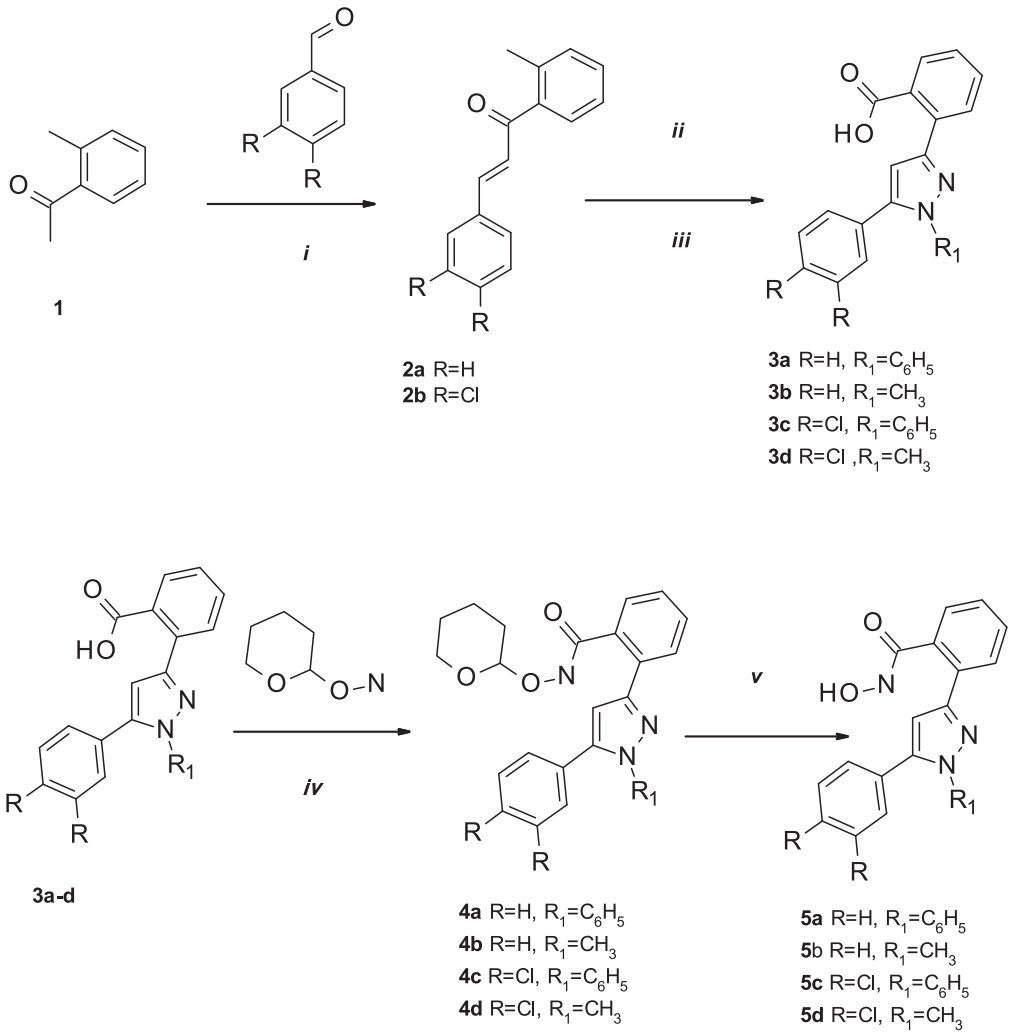

SCHEME 1 Synthesis of target compounds. Reagents and conditions: (i) Alcoholic NaOH/RT/overnight; (ii) NH_2NHR_1/Thiamine. HCl/ethanol/RT/overnight; (iii) $KMnO_4/H_2O$:pyridine (50:50)/reflux/48 h; (iv) DMF/hexafluorophosphate azabenzotriazole tetramethyl uronium (HATU)/N,N-diisopropylethylamine (DIPEA)/RT/3-4 h; (v) THF/aq. HCl/RT/overnight. DMF; dimethylformamide.

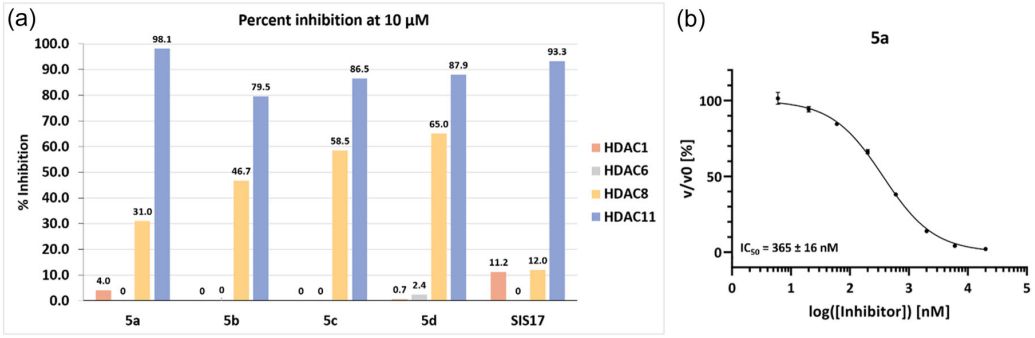

FIGURE 4 (a) Percentage inhibition of HDAC1, HDAC6, HDAC8, and HDAC11 enzyme activity at 10 µM inhibitor concentration. (b) IC_{50} curve of the best candidate **5a** for HDAC11.

TABLE 1 Percent inhibition of enzymatic activity at 10 µM concentration of compounds **5a-d** for HDAC1, HDAC6, HDAC8, and HDAC11.

			Percent inhibition at 10 µM							
			HDAC1		HDAC6		HDAC8		HDAC11	
Compound	R	R1	%	SD[a]	%	SD[a]	%	SD[a]	%	SD[a]
5a	H	C_6H_5	4.0	0.08	0	0.43	31.0	2.71	98.1	0.36
5b	H	CH_3	0	1.32	0	6.42	46.7	1.61	79.5	1.15
5c	Cl	C_6H_5	0	1.5	0	9.1	58.5	1.73	86.5	0.9
5d	Cl	CH_3	0.7	1.86	2.4	3.09	65.0	2.91	87.9	0.98

[a]Standard deviation, all tests were done in three replicates.

TABLE 2 IC_{50} values of the synthesized inhibitors in nM for HDAC11.

Compound	IC_{50} HDAC11 (nM)	SD[a]
5a	365	16
5b	4000	517
5c	3100	491
5d	3900	593
SIS17	170	20

[a]Standard deviation, all test were done in three replicates.

isoforms of HDACs and no or very weak inhibition could be observed (Figure 5). When comparing the IC_{50} with the previously reported HDAC11 inhibitor FT895, it is important to consider the variation in IC_{50} when using different substrates for the evaluation of the inhibitory activity. FT895 showed an HDAC11 IC_{50} value of 0.003 µM[9] when using a nonnative triflouroacetyl lysine substrate and an IC_{50} value of 0.74 µM[14] when using a myristoyl-H3K9 peptide which is more similar to the physiologic substrate. The HDAC11 in vitro assay used in the current work also utilized a long alkyl chain acylated peptide.[12] As a reference, we included the reported HDAC11 selective inhibitor SIS17 in our assay and measured an IC_{50} value of 0.17 µM. Thus our results show that **5a** has a similar in vitro activity compared with FT895 and SIS17 and retained promising selectivity. Interestingly the results from the in vitro enzymatic evaluation for **5a** are in agreement with the results from the docking study which further reflects the success of the adopted structure-based design approach.

Since the depletion of HDAC11 in MYCN-driven neuroblastoma cells was reported to induce cell death through caspase-mediated apoptosis[29] we further evaluated compound **5a** for its anti-neuroblastoma activity using the BE(2)-C neuroblastoma cell line. Interestingly the compound showed promising activity as it could inhibit the viability of the neuroblastoma cells with an EC_{50} value of about 3.6 µM. We also tested the reported inhibitor SIS17 for its effect in the BE(2)-C neuroblastoma cell line and measured a weaker inhibition (EC_{50} > 10.0 µM).

2.5 | Molecular dynamics simulations

To validate the observed binding mode of **5a** in the HDAC11 AlphaFold model, three independent short (50 ns) as well as single long (500 ns) molecular dynamics (MD) simulations were conducted. Analyzing the root mean square deviation (RMSD) plots of the short runs showed that the protein-backbone atoms are stabilizing between 1 and 2 Å while the zinc ion is stabilizing at about 1 Å (Figure 6a,b). The root mean square fluctuation (RMSF) plots (Supporting Information S2: Figure S3) of the protein backbone show fluctuations slightly above 2 Å for loop 1 and loop 2, while for loop 5 and loop 6, fluctuations below 2 Å are observed. Similar behavior of these surface loops was observed in our previous study.[16] It is worth noting that such RMSF values can be expected for long loops that are solvent-exposed. The ligand RMSD is similar for the three runs and is stabilizing at about 2 Å all over the simulation time indicating a stable pose (Figure 6c). Inspecting the ligand RMSF plots confirmed the observed stability as all the ligand heavy atoms are fluctuating below 2 Å with the capping phenyl rings being the most fluctuating substructure (Figure 6d).

Interaction persistence showed very high stability for the salt bridge to His142 with persistence percent above 95% for the three independent runs, while the stability of the hydrogen bond to Tyr304 was also confirmed with persistence percent ranging between 76% and 88% (Supporting Information S2: Table S1, Figures S4 and S5).

The stability of the bidentate chelation mode observed initially in the docked pose was confirmed by monitoring the stability of the distance between the two chelator oxygen atoms of the zinc-binding group and the zinc ion (Figure 7).

The RMSD plots of the protein and zinc ion obtained from the long molecular dynamics simulation are comparable to the short runs (Figure 8a) with the ligand RMSD stabilizing at 2 Å. The ligand RMSF plots showed that the most fluctuating substructures are the terminal phenyl capping groups (Figure 8b and Supporting Information S2: Figure S6 and S7) while the bidentate chelation was found to be stable all over the simulation (Figure 8c,d).

In the long-scale molecular dynamic simulation, the salt bridge stability to His142 was also confirmed with a persistence percent of about 94%, however, the persistence percent for the hydrogen bond interaction with Tyr304 decreased to 38% (Supporting Information S2: Table S1, Figures S4, and S5). It is worth noting that such behavior of the hydrogen bond interaction with this conserved tyrosine residue was

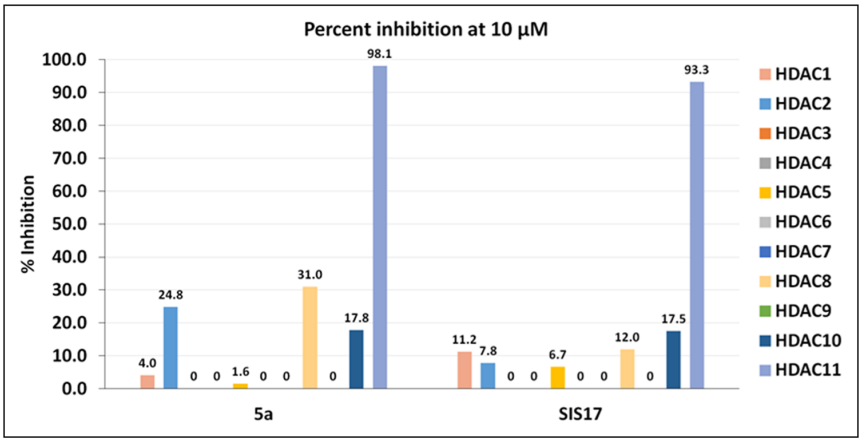

FIGURE 5 Percent inhibition at 10 µM concentration for SIS17 and compound **5a** for all histone deacetylase (HDAC) subtypes.

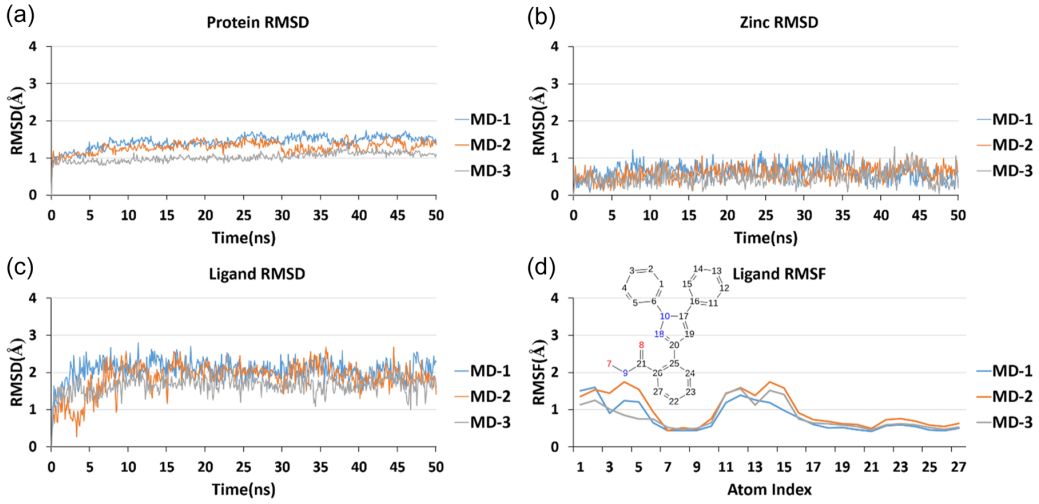

FIGURE 6 RMSD and RMSF plots of **5a** for three independent MD runs each for 50 ns. (a) RMSD plots of protein backbone heavy atoms. (b) RMSD plots of zinc ion. (c) RMSD plots of **5a** heavy atoms. (d) RMSF plots of **5a** heavy atoms. MD, molecular dynamics; RMSD, root mean square deviation; RMSF, root mean square fluctuation.

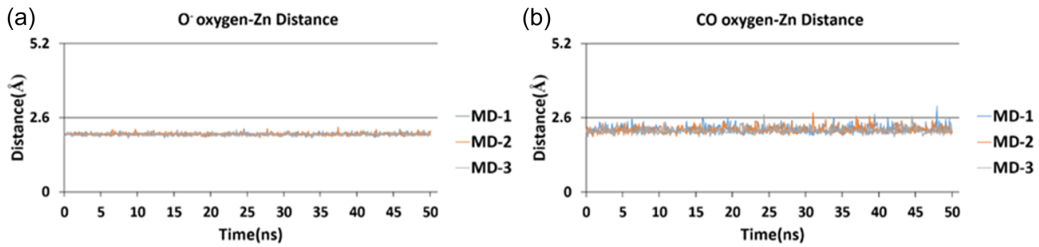

FIGURE 7 Distances to the zinc ion for three independent MD runs each for 50 ns. (a) and (b) are the hydroxyl and the carbonyl oxygen atoms of the zinc-binding group, respectively. MD, molecular dynamics.

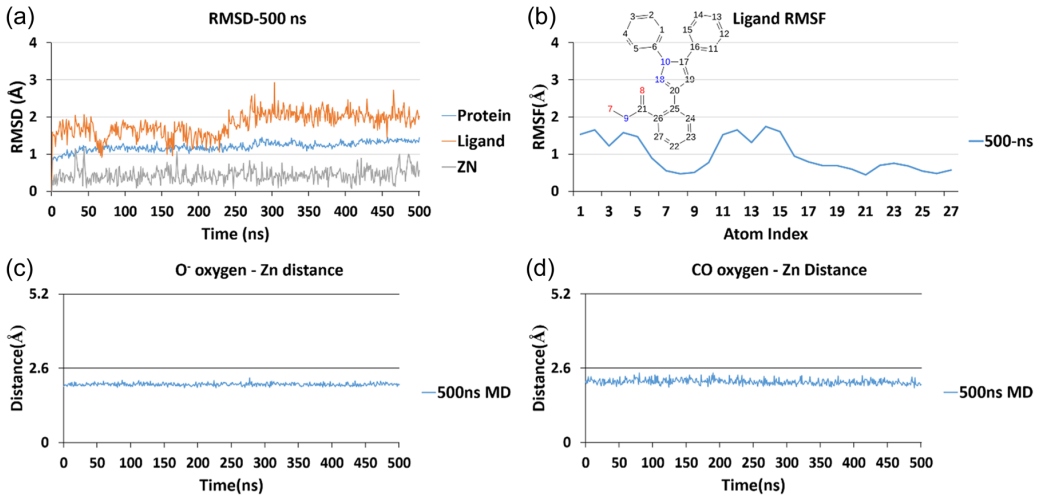

FIGURE 8 (a) RMSD plots of the protein backbone heavy atoms, zinc ion, and **5a** heavy atoms for the long MD run (500 ns). (b) RMSF plots of the **5a** heavy atom for the long MD run (500 ns). (c) and (d) are distances between the zinc ion and the hydroxyl and the carbonyl oxygen atoms of the zinc-binding group, respectively, for the long MD runs (500 ns). MD, molecular dynamics; RMSD, root mean square deviation; RMSF, root mean square fluctuation.

observed before in our previous study[16] and other studies[30] due to side-chain flexibility.[31,32]

Additionally, the hydrophobic interactions of the ligand were monitored throughout the simulation. For the three short MD simulations, **5a** showed hydrophobic interactions with Phe37 in loop 1 and Tyr209 in loop 5 that demonstrated good stability with persistence ranging between 50% and 75%. Moreover, highly persistent hydrophobic interactions with Phe152 and Tyr304 were observed (Supporting Information S2: Figure S8). While the ligand could initially form hydrophobic interactions with Pro36 of loop 1 and Leu268 of loop 6 in the obtained docking pose, these interactions were not stable during the MD simulation. This instability might be due to the flexibility of the terminal phenyl rings as observed in the RMSF plots (Figures 6d, 8b and Supporting Information S2: Figure S7). For the long MD simulation, the persistence of the hydrophobic interactions with Phe37 and Tyr209 decreased to approximately 10%–30%. However, the hydrophobic interactions of the ligand with Phe152 and Tyr304 could maintain high stability in the long MD run. Overall, the results from the MD simulations supported the results obtained from the ligand docking study.

3 | CONCLUSION

To summarize, the previously optimized HDAC11 AlphaFold model was utilized for the structure-based design of new active and selective probes bearing a novel scaffold by using the docked pose of the previously reported selective inhibitor FT895. Four compounds were synthesized and were first screened for inhibitory activity against different HDAC isoforms. Determining the IC_{50} for HDAC11 showed compound **5a** to be the most active and selective compound with an IC_{50} value of 365 nM for HDAC11 and no inhibition or weak inhibition for other HDAC subtypes at 10 µM concentration. Compound **5a** also possessed promising anti-neuroblastoma activity with EC_{50} of 3.6 µM. Docking of **5a** in the optimized HDAC11 AlphaFold model showed a comparable binding mode to FT895 with the benzohydroxamic acid moiety of **5a** being inserted deeper in the binding pocket while one terminal phenyl ring is accommodated between the side chains of Tyr209 and Leu268 of loop 5 and loop 6 and the other terminal phenyl ring is directed toward loop 1 forming hydrophobic interactions thus fulfilling the aim of the initial design. The binding mode in terms of stability of the initially observed interactions and bidentate chelation was further validated using three independent short as well as single-long molecular dynamic simulations.

Given the observed promising activity and selectivity of compound **5a**, additional chemical optimization is still to be considered to improve activity and selectivity. While compound **5a** interestingly demonstrated promising inhibition of cell viability of neuroblastoma cells, more investigations regarding the involvement of HDAC11 and the use of HDAC11 inhibitors in neuroblastoma cells are required.

In conclusion, the utilization of the optimized HDAC11 AlphaFold model for the structure-based design of new selective inhibitors with cellular activity was successful. The results of the current study show the possibility of using optimized AlphaFold models for the structure-based design of new lead structures and reflect the significance of the optimization procedure we previously adopted.

4 | EXPERIMENTAL

4.1 | Computational modelling

The computational modeling was performed using Schrödinger Suite 2019 and Maestro[33] for visualization.

4.1.1 | Protein preparation

Protein structures were prepared using the Protein Preparation Wizard[34,35] by adding hydrogen atoms and assigning bond orders. Zero-order bonds to metals were generated and water molecules (when available in the X-ray structure) 5 Å away from the ligands were removed. Ionization states of the ligands were generated using Epik[36–38] at pH 7.0 ± 2.0. The hydroxamate[16,39–42] form of the ligands was selected for further hydrogen bond optimization. Hydrogen bond optimization was assigned specifying the protonated state of His142 (HDAC11 numbering) in the HIP form with sampling water orientation and using PROPKA at pH 7.0.

4.1.2 | Ligand preparation

The designed compounds and the co-crystallized ligands were prepared using LigPrep[43] panel with OPLS3e[44–47] force fields. The compounds were prepared in the deprotonated hydroxamate form.

4.1.3 | Docking

The binding mode of the most active and selective compound **5a** was studied by docking. Receptor grids were generated using the Receptor Grid Generation panel utilizing the centroid of the co-crystallized ligands. All grids were generated with the protonated His142 in HIP state. Docking was performed using Glide[48–51] with specifying standard precision mode and flexible ligand sampling utilizing the OPLS3e force field. For HDAC11, docking was performed in the grid obtained from the TSA-HDAC11 AlphaFold model complex with flipped-out Phe152.[16] For the other HDAC isoforms, the following crystal structures were used: HDAC1 (PDB 5ICN), HDAC6 (PDB 5EDU), and HDAC8 (PDB 5FCW).

Redocking of the co-crystallized ligands was performed to validate the docking protocol. The RMSD for the docked and the native poses were found to be 2.018, 0.763, and 0.369 Å for HDAC1, HDAC6, and HDAC8, respectively.

The docking of all ligands was performed using the default settings in the Glide panel (Schrödinger Suite 2019) by including five poses per ligand for postdocking minimization and reporting the top-scored pose.

4.1.4 | Molecular dynamics simulation

The initially predicted binding mode of **5a** was further studied by molecular dynamics simulations using Desmond software.[52,53] The protein–ligand complex was solvated in the simple point charge water model. Orthorhombic box shape and buffer distance of 10 Å were specified as boundary conditions. The box volume was then minimized and neutralization of the system was performed by the addition of chloride ions 4 Å away from the ligand.[27]

The solvated protein–ligand complex was relaxed using the default Desmond relaxation protocol for the isobaric-isothermal (NPT) ensemble followed by a production run utilizing the NPT ensemble at a pressure of 1.01325 bar using Martyna–Tobias–Klein barostat and temperature of 300 K using a Nose–Hoover chain thermostat.[27]

The Simulation Event Analysis panel was employed to calculate the RMSD and the distances. For the protein RMSD, the backbone atoms were used. The ligand and zinc ion were fitted to the protein backbone before calculating their RMSD values. The RMSF and the interaction persistence of the ligand were calculated using the Simulation Interaction Diagram panel. The termini of the protein (residues: 1–14 and 321–347) were excluded from the RMSD and RMSF calculations.[27]

4.2 | Chemistry

4.2.1 | General

Materials and reagents were purchased from Sigma-Aldrich Co. Ltd and abcr GmbH. Analytically pure and dry solvents were used. Thin layer chromatography was performed on aluminum sheets coated with silica gel 60 F254 (Merck). For medium pressure chromatography (MPLC), silica gel Biotage® (Biotage) SNAP ultra-HP-sphere 25 µm containing columns were used.[27]

The purity of the final synthesized compounds was assessed using high-pressure liquid chromatography (HPLC) and employing a UV detector at a wavelength of 254 nm. The HPLC system employed two LC-10AD pumps, an SPD-M10A VP PDA detector, and a SIL-HT autosampler, all from the manufacturer Shimadzu. Merck LiChrospher 100 RP18, 125 mm x 4 mm, 5 µm column was used. The mobile phase composition was Methanol, H_2O, and 0.05% trifluroacetic acid.[27]

High-resolution mass spectrometry (HRMS-ESI) analyses were performed with an LTQ(linear ion trap) Orbitrap XL hybrid mass spectrometer (Thermo Fisher Scientific). ^{1}HNMR and ^{13}CNMR spectra were taken on a Varian Inova 400using deuterated dimethyl sulfoxide (DMSO-d_6) as solvent.[27] Residual solvent signals were used as a reference for the chemical shifts.

The InChI codes of the investigated compounds, together with some biological activity data, are provided as Supporting Information.

4.2.2 | General procedures for the synthesis of chalcones (**2a,b**)

A mixture of equimolar amounts (25 mmol) of 2-methylacetophenone **1** and the appropriate aromatic aldehyde in absolute ethanol (25 mL) containing NaOH (25 mmol), was stirred at room temperature overnight. In the case of benzaldehyde, the reaction mixture was diluted with water and extracted with ethyl acetate. The organic layer was dried over anhydrous sodium sulfate, filtered, and evaporated

under vacuum to afford yellow oil as product **2a**. In the case of 3,4-dichlorobenzaldehyde the solid precipitate was filtered, and washed with methanol to afford yellow powder as product **2b**.

(2*E*)-1-(2-Methylphenyl)-3-phenylprop-2-en-1-one (**2a**): Yellow oil, ^{1}H NMR (400 MHz, DMSO-d_6) δ 7.78–7.71 (m, 2H), 7.62–7.57 (m, 1H), 7.51–7.35 (m, 6H), 7.34–7.28 (m, 2H), 2.35 (s, 3H). Yield, 67.87%.

(2*E*)-3-(3,4-Dichlorophenyl)-1-(2-methylphenyl)prop-2-en-1-one (**2b**): Yellow powder, ^{1}H NMR (400 MHz, DMSO-d_6) δ 8.13 (d, *J* = 2.0 Hz, 1H), 7.80–7.73 (m, 1H), 7.71–7.61 (m, 2H), 7.57–7.39 (m, 3H), 7.36–7.26 (m, 2H), 2.37 (s, 3H). Yield, 72.16%.

4.2.3 | General procedures for the synthesis of pyrazol-3-yl-benzoic acids (3a–d)

A mixture of equimolar amounts (3.5 mmol) of the appropriate chalcone **2a–b** and substituted hydrazine in absolute ethanol was stirred overnight in the presence of catalytic amounts (100 mg) of thiamine HCL. The reaction mixture was diluted with water and extracted with ethyl acetate. The organic layer was dried over anhydrous sodium sulfate, filtered, and evaporated under reduced pressure to afford orange-yellow oil as a product.

The obtained crude product, without further purification, was dissolved in a mixture of water and pyridine (50:50). The mixture was heated under reflux and an excess of potassium permanganate (18 mmol) was added portion-wise. Heating under reflux was continued for 48 h. The reaction mixture was then cooled and filtered. The filtrate was neutralized with concentrated HCl affording the product as solid precipitate. The obtained precipitate was then filtered and dried. For purification, the obtained solid was dissolved in a warm aqueous solution of sodium hydroxide. The solution was filtered and re-acidified by aqueous HCl. The obtained solid was then filtered and dried to afford the products **3a–d**.

2-(1,5-Diphenyl-1*H*-pyrazol-3-yl)benzoic acid (**3a**): White solid, ^{1}H NMR (400 MHz, DMSO-d_6) δ 12.86 (s, 1H), 7.76 (dd, *J* = 7.8, 1.2 Hz, 1H), 7.61–7.52 (m, 2H), 7.48–7.33 (m, 7H), 7.32–7.21 (m, 4H), 6.87 (s, 1H). Yield, 51.2%.

2-(1-Methyl-5-phenyl-1*H*-pyrazol-3-yl)benzoic acid (**3b**): White solid, ^{1}H NMR (400 MHz, DMSO-d_6) δ 12.84 (s, 1H), 7.70–7.65 (m, 1H), 7.57–7.47 (m, 6H), 7.46–7.42 (m, 1H), 7.40–7.37 (m, 1H), 6.57 (s, 1H), 3.86 (s, 3H). Yield, 60.57%.

2-[5-(3,4-Dichlorophenyl)-1-phenyl-1*H*-pyrazol-3-yl]benzoic acid (**3c**): Yellow solid, ^{1}H NMR (400 MHz, DMSO-d_6) δ 12.86 (s, 1H), 7.73 (dd, *J* = 7.8, 1.3 Hz, 1H), 7.65–7.50 (m, 4H), 7.49–7.36 (m, 4H), 7.35–7.29 (m, 2H), 7.14 (dd, *J* = 8.4, 2.1 Hz, 1H), 7.00 (s, 1H). Yield, 61.08%.

2-[5-(3,4-Dichlorophenyl)-1-methyl-1*H*-pyrazol-3-yl]benzoic acid (**3d**): White solid, ^{1}H NMR (400 MHz, DMSO-d_6) δ 12.83 (s, 1H), 7.86 (d, *J* = 2.1 Hz, 1H), 7.76 (d, *J* = 8.4 Hz, 1H), 7.65 (dd, *J* = 7.8, 1.3 Hz, 1H), 7.59–7.47 (m, 3H), 7.43–7.35 (m, 1H), 6.68 (s, 1H), 3.89 (s, 3H). Yield, 52.67%.

4.2.4 | General procedures for amide coupling (4a–d)

A mixture of the obtained acid **3a–d** (1.3 mmol) and HATU (1.3 mmol) in dimethylformamide (DMF) was stirred for 15 min after which O-(tetrahydro-2*H*-pyran-2-yl)-hydroxylamine (1.4 mmol) and DIPEA (3.9 mmol) were added and stirring was continued for 3–4 h. The reaction mixture was diluted with water and extracted with ethyl acetate. The organic layer was washed with saturated solutions of ammonium chloride and sodium carbonate followed by brine. The organic layer was dried over anhydrous sodium sulfate and evaporated under reduced pressure. The product was purified by medium-pressure liquid chromatography (MPLC) using a gradient of ethyl acetate/n-heptane.

2-(1,5-Diphenyl-1*H*-pyrazol-3-yl)-*N*-(oxan-2-yloxy)benzamides (**4a**): White solid, ^{1}H NMR (400 MHz, DMSO-d_6) δ 11.48 (s, 1H), 7.93–7.86 (m, 1H), 7.56–7.48 (m, 1H), 7.45–7.28 (m, 10H), 7.27–7.20 (m, 2H), 6.92 (s, 1H), 5.03 (t, *J* = 3.0 Hz, 1H), 3.98–3.88 (m, 1H), 3.37–3.31 (m, 1H), 1.72–1.59 (m, 3H), 1.53–1.41 (m, 3H). Yield 81.5%.

2-(1-Methyl-5-phenyl-1*H*-pyrazol-3-yl)-*N*-(oxan-2-yloxy) benzamides (**4b**): White solid, ^{1}H NMR (400 MHz, DMSO-d_6) δ 11.43 (s, 1H), 7.80 (dd, *J* = 7.9, 1.2 Hz, 1H), 7.54–7.43 (m, 6H), 7.38–7.33 (m, 1H), 7.32–7.28 (m, 1H), 6.66 (s, 1H), 5.06 (t, *J* = 2.8 Hz, 1H), 3.98–3.90 (m, 1H), 3.87 (s, 3H), 3.42–3.35 (m, 1H), 1.73–1.62 (m, 3H), 1.53–1.43 (m, 3H). Yield 71.6%.

2-[5-(3,4-Dichlorophenyl)-1-phenyl-1*H*-pyrazol-3-yl]-*N*-(oxan-2-yloxy)benzamides (**4c**): White solid, ^{1}H NMR (400 MHz, DMSO-d_6) δ 11.49 (s, 1H), 7.87 (dd, *J* = 7.8, 1.2 Hz, 1H), 7.61 (d, *J* = 8.4 Hz, 1H), 7.56 (d, *J* = 2.1 Hz, 2H), 7.48–7.31 (m, 7H), 7.09 (dd, *J* = 8.4, 2.1 Hz, 1H), 7.04 (s, 1H), 5.06 (t, *J* = 2.8 Hz, 1H), 4.01–3.92 (m, 1H), 3.42–3.32 (m, 1H), 1.73–1.60 (m, 3H), 1.55–1.43 (m, 3H). Yield 77.2%.

2-[5-(3,4-Dichlorophenyl)-1-methyl-1*H*-pyrazol-3-yl]-*N*-(oxan-2-yloxy)benzamides (**4d**): White solid, ^{1}H NMR (400 MHz, DMSO-d_6) δ 11.46 (s, 1H), 7.83 (d, *J* = 2.1 Hz, 1H), 7.80–7.74 (m, 2H), 7.55 (dd, *J* = 8.4, 2.1 Hz, 1H), 7.51–7.44 (m, 1H), 7.40–7.34 (m, 1H), 7.33–7.28 (m, 1H), 6.76 (s, 1H), 5.10 (t, *J* = 2.5 Hz, 1H), 4.03–3.93 (m, 1H), 3.90 (s, 3H), 3.46–3.37 (m, 1H), 1.75–1.66 (m, 3H), 1.55– 1.47 (m, 3H). Yield 70.7%.

4.2.5 | General procedures for THP de-protection (5a–d)

The respective THP-protected hydroxamic acid **4a–d** (0.8 mmol) was dissolved in 20 mL of tetrahydrofuran, 1 mL of 2 N aqueous HCl was added, and the mixture was stirred overnight. The reaction mixture was diluted with water and extracted with ethyl acetate. The organic layer was dried over anhydrous sodium sulfate and evaporated under reduced pressure. The product was purified by medium-pressure liquid chromatography (MPLC) using a gradient elution with methanol and dichloromethane.

2-(1,5-Diphenyl-1*H*-pyrazol-3-yl)-*N*-hydroxybenzamide (**5a**): White solid, ^{1}H NMR (400 MHz, DMSO-d_6) δ 10.91 (s, 1H), 9.12 (s, 1H), 7.92 (dd, *J* = 7.8, 1.3 Hz, 1H), 7.52–7.46 (m, 1H), 7.44–7.30 (m, 10H), 7.26–7.22 (m, 2H), 6.84 (s, 1H). ^{13}C NMR (101 MHz, DMSO-d_6) δ 166.73, 149.98, 143.76, 140.03, 134.43, 131.04, 130.35, 129.88, 129.50, 129.07, 128.98, 128.94, 128.72, 128.43, 128.14, 125.48, 107.88. HRMS *m/z*: [M + H] $^{+}$ 356.1399; calculated $C_{22}H_{18}O_2N_3$: 356.1399. HPLC: rt 12.966 min (purity 99.60%). Yield 10.6%.

N-Hydroxy-2-(1-methyl-5-phenyl-1*H*-pyrazol-3-yl)benzamides (**5b**): White solid, ^{1}H NMR (400 MHz, DMSO-d_6) δ 10.82 (s, 1H), 9.04 (s, 1H), 7.84 (dd, *J* = 7.9, 1.3 Hz, 1H), 7.57–7.41 (m, 6H), 7.36–7.30 (m, 1H), 7.29–7.25 (m, 1H), 6.59 (s, 1H), 3.88 (s, 3H). ^{13}C NMR (101 MHz, DMSO-d_6) δ 166.80, 147.85, 144.20, 134.14, 131.55, 130.41, 129.73, 129.26, 128.96, 128.90, 128.57, 128.11, 127.58, 105.73, 38.11. HRMS m/z: [M + H] $^{+}$ 294.1237; calculated $C_{17}H_{16}O_2N_3$: 294.1243. HPLC: rt 11.091 min (purity 96.93%). Yield 38.6%.

2-[5-(3,4-Dichlorophenyl)-1-phenyl-1*H*-pyrazol-3-yl]-*N*-hydroxybenzamide (**5c**): White solid, ^{1}H NMR (400 MHz, DMSO-d_6) δ 10.91 (s, 1H), 9.11 (s, 1H), 7.90 (dd, *J* = 7.8, 1.3 Hz, 1H), 7.62 (d, *J* = 8.4 Hz, 1H), 7.55 (d, *J* = 2.1 Hz, 1H), 7.52–7.32 (m, 8H), 7.13 (dd, *J* = 8.4, 2.1 Hz, 1H), 6.92 (s, 1H). ^{13}C NMR (101 MHz, DMSO-d_6) δ 166.62, 150.16, 141.22, 139.57, 134.46, 131.85, 131.67, 131.23, 130.80, 130.79, 130.59, 129.93, 129.72, 129.06, 128.72, 128.54, 128.45, 128.31, 125.66, 108.47. HRMS *m/z*: [M + H] 424.0613; calculated $C_{22}H_{16}O_2N_3C_{l2}$: 424.0620. HPLC: rt 14.541 min (purity 99.33%). Yield 12.6%.

2-[5-(3,4-Dichlorophenyl)-1-methyl-1*H*-pyrazol-3-yl]-*N*-hydroxybenzamide (**5d**): White solid, ^{1}H NMR (400 MHz, DMSO-d_6) δ 10.83 (s, 1H), 9.06 (s, 1H), 7.85–7.80 (m, 2H), 7.77 (d, *J* = 8.3 Hz, 1H), 7.56 (dd, *J* = 8.3, 2.1 Hz, 1H), 7.49–7.42 (m, 1H), 7.38–7.32 (m, 1H), 7.30–7.26 (m, 1H), 6.66 (s, 1H), 3.90 (s, 3H). ^{13}C NMR (101 MHz, DMSO-d_6) δ 166.67, 148.00, 141.75, 134.17, 132.07, 131.77, 131.42, 131.30, 130.92, 130.57, 129.78, 129.09, 128.56, 128.15, 127.74, 106.34, 38.27. HRMS *m/z*: [M + H]$^{+}$ 362.0460; calculated $C_{17}H_{14}O_2N_3Cl_2$: 362.0463. HPLC: rt 13.398 min (purity 96.741%). Yield 37.0%.

4.3 | In vitro enzymatic assay

Human HDAC11 full-length protein was expressed and purified as described.[13] A fluorescence-based HDAC11 enzymatic assay was used.[27] For the fluorescence measurements, a PerkinElmer Envision 2104 multilabel plate reader was used at λ_{ex} = 320 nm and λ_{em} = 430 nm. The reaction mixture consisted of HDAC11, and the acylated peptide substrate derived from tumor necrosis factor-α (TNF-α) in a reaction buffer comprising 50 mM HEPES, 2 mg/mL BSA, and 70 μMTCEP, and at pH 7.4 which was adjusted with NaOH (total volume 40 μL).[27] The reactions were incubated in black 384-well plates for 30 min (scan every 30 s) at room temperature, and the increase of relative fluorescence reflecting the product formation was monitored. As a reference for HDAC11 inhibitors, we used the reported compound SIS17 (purchased from MedChemExpress LLC, 1 Deer Park Dr, Suite Q, Monmouth Junction, NJ 08852, USA).

For HDAC1, 2, 3, and HDAC6 the recombinant proteins were purchased from ENZO Life Sciences AG (Lausen, CH) whereas HDAC4, 5, 7, 9, and 10 were produced as described.[54] Human HDAC8 was produced as described.[55] The inhibitors were tested in an enzymatic in vitro assay using 384-well plates (GreinerONe, catalogue no. 784900).[27,55] After 5 min of incubation of the inhibitors with the respective enzymes (HDAC1 = 10 nM, HDAC2 and 3 = 3 nM, HDAC4 = 5 nM, HDAC5 = 10 nM, HDAC6 = 1 nM, HDAC7 = 5 nM, HDAC8 = 2 HDAC 9 = 20 nM, HDAC10 = 5 nM), the reactions were always started by the addition of substrate.

For HDAC1, 2, 3, and 6, an acetylated peptide substrate derived from p53 (Ac-RHKK(Acetyl)-AMC) was used in a discontinuous fluorescence assay.[54] All reactions were performed in assay buffer (20 mM HEPES, 140 mM NaCl, 10 mM MgCl2, 1 mM TCEP, and 0.2 mg/mL BSA, pH 7.4 adjusted with NaOH) at 37°C. The reaction was quenched after 1 h by adding trypsin and suberoylanilide hydroxamic acid (SAHA). The fluorescence intensity was measured after 1 h of incubation using an Envision 2104 Multilabel Plate Reader (PerkinElmer), with an excitation wavelength of 380 ± 8 nm and an emission wavelength of 430 ± 8 nm. HDAC4, 5, 7, 8, 9, and 10 were measured in a continuous manner using the thio-acetylated peptide substrate (Abz-SRGGK(thio-TFA)FFRR-NH2).[54] For HDAC10, an internal quenched spermidine-like substrate was utilized. The fluorescence increase was followed for 1 h with two reads per min with an excitation wavelength of 320 ± 8 nm and an emission wavelength of 430 ± 8 nm. Positive (enzyme, substrate, DMSO, and buffer) and negative (substrate, DMSO, and Buffer) controls were included in every measurement and were set as 100% and 0%, respectively and the measured values were normalized accordingly. All tests were done in three replicates.

4.4 | Anti-neuroblastoma evaluation

BE(2) C (ATCC, CRL-2268) cells were cultured in a 1:1 mixture of DMEM/F12 (with HEPES, Gibco) and eagle`s minimum essential medium (ATCC) supplemented with 10% fetal bovine serum (FBS). Cells were grown at 37°C and 5% CO2. BE(2) C cells were authenticated at Eurofins Genomics by 16 independent polymerase chain reaction (PCR) systems (D8S1179, D21S11, D7S820, CSF1PO, D3S1358, TH01, D13S317, D16S539, D2S1338, AMEL, D5S818, FGA, D19S433, vWA, TPOX and D18S51). Subsequently, a progressive dilution series of the tested inhibitor was executed, and these solutions were added to the cells alongside dimethyl sulfoxide (DMSO) as a control condition. Following a 72 h treatment duration, the cell viability was quantified and adjusted relative to the DMSO control. The determination of EC_{50} values was achieved through the utilization of GraphPad Prism software (version 10.1.1) employing nonlinear regression analysis. The tests were carried out in four replicates.

ACKNOWLEDGEMENTS

The authors thank Simone Kniesa and Dr. Matthias Schmidt for their technical assistance. This study was supported by the Deutsche Forschungsgemeinschaft (DFG) grants 469954457 and 471614207 (W.S.). This work was supported in part by the CAS (RVO: 86652036) and the Grant Agency of the Czech Republic (24-12155 S) (C.B). Open Access funding enabled and organized by Projekt DEAL.

CONFLICTS OF INTEREST STATEMENT

The authors declare no conflicts of interest.

DATA AVAILABILITY STATEMENT

The data that support the findings of this study are available on request from the corresponding author. The data are not publicly available due to privacy or ethical restrictions.

ORCID

Fady Baselious http://orcid.org/0000-0003-3242-8514
Sebastian Hilscher http://orcid.org/0009-0003-0611-7365
Cyril Barinka http://orcid.org/0000-0003-2751-3060
Wolfgang Sippl http://orcid.org/0000-0002-5985-9261

REFERENCES

[1] P. M. Lombardi, K. E. Cole, D. P. Dowling, D. W. Christianson, *Curr. Opin. Struct. Biol.* **2011**, *21*(6), 735.
[2] M. Marek, T. B. Shaik, C. Romier *Epigenetic Drug Discovery* (Eds W. Sippl, M. Jung), Wiley-VCH Verlag GmbH & Co. KGaA, Boschstr, 12, 69469 Weinheim, Germany **2019**, pp. 11Chapter 2.
[3] H. Chen, C. Xie, Q. Chen, S. Zhuang, *Front. Endocrinol.* **2022**, *13*, 989305.
[4] S. S. Liu, F. Wu, Y. M. Jin, W. Q. Chang, T. M. Xu, *Biomed. Pharmacother.* **2020**, *131*, 110607.
[5] H. E. Deubzer, M. C. Schier, I. Oehme, M. Lodrini, B. Haendler, A. Sommer, O. Witt, *Int. J. Cancer* **2013**, *132*(9), 2200.
[6] D. Gong, Z. Zeng, F. Yi, J. Wu, *Am. J. Transl. Res.* **2019**, *11*(2), 983.
[7] W. Huo, F. Qi, K. Wang, *Oncol. Rep.* **2020**, *44*(3), 1233.
[8] W. Wang, L. Fu, S. Li, Z. Xu, X. Li, *Cell Biol. Int.* **2017**, *41*(12), 1290.
[9] M. W. Martin, J. Y. Lee, D. R. Lancia, P. Y. Ng, B. Han, J. R. Thomason, M. S. Lynes, C. G. Marshall, C. Conti, A. Collis, M. A. Morales, K. Doshi, A. Rudnitskaya, L. Yao, X. Zheng, *Bioorg. Med. Chem. Lett.* **2018**, *28*(12), 2143.
[10] N. Bora-Singhal, D. Mohankumar, B. Saha, C. M. Colin, J. Y. Lee, M. W. Martin, X. Zheng, D. Coppola, S. Chellappan, *Sci. Rep.* **2020**, *10*(1), 4722.
[11] P. Bai, Y. Liu, L. Yang, W. Ding, P. Mondal, N. Sang, G. Liu, X. Lu, T. T. Ho, Y. Zhou, R. Wu, V. C. Birar, M. Q. Wilks, R. E. Tanzi, H. Lin, C. Zhang, W. Li, S. Shen, C. Wang, *J. Med. Chem.* **2023**, *66*(23), 16075.
[12] Z. Kutil, J. Mikešová, M. Zessin, M. Meleshin, Z. Nováková, G. Alquicer, A. Kozikowski, W. Sippl, C. Bařinka, M. Schutkowski, *ACS Omega* **2019**, *4*(22), 19895.
[13] Z. Kutil, Z. Novakova, M. Meleshin, J. Mikesova, M. Schutkowski, C. Barinka, *ACS Chem. Biol.* **2018**, *13*(3), 685.
[14] S. I. Son, J. Cao, C.-L. Zhu, S. P. Miller, H. Lin, *ACS Chem. Biol.* **2019**, *14*(7), 1393.
[15] T. T. Ho, C. Peng, E. Seto, H. Lin, *ACS Chem. Biol.* **2023**, *18*(4), 803.
[16] F. Baselious, D. Robaa, W. Sippl, *Comput. Biol. Med.* **2023**, *167*, 107700.
[17] L. Gao, M. A. Cueto, F. Asselbergs, P. Atadja, *J. Biol. Chem.* **2002**, *277*(28), 25748.
[18] J. Jumper; R. Evans; A. Pritzel; T. Green; M. Figurnov; O. Ronneberger; K. Tunyasuvunakool; R. Bates; A. Žídek; A. Potapenko; A. Bridgland; C. Meyer; S. a. A. Kohl; A. J. Ballard; A. Cowie; B. Romera-Paredes; S. Nikolov; R. Jain; J. Adler; T. Back; S. Petersen; D. Reiman; E. Clancy; M. Zielinski; M. Steinegger; M. Pacholska; T. Berghammer; S. Bodenstein; D. Silver; O. Vinyals; A. W. Senior; K. Kavukcuoglu; P. Kohli; D. Hassabis, *Nature* **2021**, *596*(7873), 583.
[19] A. David, S. Islam, E. Tankhilevich, M. J. E. Sternberg, *J. Mol. Biol.* **2022**, *434*(2), 167336.
[20] F. Ren; X. Ding; M. Zheng; M. Korzinkin; X. Cai; W. Zhu; A. Mantsyzov; A. Aliper; V. Aladinskiy; Z. Cao; S. Kong; X. Long; B. H. Man Liu; Y. Liu; V. Naumov; A. Shneyderman; I. V. Ozerov; J. Wang; F. W. Pun; D. A. Polykovskiy; C. Sun; M. Levitt; A. Aspuru-Guzik; A. Zhavoronkov, *Chem. Sci.* **2023**, *14*(6), 1443.
[21] W. Zhu; X. Liu; Q. Li; F. Gao; T. Liu; X. Chen; M. Zhang; A. Aliper; F. Ren; X. Ding; A. Zhavoronkov, *Bioorg. Med. Chem.* **2023**, *91*, 117414.
[22] A. M. Díaz-Rovira, H. Martín, T. Beuming, L. Díaz, V. Guallar, S. S. Ray, *J. Chem. Inf. Model.* **2023**, *63*(6), 1668.
[23] X. He, C. You, H. Jiang, Y. Jiang, H. E. Xu, X. Cheng, *Acta Pharmacol. Sin.* **2023**, *44*(1), 1.
[24] M. Holcomb, Y. T. Chang, D. S. Goodsell, S. Forli, *Protein Sci.* **2023**, *32*(1), e4530.
[25] V. Scardino, J. I. Di Filippo, C. N. Cavasotto, *iScience* **2023**, *26*(1), 105920.
[26] M. Karelina, J. J. Noh, R. O. Dror, *eLife* **2023**, *12*, RP89386.
[27] F. Baselious, S. Hilscher, D. Robaa, C. Barinka, M. Schutkowski, W. Sippl, *Int. J. Mol. Sci.* **2024**, *25*(2), c1358.
[28] N. S. M. Ismail, R. F. George, R. aT. Serya, F. N. Baselious, M. El-Manawaty, E. M. Shalaby, A. S. Girgis, *RSC Adv.* **2016**, *6*(104), 101911.
[29] T. M. Thole, M. Lodrini, J. Fabian, J. Wuenschel, S. Pfeil, T. Hielscher, A. Kopp-Schneider, U. Heinicke, S. Fulda, O. Witt, A. Eggert, M. Fischer, H. E. Deubzer, *Cell Death Dis.* **2017**, *8*(3), e2635.
[30] E. F. Bülbül, J. Melesina, H. S. Ibrahim, M. Abdelsalam, A. Vecchio, D. Robaa, M. Zessin, M. Schutkowski, W. Sippl, *Molecules* **2022**, *27*(8), 2526.
[31] J. Liu, Y. Yu, J. Kelly, D. Sha, A.-B. Alhassan, W. Yu, M. M. Maletic, J. L. Duffy, D. J. Klein, M. K. Holloway, S. Carroll, B. J. Howell, R. J. O. Barnard, S. Wolkenberg, J. A. Kozlowski, *ACS Med. Chem. Lett.* **2020**, *11*(12), 2476.
[32] L. Whitehead, M. R. Dobler, B. Radetich, Y. Zhu, P. W. Atadja, T. Claiborne, J. E. Grob, A. Mcriner, M. R. Pancost, A. Patnaik, W. Shao, M. Shultz, R. Tichkule, R. A. Tommasi, B. Vash, P. Wang, T. Stams, *Bioorg. Med. Chem.* **2011**, *19*(15), 4626.
[33] Schrödinger Release 2019-1: Maestro, Schrödinger, LLC, New York, NY, **2019**.
[34] Schrödinger Release 2019-1: Protein Preparation Wizard. Epik, Schrödinger, LLC, New York, NY, 2019; Impact, Schrödinger, LLC, New York, NY, 2019; Prime, Schrödinger, LLC, New York, NY, 2019.
[35] G. Madhavi Sastry, M. Adzhigirey, T. Day, R. Annabhimoju, W. Sherman., *J. Comput.-Aided Mol. Des.* **2013**, *27*(3), 221.
[36] Schrödinger Release 2019-1: Epik, Schrödinger, LLC, New York, NY, **2019**.
[37] J. R. Greenwood, D. Calkins, A. P. Sullivan, J. C. Shelley, *J. Comput.-Aided Mol. Des.* **2010**, *24*(6–7), 591.
[38] J. C. Shelley, A. Cholleti, L. L. Frye, J. R. Greenwood, M. R. Timlin, M. Uchimaya, *J. Comput.-Aided Mol. Des.* **2007**, *21*(12), 681.
[39] E. Ghazy, T. Heimburg, J. Lancelot, P. Zeyen, K. Schmidtkunz, A. Truhn, S. Darwish, C. V. Simoben, T. B. Shaik, F. Erdmann, M. Schmidt, D. Robaa, C. Romier, M. Jung, R. Pierce, W. Sippl, *Eur. J. Med. Chem.* **2021**, *225*, 113745.
[40] E. Ghazy, P. Zeyen, D. Herp, M. Hügle, K. Schmidtkunz, F. Erdmann, D. Robaa, M. Schmidt, E. R. Morales, C. Romier, S. Günther, M. Jung, W. Sippl, *Eur. J. Med. Chem.* **2020**, *200*, 112338.

[41] M. Marek, T. B. Shaik, T. Heimburg, A. Chakrabarti, J. Lancelot, E. Ramos-Morales, C. Da Veiga, D. Kalinin, J. Melesina, D. Robaa, K. Schmidtkunz, T. Suzuki, R. Holl, E. Ennifar, R. J. Pierce, M. Jung, W. Sippl, C. Romier, *J. Med. Chem.* **2018**, *61*(22), 10000.
[42] K. Vögerl, N. Ong, J. Senger, D. Herp, K. Schmidtkunz, M. Marek, M. Müller, K. Bartel, T. B. Shaik, N. J. Porter, D. Robaa, D. W. Christianson, C. Romier, W. Sippl, M. Jung, F. Bracher, *J. Med. Chem.* **2019**, *62*(3), 1138.
[43] Schrödinger Release 2019-1: LigPrep, Schrödinger, LLC, New York, NY, **2019**.
[44] E. Harder, W. Damm, J. Maple, C. Wu, M. Reboul, J. Y. Xiang, L. Wang, D. Lupyan, M. K. Dahlgren, J. L. Knight, J. W. Kaus, D. S. Cerutti, G. Krilov, W. L. Jorgensen, R. Abel, R. A. Friesner, *J. Chem. Theory Comput.* **2016**, *12*(1), 281.
[45] W. L. Jorgensen, D. S. Maxwell, J. Tirado-Rives, *J. Am. Chem. Soc.* **1996**, *118*(45), 11225.
[46] W. L. Jorgensen, J. Tirado-Rives, *J. Am. Chem. Soc.* **1988**, *110*(6), 1657.
[47] D. Shivakumar, J. Williams, Y. Wu, W. Damm, J. Shelley, W. Sherman, *J. Chem. Theory Comput.* **2010**, *6*(5), 1509.
[48] Schrödinger Release 2019-1: Glide, Schrödinger, LLC, New York, NY, **2019**.
[49] R. A. Friesner, J. L. Banks, R. B. Murphy, T. A. Halgren, J. J. Klicic, D. T. Mainz, M. P. Repasky, E. H. Knoll, M. Shelley, J. K. Perry, D. E. Shaw, P. Francis, P. S. Shenkin, *J. Med. Chem.* **2004**, *47*(7), 1739.
[50] R. A. Friesner, R. B. Murphy, M. P. Repasky, L. L. Frye, J. R. Greenwood, T. A. Halgren, P. C. Sanschagrin, D. T. Mainz, *J. Med. Chem.* **2006**, *49*(21), 6177.
[51] T. A. Halgren, R. B. Murphy, R. A. Friesner, H. S. Beard, L. L. Frye, W. T. Pollard, J. L. Banks, *J. Med. Chem.* **2004**, *47*(7), 1750.
[52] Schrödinger Release 2019-1. *Desmond Molecular Dynamics System, D.E. Shaw Research, New York, NY, 2019, Maestro-Desmond Interoperability Tools*, Schrödinger, New York, NY, USA **2019**.
[53] K. J. Bowers, D. E. Chow, H. Xu, R. O. Dror, M. P. Eastwood, B. A. Gregersen, J. L. Klepeis, I. Kolossvary, M. A. Moraes, F. D. Sacerdoti, J. K. Salmon, Y. Shan, D. E. Shaw. Scalable algorithms for molecular dynamics simulations on commodity clusters. In *Proceedings of the 2006 ACM/IEEE Conference on Supercomputing*, 11- 17 Nov. 2006, Tampa, FL, USA **2006**. p.43. https://doi.org/10.1109/SC.2006.54
[54] M. Zessin, Z. Kutil, M. Meleshin, Z. Nováková, E. Ghazy, D. Kalbas, M. Marek, C. Romier, W. Sippl, C. Bařinka, M. Schutkowski, *Biochemistry* **2019**, *58*(48), 4777.
[55] T. Heimburg, F. R. Kolbinger, P. Zeyen, E. Ghazy, D. Herp, K. Schmidtkunz, J. Melesina, T. B. Shaik, F. Erdmann, M. Schmidt, C. Romier, D. Robaa, O. Witt, I. Oehme, M. Jung, W. Sippl, *J. Med. Chem.* **2017**, *60*(24), 10188.

SUPPORTING INFORMATION

Additional supporting information can be found online in the Supporting Information section at the end of this article.

How to cite this article: F. Baselious, S. Hilscher, S. Hagemann, S. Tripathee, D. Robaa, C. Barinka, S. Hüttelmaier, M. Schutkowski, W. Sippl, *Arch. Pharm.* **2024**, e2400486. https://doi.org/10.1002/ardp.202400486

4. Further results

This page left intentionally blank.

4.1. Abstract

The clinical usefulness of HDAC inhibitors bearing hydroxamic acid moiety as ZBG is limited by their potential mutagenicity. Moreover, hydroxamic acids show poor selectivity that results in off-target effects and toxicity. Recently, the development of HDAC inhibitors bearing other ZBG than hydroxamic acid is emerging as an interesting scope to overcome these limitations. HDAC inhibitors carrying alkyl hydrazide ZBG have been developed and investigated in HDAC classes known to possess a foot pocket such as class I and class IV. In this chapter, the binding mode of one of the most active alkyl hydrazide HDAC11 inhibitors from the in-house library was studied by docking in the optimized HDAC11-AF2 model. MD simulation further supported the predicted binding mode. Additionally, a ligand-based virtual screening workflow to identify new HDAC11 alkyl hydrazide inhibitors was devised and implemented using a categorical classification model. Tow compounds of the identified potential inhibitors were selected for further investigations. The binding mode of the selected candidates was predicted by docking and was further verified using MD simulation studies.

4.2. Results and discussion

4.2.1. Modeling of in-house alkyl hydrazides

Hydroxamic acid is the most commonly used ZBG for the development of HDAC inhibitors as it represents a well-characterized pharmacophore for chelating the zinc ion [81, 82]. A number of hydroxamic acid HDAC inhibitors have been approved by FDA for clinical use [140], while some others have reached to clinical trials [140-144]. Examples of FDA-approved inhibitors include vorinostat for cutaneous T-Cell lymphoma [145], belinostat for peripheral T-cell lymphoma [146] and panobinostat for multiple myeloma [147]. The therapeutic usefulness of the HDAC hydroxamic acid inhibitors, however, is limited by toxicities and undesirable off-target effects as a consequence of poor selectivity over other metalloenzymes as well as within HDACs family subtypes [148, 149]. Other disadvantages of the hydroxamic acid moiety include susceptibility to metabolic inactivation via glucuronidation [150-152] and potential mutagenicity [153, 154].

Consequently, the design and development of HDAC inhibitors bearing different ZBG other than hydroxamic acid have recently gained growing interest [84, 85]. Inspired by the confirmed defatty-acylase activity of HDAC11, alkyl hydrazide inhibitors bearing long alkyl chain have been designed and reported [109]. In our group, we reported before the development of novel class I HDAC inhibitors bearing alkyl hydrazide moiety as ZBG [85]. Screening of the developed compounds against HDAC11 identified compound PSP74 (**4c**) [85] as one of the most active HDAC11 alkyl hydrazide inhibitors (HDAC11 IC_{50} 27 nM) in the series. The binding mode of PSP74 was studied by docking and molecular dynamics simulation, using the optimized HDAC11-AF2 model, to get a deeper insight about the binding mode.

The docking resulted in a pose that is leaning towards loop 5 and loop 6 with the methylindole capping group directed towards loop 5 (**Figure 6**). The ligand demonstrated bidentate chelation of the zinc ion through the carbonyl oxygen and the nitrogen of the hydrazide moiety with distances of 2.38 Å and 2.4 Å, respectively. The 6-carbon long alkyl chain is accommodated in the foot pocket and forms hydrophobic interactions with Phe37, Phe141, Phe152 and Cys153. Three hydrogen bonds were observed between the carbonyl oxygen and the two NH groups of the hydrazide moiety and Tyr304, His142 and His143, respectively. Additionally, the ligand formed a salt bridge between the protonated nitrogen of the piperazine ring and Glu94. Moreover, a π-π interaction was observed between the methylindole ring and Tyr209.

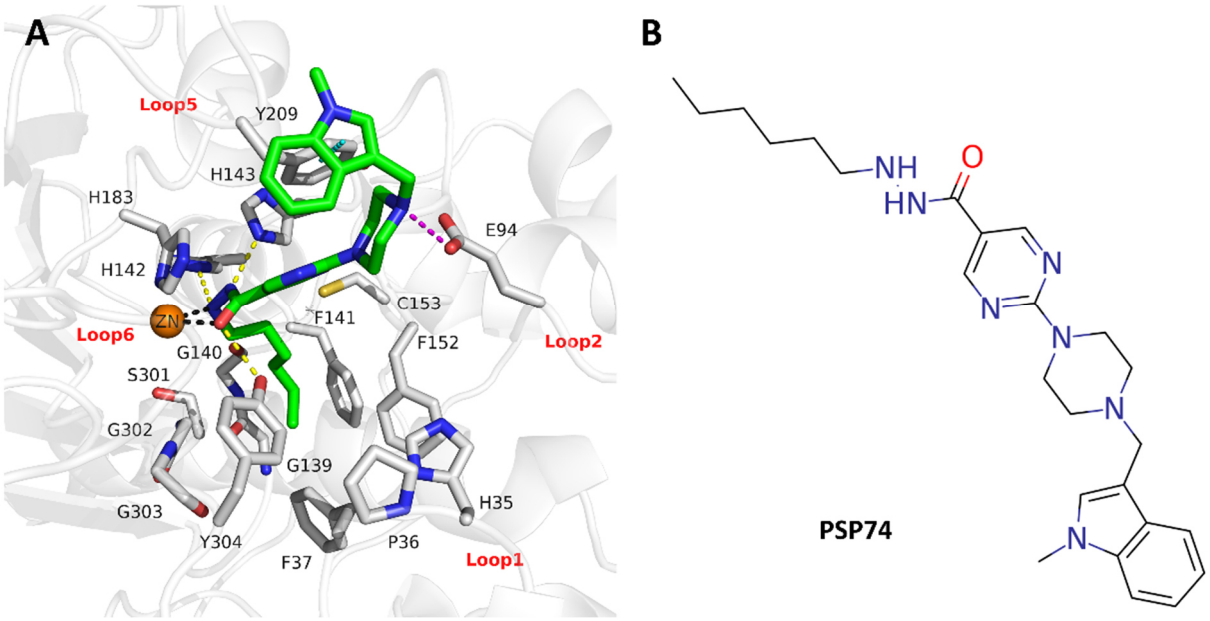

Figure 6. (**A**). The docking pose of compound PSP74 in HDAC11. The protein backbone appears as white cartoon, interacting residues of the binding site as grey sticks, zinc cofactor as orange sphere and compound PSP74 as green sticks. Hydrogen bonds are represented as yellow dashed lines, coordination bonds as grey dashed lines, π-π interactions as cyan dashed line and salt bridge as magenta dashed line. (**B**). 2D structure of PSP74.

Molecular dynamics simulation is a computational technique that is used to simulate the dynamics of molecular systems such as protein-ligand complexes [155]. MD simulation thus provides a tool to study the behavior and stability of the ligand in dynamic environment giving an advantage over docking methods that do not take protein flexibility into account. The root mean square deviation (RMSD), the root mean square fluctuation (RMSF) and the interactions persistence/occupancy are common metrics that are used to analyze and evaluate the MD simulation results. Such metrics can give a figure about protein-ligand complex stability, thus reflecting the reliability of the predicted binding mode [156].

For compound PSP74, the RMSD plots reflect the stability of the protein and the zinc ion (**Figure S21**). The protein is stabilizing at almost 1 Å while the zinc ion is stabilizing below 1 Å. For the ligand, the RMSD plots (**Figure 7A**) show that the ligand is stabilizing at around 2 Å. However, some shifts reaching up to 4 Å can be observed during the course of simulation.

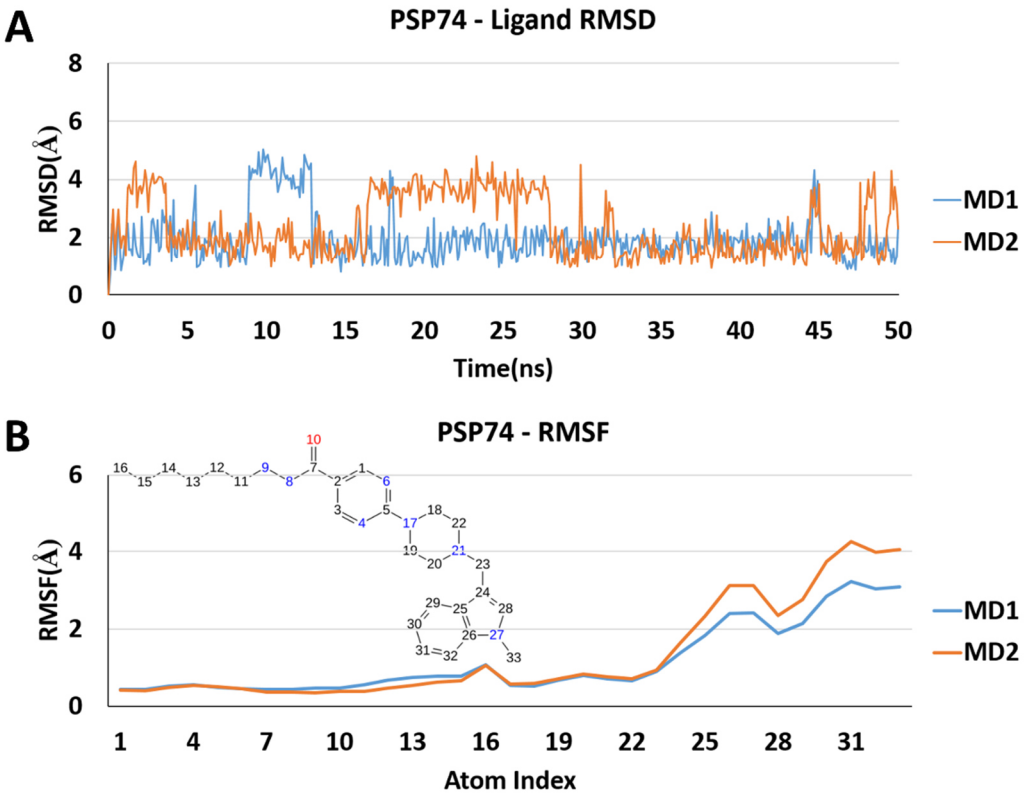

Figure 7. (**A**) and (**B**). RMSD and RMSF plots, respectively, of ligand heavy atoms of PSP74 for two 50 ns independent MD simulations.

The RMSF plots (**Figure 7B**) of the ligand heavy atoms show that the methylindole capping group is the most fluctuating part of the ligand with RMSF reaching up to 4 Å. Inspecting the trajectory snapshots can confirm this observation by showing that the capping group can move in various directions but more towards loop 5 (**Figure S22**).

The hydrogen bonds to His142 and His143, as well as the salt bridge to Glu94, showed high stability with persistence ranging between 81% and 100%. The hydrogen bond with Tyr304 was completely lost during the simulation. This was also observed in previous studies due to the flexibility of the side chain of this tyrosine residue [157]. During the MD simulation, a π-cation interaction was established between the protonated nitrogen of the piperazine ring and Tyr209. The pi-cation interaction showed high stability with persistence around 90% (**Table S2, Figures S23 and S24**). While the RMSD and RMSF plots indicate that the capping group can fluctuate freely in various directions, interestingly, this fluctuation did not significantly affect the stability of the interactions of the protonated nitrogen with either Glu94 or Tyr209. As a conclusion, the results from the MD simulation support the predicted binding mode.

4.2.2. Virtual screening

Virtual screening utilizes computational tools to identify potential hits for certain targets from large databases of compounds. Compared to experimental approaches, virtual screening is faster and more cost-effective in identifying new lead molecules, which can then be optimized to meet the desired efficacy [158-160]. ZINC20 is a publicly available database that includes nearly two billion compounds in 2D and 3D downloadable formats through a website that allows for rapid analogue search [161]. For the aim of searching for new alkyl hydrazide HDAC11 inhibitors, a focused library of N`-alkyl benzohydrazide compounds was acquired from ZINC20 database and virtually screened using a multistep workflow.

4.2.2.1. Virtual modification and filtering

In order to find new HDAC11 alkyl hydrazide inhibitors, a specific chemical space was designed by virtually modifying the structures in the obtained library. The modification was performed by replacing the various N`-alkyl substitutions of the hydrazide moiety with N`-hexyl group. A substitution of 6-carbon long alkyl chain was considered optimal for HDAC11 inhibition based on the activity results obtained from the in-house alkyl hydrazide inhibitors database. This substitution was also considered suitable when taking into account the drug-likeness of the desired hit molecules. Subsequent to this modification, several filtering procedures were performed as represented in (**Figure 8**). The new library was first filtered to remove the duplicates and fragments with less than two rings resulted from the modification step.

Molecular filters are commonly employed to narrow down the chemical space in order to remove molecules with chemical structures and properties that lie beyond the scope of interest. Most of such filters are developed with the aim of defining and extracting molecules that are drug-like and bioavailable from large libraries [162]. Drug-likeness can be defined as the desired properties often found in approved drugs, such as water solubility, oral absorption, low toxicity, suitable clearance rate, and membrane permeability [162-164]. In searching for an HDAC11 inhibitor with drug-like properties, rapid elimination of swill (REOS) and Lipinski rule of five filters were applied.

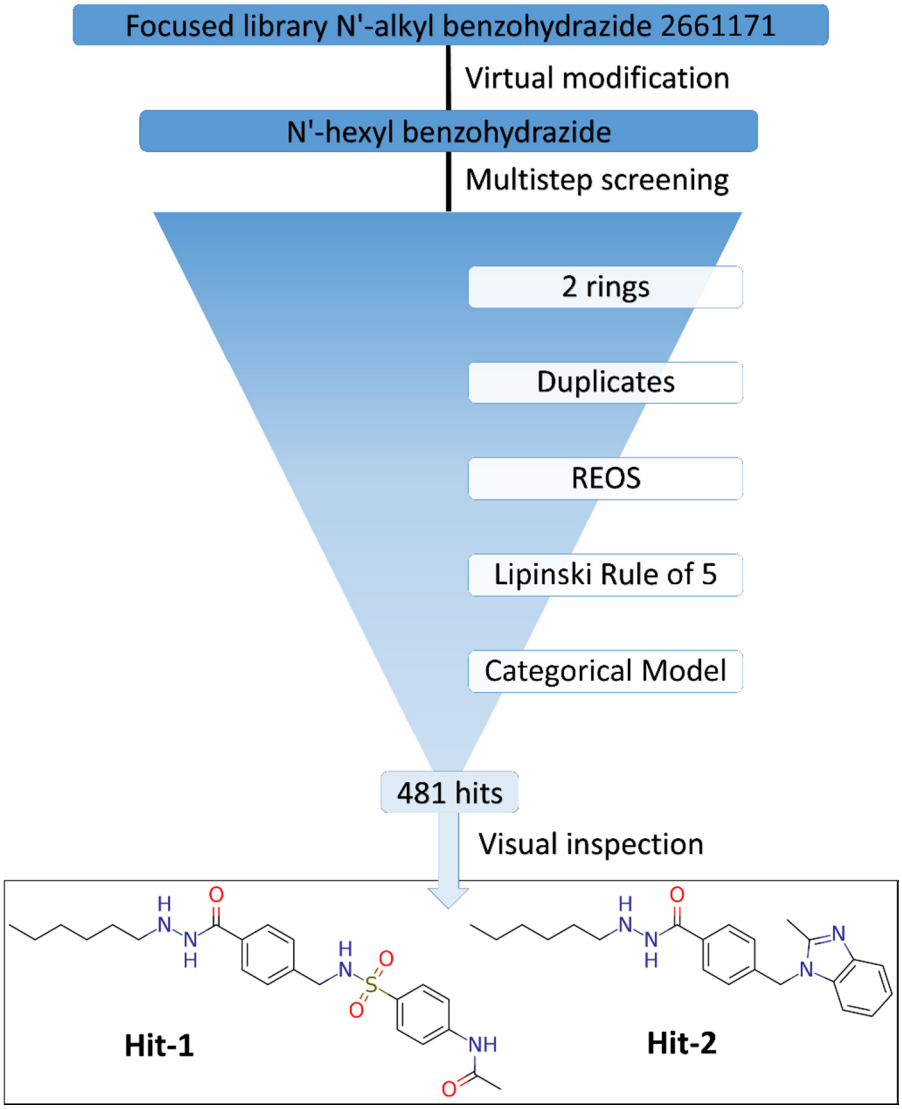

Figure 8. Schematic representation of the virtual screening workflow.

REOS filter [158, 162, 165] is a structural filter that includes 117 SMARTS strings used to define certain substructures collected from literature. It can eliminate compounds bearing certain functional groups that are associated with nondrug-like molecules or possess known toxicity. This filter can also remove compounds with known reactive groups that can induce nonspecific binding and multi-target interactions, thus interfering with the biological assays. [162, 165].

The Lipinski rule of five is a widely used molecular filter for identifying bioavailable drug-like candidates. For a compound to pass the rule of five, it must possess the following properties: molecular weight <500 Da, logP <5, H-bond donors <5, and H-bond acceptors <10 [166, 167]. The rule of five was developed based on data analysis of a set of 2245 compounds from the World Drug Index. This analysis could identify molecular properties that are probably

associated with orally available drugs [162, 166]. Screening of the designed library using the aforementioned filters resulted in 1684 hits.

4.2.2.2. Developing and utilizing the categorical classification model

4.2.2.2.1. Model development

The categorical model was built using Bayes classification model, which is a probabilistic classification based on Bayes' theorem [168], and using radial fingerprints as descriptors. Radial fingerprints [169, 170], also known as extended connectivity fingerprints (ECFPs) [171, 172], are a class of topological 2D fingerprints that was developed specifically for structure-activity modeling [172]. These fingerprints are generated by growing fragments radially from each heavy atom. Each unique fragment is then transformed to a distinct integer through hashing the description of the fragment's bonds and atoms as well as the bonds connecting it to the surrounding substructures [170, 172]. The model was developed using 80 alkyl hydrazide HDAC11 inhibitors from an in-house dataset that were assigned either active or inactive classes (**Figure 9**) as discussed in the **Materials and methods** section.

For classification models, several metrics are used to assess the performance of the developed model [173, 174]. Accuracy provides an overall assessment of the performance of the model by calculating the percentage of all correctly classified compounds. A confusion matrix (**Table 1**), which provides a representation of the model predictions in comparison to the assigned true labels, then can be used to give a more detailed insight regarding the categorical model performance [173]. Sensitivity is the ability of the model to predict the active compounds or positive instances correctly and is expressed as the ratio of true-positive results to the total number of positive data. Specificity can be defined as the ability of the model to predict the inactive compounds or negative instances correctly and represented by the ratio of true-negative results to the total number of negative instances [173, 174]. The developed model showed excellent performance with accuracy, specificity and sensitivity exceeding 90%.

Table 1. Confusion matrix of the developed categorical model.

Categorical model					
Activity	**Correct**	**Incorrect**	**Total**		
0	45	3	48	**specificity**	**93.75**
1	31	1	32	**sensitivity**	**96.88**
Total	76	4	80	**accuracy**	**95.00**

4.2.2.2.2. Model validation

In order to validate the initially obtained Bayes classification model, the compounds were classified according to their scaffolds based on the linker type and the point of attachment to the phenyl ring of the benzohydrazide moiety. The dataset was classified into eight subsets (**Figure 9**), including amide, amine and methoxy linkers attached to the meta position of the hydrazide group, and amine, amide, phenyl and piperazine linkers attached to the para position of the hydrazide group, as well as small compounds containing no linker. To ensure homogenous distribution of the chemical scaffold and activity class when selecting the training and test sets for validation, the compounds in the dataset were arranged according to their scaffold subset. Furthermore, within each subset, compounds were arranged according to their activity class. Selection of the training and test sets was then performed as discussed in **Materials and methods section** and resulted in four different training and their corresponding test sets.

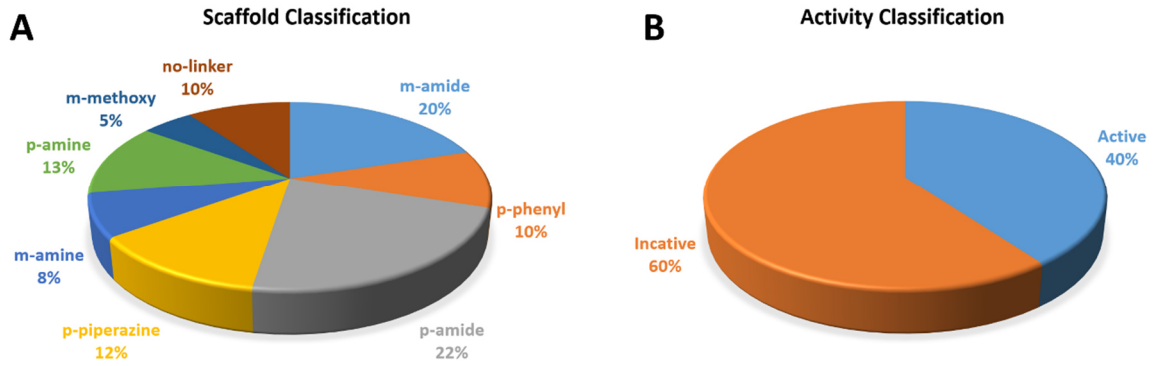

Figure 9. Classification of the in-house HDAC11 inhibitors dataset. (**A**). Classification according to scaffold. (**B**). Classification according to activity.

The external validation of the categorical model, using the four different training and test sets, demonstrated a robust performance (**Table S5**). The overall accuracy was between 80% and 85% for the four test sets, while the specificity ranged between 85% and 92%. Although the model showed a lower sensitivity range of 71% to 80%, this might not be considered problematic when screening large datasets to identify active compounds.

4.2.2.2.3. Model application

Before utilizing the categorical model to classify the designed and filtered library and to ensure that the predictions are reliable, applicability domain for the model was calculated and applied. One way of determining the applicability domain is based on the chemical

similarity/dissimilarity identified by similarity distances [175, 176]. For example, a large similarity distance indicates that a test compound is more dissimilar than can lie within the applicability domain of the training set. For this reason, Euclidian distances [175-177] were calculated using the same descriptor used to develop the model, the radial fingerprints. Distance threshold/applicability domain then was calculated and applied as discussed in the **Materials and methods section**. 1620 compounds were found to lie within the applicability domain of the developed model. The general categorical model was then applied to predict the class of these compounds. 481 compounds were predicted to be active.

Upon visual inspection of the 481 hits, two ligands were considered to be of particular interest when searching for active and selective HDAC11 inhibitors. These hits are bearing some similarity to hydroxamic acid analogues that were previously reported to exhibit selectivity towards HDAC6 over other HDACs [178-182]. X-ray crystal structures of two of these hydroxamic acid compounds were reported, namely, PDB: 7UK2 [182] and 6ZW1 [181] (**Figure 10**). Considering the absence of the foot pocket in class IIb HDACs and their inability to accommodate such alkyl chain attached to the zinc binding group, it is proposed that the replacement of the hydroxamic acid function by hexyl hydrazide will demolish the inhibitory activity towards HDAC6. This change might then provide a chance to develop inhibitors with absolute selectivity towards HDAC11.

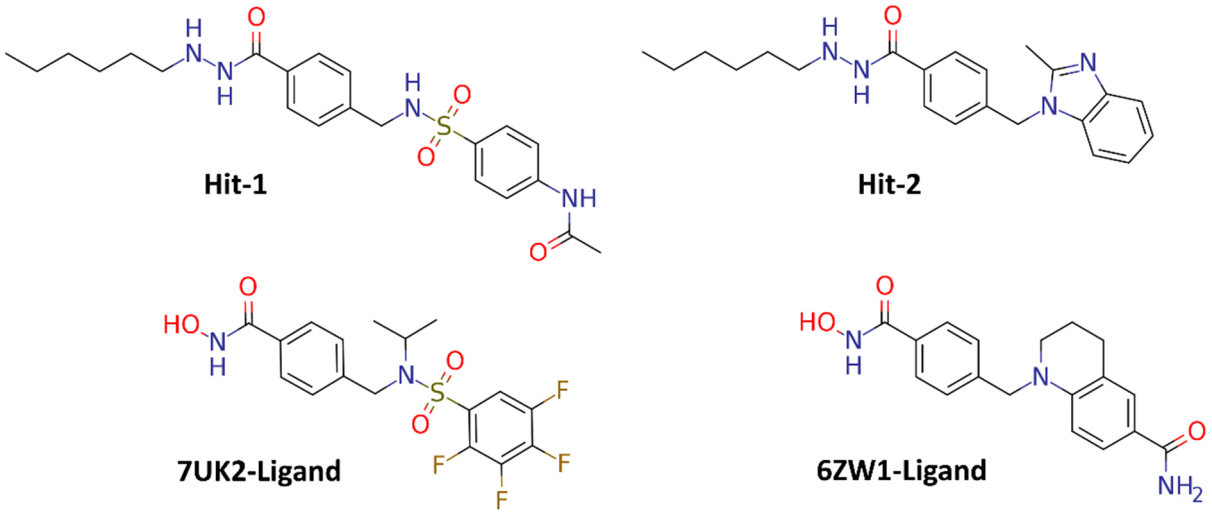

Figure 10. 2D structures of the virtual screening hits of interest and their hydroxamic acid analogues.

Interestingly, the docking poses of the selected hits in HDAC11-AF2 demonstrated an orientation similar to their co-crystallized hydroxamic acid analogues in HDAC6 (**Figures 11A and 11B**).

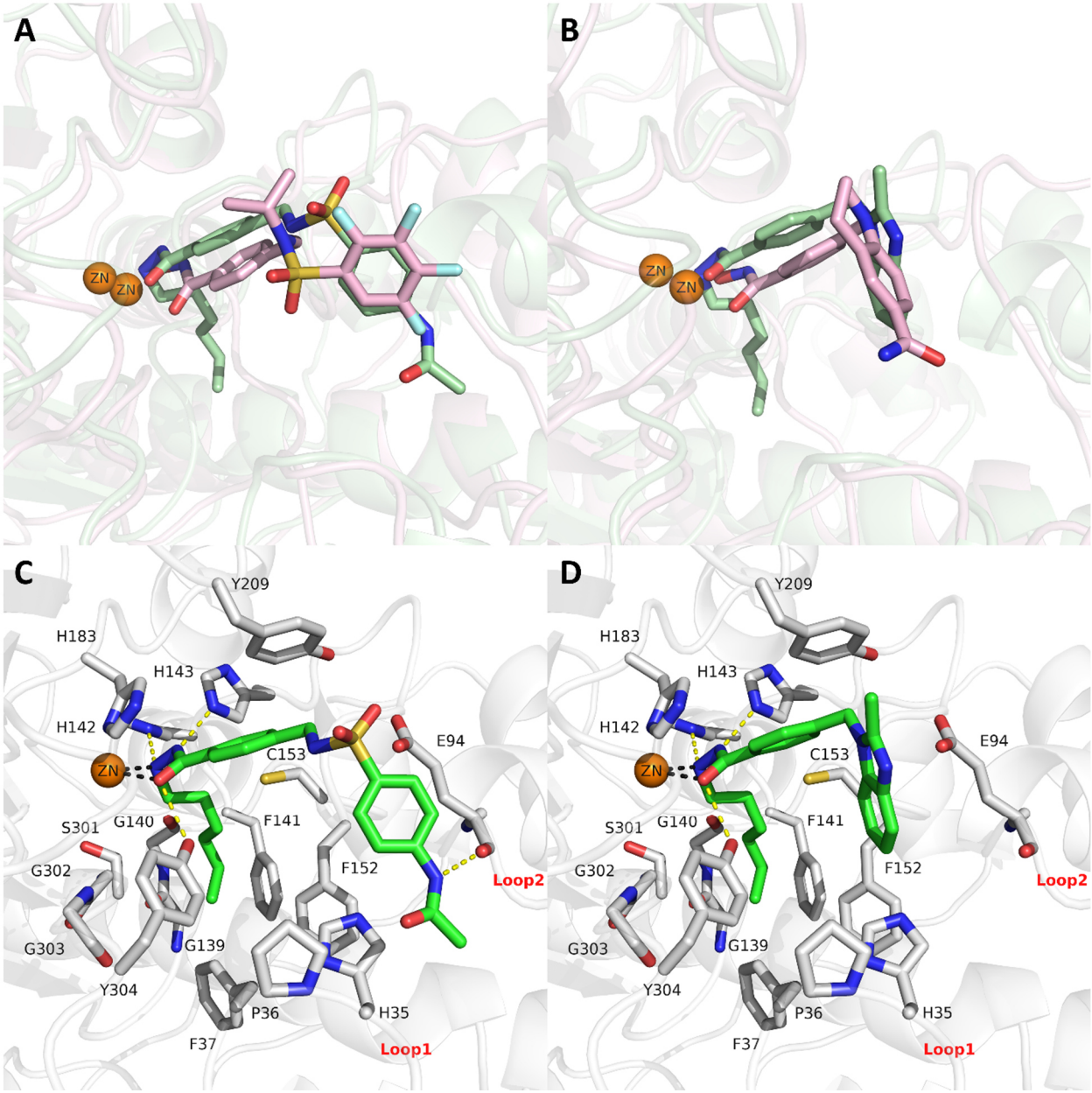

Figure 11. (**A**) and (**B**). Superposition of the docking poses of the first and second virtual screening hits in HDAC11 (pale green) with similar hydroxamic acid analogues from HDAC6 crystal structures (light pink) PDB: 7UK2 and 6ZW1, respectively. (**C**) and (**D**). The docking poses of the first and second virtual screening hits, respectively, in HDAC11. The protein backbone appears as white cartoon, interacting residues of the binding site as grey sticks, zinc cofactor as orange sphere and ligands as green sticks. Hydrogen bonds are represented as yellow dashed lines and coordination bonds as grey dashed lines.

The alkyl hydrazide moiety showed the common zinc binding group interactions. It could chelate the zinc ion in a bidentate fashion and formed hydrogen bonds with His142, His143 and Tyr304 (**Figures 11C and 11D**). The alkyl chain occupied the foot pocket and formed hydrophobic interactions with Phe37, Phe141, Phe152 and Cys153. The capping groups adopted a bent conformation directed towards loop 1 and loop 2 and formed hydrophobic

interactions with Pro36. For **hit-1**, additional hydrogen bond was observed between the NH of the terminal amide group and the backbone oxygen of Glu94.

The predicted binding modes of the virtual screening hits of interest were then evaluated by MD simulation. For both hits, the RMSD plots of the protein backbone show that the protein is stabilizing slightly above 1 Å, while the zinc ion is stabilizing below 1 Å (**Figures S25 and S27**). The ligand RMSD plots of **hit-1** (**Figure 12A**) demonstrate a shift in the pattern during the simulation that is stabilizing at around 3 Å. From the RMSF plots (**Figure 12B**), it is clear that the capping group is the most fluctuating part. To further investigate this fluctuation, the MD trajectories were analyzed. The analysis revealed that the sulfonamide group adopts an opposite conformation during the simulation compared to the starting docking pose (**Figure S26**).

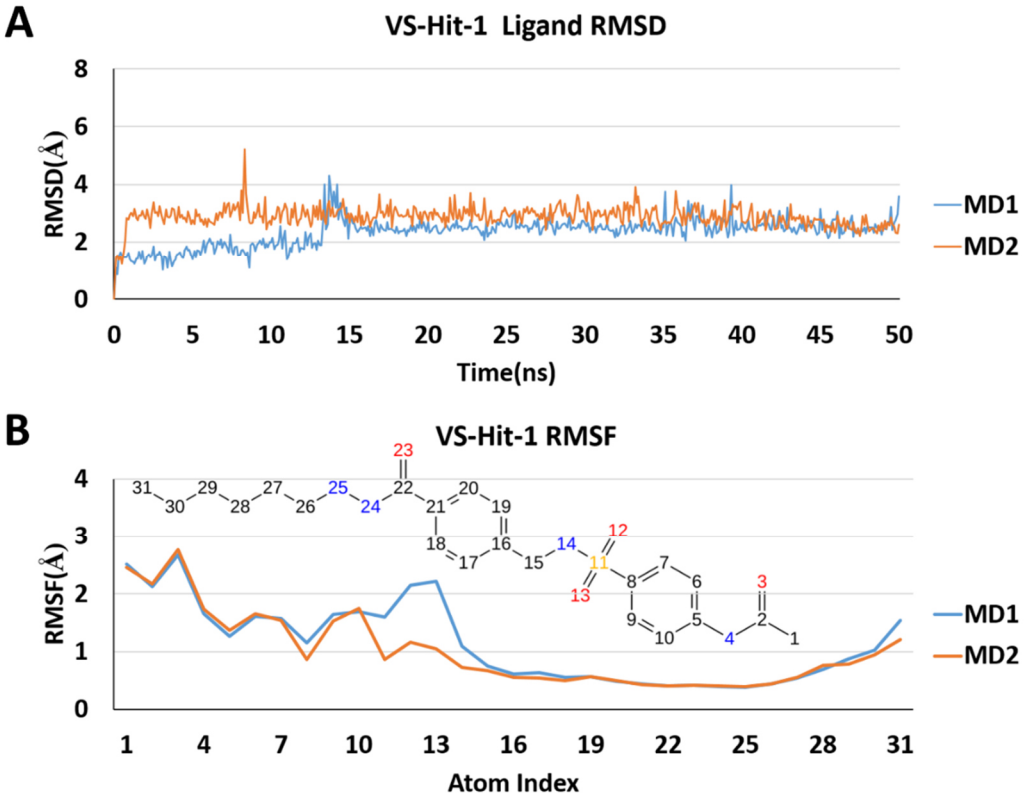

Figure 12. (**A**) and (**B**). RMSD and RMSF plots, respectively, of ligand heavy atoms of **hit-1** for two 50 ns independent MD simulations.

The new conformation brings the oxygen atoms of the sulfonamide group closer to loop 1, thus making them available for hydrogen bond formation with His35 and the fluctuating catalytic Tyr304. During the simulation, an additional hydrogen bond was also formed between the NH of the sulfonamide linker and Glu94 either directly or through a water bridge, while the

hydrogen bond between the NH of the terminal amide group and the carbonyl oxygen of Glu94 backbone was almost completely lost. The hydrogen bond stability between the ligand and the binding site interacting residues was monitored (**Table S3, Figures S29 and S31**) and demonstrated very high stability for His142 and His143 with persistence ranging between 97% and 100%. The catalytic Tyr304 fluctuation led to complete loss of the hydrogen bond with the carbonyl oxygen of the hydrazide moiety and the formation of another hydrogen bond with one of the sulfonamide oxygen atoms as discussed above. This hydrogen bond showed intermediate to high stability with persistence percent of 55% and 94% for two replicas. The stability of the newly formed hydrogen bonds with His35 and Glu94 was intermediate and ranged between 39% and 51%.

Hit-2 exhibited high stability during the course of the MD simulation which is indicated by an RMSD below 2 Å and RMSF slightly above 1 Å for the ligand heavy atoms (**Figures 13 and S28**). The interaction persistence demonstrated a similar behavior as for **hit-1** demonstrating very high stability of the hydrogen bond interactions with His142 and His143 with persistence ranging between 98% and 100%. However, for Tyr304, the hydrogen bond is completely lost (**Table S4**, **Figures 30 and S32**).

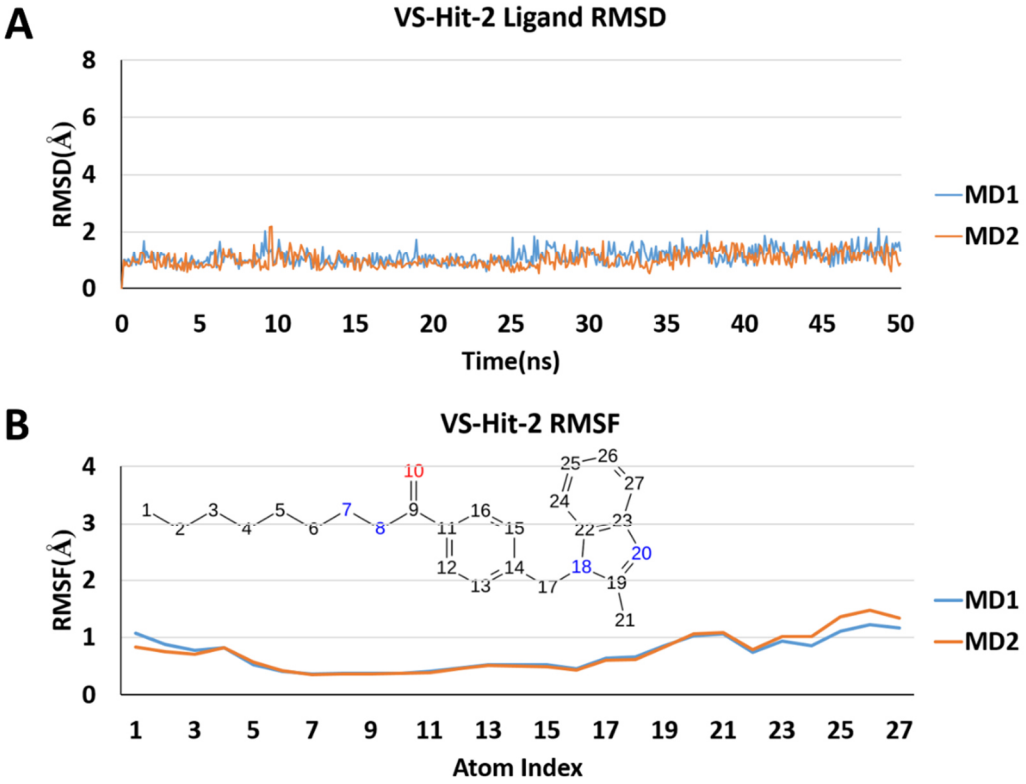

Figure 13. (**A**) and (**B**). RMSD and RMSF plots, respectively, of ligand heavy atoms of **hit-2** for two 50 ns independent MD simulations.

Considering the given results, it is important to note that the hydroxamic acid analogues also showed selectivity towards HDAC6 over HDAC11 [180, 181]. However, the selectivity profile of the hydroxamic acid analogues of **hit-1** showed variation with the alkylation pattern of the NH of the sulfonamide and the decoration of the terminal phenyl ring [178, 179]. Taking this into account and as the alkyl hydrazide hits were predicted to be active towards HDAC11 by the classification model, experimental verification of the potential activity and selectivity of the identified hits remains to be of interest.

4.3. Materials and methods

Schrodinger Suite 2019 was used for all the modeling work. Maestro [183] was utilized for visualization.

4.3.1. Ligand preparation

Ligands were prepared utilizing LigPrep [184] panel without changing the ionization states or generating tautomers or isomers.

4.3.2. Receptor grid generation

The receptor grid was generated using the Receptor Grid Generation panel and utilizing the vertical pose of SIS17 in the optimized HDAC11-AF2 model [185] as the input protein-ligand complex. The centroid of the ligand was selected as the center of the grid box. All default settings were kept while docking of ligands with length <= 25 Å option was specified to account for difference in ligand size.

4.3.3. Docking

Ligands docking was performed using Glide [186-189] and utilizing OPLS3e force fields [190-193]. SIS17 was selected as core containing molecule for the restricted docking by using reference position. The core atoms were defined by maximum common substructure. The standard precision docking and flexible ligand sampling settings were employed. The top scored poses were selected for further analysis.

4.3.4. Molecular dynamics simulation

The selected docking poses were subjected to molecular dynamics simulation using Desmond [194, 195] and employing OPLS2005 force fields. Each pose was simulated for 50 ns and the simulation was repeated twice using different random seeds. Zero order bonds to the metal were created using the Protein Preparation Panel before submitting to system preparation. The system

was solvated in SPC water model using an orthorhombic box and 10 Å distance between the solute structures and the simulation box boundary. The system was neutralized by adding chloride ions that were placed 4 Å away from the ligand.

The prepared system was relaxed using the default Desmond relaxation protocol for NPT ensemble followed by a production run utilizing the NPT ensemble at the temperature of 300 K using a Nose–Hoover chain thermostat and pressure of 1.01325 bar using Martyna-Tobias-Klein barostat. The progress of the simulation was recorded every 100 ps.

For analysis, the Simulation Event Analysis panel was used for RMSD calculations. The RMSD of the protein was calculated using the backbone atoms. For calculating the RMSD of ligands and zinc ion, fitting to the protein backbone was performed. The Simulation Interaction Diagram panel was used for analyzing the RMSF and the interaction persistence of the ligands. RMSD of the protein was calculated excluding the termini (residues: 1–14 and 321–347).

4.3.5. Properties calculations

The rule of five property was calculated using QikProp [196] properties from the Molecular Descriptor panel.

4.3.6. Categorical classification model

4.3.6.1. Building the categorical model

The categorical model was built using the Bayes classification application in Canvas [170, 197, 198] and utilizing an in-house dataset of 80 alkyl hydrazide compounds bearing different scaffolds and alkyl chain length. The dataset was classified into active and inactive categories using an IC_{50} value of 0.5 μM as a threshold.

To build the model, radial fingerprints for the compounds were generated using Binary Fingerprints from Structures panel in Canvas and were used as descriptor.

4.3.6.2. Validating the categorical model

To validate the model, compounds in the dataset were arranged based on their scaffold (position and structure of the linker). Furthermore, compounds within each scaffold subset were arranged according to their class. The training and test sets were created by selecting every forth entry as test compound. This process was repeated four times starting from different entry each time (starting from entry 1 to entry 4) and resulted in four different training and their corresponding test sets.

4.3.6.3. Applicability domain calculation

Euclidian distances were calculated for the compounds using the Similarity/Distance Matrix from Fingerprints panel and employing the generated radial fingerprints. The average of all the distances was then calculated and distances below this average were used to calculate the distance average term **Av** and the standard deviation **σ** [199]. The applicability domain or distance threshold for the developed categorical model was then calculated using the following equation in which **Z** is an empirical parameter and the default value of 0.5 was used in this work [199, 200]:

$$\text{Applicability domain} = Z\sigma + Av$$

4.3.7. Virtual screening

4.3.7.1. Dataset acquisition

A focused library of N`-alkyl benzohydrazide ligands (substructure SMILES: CN([H])N([H])C(=O)c1ccccc1) was downloaded from the ZINC20-all database [161] using the Arthor tool in the TLDR interface (tldr.docking.org) [201].

4.3.7.2. Virtual modification

The structures in the obtained library were modified virtually by converting the various N`-alkyl substitutions of the hydrazide moiety in the SMILES file to N`-hexyl group.

4.3.7.3. Multistep screening

As a first step, the modified library was filtered to remove the duplicates using the Merge Duplicates panel, followed by the removal of fragment compounds with less than 2 rings using Ligand Filtering panel.

The output was then subjected to further screening by applying the rapid elimination of swill (REOS) using the Structure Filter in Canvas. This step aimed to remove compounds with reactive groups that may interfere with biological evaluation. Any structure that can show one or more violations for the rule of five was eliminated from the library by using Ligand Filtering panel and the calculated rule of five property. Furthermore, the categorical model was used to classify the filtered dataset to active and inactive compounds subsequent to an applicability domain filtration.

This page left intentionally blank.

5. Summary and conclusions

This page left intentionally blank.

5.1. Model optimization

The HDAC11 AlphaFold model was initially optimized by adding the catalytic zinc ion and adjusting the coordination distances to match what is observed in the reported crystal structures of histone deacetylases. The direct use of the resulted model for docking of FT895 showed not to be successful as the ligand was not placed properly into the binding site and could not show any of the well-characterized interactions of HDAC inhibitors. For this reason, the optimization of the binding site was considered necessary. The binding site was optimized by applying minimization in presence of ligands that were previously described as HDAC11 inhibitors.

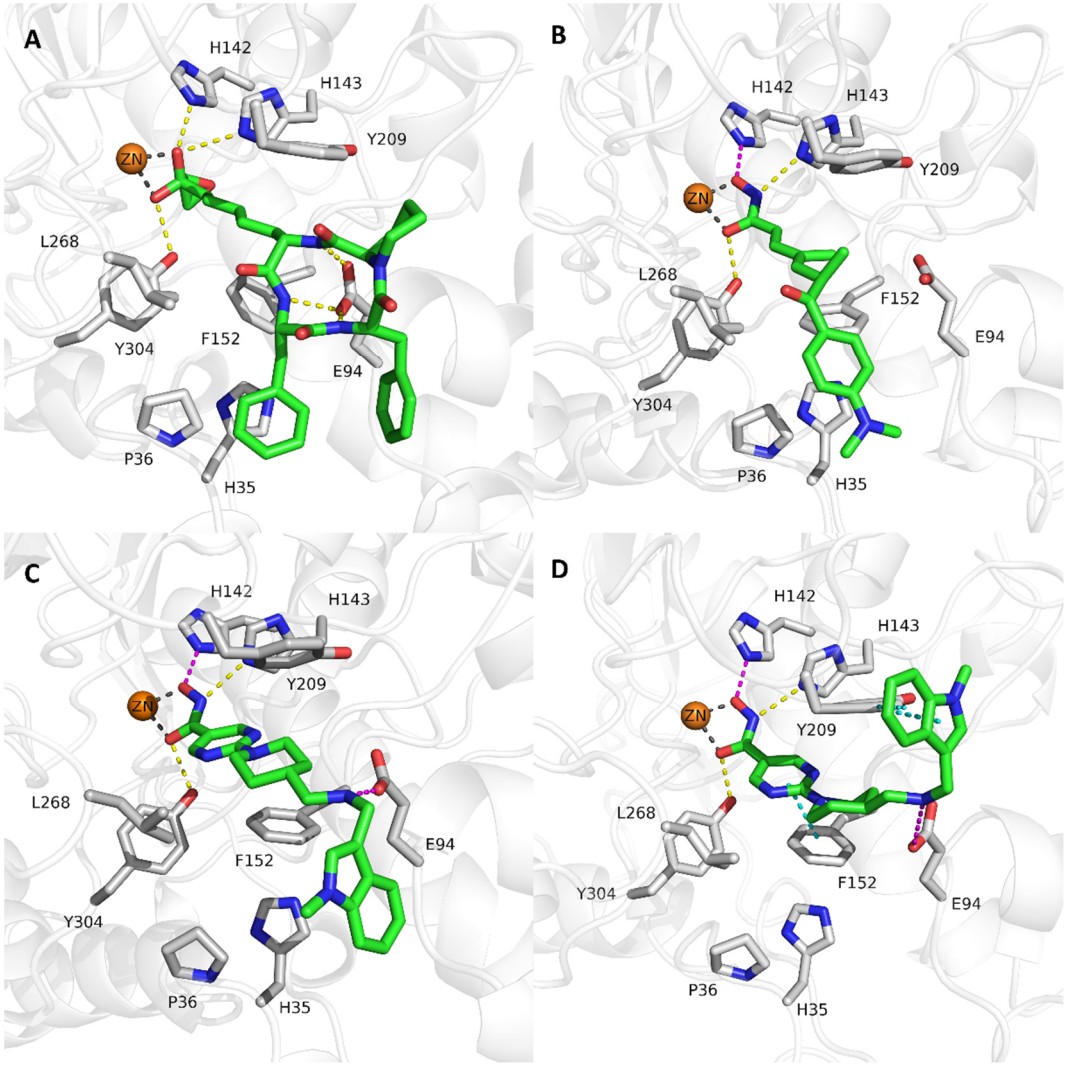

Figure 14. The four optimized ligand-HDAC11-AF2 complexes showing the poses of the ligands after merging and minimization. The protein backbone appears as white cartoon, interacting residues of the binding site as grey sticks, zinc cofactor as orange sphere and ligands as green sticks. Hydrogen bonds are represented as yellow dashed lines, salt bridges or ionic interactions as magenta dashed lines, π-π interactions as cyan dashed lines and coordination bonds as grey dashed lines. (**A**). Trapoxin A. (**B**). TSA. (**C**) and (**D**). Two different poses of quisinostat.

The merging of ligands was performed by copying the ligand's coordinates from HDAC8-ligand co-crystals after superposition with the HDAC11-AF2 model. The ligands used were trapoxin A, trichostatin A (TSA) and two different poses of quisinostat from two different HDAC8 crystal structures (**Figure 14**). Four HDAC11-ligand complexes were generated from this process and demonstrated the expected interactions that are well-characterized for HDAC inhibitors, mainly the bidentate chelation of the zinc ion and the salt bridge or hydrogen bonds with His142, His143 and Tyr304.

For the four complexes obtained after minimization, the stability of the binding mode in terms of hydrogen bond interactions and bidentate chelation, along with the stability of the protein, was confirmed by MD simulation. This reflects the feasibility of the adopted optimization protocol and affirms the usability of the obtained models for subsequent drug design studies.

5.2. Docking of known selective inhibitors

Several grids were generated using the models resulted from the optimization process. Docking of the hydroxamic acid selective inhibitor FT895 was performed in all the generated grids. The best-performing model in the docking was selected based on the docking score as well as the fulfillment of the necessary hydrogen bond interactions and bidentate chelation of the zinc ion. The selected model was then used to study the binding mode of another reported HDAC11 selective inhibitor bearing a bulky adamantine group, named MIR002 (**Figure 15**).

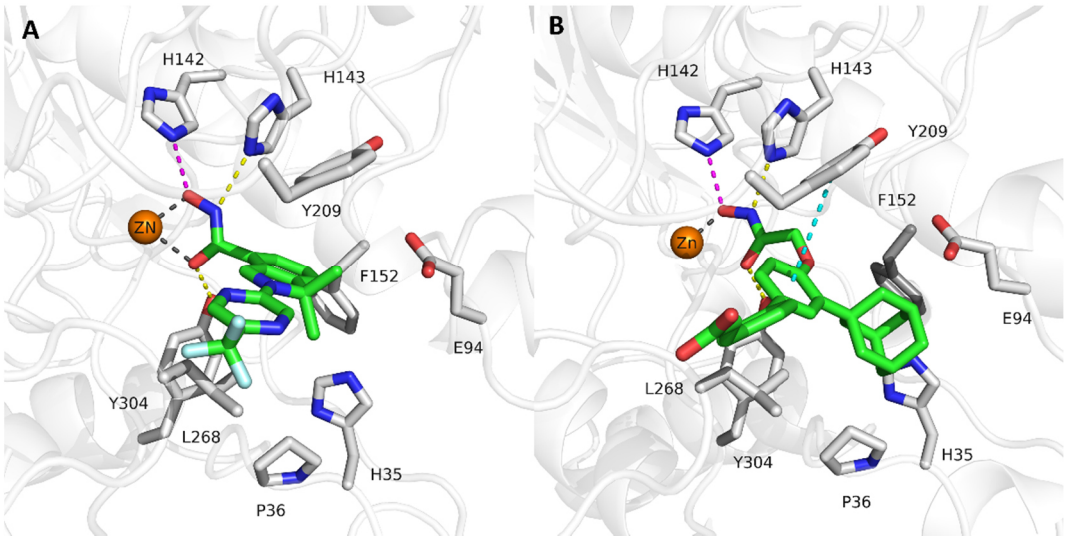

Figure 15. (**A**) and (**B**). Docking poses of FT895 and MIR002 in the optimized HDAC11-AF2 model. The protein backbone appears as white cartoon, interacting residues of the binding site as grey sticks, zinc cofactor as orange sphere and ligands as green sticks. Hydrogen bonds are represented as yellow dashed lines, salt bridges or ionic interactions as magenta dashed lines, π-π interactions as cyan dashed lines and coordination bonds as grey dashed lines.

The predicted binding modes of FT895 and MIR002 by docking were subjected to three short independent MD simulations (50 ns) as well as a single long MD run (500ns). The results from these MD simulations further confirmed the stability of the docking poses.

5.3. Exploring the foot pocket

As the defatty-acylase activity of HDAC11 was proved to be preferential over the deacetylation activity by multiple studies, docking of SIS17, a 16-carbon alkyl hydrazide selective HDAC11 inhibitor, was performed in order to investigate the foot pocket and to identify the tunnel that can accommodate such long alkyl chain. The direct docking of SIS17 in all the generated grids did not result in reasonable pose. In all poses, the long alkyl chain was positioned exposed to the solvent. For this reason, different approaches were utilized to dock SIS17. Loop 1 of the HDAC11-AF2 model demonstrated less confidence regarding its accuracy and position. This is defined by the predicted local distance difference test (pLDDT) and the predicted aligned error (PAE) scores. Therefore, the first approach adopted was to remodel loop 1 of the AF2 model to generate a knowledge-based model using HDAC6 crystal structure as a template. Remodeling loop 1 resulted in a space that could accommodate the alkyl chain. Direct docking of SIS17 in this model predicted a binding mode in which the long alkyl chain is accommodated between loop 1 and loop 7, while the necessary hydrogen bond interactions and zinc bidentate chelation were all observed. The second approach implemented a stepwise docking and minimization process utilizing two different grids generated from HDAC11-TSA optimized complex. The two grids differ in the orientation of the side chain of Phe152. The docking and minimization approach resulted in two different orientations of the alkyl chain based on the side chain conformation of Phe152. Docking in the flipped-in Phe152 grid directed the alkyl chain horizontally to be accommodated between loop 1 and loop 2. On the other hand, the flipped-out Phe152 blocked the entrance to this space, leading to a vertical pose in which the long alkyl chain is accommodated in a tunnel along loop 3 and loop 7 (**Figure 16**).

The MD simulation results for the predicted binding mode using the remodeled loop 1 were not satisfactory because the alkyl chain was not stable in its initial accommodating space. In contrast, the three short independent MD simulations (50 ns) of the vertical and horizontal poses proved the stability of the predicted poses, reflecting the probability of the long alkyl chain being conveniently accommodated within either of the identified tunnels. Based on a structural comparison with HDAC8 and since the defatty-acylase activity of HDAC8 was also previously reported, the vertical pose was selected as the most reasonable pose and its stability was further verified by a single long MD simulation (500 ns).

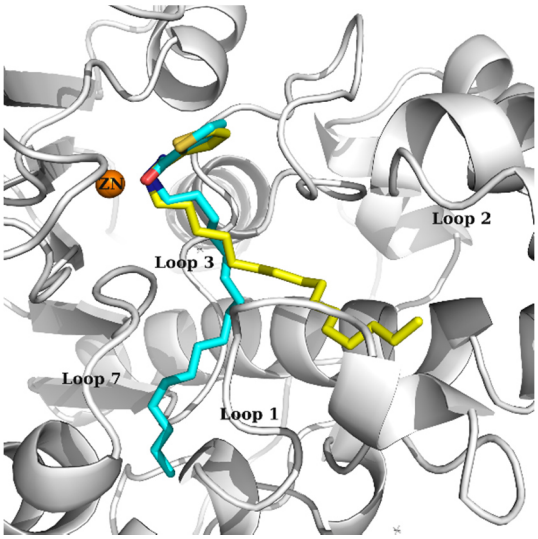

Figure 16. Docking poses of SIS17 in the optimized HDAC11-AF2 model showing the two different predicted orientations of the long alkyl chain. Protein backbone is represented as white cartoon and the zinc ion as orange sphere. SIS17 is represented as cyan-colored sticks for the vertical pose and yellow-colored sticks for the horizontal pose.

5.4. Utilization of the optimized model

5.4.1. Virtual screening

For virtual screening, a focused library of benzohydroxamic acid compounds was obtained from ZINC20 database. The library was initially prepared and filtered to obtain the ligands that do not violate the rule of five and in the hydroxamate form which demonstrated to perform better in molecular docking.

The optimized HDAC11-AF2 model was implemented in a comparative structure-based virtual screening workflow (**Figure 17**) to identify novel HDAC11 inhibitors while addressing subtype selectivity. As a first step, a structure-based pharmacophore employing the HDAC11-TSA optimized complex was used for preliminary filtration of the prepared and filtered compounds library. The aim of this step was to eliminate ligands that cannot fit into the binding site, as well as very small ligands and fragments, thus reducing the number of compounds for the subsequent more computationally demanding docking-based virtual screening. The hits from the pharmacophore screening were docked in HDAC11-AF2 model followed by pose filtration to select ligands that could adopt bidentate chelation mode of the catalytic zinc ion. To address isoform selectivity, a comparative approach was applied by docking the resulting hits from the last step into different HDAC isoform crystal structures. For this step, HDAC1, HDAC6 and HDAC8 were selected as representatives for class I and class II HDACs. Compounds that could demonstrate good poses in any of these isoforms were eliminated. Only the compounds that

could adopt good docking poses in HDAC11 model but not in any of the other HDAC isoforms were considered for further filtration. REOS filter was used to remove compounds with reactive or toxic groups that can interfere with biological assays followed by prioritization using MM-GBSA calculations.

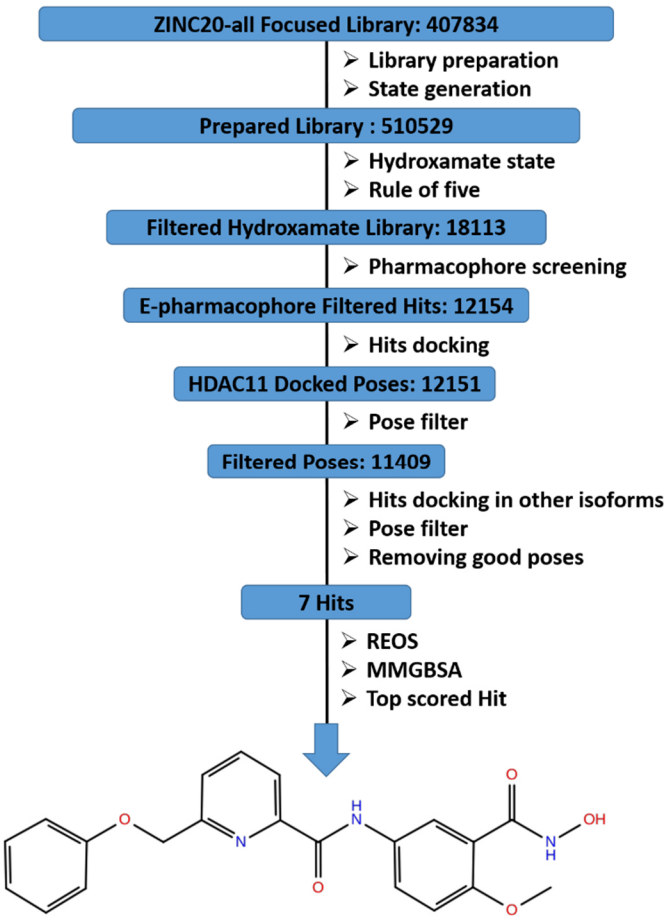

Figure 17. The workflow of the structure-based virtual screening.

The final resulted hits were all bearing a substituent in the ortho-position to the hydroxamate group. This observation might indicate that a substituent in this position can be accommodated in the binding pocket of HDAC11 but not in the other HDAC isoforms, suggesting such substitution pattern to be a selectivity determinant for HDAC11. The top-scored hit was evaluated for its inhibitory activity and demonstrated an IC_{50} of 3.5 µM for HDAC11. The hit compound was also screened against other HDAC isoforms (HDAC1-10) and was able to selectively inhibit HDAC11 at 10 µM concentration (**Figure 18A**).

Interestingly, these results are in agreement with the theoretical computational results. In contrast to HDAC1, HDAC6 and HDAC8, the hit compound from virtual screening could adopt

an ideal pose in HDAC11 by showing the bidentate chelation of the zinc ion and the expected interactions of an HDAC benzohydroxamate inhibitor (**Figure 18B**).

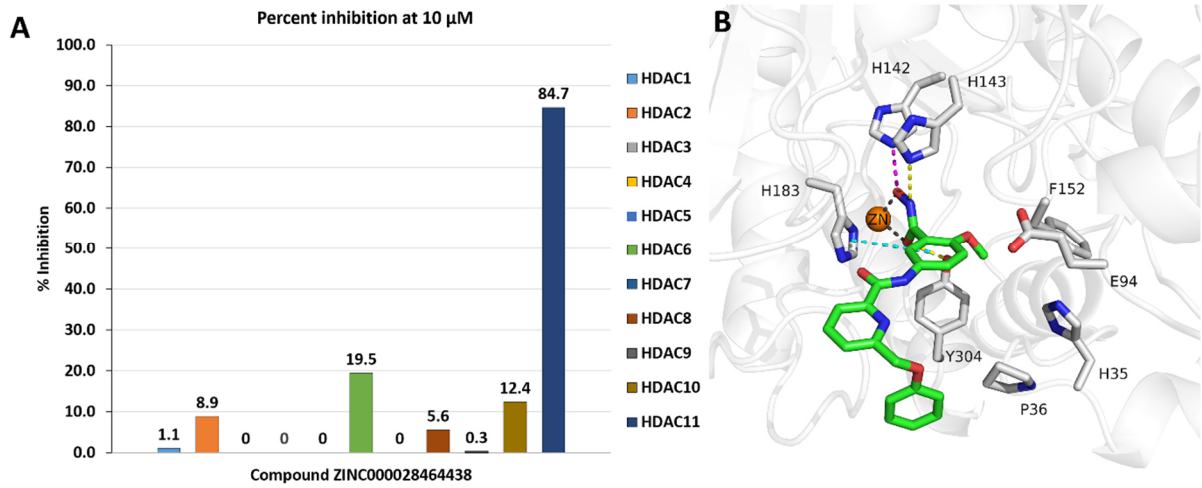

Figure 18. (**A**). Percent inhibition of the hit compound for all HDAC isoforms at 10 µM concentration. (**B**). Docking pose of the hit compound in the optimized HDAC11-AF2 model. The protein backbone appears as white cartoon, interacting residues of the binding site as grey sticks, zinc cofactor as orange sphere and ligand as green sticks. Hydrogen bonds are represented as yellow dashed lines, salt bridges or ionic interactions as magenta dashed lines, π-π interactions as cyan dashed lines and coordination bonds as grey dashed lines.

Furthermore, the predicted binding mode of the hit compound in HDAC11 was analyzed by multiple classical MD and metadynamics simulation studies. The results from these studies confirmed the binding mode in terms of the ligand and interactions stability.

5.4.2. Structure-based design

Moreover, the optimized HDAC11-AF2 model was utilized for the structure-based design of novel selective ligands employing the docking pose of the selective inhibitor FT895. In the design of the new probes, the linear shape of FT895 and the ortho substitution pattern were kept since these molecular features were defined as selectivity determinants for HDAC11.

The docking pose of FT895 in HDAC11 shows that the fused system of the ligand is sandwiched between the side chains of residues Tyr209 in loop 5 and Leu268 in loop 6. For the aim of increasing activity and maintaining selectivity, branched ligands were designed (**Figure 19A**). In the newly designed ligands, different groups are extended towards loop 1 to make interactions with loop 1 residues and further block the binding site from both sides. The most active compound **5a** exhibited an IC_{50} of 365 nM and showed almost no or very weak inhibition for other HDAC subtypes at 10 µM concentration (**Figure 19B**). Moreover, compound **5a** was

evaluated for anti-neuroblastoma activity using BE(2)-C neuroblastoma cell line and demonstrated promising activity with an EC_{50} of 3.6 µM.

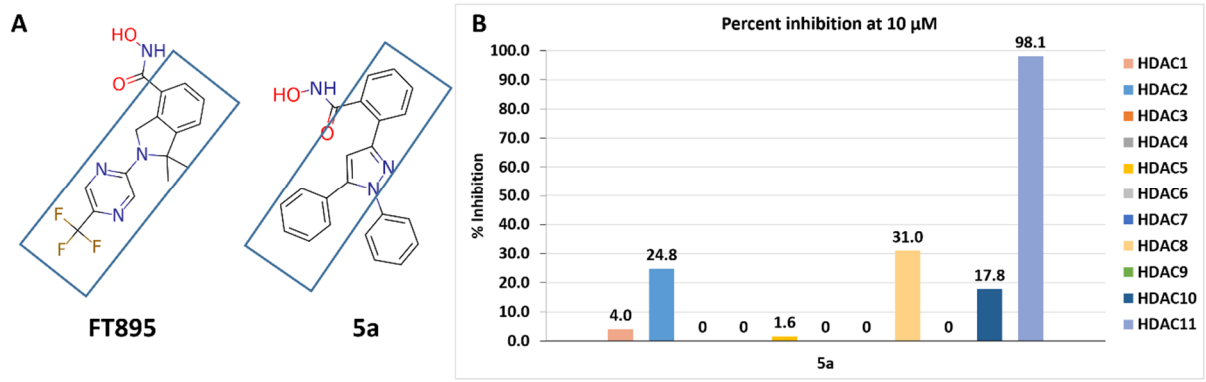

Figure 19. (**A**). Schematic representation of the strategy employed to design compound **5a** based on the ligand FT895. (**B**). Percent inhibition of compound **5a** for all HDAC isoforms at 10 µM concentration.

The docking pose of compound **5a** in the optimized HDAC11-AF2 model predicted a binding mode that is comparable to that of FT895 (**Figure 20**), in which one terminal phenyl ring is sandwiched between the side chains of Tyr209 of loop 5 and Leu268 of loop 6. The benzohydroxamic acid is accommodated deeper into the binding pocket compared to FT895, while the other terminal phenyl ring is directed to loop 1 and forms hydrophobic interactions with Pro36.

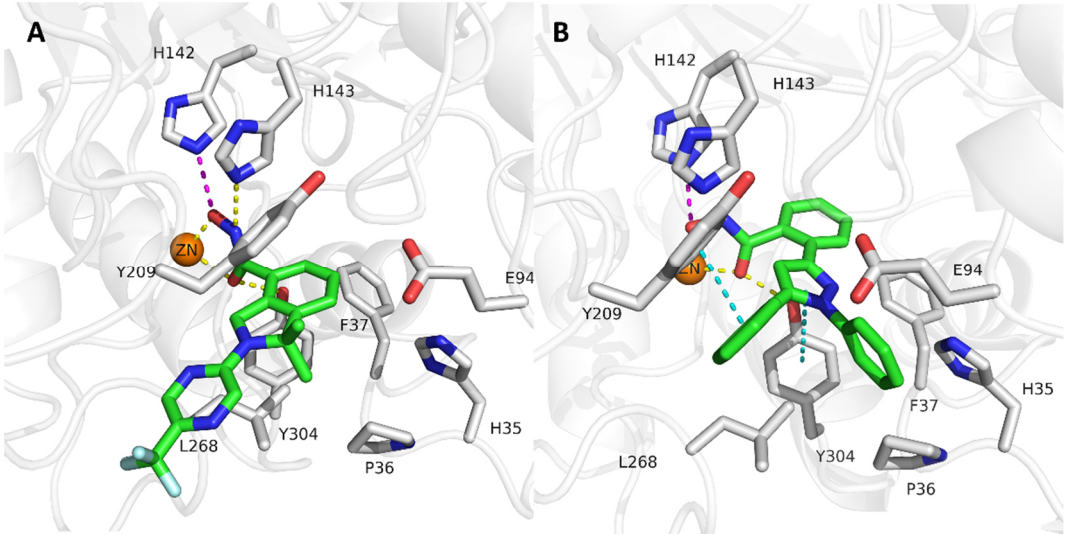

Figure 20. (**A**) and (**B**). Docking poses of FT895 and **5a**, respectively, in the optimized HDAC11-AF2 model. The protein backbone appears as white cartoon, interacting residues of the binding site as grey sticks, zinc cofactor as orange sphere and ligands as green sticks. Hydrogen bonds and coordination bonds are represented as yellow dashed lines, salt bridges or ionic interactions as magenta dashed lines and π-π interactions as cyan dashed lines.

MD simulation studies using three independent short (50 ns) and long (500 ns) runs verified the predicted binding mode and proved the stability of the ligand in terms of RMSF, RMSD and interaction persistence.

5.5. Modeling of alkyl hydrazides

In the last part of this work, the optimized model was utilized to study the binding mode of one of the most active alkyl hydrazide inhibitors from the in-house library. The predicted binding mode was further validated by MD simulation.

In order to identify new HDAC11 inhibitors bearing alkyl hydrazide moiety as a ZBG, a ligand-based multistep virtual screening workflow was devised and executed. In this workflow, a focused library of N`-alkyl benzohydrazide compounds obtained from ZINC20 database was virtually modified by replacing the different N`-alkyl substituents with N`-hexyl group. This modification was performed because it was noted that 6-carbon alkyl substitution is optimal for HDAC11 activity and selectivity.

The workflow then employed various filtration steps to remove duplicates and to discard very small compounds and fragments generated during the virtual modification. In order to identify drug-like molecules, filters like the Lipinski rule of five and REOS were further applied. Furthermore, a classification categorical model, developed utilizing 80 alkyl hydrazide inhibitors from the in-house library, was used to classify the obtained hits from the last filtration step with the aim of identifying potentially active ligands lying within the in-house chemistry toolbox.

Applying this workflow resulted in identifying 481 compounds that were further inspected visually. Two compounds were identified as hits of interest and were prioritized for further development based on the visual inspection. The interest in these two hits comes from the fact that they demonstrate some structural similarity with hydroxamic acid analogues previously reported as HDAC6 selective inhibitors. Since HDAC6 lacks the foot pocket that can accommodate the alkyl chain of alkyl hydrazide inhibitors, it is proposed that the replacement of the hydroxamic acid ZBG with alkyl hydrazide, as observed in the identified hits, might lead to selectivity towards HDAC11.

The binding modes of these two hits in HDAC11 were studied by docking. Interestingly the docking poses show similar orientation to that reported before for the hydroxamic acid analogues co-crystallized with HDAC6. The binding modes of the identified hits of interest

were studied with MD simulation. Results demonstrated that the sulfonamide linker of **hit-1** can shift its position to form additional hydrogen bonds with His35, Glu94 and Tyr304, while for **hit-2**, very high stability of the ligand was proved as given by the RMSD and RMSF plots of the ligand heavy atoms.

5.6. General conclusion and outlook

The main aim of this work is the molecular modeling, design and development of novel selective HDAC11 inhibitors. For this purpose and since there is no X-ray crystal structure reported for HDAC11 so far, the development of a suitable 3D model of HDAC11 using previously reported inhibitors and assessing its usability for drug design studies is necessary. The results from this work suggest that the models as output from the AI AlphaFold approach are usable for SBDD. However, optimization or post-modeling refinement prior to its utilization is mandatory. When interpreting the results from this work, some limitations have to be taken into consideration. One general limitation when working with homology models is the absence of water molecules which might affect the results from the docking studies as well as the stability of the ligand and its interactions during the MD simulation.

The accuracy of the homology model holds significant importance and is crucial for the reliability of the results from drug design studies. The HDAC11-AF2 model shows high confidence scores except for loop 1. Lower confidence in the accuracy of the folding prediction and the whole loop position is indicated by the pLDDT and PAE scores. Such low confidence may indicate for error in the prediction that affects the output results when using the model, thus verification through experimental 3D structure determination is of great importance and is still required.

Similarly, docking of SIS17 resulted in two potential poses and the MD simulation studies proved the stability of both poses. This process identified two possible tunnels as structural features of HDAC11 that can accommodate such long alkyl chain. While the vertical pose was selected as the more reasonable pose based on structural comparison with HDAC8, experimental validation of this result via 3D structure determination of SIS17-HDAC11 complex is necessary.

One approach to emphasize the usability of the optimized HDAC11-AF2 model involves using it for the design and development of novel inhibitors followed by experimental in vitro enzymatic evaluation. For this purpose, two different strategies were employed in this work. The first was to employ the model in a multistep structure-based virtual screening workflow to

identify a novel selective hit. While this workflow was successful in identifying a ligand that could selectively inhibit HDAC11 at 10 μM concentration, the hit ligand demonstrated only moderate inhibition for HDAC11 with IC_{50} of 3.5 μM. These results can be interpreted in the context of the capabilities of virtual screening and what it can provide in terms of lead identification by searching large chemical space. However, lead optimization of the identified hit to maximize the inhibitory activity and keep the selectivity is still of interest.

The second utilized strategy was the structure-based design of novel probes based on the docking pose of the well-characterized selective inhibitor FT895 in HDAC11. Considering the results of the most active compound **5a**, chemical optimization and development of a series of ligands bearing similar scaffold to maximize the activity and enhance selectivity is of interest. This is also important to establish a structure-activity relationship. Given the promising anti-neuroblastoma activity of compound **5a**, more investigation of the role of HDAC11 and the use of its inhibitors to combat neuroblastoma is still required.

Overall, the experimentally verified selectivity of the lead compounds from the structure-based virtual screening and the structure-based design approaches supports the usability of the adjusted HDAC11-AF2 model and validates the optimization process adopted in this work.

In the last part of this work, the ligand-based virtual screening workflow, which employed a categorical classification model, identified 481 alky hydrazide hits. Two hits were selected as potential active and selective HDAC11 inhibitors. Experimental verification through the development and in vitro enzymatic evaluation of the hits of interest is yet to be considered.

6. References

(1) Korda, Z.; Pishva, E.; van den Hove, D. L. A. Epigenetics in Drug Discovery: Achievements and Challenges. In *Modern CNS Drug Discovery : Reinventing the Treatment of Psychiatric and Neurological Disorders*, Schreiber, R. Ed.; Springer International Publishing, 2021; pp 57-75.

(2) Weber, W. W. 1.04 - Epigenetics. In *Comprehensive Medicinal Chemistry II*, Taylor, J. B., Triggle, D. J. Eds.; Elsevier, 2007; pp 251-278.

(3) Altucci, L. Epigenetics: Moving Forward. In *Epigenetic Drug Discovery*, Sippl, W., Jung, M. Eds.; Methods and Principles in Medicinal Chemistry, Wiley-VCH, 2019; pp 1-9.

(4) Li, Y. Modern epigenetics methods in biological research. *Methods* **2021**, *187*, 104-113. DOI: https://doi.org/10.1016/j.ymeth.2020.06.022

(5) Portela, A.; Esteller, M. Epigenetic modifications and human disease. *Nature Biotechnology* **2010**, *28* (10), 1057-1068. DOI: 10.1038/nbt.1685

(6) Peixoto, P.; Cartron, P. F.; Serandour, A. A.; Hervouet, E. From 1957 to Nowadays: A Brief History of Epigenetics. *International Journal of Molecular Sciences* **2020**, *21* (20), 7571. DOI: 10.3390/ijms21207571

(7) Marek, M.; Shaik, T. B.; Romier, C. Structural Biology of Epigenetic Targets: Exploiting Complexity. In *Epigenetic Drug Discovery*, Sippl, W., Jung, M. Eds.; Methods and Principles in Medicinal Chemistry, Wiley-VCH, 2019; pp 11-44.

(8) Schübeler, D. Function and information content of DNA methylation. *Nature* **2015**, *517* (7534), 321-326. DOI: 10.1038/nature14192

(9) Moore, L. D.; Le, T.; Fan, G. DNA Methylation and Its Basic Function. *Neuropsychopharmacology* **2013**, *38* (1), 23-38. DOI: 10.1038/npp.2012.112

(10) Holdgate, G. A.; Bardelle, C.; Lanne, A.; Read, J.; O'Donovan, D. H.; Smith, J. M.; Selmi, N.; Sheppard, R. Drug discovery for epigenetics targets. *Drug Discov Today* **2022**, *27* (4), 1088-1098. DOI: 10.1016/j.drudis.2021.10.020

(11) McGinty, R. K.; Tan, S. Nucleosome Structure and Function. *Chemical Reviews* **2015**, *115* (6), 2255-2273. DOI: 10.1021/cr500373h

(12) Lorch, Y.; Kornberg, R. D.; Maier-Davis, B. Role of the histone tails in histone octamer transfer. *Nucleic Acids Research* **2023**, *51* (8), 3671-3678. DOI: 10.1093/nar/gkad079

(13) Arya, G.; Schlick, T. A tale of tails: how histone tails mediate chromatin compaction in different salt and linker histone environments. *The Journal of Physical Chemistry A* **2009**, *113* (16), 4045-4059. DOI: 10.1021/jp810375d

(14) Sahu, R. K.; Singh, S.; Tomar, R. S. The mechanisms of action of chromatin remodelers and implications in development and disease. *Biochemical Pharmacology* **2020**, *180*, 114200. DOI: https://doi.org/10.1016/j.bcp.2020.114200

(15) Bannister, A. J.; Kouzarides, T. Regulation of chromatin by histone modifications. *Cell Research* **2011**, *21* (3), 381-395. DOI: 10.1038/cr.2011.22

(16) Ramazi, S.; Allahverdi, A.; Zahiri, J. Evaluation of post-translational modifications in histone proteins: A review on histone modification defects in developmental and neurological disorders. *Journal of Biosciences* **2020**, *45* (1), 135. DOI: 10.1007/s12038-020-00099-2

(17) Biswas, S.; Rao, C. M. Epigenetic tools (The Writers, The Readers and The Erasers) and their implications in cancer therapy. *European Journal of Pharmacology* **2018**, *837*, 8-24. DOI: 10.1016/j.ejphar.2018.08.021

(18) Husmann, D.; Gozani, O. Histone lysine methyltransferases in biology and disease. *Nature Structural & Molecular Biology* **2019**, *26* (10), 880-889. DOI: 10.1038/s41594-019-0298-7

(19) Marmorstein, R.; Zhou, M. M. Writers and readers of histone acetylation: structure, mechanism, and inhibition. *Cold Spring Harbor Perspectives in Biology* **2014**, *6* (7), a018762. DOI: 10.1101/cshperspect.a018762

(20) Yun, M.; Wu, J.; Workman, J. L.; Li, B. Readers of histone modifications. *Cell Research* **2011**, *21* (4), 564-578. DOI: 10.1038/cr.2011.42

(21) Lu, R.; Wang, G. G. Tudor: a versatile family of histone methylation 'readers'. *Trends in Biochemical Sciences* **2013**, *38* (11), 546-555. DOI: 10.1016/j.tibs.2013.08.002

(22) Shi, Y.; Lan, F.; Matson, C.; Mulligan, P.; Whetstine, J. R.; Cole, P. A.; Casero, R. A.; Shi, Y. Histone demethylation mediated by the nuclear amine oxidase homolog LSD1. *Cell* **2004**, *119* (7), 941-953. DOI: 10.1016/j.cell.2004.12.012

(23) Anand, R.; Marmorstein, R. Structure and mechanism of lysine-specific demethylase enzymes. *Journal of Biological Chemistry* **2007**, *282* (49), 35425-35429. DOI: 10.1074/jbc.R700027200

(24) Lombardi, P. M.; Cole, K. E.; Dowling, D. P.; Christianson, D. W. Structure, mechanism, and inhibition of histone deacetylases and related metalloenzymes. *Current Opinion in Structural Biology* **2011**, *21* (6), 735-743. DOI: 10.1016/j.sbi.2011.08.004

(25) Milazzo, G.; Mercatelli, D.; Di Muzio, G.; Triboli, L.; De Rosa, P.; Perini, G.; Giorgi, F. M. Histone Deacetylases (HDACs): Evolution, Specificity, Role in Transcriptional Complexes, and Pharmacological Actionability. *Genes* **2020**, *11* (5), 556. DOI: 10.3390/genes11050556

(26) Schemies, J.; Uciechowska, U.; Sippl, W.; Jung, M. NAD+-dependent histone deacetylases (sirtuins) as novel therapeutic targets. *Medicinal Research Reviews* **2010**, *30* (6), 861-889. DOI: https://doi.org/10.1002/med.20178

(27) Park, S.-Y.; Kim, J.-S. A short guide to histone deacetylases including recent progress on class II enzymes. *Experimental & Molecular Medicine* **2020**, *52* (2), 204-212. DOI: 10.1038/s12276-020-0382-4

(28) Yang, X.-J.; Seto, E. Collaborative spirit of histone deacetylases in regulating chromatin structure and gene expression. *Current Opinion in Genetics & Development* **2003**, *13* (2), 143-153. DOI: https://doi.org/10.1016/S0959-437X(03)00015-7

(29) Turnbull, R. E.; Fairall, L.; Saleh, A.; Kelsall, E.; Morris, K. L.; Ragan, T. J.; Savva, C. G.; Chandru, A.; Millard, C. J.; Makarova, O. V.; Smith, C. J.; Roseman, A. M.; Fry, A. M.; Cowley, S. M.; Schwabe, J. W. R. The MiDAC histone deacetylase complex is essential for embryonic development and has a unique multivalent structure. *Nature Communications* **2020**, *11* (1), 3252. DOI: 10.1038/s41467-020-17078-8

(30) Guenther, M. G.; Barak, O.; Lazar, M. A. The SMRT and N-CoR corepressors are activating cofactors for histone deacetylase 3. *Molecular and Cellular Biology* **2001**, *21* (18), 6091-6101. DOI: 10.1128/mcb.21.18.6091-6101.2001

(31) Hu, E.; Chen, Z.; Fredrickson, T.; Zhu, Y.; Kirkpatrick, R.; Zhang, G. F.; Johanson, K.; Sung, C. M.; Liu, R.; Winkler, J. Cloning and characterization of a novel human class I histone deacetylase that functions as a transcription repressor. *Journal of Biological Chemistry* **2000**, *275* (20), 15254-15264. DOI: 10.1074/jbc.M908988199

(32) Aramsangtienchai, P.; Spiegelman, N. A.; He, B.; Miller, S. P.; Dai, L.; Zhao, Y.; Lin, H. HDAC8 Catalyzes the Hydrolysis of Long Chain Fatty Acyl Lysine. *ACS Chemical Biology* **2016**, *11* (10), 2685-2692. DOI: 10.1021/acschembio.6b00396

(33) Clocchiatti, A.; Florean, C.; Brancolini, C. Class IIa HDACs: from important roles in differentiation to possible implications in tumourigenesis. *Journal of Cellular and Molecular Medicine* **2011**, *15* (9), 1833-1846. DOI: 10.1111/j.1582-4934.2011.01321.x

(34) Jayathilaka, N.; Han, A.; Gaffney, K. J.; Dey, R.; Jarusiewicz, J. A.; Noridomi, K.; Philips, M. A.; Lei, X.; He, J.; Ye, J.; Gao, T.; Petasis, N. A.; Chen, L. Inhibition of the function of class IIa HDACs by blocking their interaction with MEF2. *Nucleic Acids Research* **2012**, *40* (12), 5378-5388. DOI: 10.1093/nar/gks189

(35) Davis, F. J.; Gupta, M.; Camoretti-Mercado, B.; Schwartz, R. J.; Gupta, M. P. Calcium/Calmodulin-dependent Protein Kinase Activates Serum Response Factor Transcription Activity by Its Dissociation from Histone Deacetylase, HDAC4: IMPLICATIONS IN CARDIAC MUSCLE GENE REGULATION DURING HYPERTROPHY*. *Journal of Biological Chemistry* **2003**, *278* (22), 20047-20058. DOI: https://doi.org/10.1074/jbc.M209998200

(36) Vega, R. B.; Matsuda, K.; Oh, J.; Barbosa, A. C.; Yang, X.; Meadows, E.; McAnally, J.; Pomajzl, C.; Shelton, J. M.; Richardson, J. A.; Karsenty, G.; Olson, E. N. Histone Deacetylase 4 Controls Chondrocyte Hypertrophy during Skeletogenesis. *Cell* **2004**, *119* (4), 555-566. DOI: https://doi.org/10.1016/j.cell.2004.10.024

(37) Jensen, E. D.; Schroeder, T. M.; Bailey, J.; Gopalakrishnan, R.; Westendorf, J. J. Histone Deacetylase 7 Associates With Runx2 and Represses Its Activity During Osteoblast Maturation in a Deacetylation-Independent Manner*. *Journal of Bone and Mineral Research* **2008**, *23* (3), 361-372. DOI: 10.1359/jbmr.071104

(38) Nishino, T. G.; Miyazaki, M.; Hoshino, H.; Miwa, Y.; Horinouchi, S.; Yoshida, M. 14-3-3 regulates the nuclear import of class IIa histone deacetylases. *Biochemical and Biophysical Research Communications* **2008**, *377* (3), 852-856. DOI: 10.1016/j.bbrc.2008.10.079

(39) Hsu, K.-C.; Liu, C.-Y.; Lin, T. E.; Hsieh, J.-H.; Sung, T.-Y.; Tseng, H.-J.; Yang, J.-M.; Huang, W.-J. Novel Class IIa-Selective Histone Deacetylase Inhibitors Discovered Using an in Silico Virtual Screening Approach. *Scientific Reports* **2017**, *7* (1), 3228. DOI: 10.1038/s41598-017-03417-1

(40) Fischle, W.; Dequiedt, F.; Hendzel, M. J.; Guenther, M. G.; Lazar, M. A.; Voelter, W.; Verdin, E. Enzymatic Activity Associated with Class II HDACs Is Dependent on a Multiprotein Complex Containing HDAC3 and SMRT/N-CoR. *Molecular Cell* **2002**, *9* (1), 45-57. DOI: https://doi.org/10.1016/S1097-2765(01)00429-4

(41) Zou, H.; Wu, Y.; Navre, M.; Sang, B.-C. Characterization of the two catalytic domains in histone deacetylase 6. *Biochemical and Biophysical Research Communications* **2006**, *341* (1), 45-50. DOI: https://doi.org/10.1016/j.bbrc.2005.12.144

(42) Hook, S. S.; Orian, A.; Cowley, S. M.; Eisenman, R. N. Histone deacetylase 6 binds polyubiquitin through its zinc finger (PAZ domain) and copurifies with deubiquitinating enzymes. *Proceedings of the National Academy of Sciences* **2002**, *99* (21), 13425-13430. DOI: 10.1073/pnas.172511699

(43) Tong, J. J.; Liu, J.; Bertos, N. R.; Yang, X. J. Identification of HDAC10, a novel class II human histone deacetylase containing a leucine-rich domain. *Nucleic Acids Research* **2002**, *30* (5), 1114-1123. DOI: 10.1093/nar/30.5.1114

(44) Haberland, M.; Montgomery, R. L.; Olson, E. N. The many roles of histone deacetylases in development and physiology: implications for disease and therapy. *Nature Reviews Genetics* **2009**, *10* (1), 32-42. DOI: 10.1038/nrg2485

(45) Zhang, X.; Yuan, Z.; Zhang, Y.; Yong, S.; Salas-Burgos, A.; Koomen, J.; Olashaw, N.; Parsons, J. T.; Yang, X. J.; Dent, S. R.; Yao, T. P.; Lane, W. S.; Seto, E. HDAC6 modulates cell motility by altering the acetylation level of cortactin. *Molecular Cell* **2007**, *27* (2), 197-213. DOI: 10.1016/j.molcel.2007.05.033

(46) Hubbert, C.; Guardiola, A.; Shao, R.; Kawaguchi, Y.; Ito, A.; Nixon, A.; Yoshida, M.; Wang, X.-F.; Yao, T.-P. HDAC6 is a microtubule-associated deacetylase. *Nature* **2002**, *417* (6887), 455-458. DOI: 10.1038/417455a

(47) Tang, X.; Gao, J.-S.; Guan, Y.-j.; McLane, K. E.; Yuan, Z.-L.; Ramratnam, B.; Chin, Y. E. Acetylation-Dependent Signal Transduction for Type I Interferon Receptor. *Cell* **2007**, *131* (1), 93-105. DOI: https://doi.org/10.1016/j.cell.2007.07.034

(48) Kovacs, J. J.; Murphy, P. J. M.; Gaillard, S.; Zhao, X.; Wu, J.-T.; Nicchitta, C. V.; Yoshida, M.; Toft, D. O.; Pratt, W. B.; Yao, T.-P. HDAC6 Regulates Hsp90 Acetylation and Chaperone-Dependent Activation of Glucocorticoid Receptor. *Molecular Cell* **2005**, *18* (5), 601-607. DOI: https://doi.org/10.1016/j.molcel.2005.04.021

(49) Hai, Y.; Shinsky, S. A.; Porter, N. J.; Christianson, D. W. Histone deacetylase 10 structure and molecular function as a polyamine deacetylase. *Nature Communications* **2017**, *8* (1), 15368. DOI: 10.1038/ncomms15368

(50) Wu, Q.-J.; Zhang, T.-N.; Chen, H.-H.; Yu, X.-F.; Lv, J.-L.; Liu, Y.-Y.; Liu, Y.-S.; Zheng, G.; Zhao, J.-Q.; Wei, Y.-F.; Guo, J.-Y.; Liu, F.-H.; Chang, Q.; Zhang, Y.-X.; Liu, C.-G.; Zhao, Y.-H. The sirtuin family in health and disease. *Signal Transduction and Targeted Therapy* **2022**, *7* (1), 402. DOI: 10.1038/s41392-022-01257-8

(51) Haigis, M. C.; Sinclair, D. A. Mammalian sirtuins: biological insights and disease relevance. *Annual Review of Pathology: Mechanisms of Disease* **2010**, *5*, 253-295. DOI: 10.1146/annurev.pathol.4.110807.092250

(52) Gao, L.; Cueto, M. A.; Asselbergs, F.; Atadja, P. Cloning and functional characterization of HDAC11, a novel member of the human histone deacetylase family. *Journal of Biological Chemistry* **2002**, *277* (28), 25748-25755. DOI: 10.1074/jbc.M111871200

(53) Núñez-Álvarez, Y.; Suelves, M. HDAC11: a multifaceted histone deacetylase with proficient fatty deacylase activity and its roles in physiological processes. *The FEBS Journal* **2022**, *289* (10), 2771-2792. DOI: https://doi.org/10.1111/febs.15895

(54) Cheng, F.; Lienlaf, M.; Perez-Villarroel, P.; Wang, H. W.; Lee, C.; Woan, K.; Woods, D.; Knox, T.; Bergman, J.; Pinilla-Ibarz, J.; Kozikowski, A.; Seto, E.; Sotomayor, E. M.; Villagra, A. Divergent roles of histone deacetylase 6 (HDAC6) and histone deacetylase 11 (HDAC11) on the transcriptional regulation of IL10 in antigen presenting cells. *Molecular Immunology* **2014**, *60* (1), 44-53. DOI: 10.1016/j.molimm.2014.02.019

(55) Leipe, D. D.; Landsman, D. Histone deacetylases, acetoin utilization proteins and acetylpolyamine amidohydrolases are members of an ancient protein superfamily. *Nucleic Acids Research* **1997**, *25* (18), 3693-3697. DOI: 10.1093/nar/25.18.3693

(56) Liu, S.-S.; Wu, F.; Jin, Y.-M.; Chang, W.-Q.; Xu, T.-M. HDAC11: a rising star in epigenetics. *Biomedicine & Pharmacotherapy* **2020**, *131*, 110607. DOI: https://doi.org/10.1016/j.biopha.2020.110607

(57) Lundh, M.; Christensen, D. P.; Rasmussen, D. N.; Mascagni, P.; Dinarello, C. A.; Billestrup, N.; Grunnet, L. G.; Mandrup-Poulsen, T. Lysine deacetylases are produced in pancreatic beta cells and are differentially regulated by proinflammatory cytokines. *Diabetologia* **2010**, *53* (12), 2569-2578. DOI: 10.1007/s00125-010-1892-8

(58) Kutil, Z.; Novakova, Z.; Meleshin, M.; Mikesova, J.; Schutkowski, M.; Barinka, C. Histone Deacetylase 11 Is a Fatty-Acid Deacylase. *ACS Chemical Biology* **2018**, *13* (3), 685-693. DOI: 10.1021/acschembio.7b00942

(59) Moreno-Yruela, C.; Galleano, I.; Madsen, A. S.; Olsen, C. A. Histone Deacetylase 11 Is an ε-N-Myristoyllysine Hydrolase. *Cell Chemical Biology* **2018**, *25* (7), 849-856.e848. DOI: https://doi.org/10.1016/j.chembiol.2018.04.007

(60) Cao, J.; Sun, L.; Aramsangtienchai, P.; Spiegelman, N. A.; Zhang, X.; Huang, W.; Seto, E.; Lin, H. HDAC11 regulates type I interferon signaling through defatty-acylation of SHMT2. *Proceedings of the National Academy of Sciences* **2019**, *116* (12), 5487-5492. DOI: 10.1073/pnas.1815365116

(61) Kutil, Z.; Mikešová, J.; Zessin, M.; Meleshin, M.; Nováková, Z.; Alquicer, G.; Kozikowski, A.; Sippl, W.; Bařinka, C.; Schutkowski, M. Continuous Activity Assay for HDAC11 Enabling Reevaluation of HDAC Inhibitors. *ACS Omega* **2019**, *4* (22), 19895-19904. DOI: 10.1021/acsomega.9b02808

(62) Yanginlar, C.; Logie, C. HDAC11 is a regulator of diverse immune functions. *Biochimica et Biophysica Acta: Gene Regulatory Mechanisms* **2018**, *1861* (1), 54-59. DOI: 10.1016/j.bbagrm.2017.12.002

(63) Villagra, A.; Cheng, F.; Wang, H. W.; Suarez, I.; Glozak, M.; Maurin, M.; Nguyen, D.; Wright, K. L.; Atadja, P. W.; Bhalla, K.; Pinilla-Ibarz, J.; Seto, E.; Sotomayor, E. M. The histone deacetylase HDAC11 regulates the expression of interleukin 10 and immune tolerance. *Nature Immunology* **2009**, *10* (1), 92-100. DOI: 10.1038/ni.1673

(64) Nutsford, A. N.; Galvin, H. D.; Ahmed, F.; Husain, M. The Class IV human deacetylase, HDAC11, exhibits anti-influenza A virus properties via its involvement in host innate antiviral response. *Cellular Microbiology* **2019**, *21* (4), e12989. DOI: 10.1111/cmi.12989

(65) Yuan, Y.; Zhao, K.; Yao, Y.; Liu, C.; Chen, Y.; Li, J.; Wang, Y.; Pei, R.; Chen, J.; Hu, X.; Zhou, Y.; Wu, C.; Chen, X. HDAC11 restricts HBV replication through epigenetic repression of cccDNA transcription. *Antiviral Research* **2019**, *172*, 104619. DOI: https://doi.org/10.1016/j.antiviral.2019.104619

(66) Wu, Y.-L.; Lin, Z.-J.; Li, C.-C.; Lin, X.; Shan, S.-K.; Guo, B.; Zheng, M.-H.; Li, F.; Yuan, L.-Q.; Li, Z.-h. Epigenetic regulation in metabolic diseases: mechanisms and advances in

clinical study. *Signal Transduction and Targeted Therapy* **2023**, *8* (1), 98. DOI: 10.1038/s41392-023-01333-7

(67) Yang, H.; Chen, L.; Sun, Q.; Yao, F.; Muhammad, S.; Sun, C. The role of HDAC11 in obesity-related metabolic disorders: A critical review. *Journal of Cellular Physiology* **2021**, *236* (8), 5582-5591. DOI: 10.1002/jcp.30286

(68) Chen, H.; Xie, C.; Chen, Q.; Zhuang, S. HDAC11, an emerging therapeutic target for metabolic disorders. *Frontiers in Endocrinology* **2022**, *13*, 989305. DOI: 10.3389/fendo.2022.989305

(69) Yang, H.; Li, C.; Che, M.; Liang, J.; Tian, X.; Yang, G.; Sun, C. HDAC11 deficiency resists obesity by converting adipose-derived stem cells into brown adipocyte-like cells. *International Journal of Biological Macromolecules* **2024**, *258* (Pt 1), 128852. DOI: 10.1016/j.ijbiomac.2023.128852

(70) Sun, L.; Marin de Evsikova, C.; Bian, K.; Achille, A.; Telles, E.; Pei, H.; Seto, E. Programming and Regulation of Metabolic Homeostasis by HDAC11. *EBioMedicine* **2018**, *33*, 157-168. DOI: 10.1016/j.ebiom.2018.06.025

(71) Bagchi, R. A.; Ferguson, B. S.; Stratton, M. S.; Hu, T.; Cavasin, M. A.; Sun, L.; Lin, Y. H.; Liu, D.; Londono, P.; Song, K.; Pino, M. F.; Sparks, L. M.; Smith, S. R.; Scherer, P. E.; Collins, S.; Seto, E.; McKinsey, T. A. HDAC11 suppresses the thermogenic program of adipose tissue via BRD2. *JCI Insight* **2018**, *3* (15), e120159. DOI: 10.1172/jci.insight.120159

(72) Li, J.; Chen, X.; Liu, R.; Liu, X.; Shu, M. Engineering novel scaffolds for specific HDAC11 inhibitors against metabolic diseases exploiting deep learning, virtual screening, and molecular dynamics simulations. *International Journal of Biological Macromolecules* **2024**, *262*, 129810. DOI: https://doi.org/10.1016/j.ijbiomac.2024.129810

(73) Deubzer, H. E.; Schier, M. C.; Oehme, I.; Lodrini, M.; Haendler, B.; Sommer, A.; Witt, O. HDAC11 is a novel drug target in carcinomas. *International Journal of Cancer* **2013**, *132* (9), 2200-2208. DOI: 10.1002/ijc.27876

(74) Liu, Y.; Tong, X.; Hu, W.; Chen, D. HDAC11: A novel target for improved cancer therapy. *Biomedicine & Pharmacotherapy* **2023**, *166*, 115418. DOI: 10.1016/j.biopha.2023.115418

(75) Bora-Singhal, N.; Mohankumar, D.; Saha, B.; Colin, C. M.; Lee, J. Y.; Martin, M. W.; Zheng, X.; Coppola, D.; Chellappan, S. Novel HDAC11 inhibitors suppress lung

adenocarcinoma stem cell self-renewal and overcome drug resistance by suppressing Sox2. *Scientific Reports* **2020**, *10* (1), 4722. DOI: 10.1038/s41598-020-61295-6

(76) Gong, D.; Zeng, Z.; Yi, F.; Wu, J. Inhibition of histone deacetylase 11 promotes human liver cancer cell apoptosis. *American Journal of Translational Research* **2019**, *11* (2), 983-990.

(77) Wang, W.; Fu, L.; Li, S.; Xu, Z.; Li, X. Histone deacetylase 11 suppresses p53 expression in pituitary tumor cells. *Cell Biology International* **2017**, *41* (12), 1290-1295. DOI: 10.1002/cbin.10834

(78) Yue, L.; Sharma, V.; Horvat, N. P.; Akuffo, A. A.; Beatty, M. S.; Murdun, C.; Colin, C.; Billington, J. M. R.; Goodheart, W. E.; Sahakian, E.; Zhang, L.; Powers, J. J.; Amin, N. E.; Lambert-Showers, Q. T.; Darville, L. N.; Pinilla-Ibarz, J.; Reuther, G. W.; Wright, K. L.; Conti, C.; Lee, J. Y.; Zheng, X.; Ng, P. Y.; Martin, M. W.; Marshall, C. G.; Koomen, J. M.; Levine, R. L.; Verma, A.; Grimes, H. L.; Sotomayor, E. M.; Shao, Z.; Epling-Burnette, P. K. HDAC11 deficiency disrupts oncogene-induced hematopoiesis in myeloproliferative neoplasms. *Blood* **2020**, *135* (3), 191-207. DOI: 10.1182/blood.2019895326

(79) Thole, T. M.; Lodrini, M.; Fabian, J.; Wuenschel, J.; Pfeil, S.; Hielscher, T.; Kopp-Schneider, A.; Heinicke, U.; Fulda, S.; Witt, O.; Eggert, A.; Fischer, M.; Deubzer, H. E. Neuroblastoma cells depend on HDAC11 for mitotic cell cycle progression and survival. *Cell Death & Disease* **2017**, *8* (3), e2635. DOI: 10.1038/cddis.2017.49

(80) Melesina, J.; Simoben, C. V.; Praetorius, L.; Bülbül, E. F.; Robaa, D.; Sippl, W. Strategies To Design Selective Histone Deacetylase Inhibitors. *ChemMedChem* **2021**, *16* (9), 1336-1359. DOI: 10.1002/cmdc.202000934

(81) De Vreese, R.; D'Hooghe, M. Synthesis and applications of benzohydroxamic acid-based histone deacetylase inhibitors. *European Journal of Medicinal Chemistry* **2017**, *135*, 174-195. DOI: 10.1016/j.ejmech.2017.04.013

(82) Zhang, L.; Zhang, J.; Jiang, Q.; Zhang, L.; Song, W. Zinc binding groups for histone deacetylase inhibitors. *Journal of Enzyme Inhibition and Medicinal Chemistry* **2018**, *33* (1), 714-721. DOI: 10.1080/14756366.2017.1417274

(83) Bressi, J. C.; Jennings, A. J.; Skene, R.; Wu, Y.; Melkus, R.; De Jong, R.; O'Connell, S.; Grimshaw, C. E.; Navre, M.; Gangloff, A. R. Exploration of the HDAC2 foot pocket: Synthesis and SAR of substituted N-(2-aminophenyl)benzamides. *Bioorganic & Medicinal Chemistry Letters* **2010**, *20* (10), 3142-3145. DOI: 10.1016/j.bmcl.2010.03.091

(84) Ibrahim, H. S.; Abdelsalam, M.; Zeyn, Y.; Zessin, M.; Mustafa, A. M.; Fischer, M. A.; Zeyen, P.; Sun, P.; Bülbül, E. F.; Vecchio, A.; Erdmann, F.; Schmidt, M.; Robaa, D.; Barinka, C.; Romier, C.; Schutkowski, M.; Krämer, O. H.; Sippl, W. Synthesis, Molecular Docking and Biological Characterization of Pyrazine Linked 2-Aminobenzamides as New Class I Selective Histone Deacetylase (HDAC) Inhibitors with Anti-Leukemic Activity. *International Journal of Molecular Sciences* **2021**, *23* (1), 369. DOI: 10.3390/ijms23010369

(85) Sun, P.; Wang, J.; Khan, K. S.; Yang, W.; Ng, B. W.-L.; Ilment, N.; Zessin, M.; Bülbül, E. F.; Robaa, D.; Erdmann, F.; Schmidt, M.; Romier, C.; Schutkowski, M.; Cheng, A. S.-L.; Sippl, W. Development of Alkylated Hydrazides as Highly Potent and Selective Class I Histone Deacetylase Inhibitors with T cell Modulatory Properties. *Journal of Medicinal Chemistry* **2022**, *65* (24), 16313-16337. DOI: 10.1021/acs.jmedchem.2c01132

(86) Jiang, Y.; Xu, J.; Yue, K.; Huang, C.; Qin, M.; Chi, D.; Yu, Q.; Zhu, Y.; Hou, X.; Xu, T.; Li, M.; Chou, C. J.; Li, X. Potent Hydrazide-Based HDAC Inhibitors with a Superior Pharmacokinetic Profile for Efficient Treatment of Acute Myeloid Leukemia In Vivo. *Journal of Medicinal Chemistry* **2022**, *65* (1), 285-302. DOI: 10.1021/acs.jmedchem.1c01472

(87) Kozlov, M. V.; Konduktorov, K. A.; Shcherbakova, A. S.; Kochetkov, S. N. Synthesis of N′-propylhydrazide analogs of hydroxamic inhibitors of histone deacetylases (HDACs) and evaluation of their impact on activities of HDACs and replication of hepatitis C virus (HCV). *Bioorganic & Medicinal Chemistry Letters* **2019**, *29* (16), 2369-2374. DOI: https://doi.org/10.1016/j.bmcl.2019.06.006

(88) Li, X.; Jiang, Y.; Peterson, Y. K.; Xu, T.; Himes, R. A.; Luo, X.; Yin, G.; Inks, E. S.; Dolloff, N.; Halene, S.; Chan, S. S. L.; Chou, C. J. Design of Hydrazide-Bearing HDACIs Based on Panobinostat and Their p53 and FLT3-ITD Dependency in Antileukemia Activity. *Journal of Medicinal Chemistry* **2020**, *63* (10), 5501-5525. DOI: 10.1021/acs.jmedchem.0c00442

(89) Decroos, C.; Clausen, D. J.; Haines, B. E.; Wiest, O.; Williams, R. M.; Christianson, D. W. Variable active site loop conformations accommodate the binding of macrocyclic largazole analogues to HDAC8. *Biochemistry* **2015**, *54* (12), 2126-2135. DOI: 10.1021/acs.biochem.5b00010

(90) Clausen, D. J.; Liu, J.; Yu, W.; Duffy, J. L.; Chung, C. C.; Myers, R. W.; Klein, D. J.; Fells, J.; Holloway, K.; Wu, J.; Wu, G.; Howell, B. J.; Barnard, R. J. O.; Kozlowski, J.

Development of a selective HDAC inhibitor aimed at reactivating the HIV latent reservoir. *Bioorganic & Medicinal Chemistry Letters* **2020**, *30* (17), 127367. DOI: 10.1016/j.bmcl.2020.127367

(91) Liu, J.; Kelly, J.; Yu, W.; Clausen, D.; Yu, Y.; Kim, H.; Duffy, J. L.; Chung, C. C.; Myers, R. W.; Carroll, S.; Klein, D. J.; Fells, J.; Holloway, M. K.; Wu, J.; Wu, G.; Howell, B. J.; Barnard, R. J. O.; Kozlowski, J. A. Selective Class I HDAC Inhibitors Based on Aryl Ketone Zinc Binding Induce HIV-1 Protein for Clearance. *ACS Medicinal Chemistry Letters* **2020**, *11* (7), 1476-1483. DOI: 10.1021/acsmedchemlett.0c00302

(92) Frey, R. R.; Wada, C. K.; Garland, R. B.; Curtin, M. L.; Michaelides, M. R.; Li, J.; Pease, L. J.; Glaser, K. B.; Marcotte, P. A.; Bouska, J. J.; Murphy, S. S.; Davidsen, S. K. Trifluoromethyl ketones as inhibitors of histone deacetylase. *Bioorganic & Medicinal Chemistry Letters* **2002**, *12* (23), 3443-3447. DOI: https://doi.org/10.1016/S0960-894X(02)00754-0

(93) Porter, N. J.; Christianson, D. W. Binding of the Microbial Cyclic Tetrapeptide Trapoxin A to the Class I Histone Deacetylase HDAC8. *ACS Chemical Biology* **2017**, *12* (9), 2281-2286. DOI: 10.1021/acschembio.7b00330

(94) Lobera, M.; Madauss, K. P.; Pohlhaus, D. T.; Wright, Q. G.; Trocha, M.; Schmidt, D. R.; Baloglu, E.; Trump, R. P.; Head, M. S.; Hofmann, G. A.; Murray-Thompson, M.; Schwartz, B.; Chakravorty, S.; Wu, Z.; Mander, P. K.; Kruidenier, L.; Reid, R. A.; Burkhart, W.; Turunen, B. J.; Rong, J. X.; Wagner, C.; Moyer, M. B.; Wells, C.; Hong, X.; Moore, J. T.; Williams, J. D.; Soler, D.; Ghosh, S.; Nolan, M. A. Selective class IIa histone deacetylase inhibition via a nonchelating zinc-binding group. *Nature Chemical Biology* **2013**, *9* (5), 319-325. DOI: 10.1038/nchembio.1223

(95) Whitehead, L.; Dobler, M. R.; Radetich, B.; Zhu, Y.; Atadja, P. W.; Claiborne, T.; Grob, J. E.; McRiner, A.; Pancost, M. R.; Patnaik, A.; Shao, W.; Shultz, M.; Tichkule, R.; Tommasi, R. A.; Vash, B.; Wang, P.; Stams, T. Human HDAC isoform selectivity achieved via exploitation of the acetate release channel with structurally unique small molecule inhibitors. *Bioorganic & Medicinal Chemistry* **2011**, *19* (15), 4626-4634. DOI: 10.1016/j.bmc.2011.06.030

(96) Bürli, R. W.; Luckhurst, C. A.; Aziz, O.; Matthews, K. L.; Yates, D.; Lyons, K. A.; Beconi, M.; McAllister, G.; Breccia, P.; Stott, A. J.; Penrose, S. D.; Wall, M.; Lamers, M.; Leonard, P.;

Müller, I.; Richardson, C. M.; Jarvis, R.; Stones, L.; Hughes, S.; Wishart, G.; Haughan, A. F.; O'Connell, C.; Mead, T.; McNeil, H.; Vann, J.; Mangette, J.; Maillard, M.; Beaumont, V.; Munoz-Sanjuan, I.; Dominguez, C. Design, synthesis, and biological evaluation of potent and selective class IIa histone deacetylase (HDAC) inhibitors as a potential therapy for Huntington's disease. *Journal of Medicinal Chemistry* **2013**, *56* (24), 9934-9954. DOI: 10.1021/jm4011884

(97) Luckhurst, C. A.; Breccia, P.; Stott, A. J.; Aziz, O.; Birch, H. L.; Bürli, R. W.; Hughes, S. J.; Jarvis, R. E.; Lamers, M.; Leonard, P. M.; Matthews, K. L.; McAllister, G.; Pollack, S.; Saville-Stones, E.; Wishart, G.; Yates, D.; Dominguez, C. Potent, Selective, and CNS-Penetrant Tetrasubstituted Cyclopropane Class IIa Histone Deacetylase (HDAC) Inhibitors. *ACS Medicinal Chemistry Letters* **2016**, *7* (1), 34-39. DOI: 10.1021/acsmedchemlett.5b00302

(98) Marek, M.; Shaik, T. B.; Heimburg, T.; Chakrabarti, A.; Lancelot, J.; Ramos-Morales, E.; Da Veiga, C.; Kalinin, D.; Melesina, J.; Robaa, D.; Schmidtkunz, K.; Suzuki, T.; Holl, R.; Ennifar, E.; Pierce, R. J.; Jung, M.; Sippl, W.; Romier, C. Characterization of Histone Deacetylase 8 (HDAC8) Selective Inhibition Reveals Specific Active Site Structural and Functional Determinants. *Journal of Medicinal Chemistry* **2018**, *61* (22), 10000-10016. DOI: 10.1021/acs.jmedchem.8b01087

(99) Arts, J.; King, P.; Marin, A.; Floren, W.; Belin, A.; Janssen, L.; Pilatte, I.; Roux, B.; Decrane, L.; Gilissen, R.; Hickson, I.; Vreys, V.; Cox, E.; Bol, K.; Talloen, W.; Goris, I.; Andries, L.; Du Jardin, M.; Janicot, M.; Page, M.; van Emelen, K.; Angibaud, P. JNJ-26481585, a Novel Second-Generation Oral Histone Deacetylase Inhibitor, Shows Broad-Spectrum Preclinical Antitumoral Activity. *Clinical Cancer Research* **2009**, *15* (22), 6841-6851. DOI: 10.1158/1078-0432.CCR-09-0547

(100) Salvador, L. A.; Park, H.; Al-Awadhi, F. H.; Liu, Y.; Kim, B.; Zeller, S. L.; Chen, Q.-Y.; Hong, J.; Luesch, H. Modulation of Activity Profiles for Largazole-Based HDAC Inhibitors through Alteration of Prodrug Properties. *ACS Medicinal Chemistry Letters* **2014**, *5* (8), 905-910. DOI: 10.1021/ml500170r

(101) Auzzas, L.; Larsson, A.; Matera, R.; Baraldi, A.; Deschênes-Simard, B.; Giannini, G.; Cabri, W.; Battistuzzi, G.; Gallo, G.; Ciacci, A.; Vesci, L.; Pisano, C.; Hanessian, S. Non-Natural Macrocyclic Inhibitors of Histone Deacetylases: Design, Synthesis, and Activity. *Journal of Medicinal Chemistry* **2010**, *53* (23), 8387-8399. DOI: 10.1021/jm101092u

(102) Chen, Y.; Wang, X.; Xiang, W.; He, L.; Tang, M.; Wang, F.; Wang, T.; Yang, Z.; Yi, Y.; Wang, H.; Niu, T.; Zheng, L.; Lei, L.; Li, X.; Song, H.; Chen, L. Development of Purine-Based Hydroxamic Acid Derivatives: Potent Histone Deacetylase Inhibitors with Marked in Vitro and in Vivo Antitumor Activities. *Journal of Medicinal Chemistry* **2016**, *59* (11), 5488-5504. DOI: 10.1021/acs.jmedchem.6b00579

(103) Neelarapu, R.; Holzle, D. L.; Velaparthi, S.; Bai, H.; Brunsteiner, M.; Blond, S. Y.; Petukhov, P. A. Design, Synthesis, Docking, and Biological Evaluation of Novel Diazide-Containing Isoxazole- and Pyrazole-Based Histone Deacetylase Probes. *Journal of Medicinal Chemistry* **2011**, *54* (13), 4350-4364. DOI: 10.1021/jm2001025

(104) Yu, C.-W.; Chang, P.-T.; Hsin, L.-W.; Chern, J.-W. Quinazolin-4-one Derivatives as Selective Histone Deacetylase-6 Inhibitors for the Treatment of Alzheimer's Disease. *Journal of Medicinal Chemistry* **2013**, *56* (17), 6775-6791. DOI: 10.1021/jm400564j

(105) Muthyala, R.; Shin, W. S.; Xie, J.; Sham, Y. Y. Discovery of 1-hydroxypyridine-2-thiones as selective histone deacetylase inhibitors and their potential application for treating leukemia. *Bioorganic & Medicinal Chemistry Letters* **2015**, *25* (19), 4320-4324. DOI: https://doi.org/10.1016/j.bmcl.2015.07.065

(106) Marek, L.; Hamacher, A.; Hansen, F. K.; Kuna, K.; Gohlke, H.; Kassack, M. U.; Kurz, T. Histone Deacetylase (HDAC) Inhibitors with a Novel Connecting Unit Linker Region Reveal a Selectivity Profile for HDAC4 and HDAC5 with Improved Activity against Chemoresistant Cancer Cells. *Journal of Medicinal Chemistry* **2013**, *56* (2), 427-436. DOI: 10.1021/jm301254q

(107) Zhou, N.; Moradei, O.; Raeppel, S.; Leit, S.; Frechette, S.; Gaudette, F.; Paquin, I.; Bernstein, N.; Bouchain, G.; Vaisburg, A.; Jin, Z.; Gillespie, J.; Wang, J.; Fournel, M.; Yan, P. T.; Trachy-Bourget, M.-C.; Kalita, A.; Lu, A.; Rahil, J.; MacLeod, A. R.; Li, Z.; Besterman, J. M.; Delorme, D. Discovery of N-(2-Aminophenyl)-4-[(4-pyridin-3-ylpyrimidin-2-ylamino)methyl]benzamide (MGCD0103), an Orally Active Histone Deacetylase Inhibitor. *Journal of Medicinal Chemistry* **2008**, *51* (14), 4072-4075. DOI: 10.1021/jm800251w

(108) Martin, M. W.; Lee, J. Y.; Lancia, D. R., Jr.; Ng, P. Y.; Han, B.; Thomason, J. R.; Lynes, M. S.; Marshall, C. G.; Conti, C.; Collis, A.; Morales, M. A.; Doshi, K.; Rudnitskaya, A.; Yao, L.; Zheng, X. Discovery of novel N-hydroxy-2-arylisoindoline-4-carboxamides as potent and

selective inhibitors of HDAC11. *Bioorganic & Medicinal Chemistry Letters* **2018**, *28* (12), 2143-2147. DOI: 10.1016/j.bmcl.2018.05.021

(109) Son, S. I.; Cao, J.; Zhu, C.-L.; Miller, S. P.; Lin, H. Activity-Guided Design of HDAC11-Specific Inhibitors. *ACS Chemical Biology* **2019**, *14* (7), 1393-1397. DOI: 10.1021/acschembio.9b00292

(110) Xie, H.; Yang, E.; Wang, C.; Peng, C.; Ji, L. Targeting HDAC11 activity by FT895 restricts EV71 replication. *Virus Research* **2023**, *330*, 199108. DOI: https://doi.org/10.1016/j.virusres.2023.199108

(111) Bai, P.; Liu, Y.; Yang, L.; Ding, W.; Mondal, P.; Sang, N.; Liu, G.; Lu, X.; Ho, T. T.; Zhou, Y.; Wu, R.; Birar, V. C.; Wilks, M. Q.; Tanzi, R. E.; Lin, H.; Zhang, C.; Li, W.; Shen, S.; Wang, C. Development and Pharmacochemical Characterization Discover a Novel Brain-Permeable HDAC11-Selective Inhibitor with Therapeutic Potential by Regulating Neuroinflammation in Mice. *Journal of Medicinal Chemistry* **2023**, *66* (23), 16075-16090. DOI: 10.1021/acs.jmedchem.3c01491

(112) Ho, T. T.; Peng, C.; Seto, E.; Lin, H. Trapoxin A Analogue as a Selective Nanomolar Inhibitor of HDAC11. *ACS Chemical Biology* **2023**, *18* (4), 803-809. DOI: 10.1021/acschembio.2c00840

(113) Dallavalle, S.; Musso, L.; Cincinelli, R.; Darwiche, N.; Gervasoni, S.; Vistoli, G.; Guglielmi, M. B.; La Porta, I.; Pizzulo, M.; Modica, E.; Prosperi, F.; Signorino, G.; Colelli, F.; Cardile, F.; Fucci, A.; D'Andrea, E. L.; Riccio, A.; Pisano, C. Antitumor activity of novel POLA1-HDAC11 dual inhibitors. *European Journal of Medicinal Chemistry* **2022**, *228*, 113971. DOI: 10.1016/j.ejmech.2021.113971

(114) Prieto-Martínez, F. D.; López-López, E.; Eurídice Juárez-Mercado, K.; Medina-Franco, J. L. Chapter 2 - Computational Drug Design Methods—Current and Future Perspectives. In *In Silico Drug Design*, Roy, K. Ed.; Academic Press, 2019; pp 19-44.

(115) Sliwoski, G.; Kothiwale, S.; Meiler, J.; Lowe, E. W., Jr. Computational methods in drug discovery. *Pharmacological Reviews* **2014**, *66* (1), 334-395. DOI: 10.1124/pr.112.007336

(116) Sabe, V. T.; Ntombela, T.; Jhamba, L. A.; Maguire, G. E. M.; Govender, T.; Naicker, T.; Kruger, H. G. Current trends in computer aided drug design and a highlight of drugs discovered via computational techniques: A review. *European Journal of Medicinal Chemistry* **2021**, *224*, 113705. DOI: 10.1016/j.ejmech.2021.113705

(117) Pathak, R. K.; Singh, D. B.; Sagar, M.; Baunthiyal, M.; Kumar, A. Computational Approaches in Drug Discovery and Design. In *Computer-Aided Drug Design*, Singh, D. B. Ed.; Springer Singapore, 2020; pp 1-21.

(118) Wang, X.; Song, K.; Li, L.; Chen, L. Structure-Based Drug Design Strategies and Challenges. *Current Topics in Medicinal Chemistry* **2018**, *18* (12), 998-1006. DOI: http://dx.doi.org/10.2174/1568026618666180813152921

(119) Muhammed, M. T.; Aki-Yalcin, E. Homology modeling in drug discovery: Overview, current applications, and future perspectives. *Chemical Biology & Drug Design* **2019**, *93* (1), 12-20. DOI: 10.1111/cbdd.13388

(120) Tiwari, A.; Chauhan, R. P.; Agarwal, A.; Ramteke, P. W. Molecular Modeling of Proteins: Methods, Recent Advances, and Future Prospects. In *Computer-Aided Drug Design*, Singh, D. B. Ed.; Springer Singapore, 2020; pp 23-47.

(121) Jumper, J.; Evans, R.; Pritzel, A.; Green, T.; Figurnov, M.; Ronneberger, O.; Tunyasuvunakool, K.; Bates, R.; Žídek, A.; Potapenko, A.; Bridgland, A.; Meyer, C.; Kohl, S. A. A.; Ballard, A. J.; Cowie, A.; Romera-Paredes, B.; Nikolov, S.; Jain, R.; Adler, J.; Back, T.; Petersen, S.; Reiman, D.; Clancy, E.; Zielinski, M.; Steinegger, M.; Pacholska, M.; Berghammer, T.; Bodenstein, S.; Silver, D.; Vinyals, O.; Senior, A. W.; Kavukcuoglu, K.; Kohli, P.; Hassabis, D. Highly accurate protein structure prediction with AlphaFold. *Nature* **2021**, *596* (7873), 583-589. DOI: 10.1038/s41586-021-03819-2

(122) Tunyasuvunakool, K.; Adler, J.; Wu, Z.; Green, T.; Zielinski, M.; Žídek, A.; Bridgland, A.; Cowie, A.; Meyer, C.; Laydon, A.; Velankar, S.; Kleywegt, G. J.; Bateman, A.; Evans, R.; Pritzel, A.; Figurnov, M.; Ronneberger, O.; Bates, R.; Kohl, S. A. A.; Potapenko, A.; Ballard, A. J.; Romera-Paredes, B.; Nikolov, S.; Jain, R.; Clancy, E.; Reiman, D.; Petersen, S.; Senior, A. W.; Kavukcuoglu, K.; Birney, E.; Kohli, P.; Jumper, J.; Hassabis, D. Highly accurate protein structure prediction for the human proteome. *Nature* **2021**, *596* (7873), 590-596. DOI: 10.1038/s41586-021-03828-1

(123) David, A.; Islam, S.; Tankhilevich, E.; Sternberg, M. J. E. The AlphaFold Database of Protein Structures: A Biologist's Guide. *Journal of Molecular Biology* **2022**, *434* (2), 167336. DOI: 10.1016/j.jmb.2021.167336

(124) Borkakoti, N.; Thornton, J. M. AlphaFold2 protein structure prediction: Implications for drug discovery. *Current Opinion in Structural Biology* **2023**, *78*, 102526. DOI: https://doi.org/10.1016/j.sbi.2022.102526

(125) He, X.-h.; You, C.-z.; Jiang, H.-l.; Jiang, Y.; Xu, H. E.; Cheng, X. AlphaFold2 versus experimental structures: evaluation on G protein-coupled receptors. *Acta Pharmacologica Sinica* **2023**, *44* (1), 1-7. DOI: 10.1038/s41401-022-00938-y

(126) Lee, S.; Kim, S.; Lee, G. R.; Kwon, S.; Woo, H.; Seok, C.; Park, H. Evaluating GPCR modeling and docking strategies in the era of deep learning-based protein structure prediction. *Computational and Structural Biotechnology Journal* **2023**, *21*, 158-167. DOI: 10.1016/j.csbj.2022.11.057

(127) Heo, L.; Feig, M. Multi-state modeling of G-protein coupled receptors at experimental accuracy. *Proteins* **2022**, *90* (11), 1873-1885. DOI: 10.1002/prot.26382

(128) Karelina, M.; Noh, J. J.; Dror, R. O. How accurately can one predict drug binding modes using AlphaFold models? *Elife* **2023**, *12*, RP89386. DOI: 10.7554/eLife.89386

(129) Holcomb, M.; Chang, Y. T.; Goodsell, D. S.; Forli, S. Evaluation of AlphaFold2 structures as docking targets. *Protein science* **2023**, *32* (1), e4530. DOI: 10.1002/pro.4530

(130) Wang, R.; Fang, X.; Lu, Y.; Wang, S. The PDBbind Database: Collection of Binding Affinities for Protein−Ligand Complexes with Known Three-Dimensional Structures. *Journal of Medicinal Chemistry* **2004**, *47* (12), 2977-2980. DOI: 10.1021/jm030580l

(131) Díaz-Rovira, A. M.; Martín, H.; Beuming, T.; Díaz, L.; Guallar, V.; Ray, S. S. Are Deep Learning Structural Models Sufficiently Accurate for Virtual Screening? Application of Docking Algorithms to AlphaFold2 Predicted Structures. *Journal of Chemical Information and Modeling* **2023**, *63* (6), 1668-1674. DOI: 10.1021/acs.jcim.2c01270

(132) Scardino, V.; Di Filippo, J. I.; Cavasotto, C. N. How good are AlphaFold models for docking-based virtual screening? *iScience* **2023**, *26* (1), 105920. DOI: 10.1016/j.isci.2022.105920

(133) Zhang, Y.; Vass, M.; Shi, D.; Abualrous, E.; Chambers, J. M.; Chopra, N.; Higgs, C.; Kasavajhala, K.; Li, H.; Nandekar, P.; Sato, H.; Miller, E. B.; Repasky, M. P.; Jerome, S. V. Benchmarking Refined and Unrefined AlphaFold2 Structures for Hit Discovery. *Journal of Chemical Information and Modeling* **2023**, *63* (6), 1656-1667. DOI: 10.1021/acs.jcim.2c01219

(134) Ren, F.; Ding, X.; Zheng, M.; Korzinkin, M.; Cai, X.; Zhu, W.; Mantsyzov, A.; Aliper, A.; Aladinskiy, V.; Cao, Z.; Kong, S.; Long, X.; Man Liu, B. H.; Liu, Y.; Naumov, V.; Shneyderman, A.; Ozerov, I. V.; Wang, J.; Pun, F. W.; Polykovskiy, D. A.; Sun, C.; Levitt, M.; Aspuru-Guzik, A.; Zhavoronkov, A. AlphaFold accelerates artificial intelligence powered drug discovery: efficient discovery of a novel CDK20 small molecule inhibitor. *Chemical Science* **2023**, *14* (6), 1443-1452. DOI: 10.1039/d2sc05709c

(135) Hekkelman, M. L.; de Vries, I.; Joosten, R. P.; Perrakis, A. AlphaFill: enriching AlphaFold models with ligands and cofactors. *Nature Methods* **2023**, *20* (2), 205-213. DOI: 10.1038/s41592-022-01685-y

(136) Baek, M.; DiMaio, F.; Anishchenko, I.; Dauparas, J.; Ovchinnikov, S.; Lee, G. R.; Wang, J.; Cong, Q.; Kinch, L. N.; Schaeffer, R. D.; Millán, C.; Park, H.; Adams, C.; Glassman, C. R.; DeGiovanni, A.; Pereira, J. H.; Rodrigues, A. V.; van Dijk, A. A.; Ebrecht, A. C.; Opperman, D. J.; Sagmeister, T.; Buhlheller, C.; Pavkov-Keller, T.; Rathinaswamy, M. K.; Dalwadi, U.; Yip, C. K.; Burke, J. E.; Garcia, K. C.; Grishin, N. V.; Adams, P. D.; Read, R. J.; Baker, D. Accurate prediction of protein structures and interactions using a three-track neural network. *Science* **2021**, *373* (6557), 871-876. DOI: 10.1126/science.abj8754

(137) Baek, M.; McHugh, R.; Anishchenko, I.; Jiang, H.; Baker, D.; DiMaio, F. Accurate prediction of protein–nucleic acid complexes using RoseTTAFoldNA. *Nature Methods* **2024**, *21* (1), 117-121. DOI: 10.1038/s41592-023-02086-5

(138) Krishna, R.; Wang, J.; Ahern, W.; Sturmfels, P.; Venkatesh, P.; Kalvet, I.; Lee, G. R.; Morey-Burrows, F. S.; Anishchenko, I.; Humphreys, I. R.; McHugh, R.; Vafeados, D.; Li, X.; Sutherland, G. A.; Hitchcock, A.; Hunter, C. N.; Kang, A.; Brackenbrough, E.; Bera, A. K.; Baek, M.; DiMaio, F.; Baker, D. Generalized biomolecular modeling and design with RoseTTAFold All-Atom. *Science* **2024**, *384* (6693), eadl2528. DOI: 10.1126/science.adl2528

(139) Abramson, J.; Adler, J.; Dunger, J.; Evans, R.; Green, T.; Pritzel, A.; Ronneberger, O.; Willmore, L.; Ballard, A. J.; Bambrick, J.; Bodenstein, S. W.; Evans, D. A.; Hung, C.-C.; O'Neill, M.; Reiman, D.; Tunyasuvunakool, K.; Wu, Z.; Žemgulytė, A.; Arvaniti, E.; Beattie, C.; Bertolli, O.; Bridgland, A.; Cherepanov, A.; Congreve, M.; Cowen-Rivers, A. I.; Cowie, A.; Figurnov, M.; Fuchs, F. B.; Gladman, H.; Jain, R.; Khan, Y. A.; Low, C. M. R.; Perlin, K.; Potapenko, A.; Savy, P.; Singh, S.; Stecula, A.; Thillaisundaram, A.; Tong, C.; Yakneen, S.; Zhong, E. D.; Zielinski, M.; Žídek, A.; Bapst, V.; Kohli, P.; Jaderberg, M.; Hassabis, D.;

Jumper, J. M. Accurate structure prediction of biomolecular interactions with AlphaFold 3. *Nature* **2024**, *630*, 493–500. DOI: 10.1038/s41586-024-07487-w

(140) Sun, Y.; Sun, Y.; Yue, S.; Wang, Y.; Lu, F. Histone Deacetylase Inhibitors in Cancer Therapy. *Current Topics in Medicinal Chemistry* **2018**, *18* (28), 2420-2428. DOI: http://dx.doi.org/10.2174/1568026619666181210152115

(141) Wang, H.; Yu, N.; Chen, D.; Lee, K. C.; Lye, P. L.; Chang, J. W.; Deng, W.; Ng, M. C.; Lu, T.; Khoo, M. L.; Poulsen, A.; Sangthongpitag, K.; Wu, X.; Hu, C.; Goh, K. C.; Wang, X.; Fang, L.; Goh, K. L.; Khng, H. H.; Goh, S. K.; Yeo, P.; Liu, X.; Bonday, Z.; Wood, J. M.; Dymock, B. W.; Kantharaj, E.; Sun, E. T. Discovery of (2E)-3-{2-butyl-1-[2-(diethylamino)ethyl]-1H-benzimidazol-5-yl}-N-hydroxyacrylamide (SB939), an orally active histone deacetylase inhibitor with a superior preclinical profile. *Journal of Medicinal Chemistry* **2011**, *54* (13), 4694-4720. DOI: 10.1021/jm2003552

(142) Cai, X.; Zhai, H. X.; Wang, J.; Forrester, J.; Qu, H.; Yin, L.; Lai, C. J.; Bao, R.; Qian, C. Discovery of 7-(4-(3-ethynylphenylamino)-7-methoxyquinazolin-6-yloxy)-N-hydroxyheptanamide (CUDc-101) as a potent multi-acting HDAC, EGFR, and HER2 inhibitor for the treatment of cancer. *Journal of Medicinal Chemistry* **2010**, *53* (5), 2000-2009. DOI: 10.1021/jm901453q

(143) Ossenkoppele, G. J.; Lowenberg, B.; Zachee, P.; Vey, N.; Breems, D.; Van de Loosdrecht, A. A.; Davidson, A. H.; Wells, G.; Needham, L.; Bawden, L.; Toal, M.; Hooftman, L.; Debnam, P. M. A phase I first-in-human study with tefinostat - a monocyte/macrophage targeted histone deacetylase inhibitor - in patients with advanced haematological malignancies. *British Journal of Haematology* **2013**, *162* (2), 191-201. DOI: 10.1111/bjh.12359

(144) Huang, P.; Almeciga-Pinto, I.; Jarpe, M.; van Duzer, J. H.; Mazitschek, R.; Yang, M.; Jones, S. S.; Quayle, S. N. Selective HDAC inhibition by ACY-241 enhances the activity of paclitaxel in solid tumor models. *Oncotarget* **2017**, *8* (2), 2694-2707. DOI: 10.18632/oncotarget.13738

(145) Mann, B. S.; Johnson, J. R.; Cohen, M. H.; Justice, R.; Pazdur, R. FDA approval summary: vorinostat for treatment of advanced primary cutaneous T-cell lymphoma. *Oncologist* **2007**, *12* (10), 1247-1252. DOI: 10.1634/theoncologist.12-10-1247

(146) Lee, H. Z.; Kwitkowski, V. E.; Del Valle, P. L.; Ricci, M. S.; Saber, H.; Habtemariam, B. A.; Bullock, J.; Bloomquist, E.; Li Shen, Y.; Chen, X. H.; Brown, J.; Mehrotra, N.; Dorff,

S.; Charlab, R.; Kane, R. C.; Kaminskas, E.; Justice, R.; Farrell, A. T.; Pazdur, R. FDA Approval: Belinostat for the Treatment of Patients with Relapsed or Refractory Peripheral T-cell Lymphoma. *Clinical Cancer Research* **2015**, *21* (12), 2666-2670. DOI: 10.1158/1078-0432.Ccr-14-3119

(147) Laubach, J. P.; Moreau, P.; San-Miguel, J. F.; Richardson, P. G. Panobinostat for the Treatment of Multiple Myeloma. *Clinical Cancer Research* **2015**, *21* (21), 4767-4773. DOI: 10.1158/1078-0432.Ccr-15-0530

(148) Becher, I.; Werner, T.; Doce, C.; Zaal, E. A.; Tögel, I.; Khan, C. A.; Rueger, A.; Muelbaier, M.; Salzer, E.; Berkers, C. R.; Fitzpatrick, P. F.; Bantscheff, M.; Savitski, M. M. Thermal profiling reveals phenylalanine hydroxylase as an off-target of panobinostat. *Nature Chemical Biology* **2016**, *12* (11), 908-910. DOI: 10.1038/nchembio.2185

(149) Lechner, S.; Malgapo, M. I. P.; Grätz, C.; Steimbach, R. R.; Baron, A.; Rüther, P.; Nadal, S.; Stumpf, C.; Loos, C.; Ku, X.; Prokofeva, P.; Lautenbacher, L.; Heimburg, T.; Würf, V.; Meng, C.; Wilhelm, M.; Sippl, W.; Kleigrewe, K.; Pauling, J. K.; Kramer, K.; Miller, A. K.; Pfaffl, M. W.; Linder, M. E.; Kuster, B.; Médard, G. Target deconvolution of HDAC pharmacopoeia reveals MBLAC2 as common off-target. *Nature Chemical Biology* **2022**, *18* (8), 812-820. DOI: 10.1038/s41589-022-01015-5

(150) Wang, L. Z.; Ramírez, J.; Yeo, W.; Chan, M. Y.; Thuya, W. L.; Lau, J. Y.; Wan, S. C.; Wong, A. L.; Zee, Y. K.; Lim, R.; Lee, S. C.; Ho, P. C.; Lee, H. S.; Chan, A.; Ansher, S.; Ratain, M. J.; Goh, B. C. Glucuronidation by UGT1A1 is the dominant pathway of the metabolic disposition of belinostat in liver cancer patients. *PLoS One* **2013**, *8* (1), e54522. DOI: 10.1371/journal.pone.0054522

(151) Kang, S. P.; Ramirez, J.; House, L.; Zhang, W.; Mirkov, S.; Liu, W.; Haverfield, E.; Ratain, M. J. A pharmacogenetic study of vorinostat glucuronidation. *Pharmacogenetics and Genomics* **2010**, *20* (10), 638-641. DOI: 10.1097/FPC.0b013e32833e1b37

(152) Balliet, R. M.; Chen, G.; Gallagher, C. J.; Dellinger, R. W.; Sun, D.; Lazarus, P. Characterization of UGTs Active against SAHA and Association between SAHA Glucuronidation Activity Phenotype with UGT Genotype. *Cancer Research* **2009**, *69* (7), 2981-2989. DOI: 10.1158/0008-5472.CAN-08-4143

(153) Shen, S.; Kozikowski, A. P. Why Hydroxamates May Not Be the Best Histone Deacetylase Inhibitors—What Some May Have Forgotten or Would Rather Forget? *ChemMedChem* **2016**, *11* (1), 15-21. DOI: https://doi.org/10.1002/cmdc.201500486

(154) Smith, G. F. Designing Drugs to Avoid Toxicity. In *Progress in Medicinal Chemistry*, Lawton, G., Witty, D. R. Eds.; Vol. 50; Elsevier, 2011; pp 1-47.

(155) Sotriffer, C. A. Molecular Dynamics Simulations in Drug Design. In *Encyclopedic Reference of Genomics and Proteomics in Molecular Medicine*, Ganten, D., Ruckpaul, K. Eds.; Springer Berlin Heidelberg, 2006; pp 1153-1160.

(156) Adelusi, T. I.; Oyedele, A.-Q. K.; Boyenle, I. D.; Ogunlana, A. T.; Adeyemi, R. O.; Ukachi, C. D.; Idris, M. O.; Olaoba, O. T.; Adedotun, I. O.; Kolawole, O. E.; Xiaoxing, Y.; Abdul-Hammed, M. Molecular modeling in drug discovery. *Informatics in Medicine Unlocked* **2022**, *29*, 100880. DOI: https://doi.org/10.1016/j.imu.2022.100880

(157) Bülbül, E. F.; Melesina, J.; Ibrahim, H. S.; Abdelsalam, M.; Vecchio, A.; Robaa, D.; Zessin, M.; Schutkowski, M.; Sippl, W. Docking, Binding Free Energy Calculations and In Vitro Characterization of Pyrazine Linked 2-Aminobenzamides as Novel Class I Histone Deacetylase (HDAC) Inhibitors. *Molecules* **2022**, *27* (8), 2526. DOI: 10.3390/molecules27082526

(158) Walters, W. P.; Stahl, M. T.; Murcko, M. A. Virtual screening—an overview. *Drug Discovery Today* **1998**, *3* (4), 160-178. DOI: https://doi.org/10.1016/S1359-6446(97)01163-X

(159) Lavecchia, A.; Di Giovanni, C. Virtual screening strategies in drug discovery: a critical review. *Current Medicinal Chemistry* **2013**, *20* (23), 2839-2860. DOI: 10.2174/09298673113209990001

(160) Sadybekov, A. V.; Katritch, V. Computational approaches streamlining drug discovery. *Nature* **2023**, *616* (7958), 673-685. DOI: 10.1038/s41586-023-05905-z

(161) Irwin, J. J.; Tang, K. G.; Young, J.; Dandarchuluun, C.; Wong, B. R.; Khurelbaatar, M.; Moroz, Y. S.; Mayfield, J.; Sayle, R. A. ZINC20—A Free Ultralarge-Scale Chemical Database for Ligand Discovery. *Journal of Chemical Information and Modeling* **2020**, *60* (12), 6065-6073. DOI: 10.1021/acs.jcim.0c00675

(162) Kralj, S.; Jukič, M.; Bren, U. Molecular Filters in Medicinal Chemistry. *Encyclopedia* **2023**, *3* (2), 501-511. DOI: https://doi.org/10.3390/encyclopedia3020035

(163) Lipinski, C. A. Drug-like properties and the causes of poor solubility and poor permeability. *Journal of Pharmacological and Toxicological Methods* **2000**, *44* (1), 235-249. DOI: 10.1016/s1056-8719(00)00107-6

(164) Walters, W. P.; Murcko, M. A. Prediction of 'drug-likeness'. *Advanced Drug Delivery Reviews* **2002**, *54* (3), 255-271. DOI: 10.1016/s0169-409x(02)00003-0

(165) Walters, W. P.; Namchuk, M. Designing screens: how to make your hits a hit. *Nature Reviews Drug Discovery* **2003**, *2* (4), 259-266. DOI: 10.1038/nrd1063

(166) Lipinski, C. A.; Lombardo, F.; Dominy, B. W.; Feeney, P. J. Experimental and computational approaches to estimate solubility and permeability in drug discovery and development settings. *Advanced Drug Delivery Reviews* **2001**, *46* (1-3), 3-26. DOI: 10.1016/s0169-409x(00)00129-0

(167) Kumari, S.; Chakraborty, S.; Ahmad, M.; Kumar, V.; Tailor, P. B.; Biswal, B. K. Identification of probable inhibitors for the DNA polymerase of the Monkeypox virus through the virtual screening approach. *International Journal of Biological Macromolecules* **2023**, *229*, 515-528. DOI: https://doi.org/10.1016/j.ijbiomac.2022.12.252

(168) Bender, A. Bayesian Methods in Virtual Screening and Chemical Biology. In *Chemoinformatics and Computational Chemical Biology*, Bajorath, J. Ed.; Humana Press, 2011; pp 175-196.

(169) O'Boyle, N. M.; Sayle, R. A. Comparing structural fingerprints using a literature-based similarity benchmark. *Journal of Cheminformatics* **2016**, *8* (1), 36. DOI: 10.1186/s13321-016-0148-0

(170) Sastry, M.; Lowrie, J. F.; Dixon, S. L.; Sherman, W. Large-Scale Systematic Analysis of 2D Fingerprint Methods and Parameters to Improve Virtual Screening Enrichments. *Journal of Chemical Information and Modeling* **2010**, *50* (5), 771-784. DOI: 10.1021/ci100062n

(171) Rogers, D.; Brown, R. D.; Hahn, M. Using extended-connectivity fingerprints with Laplacian-modified Bayesian analysis in high-throughput screening follow-up. *Journal of Biomolecular Screening* **2005**, *10* (7), 682-686. DOI: 10.1177/1087057105281365

(172) Rogers, D.; Hahn, M. Extended-Connectivity Fingerprints. *Journal of Chemical Information and Modeling* **2010**, *50* (5), 742-754. DOI: 10.1021/ci100050t

(173) De, P.; Kar, S.; Ambure, P.; Roy, K. Prediction reliability of QSAR models: an overview of various validation tools. *Archives of Toxicology* **2022**, *96* (5), 1279-1295. DOI: 10.1007/s00204-022-03252-y

(174) Devillers, J. Methods for Building QSARs. In *Computational Toxicology: Volume II*, Reisfeld, B., Mayeno, A. N. Eds.; Humana Press, 2013; pp 3-27.

(175) Golbraikh, A.; Tropsha, A. QSAR/QSPR Revisited. In *Chemoinformatics: Basic Concepts and Methods*, Engel, T., Gasteiger, J. Eds.; Wiley-VCH, 2018; pp 465-495.

(176) Zhang, L.; Zhu, H.; Oprea, T. I.; Golbraikh, A.; Tropsha, A. QSAR modeling of the blood-brain barrier permeability for diverse organic compounds. *Pharmaceutical Research* **2008**, *25* (8), 1902-1914. DOI: 10.1007/s11095-008-9609-0

(177) Sippl, W.; Robaa, D. QSAR/QSPR. In *Applied Chemoinformatics: Achievements and Future Opportunities*, Engel, T., Gasteiger, J. Eds.; Wiley-VCH, 2018; pp 9-52.

(178) Toutah, K.; Nawar, N.; Timonen, S.; Sorger, H.; Raouf, Y. S.; Bukhari, S.; von Jan, J.; Ianevski, A.; Gawel, J. M.; Olaoye, O. O.; Geletu, M.; Abdeldayem, A.; Israelian, J.; Radu, T. B.; Sedighi, A.; Bhatti, M. N.; Hassan, M. M.; Manaswiyoungkul, P.; Shouksmith, A. E.; Neubauer, H. A.; de Araujo, E. D.; Aittokallio, T.; Krämer, O. H.; Moriggl, R.; Mustjoki, S.; Herling, M.; Gunning, P. T. Development of HDAC Inhibitors Exhibiting Therapeutic Potential in T-Cell Prolymphocytic Leukemia. *Journal of Medicinal Chemistry* **2021**, *64* (12), 8486-8509. DOI: 10.1021/acs.jmedchem.1c00420

(179) Olaoye, O. O.; Watson, P. R.; Nawar, N.; Geletu, M.; Sedighi, A.; Bukhari, S.; Raouf, Y. S.; Manaswiyoungkul, P.; Erdogan, F.; Abdeldayem, A.; Cabral, A. D.; Hassan, M. M.; Toutah, K.; Shouksmith, A. E.; Gawel, J. M.; Israelian, J.; Radu, T. B.; Kachhiyapatel, N.; de Araujo, E. D.; Christianson, D. W.; Gunning, P. T. Unique Molecular Interaction with the Histone Deacetylase 6 Catalytic Tunnel: Crystallographic and Biological Characterization of a Model Chemotype. *Journal of Medicinal Chemistry* **2021**, *64* (5), 2691-2704. DOI: 10.1021/acs.jmedchem.0c01922

(180) Nawar, N.; Bukhari, S.; Adile, A. A.; Suk, Y.; Manaswiyoungkul, P.; Toutah, K.; Olaoye, O. O.; Raouf, Y. S.; Sedighi, A.; Garcha, H. K.; Hassan, M. M.; Gwynne, W.; Israelian, J.; Radu, T. B.; Geletu, M.; Abdeldayem, A.; Gawel, J. M.; Cabral, A. D.; Venugopal, C.; de Araujo, E. D.; Singh, S. K.; Gunning, P. T. Discovery of HDAC6-Selective Inhibitor NN-390

with in Vitro Efficacy in Group 3 Medulloblastoma. *Journal of Medicinal Chemistry* **2022**, *65* (4), 3193-3217. DOI: 10.1021/acs.jmedchem.1c01585

(181) Shen, S.; Picci, C.; Ustinova, K.; Benoy, V.; Kutil, Z.; Zhang, G.; Tavares, M. T.; Pavlíček, J.; Zimprich, C. A.; Robers, M. B.; Van Den Bosch, L.; Bařinka, C.; Langley, B.; Kozikowski, A. P. Tetrahydroquinoline-Capped Histone Deacetylase 6 Inhibitor SW-101 Ameliorates Pathological Phenotypes in a Charcot–Marie–Tooth Type 2A Mouse Model. *Journal of Medicinal Chemistry* **2021**, *64* (8), 4810-4840. DOI: 10.1021/acs.jmedchem.0c02210

(182) Garcha, H. K.; Nawar, N.; Sorger, H.; Erdogan, F.; Aung, M. M.; Sedighi, A.; Manaswiyoungkul, P.; Seo, H.-S.; Schönefeldt, S.; Pölöske, D.; Dhe-Paganon, S.; Neubauer, H. A.; Mustjoki, S. M.; Herling, M.; de Araujo, E. D.; Moriggl, R.; Gunning, P. T. High Efficacy and Drug Synergy of HDAC6-Selective Inhibitor NN-429 in Natural Killer (NK)/T-Cell Lymphoma. *Pharmaceuticals* **2022**, *15* (11), 1321. DOI: 10.3390/ph15111321

(183) *Schrödinger Release 2019-1: Maestro, Schrödinger, LLC, New York, NY, 2019.*

(184) *Schrödinger Release 2019-1: LigPrep, Schrödinger, LLC, New York, NY, 2019*.

(185) Baselious, F.; Robaa, D.; Sippl, W. Utilization of AlphaFold models for drug discovery: Feasibility and challenges. Histone deacetylase 11 as a case study. *Computers in Biology and Medicine* **2023**, 107700. DOI: https://doi.org/10.1016/j.compbiomed.2023.107700

(186) *Schrödinger Release 2019-1: Glide, Schrödinger, LLC, New York, NY, 2019*.

(187) Friesner, R. A.; Banks, J. L.; Murphy, R. B.; Halgren, T. A.; Klicic, J. J.; Mainz, D. T.; Repasky, M. P.; Knoll, E. H.; Shelley, M.; Perry, J. K.; Shaw, D. E.; Francis, P.; Shenkin, P. S. Glide: a new approach for rapid, accurate docking and scoring. 1. Method and assessment of docking accuracy. *Journal of Medicinal Chemistry* **2004**, *47* (7), 1739-1749. DOI: 10.1021/jm0306430

(188) Friesner, R. A.; Murphy, R. B.; Repasky, M. P.; Frye, L. L.; Greenwood, J. R.; Halgren, T. A.; Sanschagrin, P. C.; Mainz, D. T. Extra precision glide: docking and scoring incorporating a model of hydrophobic enclosure for protein-ligand complexes. *Journal of Medicinal Chemistry* **2006**, *49* (21), 6177-6196. DOI: 10.1021/jm051256o

(189) Halgren, T. A.; Murphy, R. B.; Friesner, R. A.; Beard, H. S.; Frye, L. L.; Pollard, W. T.; Banks, J. L. Glide: A New Approach for Rapid, Accurate Docking and Scoring. 2. Enrichment

Factors in Database Screening. *Journal of Medicinal Chemistry* **2004**, *47* (7), 1750-1759. DOI: 10.1021/jm030644s

(190) Jorgensen, W. L.; Maxwell, D. S.; Tirado-Rives, J. Development and Testing of the OPLS All-Atom Force Field on Conformational Energetics and Properties of Organic Liquids. *Journal of the American Chemical Society* **1996**, *118* (45), 11225-11236. DOI: 10.1021/ja9621760

(191) Jorgensen, W. L.; Tirado-Rives, J. The OPLS [optimized potentials for liquid simulations] potential functions for proteins, energy minimizations for crystals of cyclic peptides and crambin. *Journal of the American Chemical Society* **1988**, *110* (6), 1657-1666. DOI: 10.1021/ja00214a001

(192) Harder, E.; Damm, W.; Maple, J.; Wu, C.; Reboul, M.; Xiang, J. Y.; Wang, L.; Lupyan, D.; Dahlgren, M. K.; Knight, J. L.; Kaus, J. W.; Cerutti, D. S.; Krilov, G.; Jorgensen, W. L.; Abel, R.; Friesner, R. A. OPLS3: A Force Field Providing Broad Coverage of Drug-like Small Molecules and Proteins. *Journal of Chemical Theory and Computation* **2016**, *12* (1), 281-296. DOI: 10.1021/acs.jctc.5b00864

(193) Shivakumar, D.; Williams, J.; Wu, Y.; Damm, W.; Shelley, J.; Sherman, W. Prediction of Absolute Solvation Free Energies using Molecular Dynamics Free Energy Perturbation and the OPLS Force Field. *Journal of Chemical Theory and Computation* **2010**, *6* (5), 1509-1519. DOI: 10.1021/ct900587b

(194) *Schrödinger Release 2019-1; Desmond Molecular Dynamics System, D.E. Shaw Research: New York, NY, USA, 2019; Maestro-Desmond Interoperability Tools, Schrödinger: New York, NY, USA, 2019*.

(195) Bowers, K. J.; Chow, D. E.; Xu, H.; Dror, R. O.; Eastwood, M. P.; Gregersen, B. A.; Klepeis, J. L.; Kolossvary, I.; Moraes, M. A.; Sacerdoti, F. D.; Salmon, J. K.; Shan, Y.; Shaw, D. E. Scalable Algorithms for Molecular Dynamics Simulations on Commodity Clusters. In *SC '06: Proceedings of the 2006 ACM/IEEE Conference on Supercomputing*, 11-17 Nov. 2006, 2006; pp 43-43. DOI: 10.1109/SC.2006.54.

(196) *Schrödinger Release 2019-1: QikProp, Schrödinger, LLC, New York, NY, 2019*.

(197) *Schrödinger Release 2019-1: Canvas, Schrödinger, LLC, New York, NY, 2019*.

(198) Duan, J.; Dixon, S. L.; Lowrie, J. F.; Sherman, W. Analysis and comparison of 2D fingerprints: insights into database screening performance using eight fingerprint methods. *Journal of Molecular Graphics and Modelling* **2010**, *29* (2), 157-170. DOI: 10.1016/j.jmgm.2010.05.008

(199) Zhang, S.; Golbraikh, A.; Oloff, S.; Kohn, H.; Tropsha, A. A Novel Automated Lazy Learning QSAR (ALL-QSAR) Approach: Method Development, Applications, and Virtual Screening of Chemical Databases Using Validated ALL-QSAR Models. *Journal of Chemical Information and Modeling* **2006**, *46* (5), 1984-1995. DOI: 10.1021/ci060132x

(200) Tropsha, A.; Gramatica, P.; Gombar, V. K. The Importance of Being Earnest: Validation is the Absolute Essential for Successful Application and Interpretation of QSPR Models. *QSAR & Combinatorial Science* **2003**, *22* (1), 69-77. DOI: https://doi.org/10.1002/qsar.200390007

(201) Tingle, B. I.; Tang, K. G.; Castanon, M.; Gutierrez, J. J.; Khurelbaatar, M.; Dandarchuluun, C.; Moroz, Y. S.; Irwin, J. J. ZINC-22─A Free Multi-Billion-Scale Database of Tangible Compounds for Ligand Discovery. *Journal of Chemical Information and Modeling* **2023**, *63* (4), 1166-1176. DOI: 10.1021/acs.jcim.2c01253

This page left intentionally blank.

7. Appendix

This page left intentionally blank.

7.1. Figures

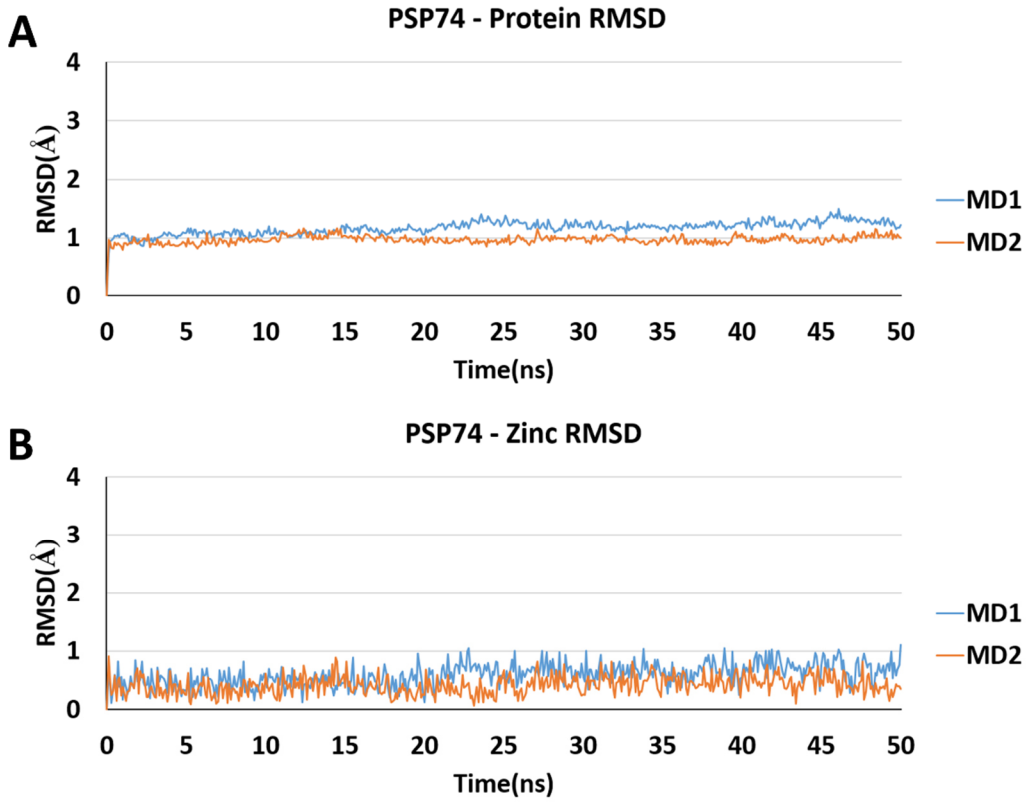

Figure S21. (**A**) and (**B**). RMSD plots of protein backbone heavy atoms and zinc ion, respectively, for two independent MD simulations of PSP74.

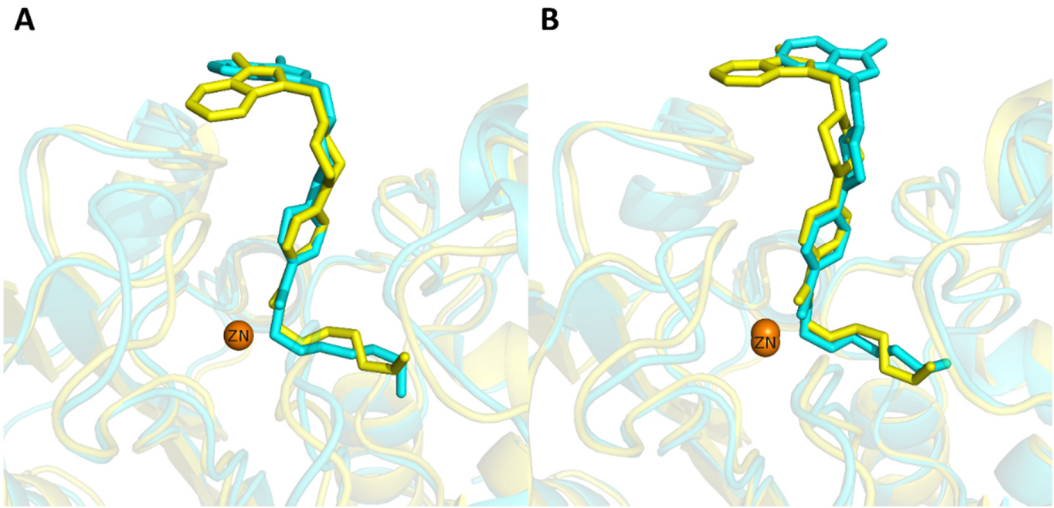

Figure S22. Superposition of the first (yellow) and last (cyan) frames demonstrating the fluctuation of the ligand. (**A**) and (**B**). Two independent MD simulations of PSP74. The zinc ion is represented as orange sphere, the protein backbone as cartoon and the ligand as sticks.

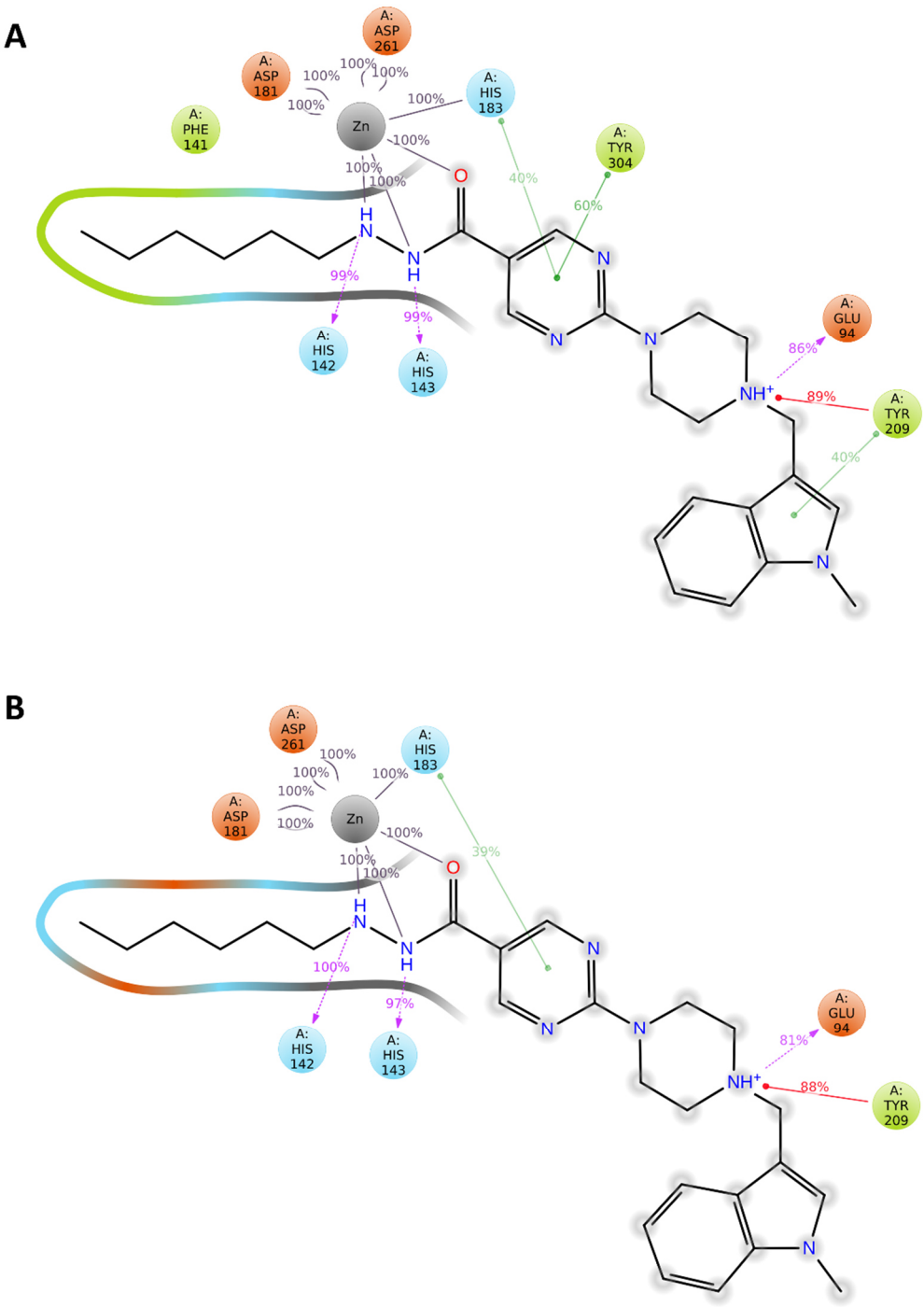

Figure S23. (**A**) and (**B**). Ligand interaction persistence diagram for the first and second independent MD simulations of PSP74, respectively. Hydrogen bonds are represented as pink arrows, π-π interactions as green lines, π-cation interactions as red lines and metal coordination bonds as grey lines.

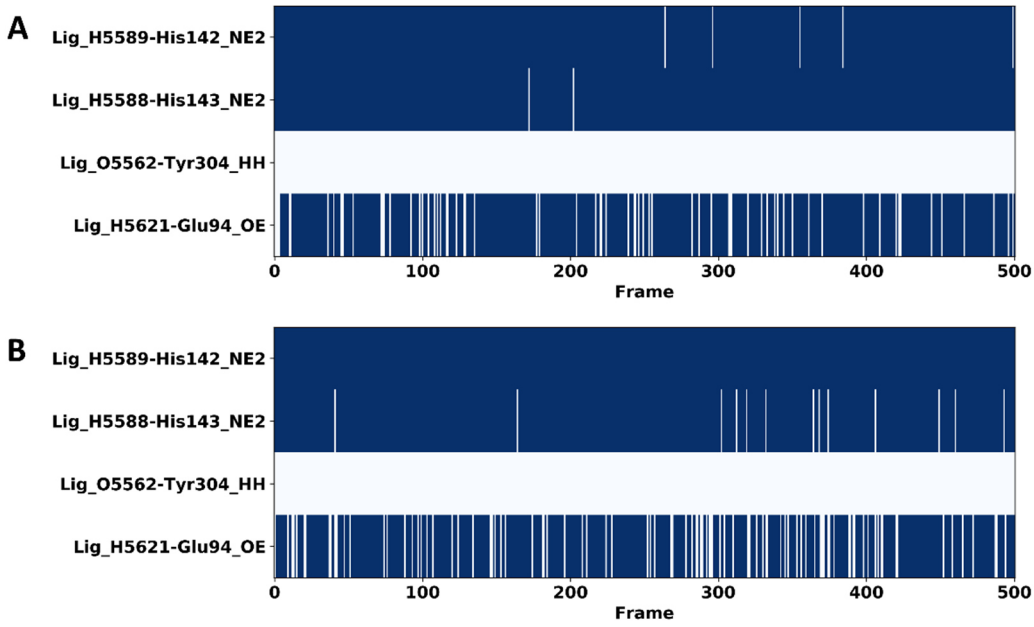

Figure S24. (**A**) and (**B**). Hydrogen bond occupancy diagrams for the first and second independent MD simulations of PSP74, respectively.

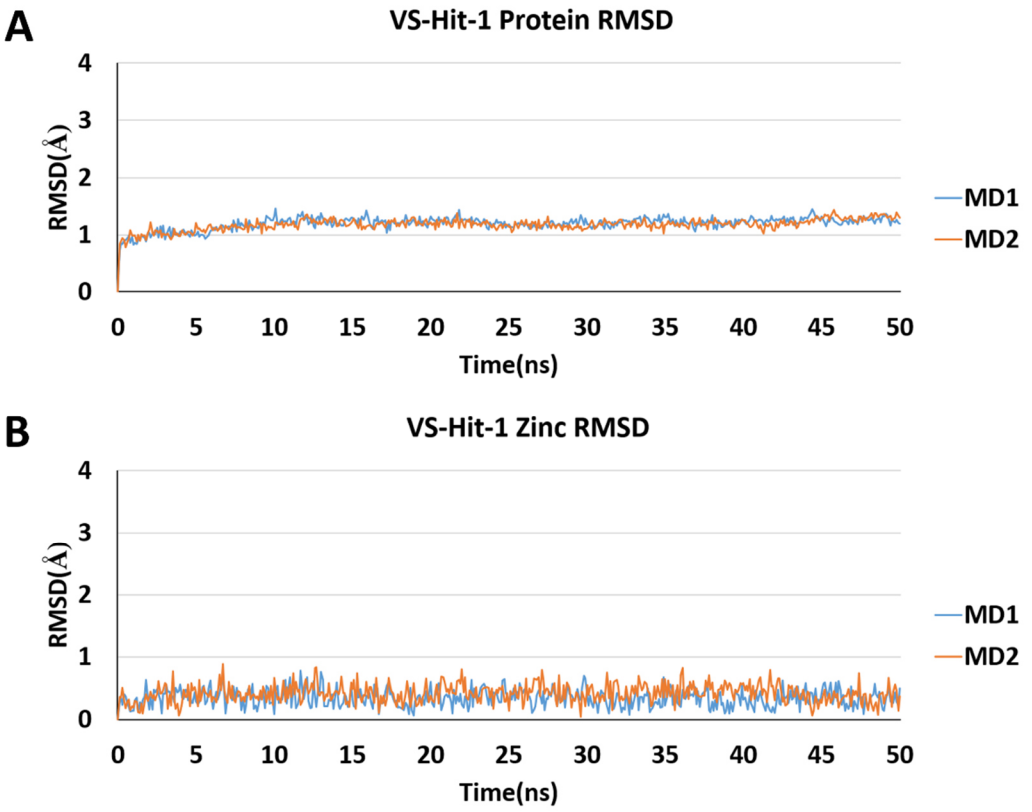

Figure S25. (**A**) and (**B**). RMSD plots of protein backbone heavy atoms and zinc ion, respectively, for two independent MD simulations of **hit-1**.

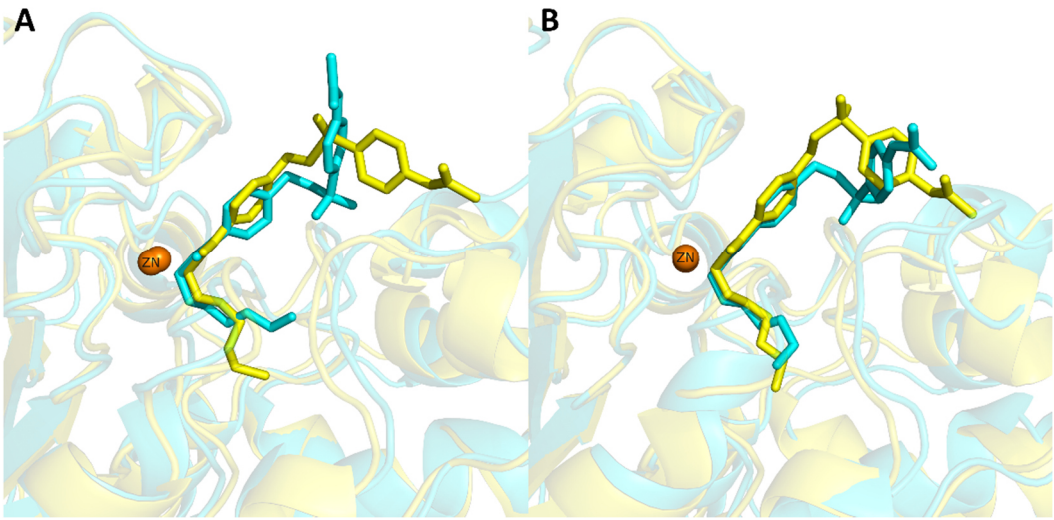

Figure S26. Superposition of the first (yellow) and last (cyan) frames demonstrating the fluctuation of the ligand. (**A**) and (**B**). Two independent MD simulations of **hit-1**. The zinc ion is represented as orange sphere, the protein backbone as cartoon and the ligand as sticks.

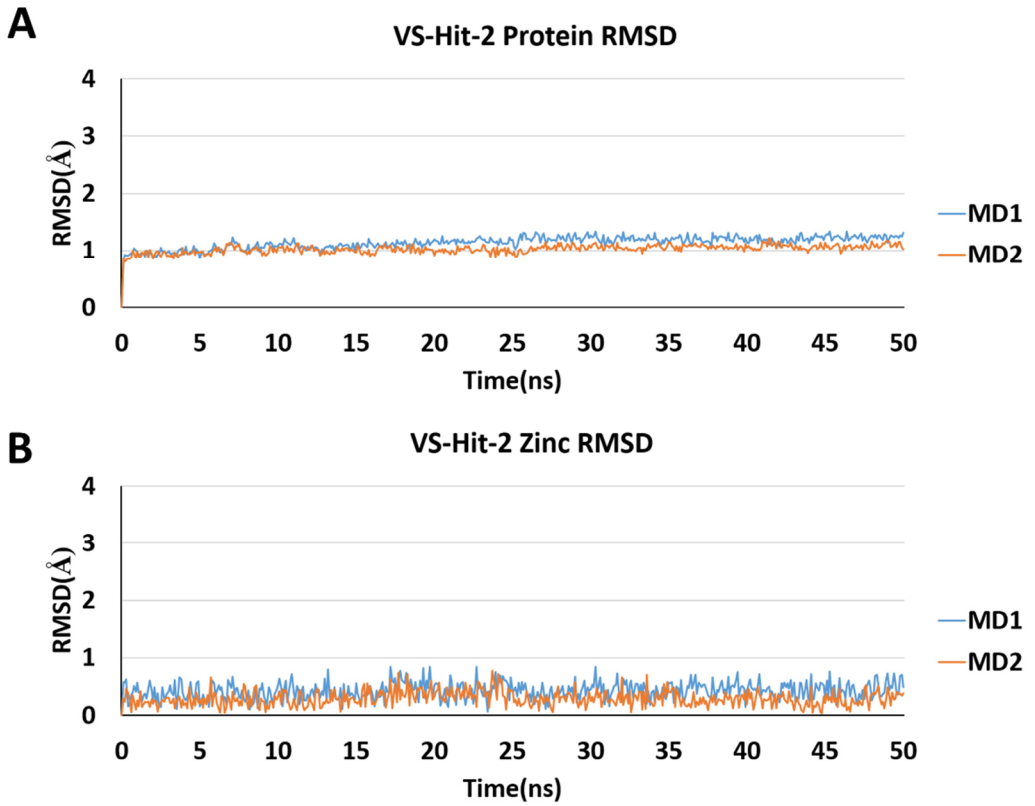

Figure S27. (**A**) and (**B**). RMSD plots of protein backbone heavy atoms and zinc ion, respectively, for two independent MD simulations of **hit-2**.

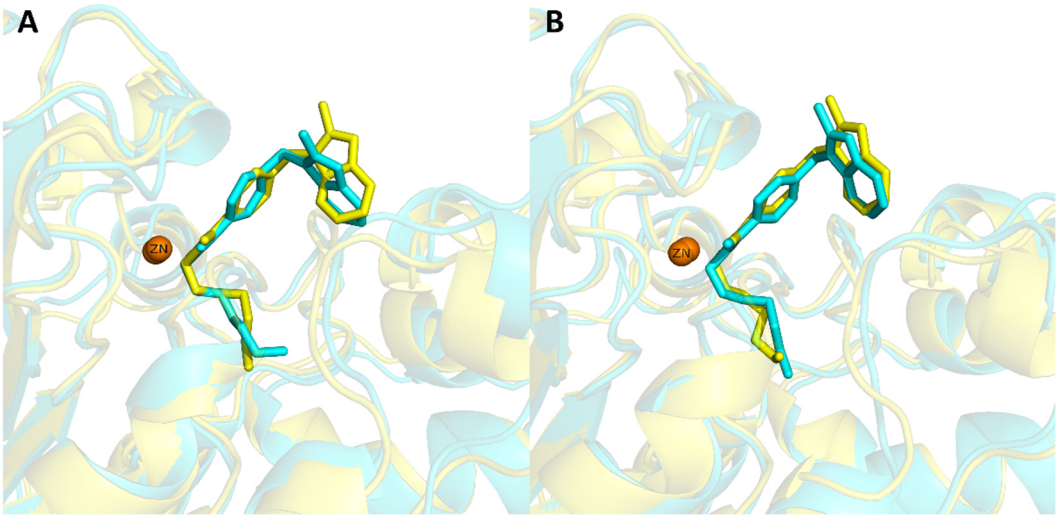

Figure S28. Superposition of the first (yellow) and last (cyan) frames demonstrating the fluctuation of the ligand. (**A**) and (**B**). Two independent MD simulations of **hit-2**. The zinc ion is represented as orange sphere, the protein backbone as cartoon and the ligand as sticks.

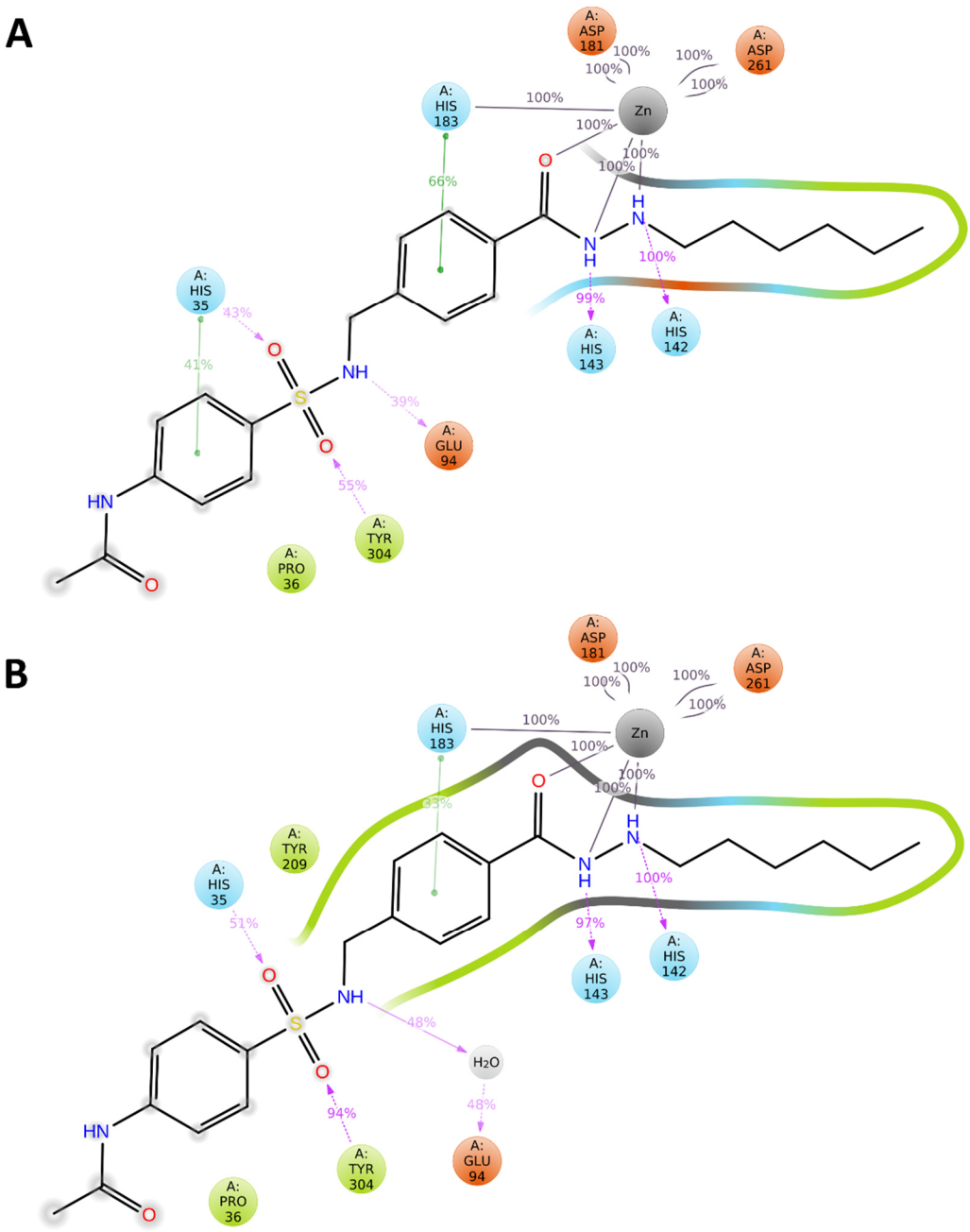

Figure S29. (**A**) and (**B**). Ligand interaction persistence diagram for the first and second independent MD simulations of **hit-1**, respectively. Hydrogen bonds are represented as pink arrows, π-π interactions as green lines and metal coordination bonds as grey lines.

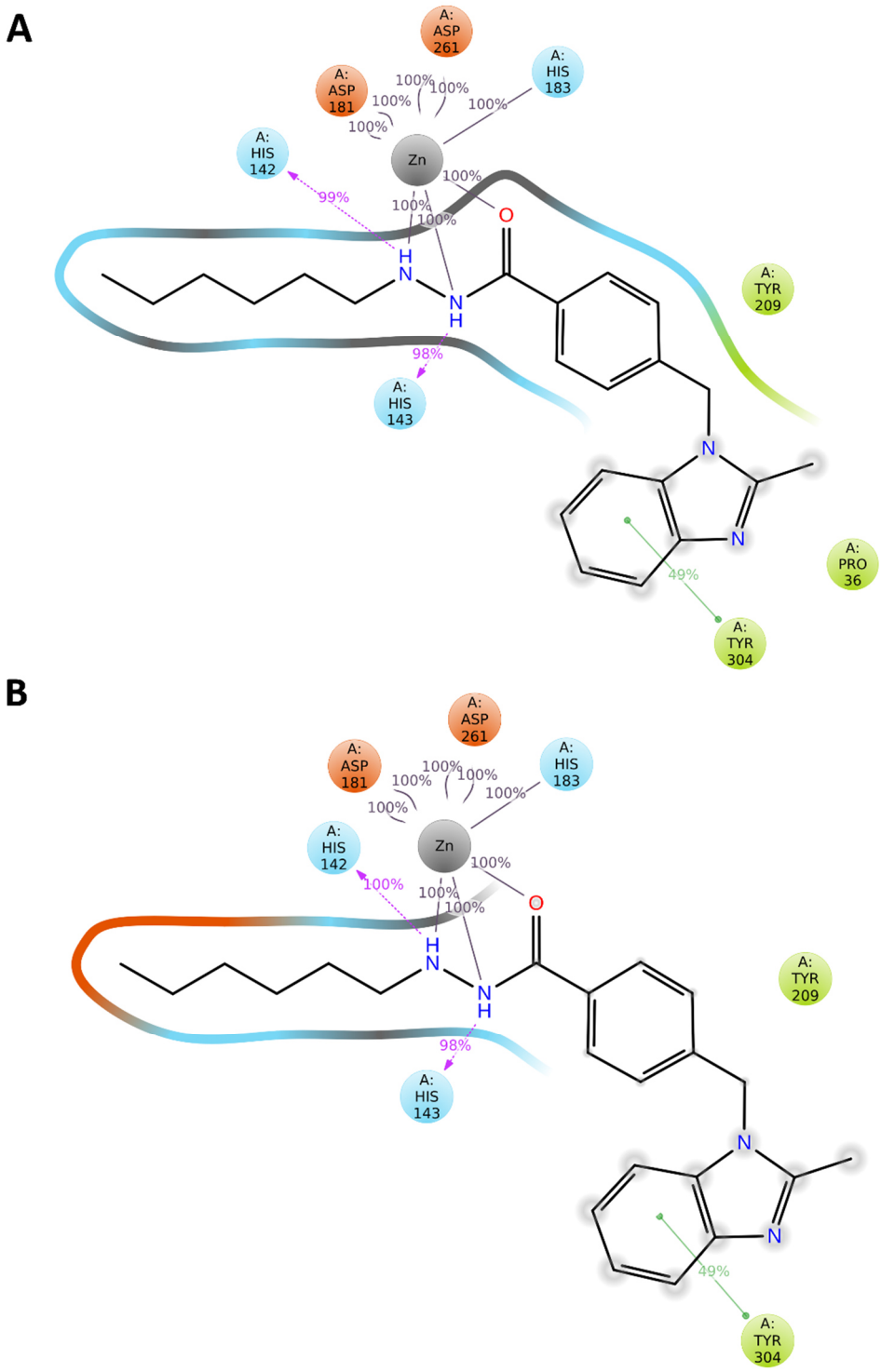

Figure S30. (**A**) and (**B**). Ligand interaction persistence diagram for the first and second independent MD simulations of **hit-2**, respectively. Hydrogen bonds are represented as pink arrows, π-π interactions as green lines and metal coordination bonds as grey lines.

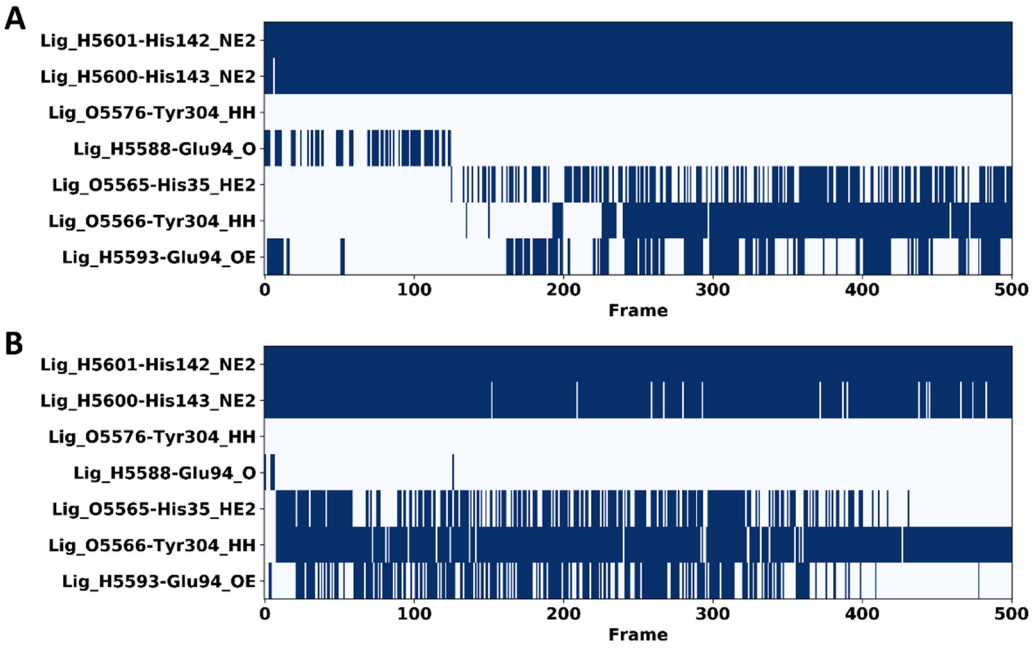

Figure S31. (**A**) and (**B**). Hydrogen bond occupancy diagrams for the first and second independent MD simulations of **hit-1**, respectively.

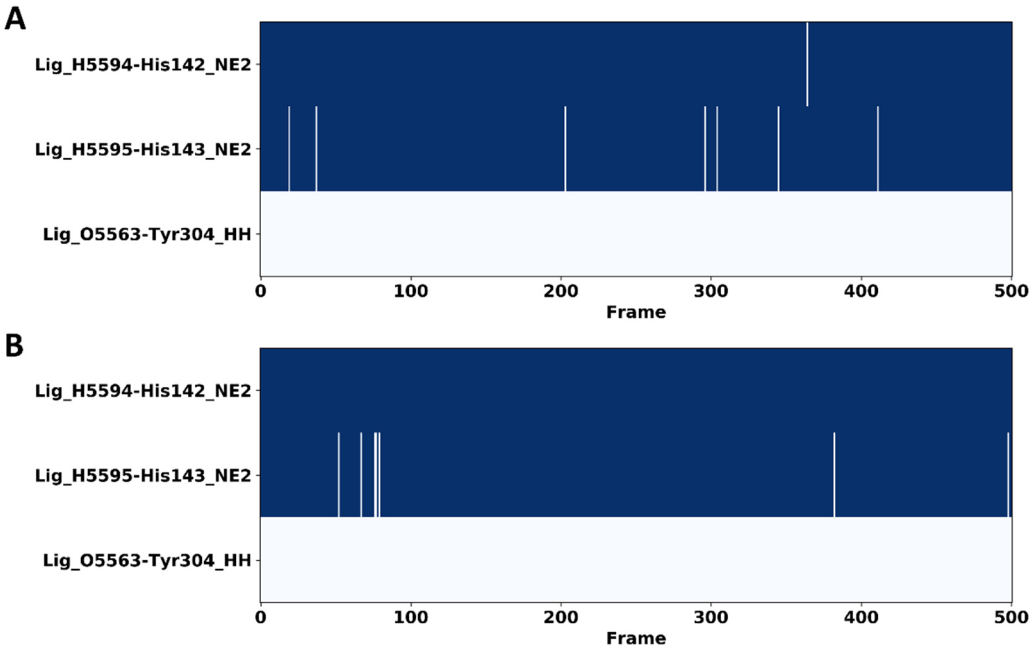

Figure S32. (**A**) and (**B**). Hydrogen bond occupancy diagrams for the first and second independent MD simulations of **hit-2**, respectively.

7.2. Tables

Table S2. Hydrogen bond persistence for 2 independent 50 ns MD simulations of PSP74.

	PSP74			
	HIS142	**HIS143**	**Tyr304**	**Glu94**
MD-1	99.00	99.60	3.79	86.63
MD-2	100.00	97.41	0	81.44

Table S3. Hydrogen bond persistence for 2 independent 50 ns MD simulations of **hit-1**.

	VS-hit1						
	His142	**His143**	**Tyr304-C=O**	**Tyr304-S=O**	**His35**	**Glu94_O**	**Glu94_OE**
MD-1	100.00	99.80	0.00	55.29	43.11	13.57	39.12
MD-2	100.00	97.01	0.00	94.41	51.30	1.00	48.10

Table S4. Hydrogen bond persistence for 2 independent 50 ns MD simulations of **hit-2**.

	VS-hit2		
	His142	**His143**	**Tyr304**
MD-1	99.80	98.60	0.00
MD-2	100.00	98.60	0.00

Table S5. Validation of the developed categorical model using different training and test sets.

Set 1							
Training set				**Test set**			
Activity	**Correct**	**Incorrect**	**Total**	**Activity**	**Correct**	**Incorrect**	**Total**
0	33	2	35	0	11	2	13
1	24	1	25	1	5	2	7
Total	57	3	60	**Total**	16	4	20
specificity	**94.29**			**specificity**	**84.62**		
sensitivity	**96.00**			**sensitivity**	**71.43**		
accuracy	**95.00**			**accuracy**	**80.00**		
Set 2							
Training set				**Test set**			
Activity	**Correct**	**Incorrect**	**Total**	**Activity**	**Correct**	**Incorrect**	**Total**
0	34	2	36	0	11	1	12
1	23	1	24	1	6	2	8
Total	57	3	60	**Total**	17	3	20
specificity	**94.44**			**specificity**	**91.67**		
sensitivity	**95.83**			**sensitivity**	**75.00**		
accuracy	**95.00**			**accuracy**	**85.00**		

Set 3							
Training set				**Test set**			
Activity	**Correct**	**Incorrect**	**Total**	**Activity**	**Correct**	**Incorrect**	**Total**
0	33	2	35	0	11	2	13
1	24	1	25	1	5	2	7
Total	57	3	60	**Total**	16	4	20
specificity	**94.29**			**specificity**	**84.62**		
sensitivity	**96.00**			**sensitivity**	**71.43**		
accuracy	**95.00**			**accuracy**	**80.00**		
Set 4							
Training set				**Test set**			
Activity	**Correct**	**Incorrect**	**Total**	**Activity**	**Correct**	**Incorrect**	**Total**
0	36	2	38	0	9	1	10
1	21	1	22	1	8	2	10
Total	57	3	60	**Total**	17	3	20
specificity	**94.74**			**specificity**	**90.00**		
sensitivity	**95.45**			**sensitivity**	**80.00**		
accuracy	**95.00**			**accuracy**	**85.00**		

Table S6. List of compounds used in the categorical model with their actual and predicted activity classes.

Categorical Model				
NO.	**Compound**	**Model Set**	**Activity**	**Predicted**
1	FM18	training	1	1
2	FM19	training	1	1
3	FM39	training	1	1
4	FM40	training	1	1
5	FM42	training	1	1
6	FM43	training	1	1
7	FM44	training	1	1
8	FM46	training	1	1
9	FM47	training	1	1
10	FM48	training	1	1
11	FM77	training	1	1
12	FM9	training	0	0
13	FM45	training	0	1
14	FM49	training	0	1
15	NM-H-1	training	0	0
16	NM-H-3	training	0	0
17	PR4	training	1	1
18	PR8	training	1	1
19	PSP42	training	1	1

Categorical Model				
NO.	**Compound**	**Model Set**	**Activity**	**Predicted**
20	PSP43	training	1	0
21	PR3	training	0	0
22	PSP40	training	0	0
23	PSP41	training	0	0
24	PSP81	training	0	0
25	FM80	training	1	1
26	FM122	training	1	1
27	FM128	training	1	1
28	FM129	training	1	1
29	FM130	training	1	1
30	FM131	training	1	1
31	FM132	training	1	1
32	FM133	training	1	1
33	PR18	training	1	1
34	FM11	training	0	0
35	FM76	training	0	0
36	FM123	training	0	0
37	FM124	training	0	0
38	FM125	training	0	0
39	FM126	training	0	0
40	FM127	training	0	0
41	PSP39	training	0	0
42	PSP67	training	0	0
43	PSP50	training	1	1
44	PSP51	training	1	1
45	PSP52	training	1	1
46	PSP71	training	1	1
47	PSP72	training	1	1
48	PSP73	training	1	1
49	PSP74	training	1	1
50	PSP45	training	0	0
51	PSP49	training	0	1
52	PSP84	training	0	0
53	NI82	training	0	0
54	PR2	training	0	0
55	PR2.1	training	0	0
56	PR6	training	0	0
57	PR14	training	0	0
58	PR15	training	0	0
59	NI16	training	0	0
60	NI26	training	0	0

Categorical Model				
NO.	**Compound**	**Model Set**	**Activity**	**Predicted**
61	NI32	training	0	0
62	NI173	training	0	0
63	PSP47	training	0	0
64	PSP48	training	0	0
65	PSP69	training	0	0
66	PSP70	training	0	0
67	PSP82	training	0	0
68	PSP83	training	0	0
69	FM21	training	0	0
70	FM22	training	0	0
71	PR1	training	0	0
72	PR19	training	0	0
73	SIS17	training	1	1
74	PR11	training	0	0
75	PR12	training	0	0
76	PR16	training	0	0
77	PR20	training	0	0
78	PR21	training	0	0
79	PR22	training	0	0
80	PR23	training	0	0

Table S7. List of training and test compounds used in validation set 1 with their actual and predicted activity classes.

Set 1				
NO.	**Compound**	**Model Set**	**Activity**	**Predicted**
1	FM18	training	1	1
2	FM19	training	1	1
3	FM39	training	1	1
4	FM40	test	1	1
5	FM42	training	1	1
6	FM43	training	1	1
7	FM44	training	1	1
8	FM46	test	1	1
9	FM47	training	1	1
10	FM48	training	1	1
11	FM77	training	1	1
12	FM9	test	0	1
13	FM45	training	0	1
14	FM49	training	0	1
15	NM-H-1	training	0	0
16	NM-H-3	test	0	0

Set 1				
NO.	**Compound**	**Model Set**	**Activity**	**Predicted**
17	PR4	training	1	1
18	PR8	training	1	1
19	PSP42	training	1	0
20	PSP43	test	1	0
21	PR3	training	0	0
22	PSP40	training	0	0
23	PSP41	training	0	0
24	PSP81	test	0	0
25	FM80	training	1	1
26	FM122	training	1	1
27	FM128	training	1	1
28	FM129	test	1	1
29	FM130	training	1	1
30	FM131	training	1	1
31	FM132	training	1	1
32	FM133	test	1	1
33	PR18	training	1	1
34	FM11	training	0	0
35	FM76	training	0	0
36	FM123	test	0	0
37	FM124	training	0	0
38	FM125	training	0	0
39	FM126	training	0	0
40	FM127	test	0	0
41	PSP39	training	0	0
42	PSP67	training	0	0
43	PSP50	training	1	1
44	PSP51	test	1	1
45	PSP52	training	1	1
46	PSP71	training	1	1
47	PSP72	training	1	1
48	PSP73	test	1	0
49	PSP74	training	1	1
50	PSP45	training	0	0
51	PSP49	training	0	0
52	PSP84	test	0	0
53	NI82	training	0	0
54	PR2	training	0	0
55	PR2.1	training	0	0
56	PR6	test	0	0
57	PR14	training	0	0
58	PR15	training	0	0

Set 1				
NO.	**Compound**	**Model Set**	**Activity**	**Predicted**
59	NI16	training	0	0
60	NI26	test	0	0
61	NI32	training	0	0
62	NI173	training	0	0
63	PSP47	training	0	0
64	PSP48	test	0	0
65	PSP69	training	0	0
66	PSP70	training	0	0
67	PSP82	training	0	0
68	PSP83	test	0	0
69	FM21	training	0	0
70	FM22	training	0	0
71	PR1	training	0	0
72	PR19	test	0	0
73	SIS17	training	1	1
74	PR11	training	0	0
75	PR12	training	0	0
76	PR16	test	0	1
77	PR20	training	0	0
78	PR21	training	0	0
79	PR22	training	0	0
80	PR23	test	0	0

Table S8. List of training and test compounds used in validation set 2 with their actual and predicted activity classes.

Set 2				
NO.	**Compound**	**Model Set**	**Activity**	**Predicted**
1	FM18	training	1	1
2	FM19	training	1	1
3	FM39	test	1	1
4	FM40	training	1	1
5	FM42	training	1	1
6	FM43	training	1	1
7	FM44	test	1	1
8	FM46	training	1	1
9	FM47	training	1	1
10	FM48	training	1	1
11	FM77	test	1	0
12	FM9	training	0	0
13	FM45	training	0	1
14	FM49	training	0	1

Set 2				
NO.	**Compound**	**Model Set**	**Activity**	**Predicted**
15	NM-H-1	test	0	0
16	NM-H-3	training	0	0
17	PR4	training	1	1
18	PR8	training	1	1
19	PSP42	test	1	0
20	PSP43	training	1	0
21	PR3	training	0	0
22	PSP40	training	0	0
23	PSP41	test	0	0
24	PSP81	training	0	0
25	FM80	training	1	1
26	FM122	training	1	1
27	FM128	test	1	1
28	FM129	training	1	1
29	FM130	training	1	1
30	FM131	training	1	1
31	FM132	test	1	1
32	FM133	training	1	1
33	PR18	training	1	1
34	FM11	training	0	0
35	FM76	test	0	0
36	FM123	training	0	0
37	FM124	training	0	0
38	FM125	training	0	0
39	FM126	test	0	0
40	FM127	training	0	0
41	PSP39	training	0	0
42	PSP67	training	0	0
43	PSP50	test	1	1
44	PSP51	training	1	1
45	PSP52	training	1	1
46	PSP71	training	1	1
47	PSP72	test	1	1
48	PSP73	training	1	1
49	PSP74	training	1	1
50	PSP45	training	0	0
51	PSP49	test	0	1
52	PSP84	training	0	0
53	NI82	training	0	0
54	PR2	training	0	0
55	PR2.1	test	0	0
56	PR6	training	0	0

Set 2				
NO.	**Compound**	**Model Set**	**Activity**	**Predicted**
57	PR14	training	0	0
58	PR15	training	0	0
59	NI16	test	0	0
60	NI26	training	0	0
61	NI32	training	0	0
62	NI173	training	0	0
63	PSP47	test	0	0
64	PSP48	training	0	0
65	PSP69	training	0	0
66	PSP70	training	0	0
67	PSP82	test	0	0
68	PSP83	training	0	0
69	FM21	training	0	0
70	FM22	training	0	0
71	PR1	test	0	0
72	PR19	training	0	0
73	SIS17	training	1	1
74	PR11	training	0	0
75	PR12	test	0	0
76	PR16	training	0	0
77	PR20	training	0	0
78	PR21	training	0	0
79	PR22	test	0	0
80	PR23	training	0	0

Table S9. List of training and test compounds used in validation set 3 with their actual and predicted activity classes.

Set 3				
NO.	**Compound**	**Model Set**	**Activity**	**Predicted**
1	FM18	training	1	1
2	FM19	test	1	1
3	FM39	training	1	1
4	FM40	training	1	1
5	FM42	training	1	1
6	FM43	test	1	1
7	FM44	training	1	1
8	FM46	training	1	1
9	FM47	training	1	1
10	FM48	test	1	1
11	FM77	training	1	1
12	FM9	training	0	0

Set 3				
NO.	**Compound**	**Model Set**	**Activity**	**Predicted**
13	FM45	training	0	1
14	FM49	test	0	1
15	NM-H-1	training	0	0
16	NM-H-3	training	0	0
17	PR4	training	1	1
18	PR8	test	1	0
19	PSP42	training	1	1
20	PSP43	training	1	0
21	PR3	training	0	0
22	PSP40	test	0	0
23	PSP41	training	0	0
24	PSP81	training	0	0
25	FM80	training	1	1
26	FM122	test	1	0
27	FM128	training	1	1
28	FM129	training	1	1
29	FM130	training	1	1
30	FM131	test	1	1
31	FM132	training	1	1
32	FM133	training	1	1
33	PR18	training	1	1
34	FM11	test	0	0
35	FM76	training	0	0
36	FM123	training	0	0
37	FM124	training	0	0
38	FM125	test	0	0
39	FM126	training	0	0
40	FM127	training	0	0
41	PSP39	training	0	0
42	PSP67	test	0	0
43	PSP50	training	1	1
44	PSP51	training	1	1
45	PSP52	training	1	1
46	PSP71	test	1	1
47	PSP72	training	1	1
48	PSP73	training	1	1
49	PSP74	training	1	1
50	PSP45	test	0	1
51	PSP49	training	0	1
52	PSP84	training	0	0
53	NI82	training	0	0
54	PR2	test	0	0

Set 3				
NO.	**Compound**	**Model Set**	**Activity**	**Predicted**
55	PR2.1	training	0	0
56	PR6	training	0	0
57	PR14	training	0	0
58	PR15	test	0	0
59	NI16	training	0	0
60	NI26	training	0	0
61	NI32	training	0	0
62	NI173	test	0	0
63	PSP47	training	0	0
64	PSP48	training	0	0
65	PSP69	training	0	0
66	PSP70	test	0	0
67	PSP82	training	0	0
68	PSP83	training	0	0
69	FM21	training	0	0
70	FM22	test	0	0
71	PR1	training	0	0
72	PR19	training	0	0
73	SIS17	training	1	1
74	PR11	test	0	0
75	PR12	training	0	0
76	PR16	training	0	0
77	PR20	training	0	0
78	PR21	test	0	0
79	PR22	training	0	0
80	PR23	training	0	0

Table S10. List of training and test compounds used in validation set 4 with their actual and predicted activity classes.

Set 4				
NO.	**Compound**	**Model Set**	**Activity**	**Predicted**
1	FM18	test	1	1
2	FM19	training	1	1
3	FM39	training	1	1
4	FM40	training	1	1
5	FM42	test	1	0
6	FM43	training	1	1
7	FM44	training	1	1
8	FM46	training	1	1
9	FM47	test	1	1
10	FM48	training	1	1

Set 4				
NO.	**Compound**	**Model Set**	**Activity**	**Predicted**
11	FM77	training	1	1
12	FM9	training	0	0
13	FM45	test	0	0
14	FM49	training	0	1
15	NM-H-1	training	0	0
16	NM-H-3	training	0	0
17	PR4	test	1	1
18	PR8	training	1	1
19	PSP42	training	1	1
20	PSP43	training	1	0
21	PR3	test	0	1
22	PSP40	training	0	0
23	PSP41	training	0	0
24	PSP81	training	0	0
25	FM80	test	1	1
26	FM122	training	1	1
27	FM128	training	1	1
28	FM129	training	1	1
29	FM130	test	1	1
30	FM131	training	1	1
31	FM132	training	1	1
32	FM133	training	1	1
33	PR18	test	1	0
34	FM11	training	0	0
35	FM76	training	0	0
36	FM123	training	0	0
37	FM124	test	0	0
38	FM125	training	0	0
39	FM126	training	0	0
40	FM127	training	0	0
41	PSP39	test	0	0
42	PSP67	training	0	0
43	PSP50	training	1	1
44	PSP51	training	1	1
45	PSP52	test	1	1
46	PSP71	training	1	1
47	PSP72	training	1	1
48	PSP73	training	1	1
49	PSP74	test	1	1
50	PSP45	training	0	0
51	PSP49	training	0	1
52	PSP84	training	0	0

Set 4				
NO.	**Compound**	**Model Set**	**Activity**	**Predicted**
53	NI82	test	0	0
54	PR2	training	0	0
55	PR2.1	training	0	0
56	PR6	training	0	0
57	PR14	test	0	0
58	PR15	training	0	0
59	NI16	training	0	0
60	NI26	training	0	0
61	NI32	test	0	0
62	NI173	training	0	0
63	PSP47	training	0	0
64	PSP48	training	0	0
65	PSP69	test	0	0
66	PSP70	training	0	0
67	PSP82	training	0	0
68	PSP83	training	0	0
69	FM21	test	0	0
70	FM22	training	0	0
71	PR1	training	0	0
72	PR19	training	0	0
73	SIS17	test	1	1
74	PR11	training	0	0
75	PR12	training	0	0
76	PR16	training	0	0
77	PR20	test	0	0
78	PR21	training	0	0
79	PR22	training	0	0
80	PR23	training	0	0

Curriculum vitae

Fady Baselious

Email address: f_noshy@yahoo.com

Website: https://www.researchgate.net/profile/Fady_Baselious

Website: https://www.linkedin.com/in/fady-baselious-1345978b/

Website: https://scholar.google.com/citations?user=iUZOF1MAAAAJ&hl=en

WORK EXPERIENCE

PhD Researcher

Martin Luther University [01/06/2021 – Current]

City: Halle (Saale) **| Country:** Germany

Department of Medicinal Chemistry, Institute of Pharmacy, Martin-Luther-University of Halle-Wittenberg

Thesis Project: **Computational molecular modeling and design of novel histone deacetylase (HDAC) inhibitors and PROTACs**.

Visiting Researcher

Goethe University [01/03/2021 – 31/05/2021]

City: Frankfurt **| Country:** Germany

Project: **Design and synthesis of tropane based chalcones and bis-benzylidene hydrazones as novel Rpn13 inhibitors and active site probes.**

Research and Development Unit Head (Methodology Lab.)

Global Napi Pharmaceuticals [08/2019 – 28/02/2021]

City: 6th October City **| Country:** Egypt

Research and Development Supervisor (Methodology Lab.)

Global Napi Pharmaceuticals [08/2016 – 07/2019]

City: 6th October City **| Country:** Egypt

Research and Development Senior Specialist (Methodology Lab.)

Global Napi Pharmaceuticals [09/2015 – 07/2016]

City: 6th October City **| Country:** Egypt

Research and Development Specialist (Methodology Lab.)

Global Napi Pharmaceuticals [07/2011 – 08/2015]

City: 6th October City

Quality control analyst (bulk and finished products)

Marcyrl Pharmaceutical Industries [09/2010 – 07/2011]

City: El-Obour City **| Country:** Egypt

Community Pharmacist

Metro Pharmacy/Mohsen Ramzy Pharmacy/Oscar Pharmacy [08/2009 – 08/2010]

City: Cairo **| Country:** Egypt

EDUCATION AND TRAINING

Master of Science in Pharmaceutical Chemistry

Faculty of Pharmacy, Ain Shams University [09/2012 – 05/2017]

City: Cairo **| Country:** Egypt **| NQF Level:** Excellent (85%) Pre-master Course

Bachelor of Pharmaceutical Sciences

Faculty of Pharmacy, Cairo University [09/2004 – 05/2009]

City: Cairo **| Country:** Egypt **| NQF Level:** Very Good (80.81%)

General Secondary Certificate

Greek Catholic Patriarchal Collage [09/2001 – 05/2004]

City: Cairo **| Country:** Egypt **| NQF Level:** 96.7%

COURSES

[16/03/2024]

Programming for Everybody (Getting Started with Python)

Coursera - University of Michigan

[07/01/2023]

Python for Genomic Data Science

Coursera - Johns Hopkins University

LANGUAGE SKILLS

Mother tongue(s): Arabic

Other language(s):

English

LISTENING C1 **READING** C1 **WRITING** C1

SPOKEN PRODUCTION C1 **SPOKEN INTERACTION** C1

German

LISTENING A1 **READING** A1 **WRITING** A1

SPOKEN PRODUCTION A1 **SPOKEN INTERACTION** A1

Levels: A1 and A2: Basic user; B1 and B2: Independent user; C1 and C2: Proficient user

JOB-RELATED SKILLS

- Computational modeling and drug design techniques including pharmacophore modeling, virtual screening, docking, QSAR techniques, homology modeling and molecular dynamics simulations (through Master degree and PhD studies).
- Organic synthetic chemistry techniques (through Master degree study).
- Analytical method development using various analytical techniques for example: HPLC, GC, UV spectroscopy, atomic absorption spectroscopy, various titration techniques.
- Analytical method validation.

CONFERENCES AND SEMINARS

[13/05/2024 – 15/05/2024] Leiden - Netherlands

2024 Workshop on Free Energy Methods in Drug Design

[25/09/2023 – 27/09/2023] Leipzig - Germany

European RosettaCon - Protein Design in The Age of Artificial Intelligence

[10/09/2023 – 15/09/2023] Vienna - Austria

Vienna Summer School on Drug Design

[26/09/2022 – 30/09/2022] Heidelberg- Germany

23rd European Symposium on Quantitative Structure Activity Relationship

[13/09/2021 – 17/09/2021] Online version

Vienna Summer School on Drug Design

HONOURS AND AWARDS

[01/03/2021] DAAD Stiftung -DAAD

Professor Mahfouz Kasem Scholarship Three months short term research scholarship.

[01/06/2021] Al-Alfi Foundation for Human and Social Development

Al-Alfi Foundation Scholarship Fully funded three years PhD scholarship.

POSTER PRESENTATION

[26/09/2022 – 30/09/2022]

AlphaFold HDAC11 Homology Model Optimization and Utilization for Docking and Molecular Dynamics Simulation of Selective Inhibitors.

EuroQSAR Symposium - Heidelberg - Germany

[10/09/2023 – 15/09/2023]

Exploration of the Foot Pocket of HDAC11 Utilizing Optimized AlphaFold Model and Selective Inhibitors

EUROPIN Summer School on Drug Design – Vienna- Austria

PUBLICATIONS

- **Baselious F**, Hilscher S, Hagemann S, Tripathee S, Robaa D, Barinka C, Hüttelmaier S, Schutkowski M, Sippl W. Utilization of an Optimized AlphaFold Protein Model for Structure-Based Design of a Selective HDAC11 Inhibitor with Anti-neuroblastoma Activity. Arch Pharm. 2024 Jul 12; e2400486.

- **Baselious F**, Hilscher S, Robaa D, Barinka C, Schutkowski M, Sippl W. Comparative Structure-Based Virtual Screening Utilizing Optimized AlphaFold Model Identifies Selective HDAC11 Inhibitor. Int J Mol Sci. 2024 Jan 22;25(2):1358.

- **Baselious F**, Robaa D, Sippl W. Utilization of AlphaFold models for drug discovery: Feasibility and challenges. Histone deacetylase 11 as a case study. Comput Biol Med. 2023 Dec;167:107700.

- Odeh DM, Allam HA, **Baselious F**, Mahmoud WR, Odeh MM, Ibrahim HS, Abdel-Aziz HA, Mohammed ER. Design, synthesis, and biological evaluation of dinaciclib and CAN508 hybrids as CDK inhibitors. Drug Dev Res. 2024 May 29;85(3).

- Metwally HM, Abdelrasheed Allam H, **Baselious F**, Bonardi A, Seif EM, Moussa SA, Abdel-Latif E, Supuran CT, Ibrahim HS. Arylidine extensions of 3-methyl-5-oxo-4,5-dihydro-1H-pyrazol-benzenesulfonamide derivatives: Synthesis, computational simulations and biological evaluation as tumor-associated carbonic anhydrase inhibitors. Bioorg Chem. 2023 Jun;135:106492.

- Opitz A, Seitz LM, Krystof V, **Baselious F**, Holzer M, Sippl W, Hilgeroth A. Novel effective small-molecule inhibitors of protein kinases related to tau pathology in Alzheimer's disease. Future Med Chem. 2022;14(16): 1175–86.

- Ismail NSM, Elzahabi HSA, Sabry P, **Baselious FN**, AbdelMalak AS, Hanna F. A study of the allosteric inhibition of HCV RNA-dependent RNA polymerase and implementing virtual screening for the selection of promising dual- site inhibitors with low resistance potential. J Recept Signal Transduct. 2017; 37(4):341–54.

- Ismail NSM, George RF, Serya RAT, **Baselious FN**, El-Manawaty M, Shalaby EM, Girgis AS. Rational design, synthesis and 2D-QSAR studies of antiproliferative tropane-based compounds. RSC Adv. 2016;6(104):101911– 23.

- Mabied AF, Girgis AS, Shalaby E-SM, George RF, El-Gendy BE-DM, **Baselious FN**. Stereoselective Synthesis, Structural and Spectroscopic Study of 4,5,11-Triazatricyclo[6.2.1.0*2,6*]Undec-5-ene. J Heterocycl Chem. 2016; 53(4):1074–80.

Selbstständigkeitserklärung/Declaration of Authorship

Hiermit erkläre ich, dass ich die vorliegende Dissertationsschrift selbständig und ohne fremde Hilfe angefertigt, keine anderen als die angegebenen Quellen und Hilfsmittel benutzt und die aus ihnen wörtlich oder inhaltlich entnommenen Stellen als solche kenntlich gemacht habe. Die Arbeit wurde ausschließlich der Naturwissenschaftlichen Fakultät I Biowissenschaften der Martin-Luther-Universität Halle-Wittenberg vorgelegt und an keiner anderen Universität oder Hochschule weder im In- und Ausland zur Erlangung des Doktorgrades eingereicht.

I hereby declare that I am the sole author of this thesis and that I have not used any sources other than those listed in the bibliography and identified as references. I further declare that I have not submitted this thesis at any other institution in order to obtain a degree.

Halle (Saale), 06.08.2024